The Rapidity Dependence of High p_T Suppression in Au+Au Collisions at BRAHMS Experiment

Dissertation
presented for the degree of
Doctor of Philosophy in Physics
by

Cătălin Ristea

August, 2007

NIELS BOHR INSTITUTE
faculty of science – university of copenhagen

The Rapidity Dependence of High p_T Suppression in Au+Au Collisions at BRAHMS Experiment

by Cătălin Ristea
Supervisor: Prof. Dr. Jens Jørgen Gaardhøje

This dissertation is approved by:

Prof. Dr. Mogens Dam (chair)
University of Copenhagen

Prof. Dr. Michel Gonin
École Polytechnique

Prof. Dr. Hans-Åke Gustafsson
University of Lund

2007

NIELS BOHR INSTITUTE
FACULTY OF SCIENCE – UNIVERSITY OF COPENHAGEN

Abstract

Heavy ion collisions at relativistic energies aim to produce and study in laboratory the quark-gluon plasma (QGP), a new state of matter in which the quarks and gluons are deconfined. These collisions give the opportunity to have an insight into the early stages of the Universe, a few microseconds after Big Bang, when it is believed that the QGP existed.

In such collisions, the high transverse momentum particles are produced from hard scatterings of the partons. If deconfined matter is formed by Au+Au collisions, it is expected that the scattered partons lose important fraction of their energy while traversing the hot and dense matter and production of high p_T particles is suppressed.

Exploring the rapidity dependence of the high p_T suppression is important to extract information about the properties of the dense matter in the longitudinal direction in the very early stage of a central Au+Au collision. Jet energy loss is proportional to the density of the local medium and to the jet path length through the medium. Different rapidities provide different densities of the medium, through which the high momentum jet travels. At forward rapidities the overall charged-particle density is smaller than at mid-rapidity, suggesting a less dense medium and, correspondingly, a reduced energy loss. However, it is possible that the average path lengths for jets through the medium may be different at forward rapidity than at midrapidity, possibly compensating for the lower medium density.

This thesis presents the rapidity and centrality dependence of the transverse momentum spectra and yields of charged hadrons, as well as identified pions, kaons, protons and their antiparticles produced in Au+Au and p+p collisions at $\sqrt{s_{NN}}$=200 GeV with the BRAHMS experiment at RHIC. BRAHMS has the unique capability to measure particle production, not only at midrapidity, but over a wide p_T and rapidity range.

We report on the (pseudo)rapidity dependence of nuclear modification factors in Au+Au collisions at $\sqrt{s_{NN}}$=200 GeV. For the most central Au+Au collisions the suppression persists over 3 units in pseudorapidity for charged hadrons. The results are compared with the prediction of several theoretical models.

The nuclear modification factor for identified particles shows a distinct meson/baryon dependence. In central Au+Au collisions at $\sqrt{s_{NN}}$=200 GeV, there is a significant suppression in meson yield compared to a binary scaled p+p reference. In contrast, an enhancement of baryons relative to mesons is observed in the intermediate p_T region. The mechanism based on initial hard parton scattering and jet fragmentation is not sufficient to explain this particle type dependence. Hadronization processes through multi-parton dynamics such as recombination and coalescence models are likely to be important for explaining baryon enhancement in high-energy Au+Au collisions.

Acknowledgements

The last three years have passed like a blink of an eye, loaded with tons of interesting experiences and hard work. There are even more years since I've started to work aside people from the BRAHMS Collaboration.

First of all I am extremely grateful to Jens Jørgen Gaardhøje for giving me the once in a lifetime opportunity to join this dedicated, professional and challenging group that HEHI is. He was an excellent supervisor and a great support over all these three years.

I do not have enough words to thank Ian Bearden for everything. No matter what time, or how busy he was, Ian had always the time to come up with great suggestions and ideas "out of the pattern".

I did the first steps here at NBI helped by Peter Christiansen and Claus Jørgensen. I am only sorry that I did not have the chance to work more together with them. I will always remember nice discussions and the help with the teaching that I've got from Hans Bøggild and Børge Nielsen.

I have only the best things to say about Christian Holm Christensen and Truls Martin Larsen, with whom I have shared the work as Ph.D. student. Thank you, guys, and the same for Kristján Gulbrandsen and Gael Renault. Thanks for the nice atmosphere created in our working room by all the HEHI students: Casper, Hans, Per, Stephan, Rasmus, David, Carsten, Henrik, Frederik, Johann.

I owe special thanks to Flemming Videbæk for guiding my work, for the patience and the encouragements over the last, how many, seven years, for the example given in perseverance and achievement of (always) better results. From him I have learnt the most. I am grateful to everyone of the handful of people that BRAHMS is, it was a pleasure working with you.

I am also grateful to the people from Bucharest University, that helped me become who I am. I especially thank to Calin Besliu, for bringing forward the scent of old physics fashion, the enthusiasm and the passion for the physics, and to Alexandru Jipa, for everything that he taught me. I thank also to the people from my former workplace, the Institute of Space Sciences from Bucharest, and I am thinking to Sorin, Daniel, Ionut, Mihaela, Andrei and many others.

Very special thanks to Ian and Flemming, for revisiting this work.

Finally, I owe big thanks to my family for all the support and encouragements, and to my sister and brother in law, Cristina and Costin. I don't have enough words for Oana, my wife... everything I do it is dedicated to her. Ne intoarcem acasa.

Catalin Ristea,
NBI, August 2007.

Contents

Chapter 1

Relativistic Heavy-Ion Collisions. Quark Gluon Plasma.

1.1 Quantum Cromodynamics

Quantum Cromodynamics (QCD), the theory of strong interactions, describes the structure of the hadrons and their interactions. The hadrons are combinations of fundamental particles called quarks [1] - three quarks qqq for baryons and a quark-antiquark pair $q\bar{q}$ for mesons - bound together by the strong force. In QCD, the strong force (or color force) between the quarks is mediated by massless particles called gluons.

There are six flavors of quarks with distinct masses and properties: up (u), down (d), strange (s), charm (c), bottom (b) and top (t), grouped into three families or generations (u,d), (c,s), and (t,b). For every quark, an anti-quark exists having opposite quantum numbers. Table 1.1 lists known characteristics of the quarks [2].

Quarks having spin s = 1/2 are fermions and carry a fractional baryon number B = 1/3 (so that a baryon has baryon number of 1 and a meson has baryon number of 0) and electric charges that are fractions of the electron charge (either -1/3 or 2/3). The Pauli exclusion principle states that no two fermions may exist in the same quantum state. Therefore, it's not possible to make hadrons from quarks with the same quantum numbers. Hence the need of an additional quantum number for the strong interaction, the color. The color quantum number (called "color charge", also) can take three values for quarks (plus three opposite values for anti-quarks). These values are conventionally designated red (r), green (g) and blue (b). Experimentally, the support for color quantum number came from the study of particles such as $\Delta^{++}(uuu)$, $\Delta^{-}(ddd)$, $\Omega^{-}(sss)$. Each of these particles consists of three identical spin 1/2 quarks and has a spin of 3/2 so all three quarks appear to be in identical quantum states. The Pauli's principle gets fulfilled by requiring different color charge for each of the constituent quarks.

Isolated quarks have never been observed in nature, which leads to the idea that all hadrons must

$Name$	$Symbol$	$Mass[MeV]$	$Charge(e)$	$QuantumNumber$
Up	u	$1.5 \rightarrow 3$	$+\frac{2}{3}$	$Isospin = +\frac{1}{2}$
$Down$	d	$3 \rightarrow 7$	$-\frac{1}{3}$	$Isospin = -\frac{1}{2}$
$Strange$	s	95 ± 25	$-\frac{1}{3}$	$Strange = -1$
$Charm$	c	1250 ± 90	$+\frac{2}{3}$	$Charm = +1$
$Bottom$	b	4200 ± 70	$-\frac{1}{3}$	$Bottom = -1$
Top	t	174200 ± 3300	$+\frac{2}{3}$	$Top = +1$

Table 1.1: Quarks properties.

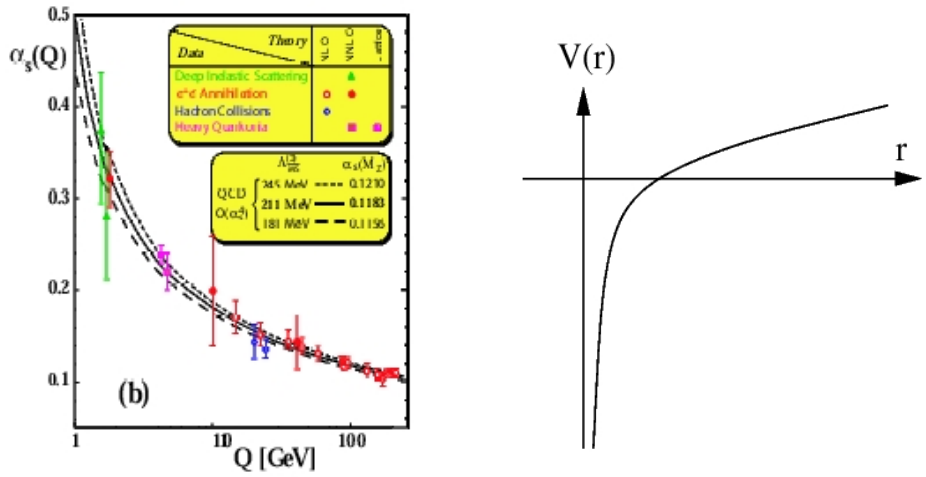

Figure 1.1: Left: The strong coupling constant α_s as a function of the momentum transfer Q. The figure is taken from ref. [3]. Right: The quark potential as a function of the distance between the quarks.

be color-neutral objects. In the case of mesons ($q\bar{q}$), the anti-quark must carry the anti-color charge of the quark to remain a color-neutral combination.

One particular feature of QCD is that not only the quarks carry color charge, but also the gluons. There are 8 physical gluons carrying both a color charge and an anti-color charge. Since the gluons carry color charges, they can interact directly with each other. This selfinteraction is thought to be the reason for parton confinement within hadrons.

The effective coupling constant, which describes the probability to have an interaction between a quark and a gluon, depends on the energy scale at which the interaction occurs. It is expressed as:

$$\alpha_s(Q^2) = \frac{12\pi}{(33 - 2n_f)ln(\frac{Q^2}{\Lambda^2_{QCD}})} \tag{1.1}$$

where n_f is the number of quark flavors, Q^2 is the momentum transfer between the interacting particles and Λ_{QCD} is the renormalization parameter of the QCD. The Λ_{QCD} constant is regarded as defining the scale of the strong interactions, and has been measured to be 200MeV [4]. It differentiates between a system of confined hadrons, and a system where the partons no longer feel the strong force ($Q^2 \gg 200$MeV). Left panel of Figure 1.1 shows α_s dependency on the momentum transfer.

- at short distances (or large momentum transfer, Q) the coupling constant decreases logarithmically. Therefore the quarks and gluons are weakly coupled and they behave as free particles. This property of QCD is known as asymptotic freedom [5].

- at large distances (or small momentum transfer, Q), the coupling constant is large and the quarks and gluons are confined in hadrons.

"Hard" processes are interactions which occur with large momentum transfer and are characterized by $\alpha_s \ll 1$. These processes allow calculations to be performed within perturbative framework (pQCD), based on an expansion in powers of the coupling constant (and physics quantities can be calculated in a power series as leading order, next-to-leading order). Typically the lower limit of momentum transfer favorable for pQCD is $Q^2 \sim 2\ GeV^2$, which corresponds to $\alpha_s \sim 0.3$ [6]. In fact, pQCD has been proven to describe a large set of high energy, large momentum transfer processes with outstanding accuracy.

The first experimental evidence for quarks as real constituent elements of hadrons was obtained in Deep Inelastic Scattering (DIS) experiments [7]. DIS experiments measure the total inelastic cross-section of leptons scattering from nucleons and it was found that the cross-section is approximately independent of the Q^2 of the collisions. This fact can be understood as projectile leptons scattering from point-like objects inside the nucleons. These point-like constituents were first called partons (since they were part of the hadrons) and later identified with the quarks. In these experiments, the incident electron interacts with a quark within a hadron and is accompanied by the momentum transfer from the electron to the quark. The measurement of the electron momentum before and after the interaction allows a probe of the momentum distribution of partons inside the nucleons.

Interactions that occur at small momentum transfer are "soft" processes and can not be treated perturbatively. Soft processes create the hadrons that are measured by experiment. Among non-perturbative approaches to compute QCD predictions in this regime, the most well established one is lattice QCD. Lattice calculations are numerical solutions of the QCD equations of motion on a four dimensional lattice of space-time points.

1.1.1 Confinement

The interaction between quarks is based on their intrinsic color charge, just as that between electrons and protons or nuclei is determined by their electric charge. The form of the interaction is quite different, however. The Coulomb potential vanishes for large separation distance, so that electric charges can be separated and have an independent existence. In contrast, the potential between quarks increases with separation, so that an infinite energy would be needed to isolate a quark. In other words, the quark constituents of a hadron are confined, not just bound.

At zero temperature the potential between a heavy quark and an anti-quark may be considered as the sum of a coulomb like, 1/r type term, and a term which is linear in r, as given by

$$V(r) = \sigma r - \frac{4}{3}\frac{\alpha_s}{r} \tag{1.2}$$

where α_s is the strong coupling constant, r is the separation between the two quarks and σ is a constant named the string tension (>1 GeV/fm), which measures the energy per unit separation distance [8, 9]. Right panel of Figure 1.1 shows this potential as a function of the distance.

At large separation distance, the first term is dominant and the potential is approximately linear. For a simple intuitive picture of confinement at large r, a quark and an anti-quark can be viewed as being connected by a "string" whose potential increases linearly as they are pulled apart. At some point, the string breaks but instead of isolating the quark and anti-quark, there are now two strings, each with a $q - \bar{q}$ pair; confinement persists. This analogy illustrates the idea that at some point during the $q - \bar{q}$ separation, it becomes energetically favorable to spontaneously produce a $q - \bar{q}$ pair out of the QCD vacuum. The new quarks recombine with the original ones forming hadrons, and the confinement is preserved.

Decreasing the distance between the quarks, the "Coulomb" like term, which comes from single gluon exchange, dominates the potential. Therefore, the quark-quark interaction becomes weaker; in the limit $r \to 0$, the quarks act as quasi-free particles (asymptotic freedom).

1.1.2 Debye Screening

In a high temperature, deconfined medium, screening effects due to the large density of charge carriers may become important and thus the form of the potential changes to a Yukawa type potential

$$V(r) = \sigma r \left[\frac{1 - e^{-\mu_D r}}{\mu_D r}\right] - \frac{4}{3}\frac{\alpha_s}{r}e^{-\mu_D r} \tag{1.3}$$

where $\mu_D = 1/\lambda_D$ is the Debye mass and $\lambda_D(T) \sim 1/T$ is the Debye screening length for color charges, defining the range of the force remaining effective between charges in the medium [8, 9]. This phenomenon is called Debye screening [1] , in analogy to the dielectric screening in QED.

Screening is a global feature of the medium, shortening the range of the binding potential. The color screening radius λ_D, which determines this range, is inversely proportional to the density of charges, so that it decreases with increasing temperature. As a result, the $q\bar{q}$ interaction becomes more and more short-ranged. When $\lambda_D(T)$ falls below the binding radius r_i of a $q\bar{q}$ state i, the q and the $\bar{q}$ can no longer bind, so that the bound state i cannot exist [10, 11]. The bound state dissociation points T_i, specified through $\lambda_D(T_i) \approx r_i$, thus determine the temperature of the deconfined medium. Above T_c, the quarks and gluons become deconfined color charges, and this quark-gluon plasma (see section 1.1.3) leads to a color screening, which limits the range of the strong interaction.

Because of the Debye screening process, it is therefore expected that with increasing temperature, strongly interacting matter will undergo a transition from a hadronic phase, in which the constituents are color-neutral bound states, to a plasma of deconfined color-charged quarks and gluons [12, 13, 14, 15]. The process of Debye screening is important for calculating the conditions necessary for deconfinement, as it occurs at much lower energy density than those required for an asymptotically free plasma.

1.1.3 Quark gluon plasma

The prediction of a new state of strongly interacting deconfined matter led quite naturally to the question of where and how to observe it. The only way to achieve this, as far as we know, is to collide two highly energetic heavy nuclei and study the resulting small and short-lived droplets of hot and dense medium. For such studies it is essential to have viable probes which can determine if the created matter in the early stages of nuclear collisions indeed consisted of unbound quarks and gluons: we have to find signatures of color deconfinement.

Knowledge about QGP and its properties allow us to get informations on the very first moments of the Universe, right after the Big Bang. It is thought that for a few microseconds after the Big Bang [16], the energy density and temperature of the universe was still sufficiently high to produce this deconfined quarks and gluons. As the universe expanded and cooled, this plasma coalesced into protons and neutrons (hadronization), followed by the formation of bound nuclei (nucleosyntesis) and later, the atoms and molecules were formed. The QGP of the early universe was characterized by low baryon density due to almost equal numbers of quarks and antiquarks.

In the modern universe, the naturally formed QGP might be in the core of dense neutron stars [17, 18]. They are formed when a heavy star has spent all its fusionable fuel and collapses under its own gravity. At the very high pressure involved in this collapse, it is energetically favorable to combine protons and electrons to form neutrons plus neutrinos. The neutrinos escape and the neutrons settle

[1] Such an effect is observed in quantum electrodynamics (QED). An electron constantly emits and reabsorbs virtual photons which can produce virtual e^+e^- pairs. This cloud of virtual electrons and positrons produces a shielding effect called vacuum polarization in QED. In the vicinity of a charge, the vacuum becomes polarized: virtual particles of opposing charge are attracted to the charge, and virtual particles of like charge are repelled. Outside the system the charge of electron appears smaller than the charge for an isolated system. The effect could also be understood as an overlapping between the charge density of the electron and the charge density of the virtual pairs. In this manner the vacuum acts like a dielectric medium, which has the effect of reducing the magnitude of the electric field in the vicinity of the original electron. Therefore, as a test charge moves closer to the original electron, the value of the electric charge of the electron it sees increases, until at very small distances, it reaches the full value of the bare charge.

In QCD, the gluons are massless, and their strong interaction is not characterized by a small coupling parameter. As a result, the QCD vacuum polarization effect is extremely strong, and the vacuum is not empty at all - it contains a "soup" of spontaneously appearing, interacting, and disappearing gluons. Moreover, in the "soup" there also must be virtual quark-antiquark pairs that are also color-charged, and emit and absorb more virtual gluons. An individual quark is surrounded by $q\bar{q}$ pairs, which are analogous to the e^+e^- pairs in QED, and also have a screening effect on the quark's color charge. The gluon pairs, which carry a net color charge, have an anti-screening effect. Getting closer to a quark diminishes the antiscreening effect of the surrounding virtual gluons, so the contribution of this effect would be to weaken the effective charge with decreasing distance.

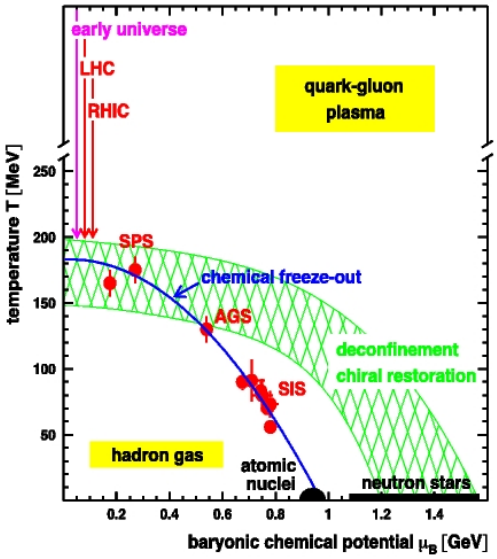

Figure 1.2: The phase diagram of nuclear matter shows how deconfinement can occur in extreme conditions of temperature (Big Bang, RHIC) and density (dense stellar matter like neutron stars). The cross-hatched region indicates the expected phase transition and it's present theoretical uncertainty based on lattice QCD calculations at $\mu_B = 0$. The points indicate the region reached by different experiments (ref. [19]).

down to become a neutron star. Some models predict that this can result in cold matter at about 5 times the density of normal nuclear matter where the nucleons merge together and lose their identity.

But the big bang was long ago, and neutron stars are far away. At present, in laboratory, there are two ways to produce QGP through the relativistic collisions of heavy ions, as can be seen from the phase diagram of nuclear matter $T - \mu_B$, where T is the temperature and μ_B is the baryon chemical potential [19].

- compressing the nuclear matter. Because the baryon number, which is carried by neutrons and protons, is conserved, the nucleons cannot disappear and will start to overlap when the average inter-particle distance is smaller than the nucleon radius $r_N \sim 1$Fm (the inter-nucleon separation is smaller than r_N at densities larger than $\sim 6\rho_0$, where $\rho_0 = 0.17$ Fm^{-3} is the normal nuclear matter density). Eventually each quark finds within its immediate vicinity a considerable number of other quarks. At extreme density, it becomes impossible to identify among all the overlapping states a specific quark-antiquark pair or quark triplet as belonging to a certain hadron. The medium becomes instead a dense multi-quark environment in which any quark can move freely throughout the system volume.

- heating the nuclear matter (or the hadron gas). In the contrast to the baryon or lepton number, which are the conserved quantities, the particle number is not. Therefore, when the gas temperature (measured in units of energy) becomes comparable to the particle mass, further heating leads not only to the increase of the average particle kinetic energy but to the growth of the average particle number. The particles produced can not violate conservation laws - baryon number and electrical charge are conserved - thus, particles are produced in particle-antiparticle pairs. For example, to keep the baryon number of the system conserved, only pairs of baryon and anti-baryon are added to the system. Neutral charge particles, not having conserved charges, can be added to the system without restrictions, although the average particle number is controlled by the equilibrium conditions. More specifically, the numbers are determined by the minimum

of the system free energy when the system temperature and volume are fixed [20].

In either case, the medium will undergo a transition from a state in which its constituents were colorless, i.e. color-singlet bound states of colored quarks and gluons, to a state in which the constituents are colored.

As illustrated in the Figure 1.2, as the available energy is larger, the baryon chemical potential decreases and the temperature increases. Depending on the species of the collision partners and their energy, different regions of the phase diagram can be explored. The points show the systematic measurements done for beam energies starting with SIS up to the RHIC, obtained from an analysis of particle yield ratios. The two cases for a QGP in nature mark the extreme points in the phase diagram: neutron stars with low temperature and high net baryon density, and the early universe almost net-baryon free at high temperature.

The region studied by heavy ion collisions at the Relativistic Heavy Ion Collider (RHIC) from the Brookhaven National Laboratory (BNL) is characterized by large temperatures and almost zero baryon chemical potential [21].

1.2 Lattice QCD

Lattice Quantum Chromodynamics (Lattice QCD) [22, 23, 24] is the QCD theory of quarks and gluons formulated on a space-time lattice (a discrete set of space-time points) of size $N_\sigma^3 \times N_\tau$. Quarks are placed in the points of the lattice and are connected via gluons. Therefore it becomes possible to simulate the quark interactions. The lattice spacing, a, is the quark separation distance and relates the spatial (N_σ) and temporal (N_τ) size of the lattice to the physical volume $V = (N_\sigma a)^3$ and temperature $T = 1/N_\sigma a$, respectively. It was shown that, as this dimension is reduced, the value of strong coupling constant is smaller, as one expects theoretically. The number of lattice points used in a calculation is limited by the available computing power.

Detailed information on the temperature dependence of thermodynamic observables, such as pressure or energy density, and how these quantities change as the system passes through the deconfinement transition have been obtained through lattice calculations performed in the limit of vanishing baryon number density or, equivalently, vanishing quark chemical potential ($\mu_q = 0$). This limit is most relevant for our understanding of the evolution of the early universe. It also corresponds to the regime which currently is studied experimentally in heavy ion collisions at RHIC (BNL) and soon will be explored also at the LHC (CERN).

The experimental accessibility of this regime of dense matter also asks for a quantitative study of the QCD phase transition and of basic parameters that characterize the thermodynamics of dense matter at high temperature, e.g. the transition temperature T_c and the energy density ϵ_c at this temperature. Current estimates suggest a transition temperature of Tc = 192(7)(4) MeV, with almost physical light quark masses and a heavier strange quark mass [25]. The value of the critical temperature obtained recently is about 10% larger than the frequently quoted value $\sim$ 175 MeV. Also, an energy density $\epsilon_c \sim 1$ GeV/fm^3 was found, though with an error of about 50% due to the uncertainty on the calculated T_c.

Left panel of Figure 1.3 shows the energy density, ϵ, scaled by T^4, as a function of system temperature T scaled by T_c, at $\mu_B = 0$. The values are computed for three cases: system with 2, 3 and 2+1 flavors [22]. At high temperature, it is expected that ϵ/T^4 will asymptotically approach the ideal gas limit (Stefan-Boltzmann limit), which is roughly proportional to the number of particle degrees of freedom. At temperatures below the critical temperature T_c the number of degrees of freedom is $g_h = 3$ for the hadronic gas (only pions). Above T_c, there are g_g=2×8 for the gluons and N_q=3×2×2×N_f for the quarks, where N_f is the number of flavors. Therefore, the number of degrees of freedom for a QGP is ∼40-50. Because the energy density and the pressure are proportional with the NDF of the QGP (from the equipartition of the energy theorem), one concludes that such a large increase of the energy density in a narrow range of temperature $\Delta T \sim 10 - 20$ MeV could be related

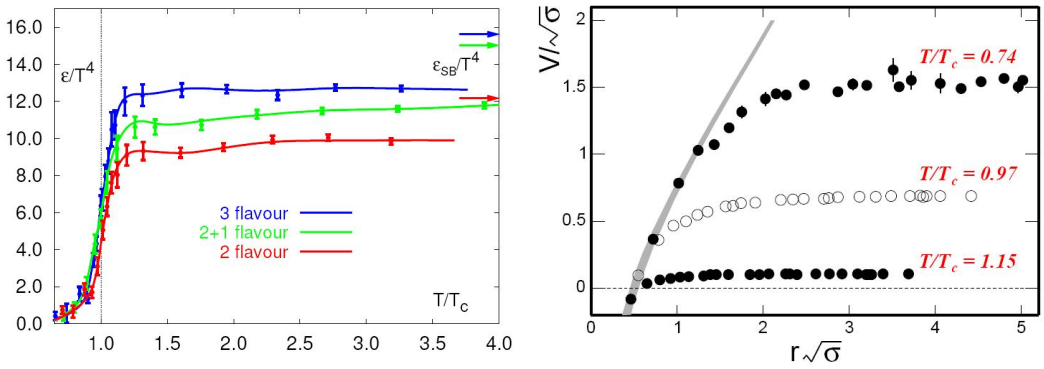

Figure 1.3: Left: Lattice QCD results show the energy density vs. the temperature, arrows indicate the ideal gas value, figure from ref. [22]. Right: The heavy-mass quark potential in different temperature cases [26]. The band depicts the potential $V(r) = -\alpha/r + \sigma r$ with $\alpha = 0.25 \pm 0.05$.

to a dramatic increase of the number of degrees of freedom associated to the transition from hadronic matter to quark-gluon plasma. The curves clearly reflect the strong change in the number of degrees of freedom when going through the transition. From the figure, it is evident that even at $T > 4T_c$ the Stefan-Boltzmann limit (indicated by the arrows in the figure) is not reached. This has been taken as an indication of a significant amount of strong interactions among the partons in the high temperature phase.

Lattice QCD calculation of the potential between two heavy-mass quarks [26] also offers evidence of deconfinement. Right panel of Figure 1.3 shows the potential in different temperature conditions for three flavors: with the increase of the temperature the potential is changing. As the temperature exceeds the critical temperature T_c, the quark binding potential deviates from the vacuum potential and decrease to zero, indicating that the interaction among partons becomes very weak above the critical temperature. Thus, they become asymptotically free at high temperature.

The question on the order of the phase transition (1 or 2) is still under investigation, because this order is dependent on the number of the quark flavors and the quark masses used in the computation [27]. Many lattice calculations, performed in recent years, suggest that for physical values of the quark masses, the transition to the high temperature phase of QCD is not a phase transition but rather a rapid crossover that occurs in a small, well defined, temperature interval.

What is very important is that the lattice QCD calculations indicate that the critical temperature is approximately 190 MeV, a temperature accessible to actual colliders. The RHIC collider accelerates and collides heavy ions at relativistic energies to produce matter at a temperature above the T_c in order to study this phase transition.

1.3 Relativistic heavy ion collisions

Normal nuclear matter consists of nucleons of mass 0.94 GeV and has a density of 0.17 nucleons/fm^3; hence it's energy density is 0.16 GeV/fm^3, i.e., well below the 1 - 2 GeV/fm^3 necessary for deconfinement. We want to collide two heavy nuclei with the aim of increasing the density of matter as far as possible beyond this value. This can be achieved either by shooting accelerated ions at a stationary target, or by head-on collisions of two ion beams. In order to achieve the biggest volume of excited nuclear matter, very heavy nuclei such as gold (Au) or lead (Pb) are used. The kinetic energy of the incident projectiles would be dissipated in the large volume of nuclear matter involved in the reaction. The system is expected to come to equilibrium, thus heating and compressing the nuclear matter so that it undergoes a phase transition from a state of nucleons containing bound quarks and gluons to a state of deconfined quarks and gluons, the Quark Gluon Plasma, covering the fireball volume.

Currently there are four major facilities where such experiments are carried out. At the Schwerionen-

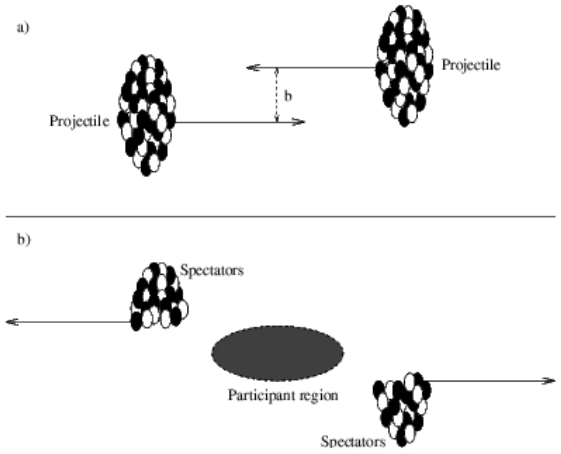

Figure 1.4: Schematic view of a relativistic heavy ion collision (a) before and (b) after the collision. Non interacting nucleons are spectators, while interacting nucleons are participants.

Synchrotron (SIS) at the Gesellschaft fur Schwerionenforschung (GSI) nucleus-nucleus collisions at beam energies of up to 1 GeV per nucleon (for Uranium) are studied. Higher energies are reached at the Alternating Gradient Synchrotron (AGS) and the Relativistic Heavy Ion Collider (RHIC) at Brookhaven National Laboratory (BNL), and the Super Proton Synchrotron (SPS) at the Conseil Europeen pour la Recherche Nucleaire (CERN). SIS, AGS and the SPS have fixed-target experimental programs, while RHIC, which began operation in 2000, collides two ion beams, thus reaching much higher center-of-mass energies.

1.3.1 Collision Geometry

In a low energy nucleus-nucleus collision, the two nuclei will remain intact and simply "bounce off" each other. With increasing energy, they will start to see each other as "clouds" of nucleons and penetrate each other more and more, leading to highly excited nuclear matter. If the collision energy is increased still further, nuclear transparency begins to set in and the two colliding nuclei pass through each other.

A schematic drawing of a relativistic heavy ion collision in the center of mass system is shown in Fig. 1.4. In the region of overlap, the participating nucleons interact with each other leading to the formation of a hot and dense region, the fireball, while in the non-overlap regions, the spectator nucleons simply continue on their original trajectories.

The nuclear collisions can be reliably classified according to their centrality - a variable measuring the degree of overlapping between two colliding nuclei. Centrality is closely related to the impact parameter b, that is defined as the transverse distance between the centers of two colliding nuclei, with b$\sim$0, being the most central and b$\sim$2R, the most peripheral. The plane defined by the beam axis (z) and $\vec{b}$ is called "reaction plane", which represents the relative orientation of the colliding nuclei.

It is not possible to directly measure the impact parameter of the collision, so one must use an indirect measure. The event multiplicity is one of the observables that is correlated to the impact parameter. Usually, the centrality is determined by measuring the multiplicity of the charged particles produced in the collision [28].

Two additional concepts correlated with the impact parameter are the number of participants, N_{part}, and the number of binary collisions, N_{bin}. In highly energetic nuclear collisions, charged particles can be produced by hadronic (soft) as well as partonic (hard) collision processes. The scaling of multiplicity with the number of participants is considered to be a reflection of the particle

production due to soft processes. At high energy, it is expected that there will be an increased particle production from hard processes. Hard process cross section in pA collisions, e.g. the p_T distributions at high p_T are found to be proportional to the number of elementary nucleon-nucleon collisions (called the number of binary collisions). Some models include for example the assumption that the particle production is derived from a linear combination of the soft and hard processes, i.e. linear combination of N_{part} and N_{bin} [29, 30].

N_{part} refers to the number of nucleons that were hit or that interacted, which is why they are also sometimes called "wounded nucleons". For a head-on collision (b=0) ^{197}Au+^{197}Au collision, assuming the nucleus to be a hard sphere, or rather, to be a bag filled with hard spheres, $N_{part} = A + A = 394$. There will be deviations from this, as one introduces a more realistic density profile for the Au nucleus (Woods-Saxon distribution). N_{bin} refers to the number of elementary nucleon-nucleon collisions. Since each nucleon in a nucleus can interact many times as it punches through the other nucleus, then $N_{bin} \geq N_{part}$. Neither the number of participants not the number of binary collisions is a directly observable experimental quantity and it is necessary to rely on model calculations for these values. They can be estimated by the Glauber model [31, 32].

1.3.2 Landau vs. Bjorken

There are two extreme scenarios for the formation of the collision fireball depending on the nuclear stopping in the reaction: full stopping (Landau model) and full transparency (Bjorken model).

Full stopping (Landau model)

As the $\sqrt{s_{NN}} < 10GeV$, the two Lorentz contracted nuclei, having the radius R/γ, are stopping completely each other in the center of mass reference frame (CMS) and generate a dense fireball [33]. In this scenario, the initial nucleons have less energy and have secondary and tertiary interactions until they are all stopped in the CMS. A baryon-rich plasma is produced, as all of the initial baryons are concentrated at mid-rapidity. Energy density gets as high as few GeV/Fm^3 inside the stopped matter, but the baryon density are 10 times higher than normal nuclear matter density. Consequently, one may consider that all the available energy in the CMS, $W = 2Am_N\gamma$ and the total baryon number, $N_B = 2A$ reach the equilibrium inside the full volume of the Lorentz contracted nuclei, $V_{cm} = V_0/\gamma$, where γ is the relativistic factor equal to $\gamma = 1/\sqrt{1 - v^2/c^2}$. Therefore, the energy density and

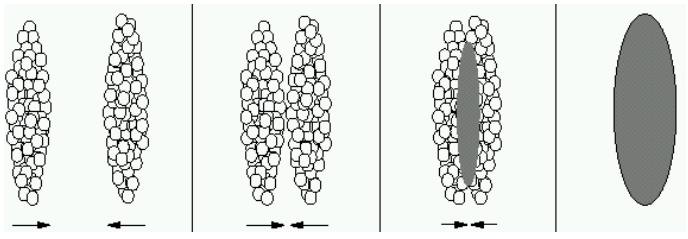

Figure 1.5: The description of a central heavy ion collision in Landau's model (full stopping).

baryon density are, as a function of γ:

$$\epsilon = \frac{W}{V_{cm}} = 2\epsilon_0\gamma^2, \qquad n_B = \frac{N_B}{V_{cm}} = 2n_0\gamma \tag{1.4}$$

where $\epsilon_0 = Am_N/V_0 = 0.16$ GeV/Fm^3 and $n_0 = A/V_0 = 0.17$Fm^{-3} are the normal nuclear matter energy and baryon densities. In the participant region the system reaches local equilibrium because of the collisions between the participants. Then the system expands hydrodynamically.

Transparency (Bjorken model)

As the $\sqrt{s_{NN}} > 10GeV$, nuclear transparency sets-in, because the two nuclei are passing through each other, rather than stopping each other. In 1983, it was Bjorken [34] who proposed this scenario of the fireball evolution from relativistic heavy ions collisions, based on two assumptions, namely:

- for the nucleus-nucleus collisions, there is a "central-plateau" structure in the inclusive particle production as a function of the rapidity. Therefore, the rapidity density dN/dy of the produced particles is independent of rapidity over few units around the midrapidity, namely the boost invariance (boost transformations are Lorentz transformations along the beam axis). Thus, in the central rapidity region, the evolution looks the same no matter what the reference frame.

- for a transparent collision, the net-baryon number, $N(B)-N(\bar{B})$, is shifted toward higher rapidity and the collision's transparency depends on the dynamic of baryon number transport ("leading-baryon" effect).

Due to increased energy available in one collision, the time of particle production is larger than the time it takes the nuclei to pass through each other. The time it takes to produce a particle is $t_0 \sim \hbar/mc^2$ (for a π, $t_0 \sim 1$Fm/c). This time is larger in the laboratory frame of reference, by the Lorentz factor γ, $t = \gamma t_0$. This time is considerably large in the case of relativistic energies, because of the large Lorentz factor, $t \sim 100$Fm/c. New particles are produced consequently after the nuclei have passed through each other, $t > 2R/c$, and therefore there is transparency in the collision.

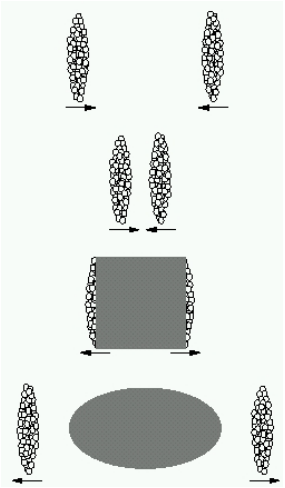

Figure 1.6: The evolution of a heavy ion collision according to Bjorken.

Since, in the central region, the time evolution of plasma-like matter is invariant under boost transformations, observables like energy density ϵ, pressure p, entropy density s, depend only on the proper time τ_0, where $\tau_0 = t/\gamma = \sqrt{t^2 - z^2}$. This gives rise to hyperbolas of constant energy densities that can be used to distinguish between the different phases in the collision evolution.

Such a scenario results into a free net-baryon region around the midrapidity where particle production is dominated mainly by pair production from breaking of the color strings. At higher rapidities the particle production gets increasingly contributions from the original baryon content of the colliding nuclei.

Since the baryon number is a conserved quantity, the distribution of net baryons, given by the difference of baryons - antibaryons, provides information about the collision dynamics. Initially, the total baryon number is contained in the projectile and the target, while after the collision, non-vanishing net-baryon yields are observed far from beam rapidity. This is a consequence of stopping and baryon transport. The rapidity loss of the incoming baryons determines the available energy for particle production.

Figure 1.7 shows the rapidity distribution of net protons ($p - \bar{p}$) as a function of rapidity, for 3 different beam energies (AGS, SPS and RHIC) [35, 36, 37]. At AGS energies the number of produced antiprotons is quite small and the net-baryon distribution is similar to the proton distribution [38, 39]. The net-proton rapidity distribution is centered around y = 0 and is rather narrow. At CERN-SPS energies ($\sqrt{s_{NN}} = 17$ GeV for Pb + Pb reactions) the net proton rapidity distribution shows a double "hump" with a dip around midrapidity [40]. This shape results from the finite rapidity loss of the colliding nuclei and the finite width of each of the humps, which reflect the rapidity distributions of the protons after the collisions. This picture suggests that the reaction at the SPS is beginning to be transparent in the sense that fewer of the original baryons are found at midrapidity after

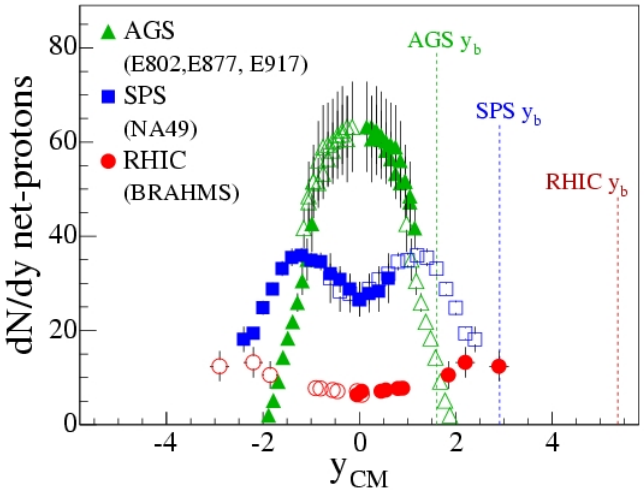

Figure 1.7: Rapidity density of net protons (i.e., number of protons minus number of antiprotons) measured at AGS (Au+Au at $\sqrt{s_{NN}}$ = 5GeV), SPS (Pb+Pb at $\sqrt{s_{NN}}$ = 17GeV), and RHIC-BRAHMS (Au+Au at $\sqrt{s_{NN}}$ = 200GeV) for central collisions (ref. [35]).

the collision, in contrast to the situation at lower energies. There is still a sizeable energy loss of the colliding nuclei, which is available for particle production and other excitations, transverse and longitudinal expansion.

The BRAHMS (Broad RAnge Hadron Magnetic Spectrometers) experiment at RHIC, has measured the net proton rapidity distribution in the interval y = 0-3 for the (0-5%) most central Au + Au collisions at full energy [35, 36, 37]. At RHIC a broad minimum has developed spanning several units of rapidity, indicating that at RHIC energies collisions are quite transparent and the system formed near midrapidity is very different from that at lower energies.

1.3.3 Space-time evolution for relativistic nuclear collisions

The collision of two ultrarelativistic heavy ions can be considered as the scattering of two-dimensional sheets of colored glass [41, 42, 43], as shown in Figure 1.8. The nuclei appear as sheets at ultrarelativistic energies because of Lorentz contraction. These sheets pass through one another and in their wake is left melting colored glass, which eventually materializes as quarks and gluons.

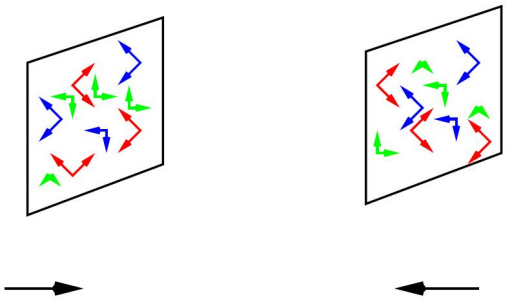

Figure 1.8: A collision of two ultrarelativistic nuclei [41]. The CGC gluons are shown as vectors which represent the polarization of the gluons, and by colors corresponding to the various colors of gluons.

At very early times after the collision the matter is at very high energy density and in the form of a Color Glass Condensate (CGC). The CGC is the fundamental matter of which high energy hadrons are composed and controls the high energy limit of strong interactions. This matter is believed to be universal in that it should describe the high gluon density part of any hadron wavefunction at sufficiently small x, and exists over sizes large compared to the typical microphysics size scales [2] important for high energy strong interactions. It is called a Color Glass Condensate because it is composed of colored particles,

[2]The microphysics size scale here is about 1 Fm and the microphysics time scale is the time it takes light to fly 1 Fm, t $\sim 10^{-23}$ sec.

evolves on time scales long compared to microphysics time scales and therefore has properties similar to glasses, and a condensate since the phase space density of gluons is very high [41, 42, 43].

The Color Glass Condensate evolves into a distribution of gluons at very early times. As time goes on, the matter expands. As it expands the density of gluons decreases, and gluons begin to propagate with little interaction. At later times, the interaction strength increases and there is sufficient time for the matter to thermalize and form a Quark Gluon Plasma. The Color Glass Condensate therefore provides the initial conditions for the Quark Gluon plasma to form in these collisions. The system begins as a Color Glass Condensate, then melts to Quark Gluon Matter which may eventually thermalize to a Quark Gluon Plasma.

This scenario is shown in the left panel of Figure 1.9, with realistic estimates for energy density and time scales appropriate for the RHIC heavy ion accelerator [41]. During the time $0 < t < \tau_{form}$, the Color Glass melts into quarks and gluons. It is estimated that τ_{form} ~0.1 - 0.3 Fm/c at RHIC energy. The matter expands and thermalizes during $\tau_{form} < t < \tau_{therm}$. Typical thermalization time is estimated to be $\tau_{term} \sim 0.5$ - 1 Fm/c.

The rapid collective expansion of the QGP, mainly in the longitudinal direction, lower the system temperature below T_c and energy density below $\sim$ 1GeV/Fm^3 and the QGP begin to hadronize through some mixture of hadrons and quarks and gluons. At a time $\sim$ 3 Fm/c, the plasma becomes a mixture of quarks, gluons and hadrons which further expand together. Eventually, all the quarks and gluons become confined into hadrons that still interact as hadronic matter before being detected.

As the system expands and cools down, there is not enough energy in each collision to produce new particles and further change the population of the different types of particles - the ratios of produced particles "freeze out". The system reaches the stage of chemical freeze-out, characterized by the freeze-out chemical temperature, T_{ch}.

At later times of the system evolution there are only elastic collisions between the produced particles. Eventually, the energy is small enough and the system dilute enough (when the mean free path of the produced particles is of the order of the strong interaction radius or the particle density is very low) such that the interactions cease and each particle's momentum is fixed. Therefore the system reaches the stage of kinetic freeze-out, characterized by the freeze-out thermic temperature, T_{th}. After this moment, the momentum spectra of the produced particles do not change further and the hadrons can propagate freely (right panel of Figure 1.9).

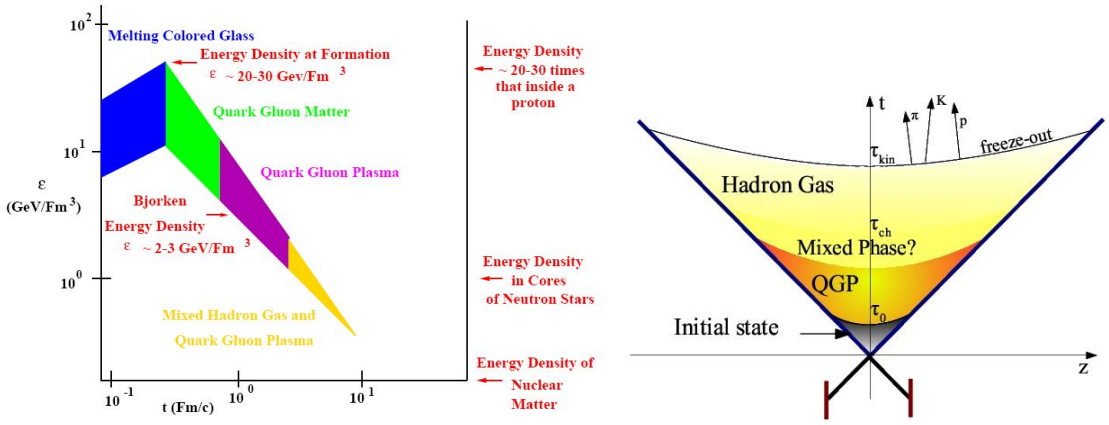

Figure 1.9: Left: The evolution of a heavy ion collision at RHIC energy [41]. Right: Space-time picture of a heavy ion collision.

All the system evolution, from the first contact of the colliding nuclei up to the freeze-out of the created fireball, is characterized by a proper time scale of the order of 10 Fm/c and it's governed by complex dynamics. The initial state and/or pre-equilibrium nuclear effects that occur before QGP formation (like primary quarks and gluons undergo multiple scattering or experience shadowing in

the nucleus before they interact to form a $q\bar{q}$ pair or a hard transverse parton) have to be understood and taken into account before any QGP analysis. It is therefore necessary to study them in processes which are not effected by the subsequent medium. There could be also significant rescatterings among the different system components, which could hide specific signals related to the QGP and the phase transition. Therefore, in order to extract informations about early stages of the collisions it is necessary to exploit the system features established early on and not modified by collective expansion and final-state interactions, or that could be extrapolated back. The next paragraphs presents the most important experimental signals for the quark gluon plasma.

1.4 Quark gluon plasma signatures

The quark gluon plasma is not directly measurable because of the small size and lifetime of this system - at most a few fm in diameter and perhaps 5 to 10 Fm/c in time. Therefore the experimental signals of the QGP imply finding appropriate observables to describe its formation and studying its properties. However, it is generally recognized that there is no single unique signal which allows an unequivocal identification of the quark-gluon phase. Only with the combination of many experimental observations it will be possible to establish convincing evidence for the existence of this new state of matter. These observables and their relation to the possible QGP phase in the collision will be presented in the following.

1.4.1 Kinematical signals

This type of signals relies on determining the energy density ϵ, the pressure p and the entropy density s, which characterize the dense hot matter as a function of temperature T and baryochemical potential μ_B. A QGP signal of this type shows itself like a sharp change in the number of effective degrees of freedom, expressed by the ratios ϵ/T^4 or s/T^3 over a narrow temperature interval.

Measurable observables related to T, s and ϵ variables are the average transverse momentum $\langle p_T \rangle$, the hadron rapidity distribution dN/dy and the transverse energy dE_T/dy, respectively. One can invert the $\epsilon - T$ diagram and plot $\langle p_T \rangle$ as a function of dN/dy or dE_T/dy. A rapid increase in the number of degrees of freedom would appear in such a dependency as a "S" shape, whose main feature is the saturation of $\langle p_T \rangle$ during the mixt phase, followed by a second rise when the matter undergoes a structural change to its colored constituents (Fig. 1.10) [44].

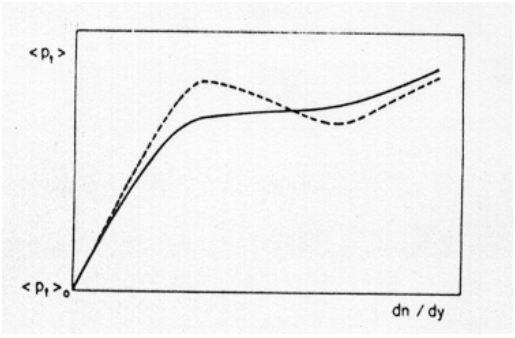

Figure 1.10: $\langle p_T \rangle$ as a function of dN/dy. The same dependence for a given impact parameter (dashed line). (ref. [44]).

This simple picture however has several caveats. We discuss here a few of them. It could be too simple to identify $\langle p_T \rangle$ or the inverse slope parameter of a transverse momentum spectrum directly with the temperature of the system. If the system formed in AA collisions thermalize through collisions, the final state particles observed in the experiments, and in particular the momentum spectra, will only reflect the coolest phase of the system evolution (hadrons do interact after the chemical freeze-out so that the direct connection to the temperature is distorted) [45, 46]. Thus, if thermalization occurs, the effective temperature extracted from the spectrum will probably not carry information of the hot initial phase, smearing any structure in a $\langle p_T \rangle$vs.dN/dy plot. In addition, a visible flat structure in the Tvs.ϵ diagram necessitates a significant duration of a mixed phase, an effect that probably requires the presence of a strong first-order phase transition. However, lattice simulations currently favor a more smooth cross over, perhaps a second order transition.

Identical particle interferometry, $\pi\pi$, KK or NN may reveal informations on the reaction geometry and on the space-time dynamics of the nuclear collisions. By studying the two-particle correlation function along various directions in the phase space, it is possible to obtain measurements of the transverse and longitudinal size, of the lifetime and the flow of the hadronic fireball at the moment when it breaks up into separate hadrons [47, 48].

1.4.2 Elliptic Flow

Anisotropic flow provides indirect access to the equation of state (EOS) of the hot and dense matter formed in the reaction zone and helps us understand processes such as thermalization, creation of the QGP, phase transitions, etc., since the flow is likely influenced by the compression in the initial stages of the collision.

In non-central heavy ion collisions, the overlapping region defined by the nuclear geometry has an almond shape and will form an anisotropy in coordinate space. Because of rescatterings among the produced particles/partons, the azimuthally anisotropic pressure gradient will transfer this spatial deformation onto momentum space, i.e. the initially locally isotropic transverse momentum distribution of the produced matter begins to become anisotropic. The dynamic expansion of the system will wash out the coordinate-space anisotropy, while the momentum-space anisotropy will saturate during the evolution of the system [49]. Since this happens quite early in the collision, the finally observed momentum anisotropy opens a window onto the early stage of the fireball expansion.

The final state particle spectrum in momentum space can be expanded into a Fourier series as

$$E\frac{d^3N}{dp^3} = \frac{1}{2\pi}\frac{d^2N}{p_T dp_T dy}(1 + \sum_{n=1}^{\infty} 2v_n cos[n(\phi - \Psi_r)]) \tag{1.5}$$

where Ψ_r is the reaction plane angle and and ϕ is the particle's azimuthal angle in momentum space. The Fourier expansion coefficient v_n stands for the nth harmonic of the event azimuthal anisotropies. v_1 is so called directed flow and $v_2 = \langle cos[2(\phi - \Psi_r)]\rangle$ is the elliptic flow[3], where angular brackets denote an average over events and over all particles in a given transverse momentum and rapidity window.

Since v_2 is driven by pressure anisotropies and the spatial deformation of the reaction zone creating such anisotropies quickly decreases as time proceeds, the elliptic flow is "self-quenching" as the system continues to expand [52]. Therefore, the elliptic flow is sensitive to the EOS only during the early expansion stage (the first $\sim$ 5 Fm/c in semicentral Au+Au collisions [53]), until the spatial deformation has disappeared. Being dependent on rescattering, elliptic flow is sensitive to the degree of thermalization of the system at this early time.

Left panel of Figure 1.11 shows that the identified particle $v_2(p_T)$ are consistent with the hydrodynamical calculations and have mass dependence in low $p_T$region, where at a given p_T, the higher the hadron mass the lower the value of v_2 [50]. This supports the hypothesis of early thermalization, i.e. that strongly interacting matter with a very short mean free path dominates the early stages of the RHIC collisions.

Right panel of Figure 1.11 [51] shows the v_2 results as a function of p_T (left) and KE_T (right), divided by the number of constituent quarks n_q for mesons ($n_q = 2$) and baryons ($n_q = 3$), where $KE_T = m_T - m$ is the transverse kinetic energy and m_T is the transverse mass of the particle. We see that v_2/n_q shows such good scaling over the entire range of KE_T/n_q and does not for p_T/n_q. This as an indication of the inherent quark-like degrees of freedom in the flowing matter. These degrees of freedom are gradually revealed as KE_T increases above $\sim$1 GeV and are apparently hidden by the strong hydrodynamic mass scaling, which predominates at low KE_T. Coalescence models [54,

[3]The word "directed" (also called sideward flow) comes from the fact that such flow looks like a sideward bounce of the fragments away from each other in the reaction plane, and the word "elliptic" is due to the fact that the azimuthal distribution with non-zero second harmonic deviates from isotropic emission in the same way that an ellipse deviates from a circle.

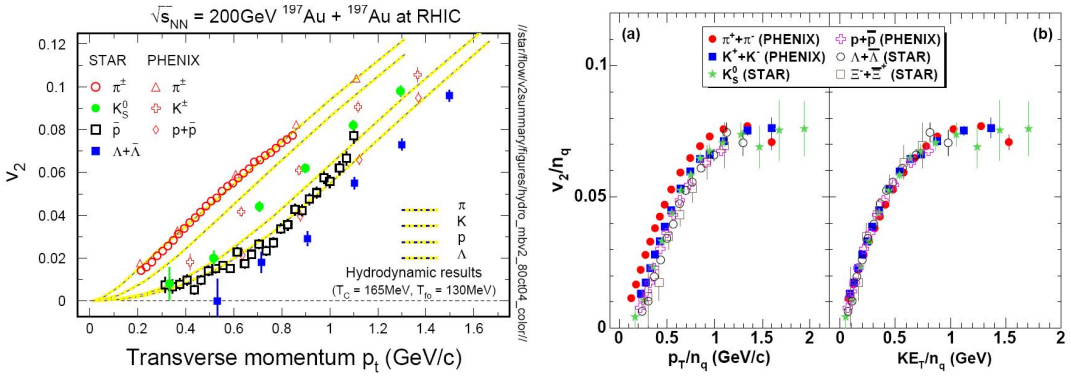

Figure 1.11: Left: Transverse momentum dependence of the elliptic flow parameter in 200 GeV Au+Au collisions for identified particles [50]. Hydrodynamics calculations assuming early thermalization, ideal fluid expansion, an equation of state consistent with LQCD calculations including a phase transition at Tc=165 MeV and a sharp kinetic freezeout at a temperature of 130 MeV, are shown as dot-dashed lines. Right: v_2/n_q vs p_T/n_q and v_2/n_q vs KE_T/n_q for identified particle species obtained in minimum bias Au+Au collisions, where $KE_T = m_T - m$ is the transverse kinetic energy and m_T is the transverse mass of the particle. Figure taken from [51].

55, 56], which assume hadrons are formed through coalescing of constituent quarks provide a viable explanation for these observations. This indicates the flow developed during a partonic stage and offers a strong evidence of deconfinement at RHIC.

Flow measurements as a function of pseudorapidity provide information crucial in constraining the three-dimensional hydrodynamic models and others that seek to better understand what role the longitudinal dimension plays in the collision. The large pseudorapidity coverage of the BRAHMS detector makes it suited for probing the longitudinal structure of the collision, the dynamics of which have to be yet understood away from midrapidity. The BRAHMS integrated v_2 versus centrality and η dependencies [57] are shown in the left panel of Fig.1.12 and are consistent with the PHOBOS and STAR results [59, 50]. The flow decreases as one moves away from mid-rapidity.

Another interesting result obtained by PHOBOS [60], is the pseudorapidity dependence of the elliptic flow within the context of limiting fragmentation and found that the elliptic flow at four different beam energies appears to be independent of energy in $\eta' = |\eta| - y_{beam}$, displaying limiting fragmentation throughout the entire range of η'. This is another surprising feature of elliptic flow results at RHIC, given that particle production in the limiting fragmentation region is thought generally to be distinct from that at midrapidity, but in this case there is no evidence for two separate regions in any of the four energies analyzed.

BRAHMS expands the study of identified-particle elliptic flow to forward rapidity [58] and shows the results of v_2 of charged pions as a function of transverse momentum at two pseudorapidities: 0 and 3.4. The v_2 behavior for identified pions is an increasing function of p_T at both rapidities, with indication of saturation above 1.5 GeV/c. The dependence on pseudorapidity is very small (right panel of Fig.1.12). It seems that this perfect fluid extends far away from mid-rapidity.

The strong elliptic flow of hadrons observed in relativistic heavy ion collisions at RHIC have led to the important conclusion that the quark-gluon plasma (QGP) created in these collisions acts like a strongly coupled plasma with almost perfect liquid behavior.

1.4.3 Jet Quenching

High transverse momentum[4] (high p_T) hadron production is thought to probe the early stage of heavy-ion collisions. It is presumed that the production of particles with high p_T results from hard

[4] $p_T \geq 2$ GeV/c

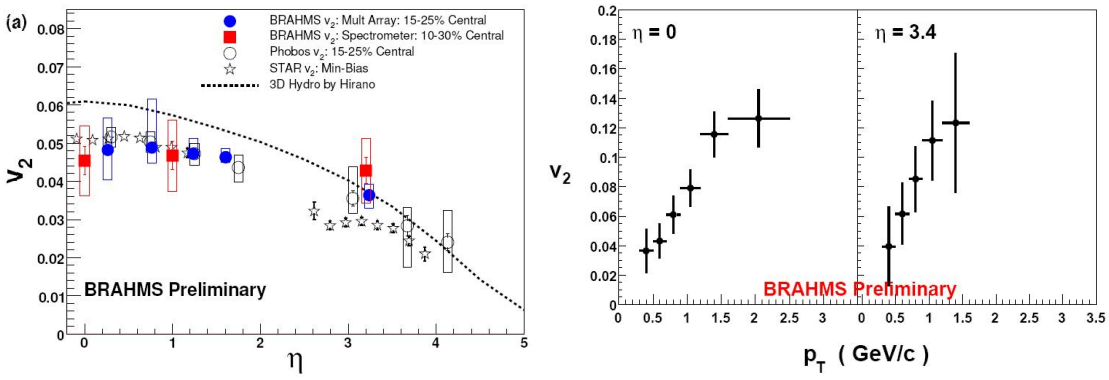

Figure 1.12: Left: Integrated v2 vs. η for charged hadrons. The BRAHMS spectrometer results are consistent, but systematic errors with the spectra may distort the shape. For comparison, a 3D hydro model results are plotted. Figure taken from [57]. Right: Elliptic flow of charged pions at $\eta = 0$ (left) and $\eta = 3.4$ (right). The data correspond to 10%-20% central events. Only the statistical errors are shown in the figure [58].

(large momentum transfer) parton-parton scatterings in the initial crossing of the two colliding nuclei. The hard-scattered partons have to traverse the hot and dense medium before they fragment to create jets (clusters) of particles.

A high momentum parton traversing a dense colored medium is predicted to experience substantial energy loss through induced gluon radiation (gluon bremsstrahlung), effectively quenching jet production [61, 62]. The parton energy loss is expected to depend strongly on the gluon density of the created system and the traversed path length of the propagating parton [63, 64, 65]. The reduction of the parton energy translates to a reduction in the momentum of the fragmentation hadrons, which produces a suppression in the yield of the high p_T hadrons in the final state relative to a baseline expectation in the absence of energy loss [66]. Thus, measurement of the high p_T hadron suppression provides a direct experimental probe of the density of color charges in the medium through which the parton passes.

The high p_T suppression was one of the most exciting observations made at RHIC in Au+Au collisions at $\sqrt{s_{NN}}$=130 GeV [67, 68] and later on at $\sqrt{s_{NN}}$=200 GeV [69, 70, 71, 72]. High p_T production in p+p collisions at the same energy provides the baseline reference to which one compares heavy ion results in order to extract information about the properties of the hot and dense medium produced in Au+Au collision. One can quantify the (initial and final state) medium effects[5] on the particle production at high p_T via the nuclear modification factor (NMF):

$$R_{AB} = \frac{"hot/denseQCDmedium"}{"QCDvacuum"} = \frac{d^2N_{AB}/dydp_T}{\langle T_{AB}(b)\rangle \times d^2\sigma_{pp}/dydp_T} \tag{1.6}$$

where $T_{AB}(b) = N_{bin}/\sigma_{inel}$ is the nuclear overlap function and accounts for the collision geometry, averaged over the event centrality class, and N_{bin} is the number of binary collisions calculated with Glauber model. In the absence of nuclear effects, the nuclear collisions can be seen, at high p_T, as a superposition of elementary hard nucleon-nucleon collisions and $R_{AB} = 1$. At low p_T, where the particle production follows a scaling with the number of participants, $R_{AB} < 1$ for $p_T < 2$ GeV/c. If $R_{AB} > 1$, the nuclear effects enhance the particle production compared to p+p collisions, and if $R_{AB} < 1$, the nuclear effects suppress the particle production.

However, the observed suppression at RHIC was not yet a definitive proof of jet quenching since there are many other effects than final state energy loss that could produce a nuclear modification of

[5]By "initial" and "final" effects we are referring to "before" and "after" the hard scattering of the two partons took place.

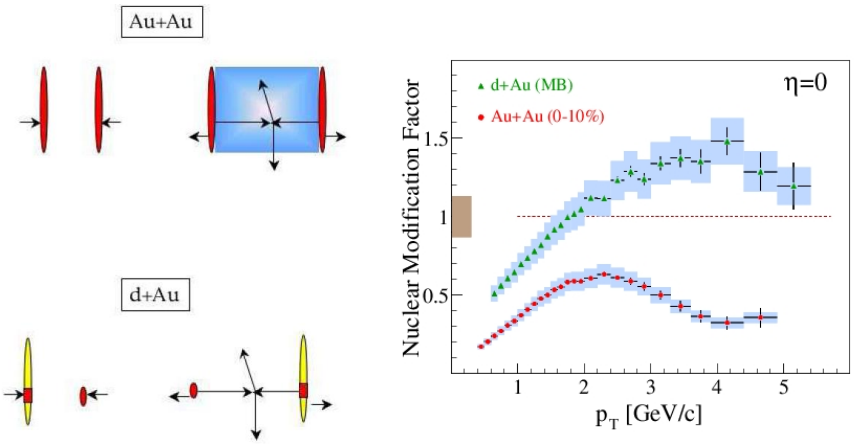

Figure 1.13: Left: The evolution of a heavy ion collision at RHIC energy. Right: Nuclear modification factors measured for central Au+Au collisions and minimum bias d+Au collisions at 200 GeV [69]. The shaded band around the points indicates the systematic errors. The shaded box around unity shows the estimated uncertainty on the value of N_{bin}.

high p_T hadronic spectra (gluon saturation effects, Cronin effect). In order to check how the initial state nuclear modifications affect the spectra of high p_T particles, RHIC collided deuteron and gold at $\sqrt{s_{NN}} = 200$ GeV. In d+Au collisions, we do not expect the formation of a hot and dense medium and there should be no final state medium induced effects on particle production. The measured R_{dAu} from all the four RHIC experiments shows no suppression on high p_T particle production at midrapidity [69, 70, 71, 72].

Right panel of Figure 1.13 shows the R_{AA} obtained in central Au+Au and minimum bias d+Au collisions at $\sqrt{s_{NN}} = 200$ GeV by the BRAHMS collaboration. The very large high p_T suppression observed in central Au+Au collisions and its absence in d+Au collisions proves that the high p_T hadron suppression is a final-state effect of the dense medium created in A+A collisions, and hence a proof of jet quenching at RHIC [69].

A detailed description of the high p_T particle production in Au+Au collisions at $\sqrt{s_{NN}} = 200$ GeV will be given in the next chapter.

1.4.4 Strangeness Enhancement

The study of strange particles offers interesting possibilities since the strangeness is not present in the incoming nuclei; it has to be produced in the collision. Therefore, it provides essential information about the physical environment created in nucleus-nucleus collisions. Rafelski proposed the production of strange (s) and anti-strange ($\bar{s}$) quarks as a probe to study the QGP phase transition two decades ago [73]. If matter went through a phase transition to a QGP, then there would be an enhancement of strange particles in the final state. This enhancement is relative to a collision system where a transition to a QGP phase does not take place, such as p+p or p+A collisions where the system size is very small [74].

In the absence of a QGP, strangeness production occurs via hadronic channels and involve relatively high energy thresholds. Since the strangeness is conserved for strong interactions, a hadron with an s quark has to be produced the same reaction with one hadron containing an $\bar{s}$ quark. For example, in order to have the reaction $N + N \rightarrow \Lambda + K^+ + N$, one needs a threshold energy of 700 MeV. The strange particles can be produced also in secondary reactions of hadrons generated in collision, like $\pi + N \rightarrow K + \Lambda$ and $\pi + \pi \rightarrow K + \bar{K}$, which have lower energy thresholds than those in primary interactions.

The production mechanisms for strange quarks in a QGP are different to a hadronic gas as there

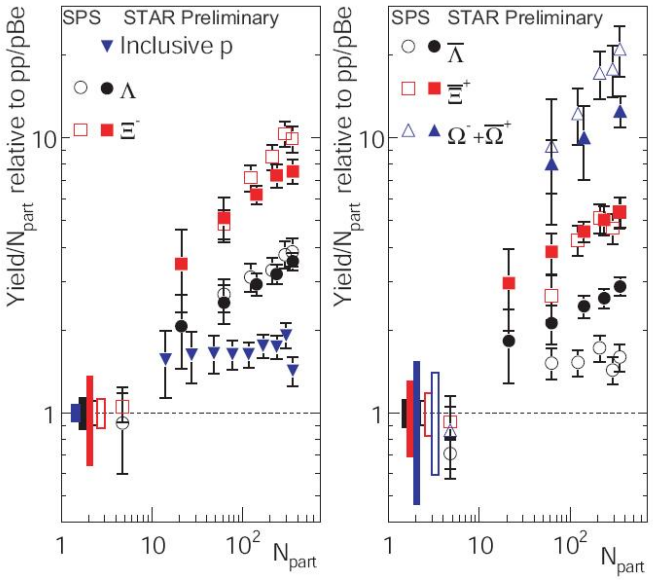

Figure 1.14: Yields per participant N_{part}, for NA57-SPS PbPb at 17.3GeV (open symbols) relative to pBe and for STAR-RHIC Au-Au at 200GeV (filled symbols) relative to pp. On left baryons, on right antibaryons and $\Omega + \bar{\Omega}$ (triangles), circles are Λ and $\bar{\Lambda}$, squares are Ξ^- and $\Xi+$. Error bars represent those from the heavy-ion measurement. Ranges for pp and pBe reference data indicate the statistical and systematic uncertainty. Figure taken from [80].

are more available production channels for $s\bar{s}$ pairs, due to gluon fusion $gg \rightarrow s\bar{s}$, as well as the annihilation of light $q\bar{q}$ pairs $q\bar{q} \rightarrow s\bar{s}$ [74, 75]. As the plasma is expected to be initially gluon rich, and the equilibration of gluons takes time $\tau_g \sim 0.3$ fm/c compared to the quark equilibration time of $\tau_q \sim 2$ fm/c [76], the gluonic channels contribute more than 80% to the total production rate for strange quarks [75].

In the QGP we expect deconfinement to be accompanied by a partial restoration of the chiral symmetry. As chiral symmetry is restored, the mass of the strange quark is expected to decrease to its current value of about 150 MeV. Thus, the energy threshold for strangeness production is now reduced to $\sim$ 300MeV, or twice the strange quark mass. Thus strange quarks become much more abundant and upon hadronization the relative density of (multi-)strange particles is significantly enhanced over that resulting from a hadron gas.

CERN SPS experiments showed the expected enhancement of the multi-strange particles, from proton-nucleus (p+A) to nucleus-nucleus (A+A) collisions [77, 78]. STAR also reported the increase of the total yield of multi-strange baryons per h^- in Au+Au collisions at $\sqrt{s_{NN}} = 130$ GeV compared to that at the top SPS energies [79].

Figure 1.14 shows the enhancement of strange baryons and anti-baryons as a function of centrality as measured by STAR for Au+Au collisions at $\sqrt{s_{NN}} = 200$ GeV [79] and by NA57 for Pb+Pb collisions at $\sqrt{s_{NN}} = 17.3$ GeV [78]. Comparing the Λ, Ξ and Ω and antiparticle yields in Pb+Pb to those in p+Be interactions, considerable enhancement of yield per participant is observed. This enhancement increases linearly with the collision centrality, reaching a factor of about 20 for the $\Omega+\bar{\Omega}$ in the central Pb-Pb collisions. The solid symbols, in Figure 1.14, correspond to the STAR yields of (multi)strange baryons and antibaryons per participant[6], obtained in Au+Au at $\sqrt{s_{NN}} = 200$ GeV divided by a reference yield obtained in p+p reactions at the same energy.

It can be seen that the enhancement increases with increasing strangeness content and that, at RHIC, the anti-baryon enhancements are approximately those of the baryons. The enhancement pattern of Λ and $\bar{\Lambda}$ is influenced by the prevailing baryon density, for $\bar{\Lambda}$ the enhancement is greater at

[6]It is believed that there is a linear correlation between the geometric overlap volume of the collision and N_{part}.

RHIC where the baryon density is smaller than at SPS, while the reverse is true for Λ. This reflects the near zero net-baryon density at RHIC. The enhancement of $\Omega + \bar{\Omega}$ is largest, since production of these particles is very difficult in the elementary reactions.

Within error, the enhancement at RHIC and SPS appears the same, although the collision energy and the system dynamics is different. However, we have to consider that the enhancement computed by NA57 is based on p+Be, where some enhancement of Λ is expected to be present, as compared to pp results.

In conclusion, although the QGP formation would lead to the strangeness enhancement, the observed enhancement does not unequivocally indicate the formation of QGP.

1.4.5 Electromagnetic probes

Photons and dileptons (lepton pairs) are a useful probe of the thermodynamics of the fireball as they only interact electro-magnetically and have a large mean free path compared to the size of the fireball. As neither the photons nor dileptons are strongly interacting, they emerge from a QGP or hadronic system without interacting and thus are sensitive to the entire thermal history of the system, especially the early stage where the QGP should appear [81]. Unfortunately, these probes have rather small yields and must compete with large backgrounds from hadronic processes, especially electromagnetic hadron decays.

Direct photons

Due to the excess of gluons in a QGP, an enhancement in direct photons is expected as they are produced through the gluonic channels $gq \rightarrow \gamma q$, $q\bar{q} \rightarrow \gamma g$, $g\bar{q} \rightarrow \gamma \bar{q}$. These direct photons carry information about the thermodynamics of the QGP phase as their momentum distributions are determined by those of the quarks, antiquarks and gluons in the plasma. In principle, the initial temperature of the system, T_i can be determined from the rate of thermal photon production [82]. As the QGP should be formed at temperatures higher than those present in the hadronic phase, the momentum distributions of the photons should show an excess at higher transverse momentum.

Direct thermal photons are difficult to measure experimentally, due to the large backgrounds. These can be thought of as two distinct groups, prompt photons from initial hard collisions, and photons emanating from a hot hadronic gas (like $\pi^{\pm}\rho \rightarrow \gamma\pi^{\pm}$, $\pi^{+}\pi^{-} \rightarrow \gamma\rho$) [84].

PHENIX studied direct photons production in Au+Au collisions at the RHIC top energy [83]. As shown in Figure 1.15, an excess of photons is observed at high p_T with a magnitude that increases with increasing centrality of the collision. Such results confirms the theory of dense medium where high p_T hadrons are suppressed because of the parton energy loss, and high p_T direct photons leave the QGP without any changes.

Dileptons

The advantage of measuring lepton pairs over direct photons is that the mass of the meson which decayed into the lepton pair can be calculated, which means that their production processes may be determined.

Lepton pairs from hadronic sources in the invariant mass range between 0.5 and 1 GeV provide information about possible medium modifications of hadronic properties (mass and/or width) which could be linked to chiral symmetry restoration. By analyzing ρ meson decay inside the medium and measuring the dileptons invariant mass spectrum, one hope to measure the in-medium modification of ρ meson (dropping of its mass and/or broadening of its width) [85].

Another strategy for using the leptonic ρ meson decay as a probe of the hadronic phase of the fireball is based on the idea that the ρ(770MeV) peak is expected to grow strongly relative to the ω(782MeV) peak in the invariant mass spectrum of the produced dileptons if the fireball substantially

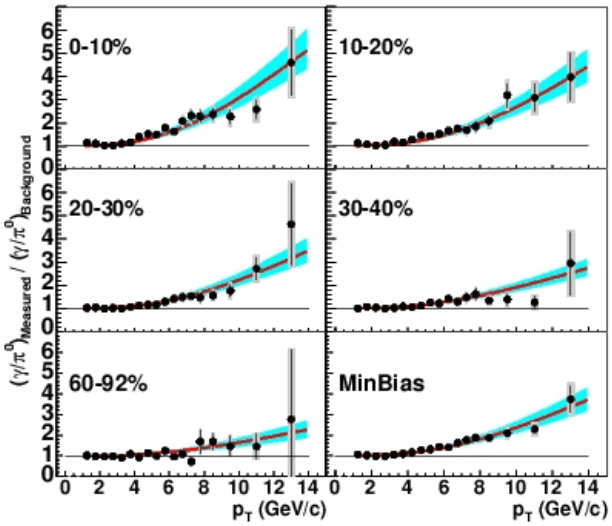

Figure 1.15: Double ratio of measured $(\gamma/\pi^0{}_{Measured})$ invariant yield ratio to the background decay $(\gamma/\pi^0{}_{Background})$ ratio as a function of p_T for minimum bias and for five centralities of Au+Au collisions at 200 GeV. Statistical and total errors are indicated separately on each data point by the vertical bar and shaded region, respectively. The solid curves are the ratio of pQCD predictions to the background photon invariant yield based on the measured π^0 yield for each centrality(ref. [83]).

lives longer than 2 fm/c. Because of the shorter timelife of ρ meson (1.3 Fm/c) compared to ω (23 Fm/c), the ratio ρ/ω may be used as a accurate "clock" for the fireball lifetime [81].

The ρ meson decays into a pair of e^+e^- or $\mu^+\mu^-$ which escape from the fireball without further interactions. After one generation of ρ's has decayed, a second generation is created via $\pi\pi$ interactions, which consequently decay into dileptons, etc. Hence, the number of extra dileptons with the ρ invariant mass is a measure of the time during the fireball's hadrons interact strongly. Since the ρ mesons do not exist before the hadrons appear in the fireball, this method says nothing about a possible QGP phase which can occur in the initial stages of the collisions. Anyway, dileptons allow an insight to the strongly interacting hadronic fireball at a later stage, still long before the hadrons decouple, though.

CERES/NA45 collaborations measured dilepton e^+e^- spectrum in Pb-Au reactions at 158 AGeV/c [86] and reported an excess in the low-mass dilepton yield in the mass region starting at 200 MeV/c^2 up to the mass region of ρ (comparing with the expectation from hadron decays, the increase for the region [0.25, 0.70] GeV/c^2 is 2.6±0.5(stat)±0.5(syst), but a clear peak for m_ρ=770 MeV was not found) (see left panel of Figure 1.16).

The reason for the enhancement below the ρ(770MeV) and ω(782MeV) masses is currently an unresolved topic of debate. It has been suggested that it is a product of partial chiral symmetry restoration, where the mass of the ρ decreases. Another explanation is collision broadening and is based on the fact that pion annihilation ($\pi^+\pi^- \rightarrow \rho \rightarrow e^+e^-$) could be an important source for dilepton production in a dense fireball. Because of the strong pion rescatterings, not only among each other, but also with the baryons in the hadron gas, their spectral densities are modified and, as a consequence, lead to a smearing of the ρ-resonance in the $\pi\pi$ scattering cross section [88].

The fact that the low-mass dileptons outnumber those from the decay of unmodified ρ's emitted at thermal freeze-out (in the region 770MeV) shows that the hadron rescattering stage lasted at least several ρ lifetimes.

At RHIC energies, a calculation of the light vector meson yield as a function of invariant mass of e^+e^- pairs is displayed in the right panel of Fig.1.16 [87]. Peaks for the ρ and ϕ mesons are

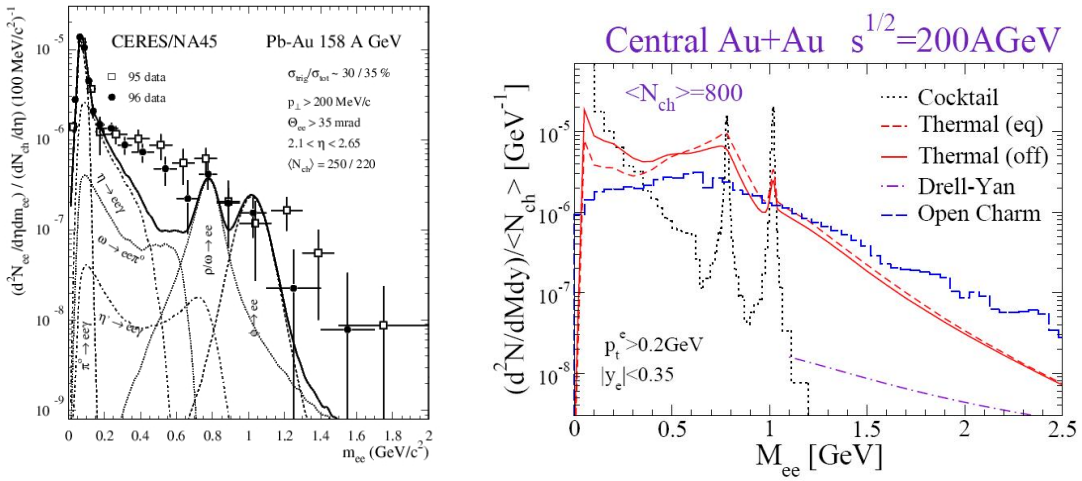

Figure 1.16: Left: Inclusive e^+e^- mass spectrum from the CERES experiment for Pb+Au collisions at 158 AGeV. The solid line is the expected spectrum (the sum of the many shown contributions) from the decays of hadrons produced in pp and pA collisions, properly scaled to the Pb+Au case (ref. [86]). Right: Low mass e^+e^- pair spectrum from [87]. Contributions from the hadronic "cocktail", thermal and non-equilibrium photons, Drell-Yan, and open charm are displayed.

observed, but are swamped by e^+e^- pairs from thermal and non-equilibrium photons and open charm. Careful investigation of medium modification of low mass vector mesons requires measuring and understanding all contribution to the dilepton spectrum including detailed charm studies that require RHIC II[7] luminosities [90].

1.4.6 J/Ψ Suppression

The bound states of a heavy quark q and its antiquark $\bar{q}$ are generally referred to as quarkonia. It is considered to be one of the best probes for the earliest, most energetic stages of collisions since $q\bar{q}$ pairs can be produced only in hard parton interactions (dominantly gluon fusion at RHIC energies) and final state leptons do not interact strongly with hadronic matter in the later stages of the collisions. These heavy quarks first showed up in the discovery of the J/Ψ meson [8], of mass of 3.1 GeV [91, 92]; it is a bound state of a charm quark (c) and it's antiquark ($\bar{c}$), each having a mass of some $1.2 - 1.5$ GeV.

If a J/Ψ is placed into a hot medium of deconfined quarks and gluons, color Debye screening will dissolve the binding, so that the c and the $\bar{c}$ separate. When the medium cools down to the confinement transition point, they will therefore in general be too far apart to see each other. Since thermal production of further $c\bar{c}$ pairs is negligibly small because of the high charm quark mass, the c must combine with a light antiquark to form a D, and the $\bar{c}$ with a light quark for a $\bar{D}$ [94]. The presence of a quark-gluon plasma will thus lead to a suppression of J/Ψ production.

As the temperature increases, the excited states of $c\bar{c}$, like ψ' and χ_c, dissociate easier because or their larger binding radii [9]. Both ψ' and χ_c melt at the critical deconfinement point, the J/Ψ, being smaller and more tightly bound, survives to about $2T_c$ and hence about twice the critical energy

[7] The analysis of Run-4 data taken with PHENIX shows that the signal to background ratio, S/B, at the invariant mass of electron pairs $m_{ee} \sim 500$ MeV/c^2 is approximately 1/500 and does not allow any conclusive statement. PHENIX detector will be upgraded in RHIC II in order to perform such a measurement [89].

[8] The J/Ψ meson was discovered simultaneously and independently in 1974 by experimenters at Stanford Linear Accelerator Center (Burton Richter) and Brookhaven National Laboratory (Samuel Ting). Richter and Ting shared the 1976 Nobel Prize for their discovery.

[9] If $\lambda_D \sim 1/T < r_i$, the effective potential between quarks has become so short-ranged that the two can no longer bind.

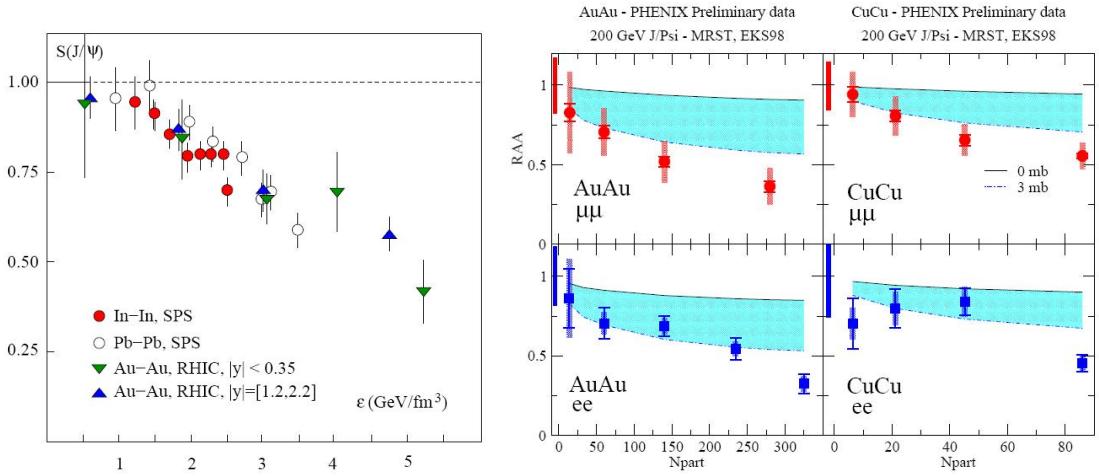

Figure 1.17: Left: The dependence on energy density of J/Ψ suppression measurements at RHIC and at the SPS. Figure taken from [8]. Right: J/Ψ suppression in Au+Au and Cu+Cu collisions for forward rapidity and central rapidity compared to predictions for CNM from a theoretical calculation that includes absorption and EKS (Eskola-Kolhinen-Salgado) shadowing. Figure taken from [93].

density [8, 9]. A similar pattern holds for the bottonium states, $b\bar{b}$. With increasing temperature, a hot medium will thus lead to successive quarkonium melting, so that the suppression or survival of specific quarkonium states serves as a thermometer for the medium [95].

In order to determine whether J/Ψ production in heavy ion collision is different from the production in the absence of QGP, it is critical to have a solid baseline from p+p, p+A or light A+B collisions to constrain the effects already present for cold nuclear matter CNM (gluon shadowing, transverse momentum broadening, parton energy loss or absorption). Previous studies at lower energy, which have claimed to see QGP relied on such baseline.

Left panel of Figure 1.17 shows the J/Ψ survival probability $S_{J/\Psi}$ for a combination of SPS and RHIC data as a function of energy density ϵ achieved in the collision. The J/Ψ survival probability $S_{J/\Psi}$ in A+A collisions is defined as the ratio of the measured rate to that expected if the only modifications are due to the presence of normal nuclear matter. If the absorption of the J/Ψ were only due to the normal nuclear absorption, the data would follow the dashed line. The data clearly deviate from this expectation at the energy density above 2.5 GeV/fm^3. The CERN SPS considered that the initial suppression from $\epsilon \sim 2.3$GeV/Fm^3 describes χ_c meson suppression (which decays into a J/Ψ meson and a γ photon) and the second decrease (or "shoulder"), observed at $\epsilon \sim 3.1$GeV/Fm^3, is assigned to the suppression of stronger bound J/Ψ mesons [96].

At RHIC, it becomes possible the J/Ψ formation by "recombination", i.e., by the binding of c and $\bar{c}$ quarks originating from different nucleon-nucleon collisions. This regeneration mechanism asserts that if the total production of charm is high enough then densities in the final state will be sufficient to have substantial formation of J/Ψ's from the large number of independent charm quarks created in the collision [97, 8]. This production mechanism was almost insignificant at SPS energies but at RHIC may be substantial because of abundant $c\bar{c}$ production. This leads to a scenario in which strong screening or dissociation by a very high-density gluon density occurs to a level of J/Ψ suppression stronger than the RHIC data shows, but the regeneration mechanism compensates for this and brings the net J/Ψ suppression back up to where the data lies.

An alternative interpretation of the RHIC preliminary results, sequential screening, is given by Karsch, Kharzeev and Satz [98]. In this picture, they assume that the J/Ψ is never screened, not at SPS nor at RHIC. Then the observed suppression comes from screening of the higher-mass states alone (ψ' and χ_c) that, by their decay, normally provide ~40% of the observed J/Ψ's. This scenario is consistent with the apparently identical suppression patterns seen at the SPS and RHIC shown in

the left panel of Figure 1.17.

It is important to understand what the normal CNM J/Ψ suppression should look like in these A+A collisions. This is illustrated by the blue error bands for A+A collisions at RHIC top energy in right panel of Fig.1.17 [93]. The present d+Au RHIC data lacks enough precision to provide a good constraint on the CNM effects. As a result it is difficult to be very quantitative about the amount of "anomalous" suppression observed in A+A collisions, although there does seem to be a clear suppression beyond CNM for the most central collisions.

More precise data from RHIC II and the new data at higher energy from LHC in the future will give a clearer understanding of the charm production physics.

In conclusion, in the Figure 1.18 [99] we present the fireball evolution and the experimental signals assigned to each of the stages involved. The relativistic heavy ions collide and reach initial conditions in terms of energy density and temperature well above the critical values for deconfinement. If the evolution of the fireball includes the QGP, such a phase transition may be emphasized by hard probes, like J/Ψ (SPS,RHIC), high p_T/intermediate mass photons/dileptons (SPS, RHIC) and high p_T hadrons (RHIC). The fireball then expands under pressure (more at RHIC than at the SPS), hadronizes with parameters close to the expected phase boundary, possibly shows the influence of chiral restoration at that boundary as evidenced by low mass dileptons (SPS), strongly expands further under pressure and finally, after thermal freeze-out, ends as a cloud of non-interacting hadrons.

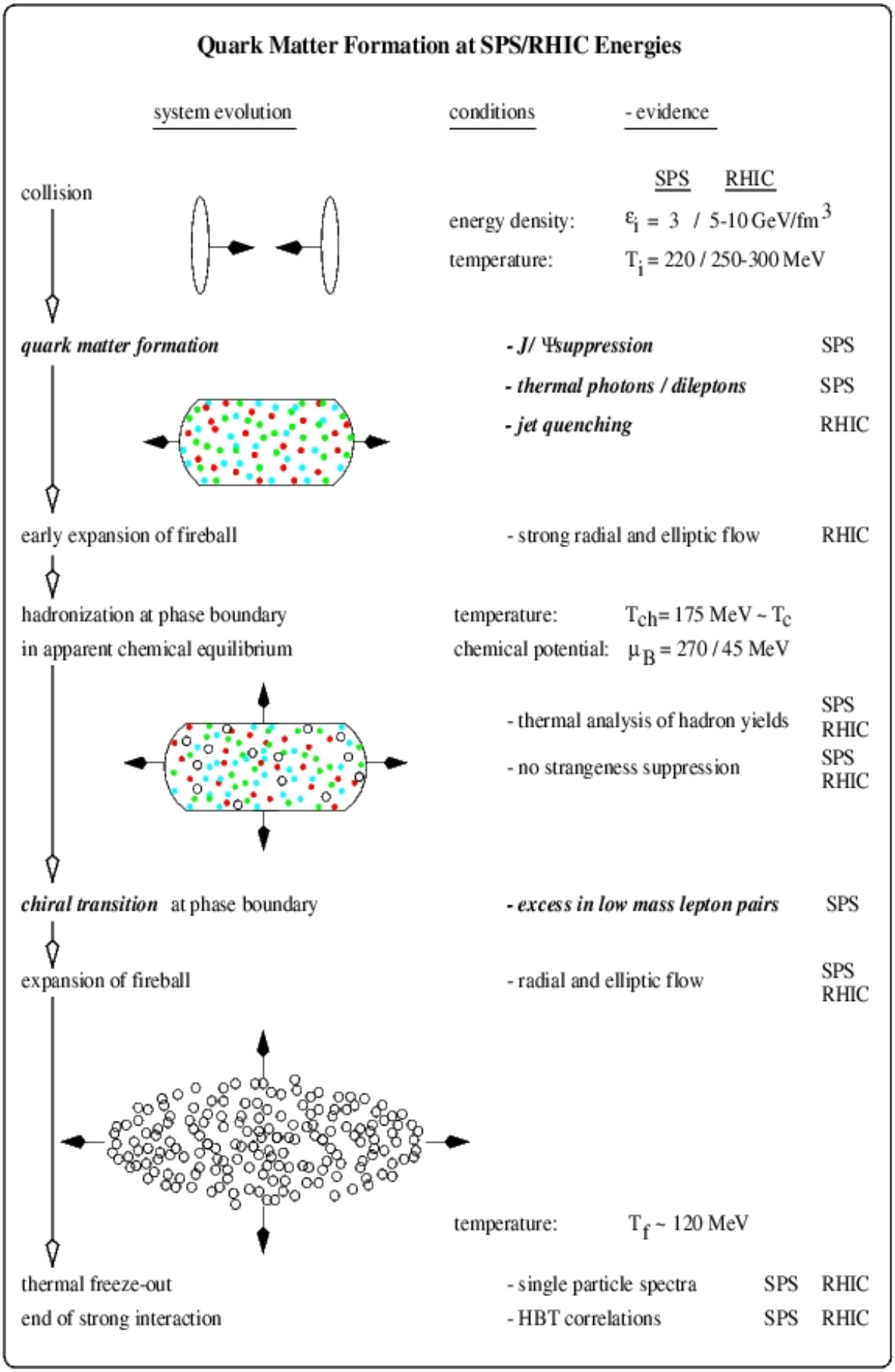

Figure 1.18: Fireball evolution following the impact of two heavy nuclei at ultrarelativistic energies. The various stages in the evolution are confronted with the experimental evidence and the experimentally determined conditions of the respective stage. (ref. [99]).

Chapter 2

High p_T particle production at RHIC

2.1 Perturbative QCD, Parton Distribution Functions and Fragmentation Functions

In nucleon-nucleon collision, it has been well established that hadrons with $p_T \geq 2$ GeV/c result primary from the fragmentation of hard-scattered partons, and that the p_T spectra of these hadrons can be calculated using perturbative QCD (pQCD) [100]. The standard pQCD calculations of hard scattering processes rely on the factorization theorem[1], which provides a way to separate the long-distance non-perturbative effects from the short-distance perturbative effects.

The expression for the inclusive hadron production cross section in nucleon-nucleon collisions $N + N \rightarrow h + X$ can be written as

$$\begin{aligned}\frac{d\sigma^{NN}}{dyd^2p_T} =& K \sum_{abcd} \int_0^1 dz_c \int_{x_a min}^1 dx_a \int_{x_b min}^1 dx_b f_{a/p}(x_a, Q^2) f_{b/p}(x_b, Q^2) \\ & \times \frac{d\sigma^{(ab\rightarrow cd)}}{d\widehat{t}} \frac{D^0_{h/c}(z_c, Q^2)}{\pi z_c^2}\end{aligned} \tag{2.1}$$

where x_a, x_b are the initial momentum fractions carried by the interacting partons, $z_c = p_h/p_c$ is the momentum fraction of the final observable hadron, $\widehat{t} \equiv (p_a - p_c)^2$ is the invariant momentum transfer from parton a to parton c and $d\sigma^{(ab\rightarrow cd)}/d\widehat{t}$ is the hard parton-parton cross section to produce the outgoing partons c and d, which fragment into jets of hadrons. The parton distribution function (PDF), $f_{a/p}(x_a, Q^2)$, is defined as the probability that a nucleon contains a parton a which is carrying a fraction x_a of the nucleon momentum p_A, $0 \leq x_a \leq 1$. The fragmentation function (FF) for the parton of flavor c into the hadron h, $D_c(z_c, Q^2)$, is defined as the probability that a parton c produces a hadron carrying a momentum fraction z_c, $0 \leq z_c \leq 1$. The K is a phenomenological factor that is meant to account for higher order QCD (next-to-leading order NLO) corrections to the jet production cross-section and takes typical values $\sim 1 - 4$. Thus, the cross section to produce a hadron h from a N+N collision is the probability that two partons a and b, one within each nucleon, produce a parton c that subsequently fragments into a hadron h.

The formula 2.1 factorizes the soft-QCD processes which are responsible for the partons being bound within the nucleon (proton) and the process of the hard scattering, which can be calculated perturbatively. Since the PDF represents a soft process - a long distance phenomenon, due to confinement of the partons within the proton - they will factorize from hard parton-parton scattering, a short distance phenomenon. Therefore, the PDF cannot be calculated theoretically and must be

[1] In order to perform the factorization, a hard scale - factorization scale - has to be introduced (defines the boundary between perturbative and non-perturbative regions). The long range (non-perturbative) processes are absorbed into the PDFs and FFs. On the other hand, the cross section for the hard process is a short-ranged process and can be perturbatively calculated.

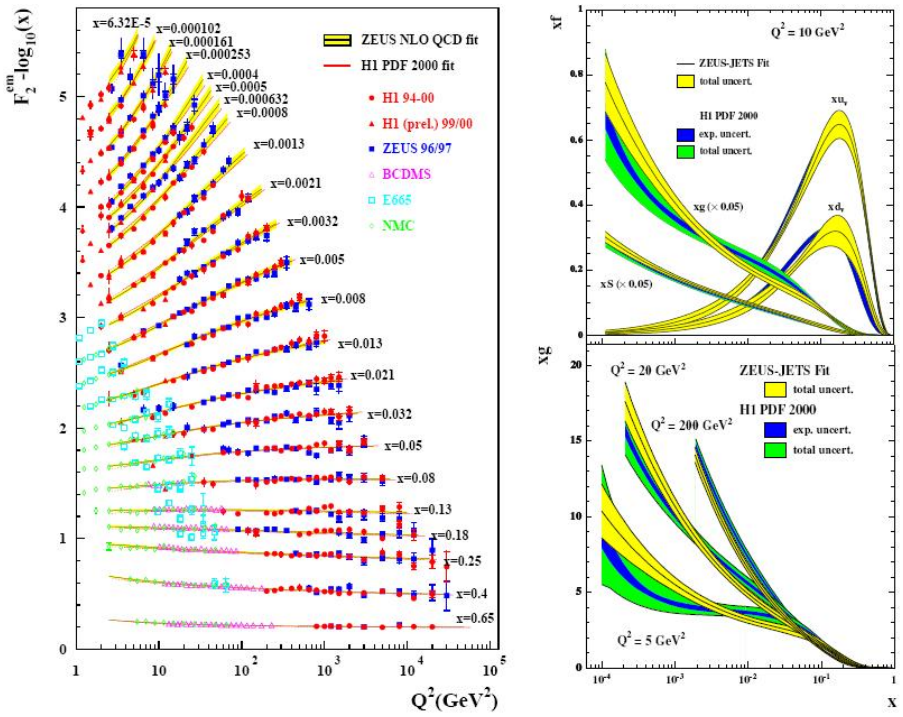

Figure 2.1: Left: Measurements of the proton structure function F_2 as a function of Q^2, at x fixed values, from HERA. Right: Comparison of PDFs from ZEUS and H1 analyzes at $Q^2 = 10\text{GeV}^2$ (up) and a comparison of gluon from ZEUS and H1 analyzes, at various Q^2 (down). Figures taken from [101, 102].

determined from experiments. Hadronic PDFs are assumed to be universal; that is, the PDFs derived from any process are assumed to be applicable to other processes. Nucleon PDFs are determined in deep inelastic lepton-nucleon scattering processes.

2.1.1 Parton distribution functions (PDF)

The structure functions contain information about the inner structure of the target nucleon in DIS and thus, define the partonic content of the proton. The structure functions are functions of the parton distribution function(PDF) of quarks and antiquarks inside the nucleon[2]. These structure functions have been investigated in deep inelastic scatterings in great detail over the last decades using both electron and muon beams.

Experimental measurements of the structure function F_2 as a function of Q^2 for a broad range of x from HERA are shown in the left panel of figure 2.1 [101]. From the Q^2 dependence of the structure function F_2 at fixed x shown in the figure 2.1 one can see there is essentially no Q^2 dependence, but at small x the Q^2 dependence starts to appear. The resulting logarithmic dependence of the F_2 on the Q^2 at fixed x is known as scaling violation [101].

The main origin of the Q^2 dependence of the PDFs is that a quark seen at a certain scale Q_0^2 as carrying a certain fractional momentum of the hadron x_0 can be resolved into more quarks and gluons if it is probed at a higher scale Q^2. The smaller the wavelength of the probe (i.e. the larger the scale Q^2) the amount of $q\bar{q}$ pairs and gluons in the partonic "sea" increases. Although these sea partons carry only a smaller fraction of the nucleon momentum ($x < x_0$), their increasing number leads to a softening of the valence quark distributions as Q^2 increases. Thus F_2, which contains both valence and sea quark distributions, will rise with Q^2 at small x, where gluons and sea quarks dominate, and fall with Q^2 at large x, where valence quarks dominate. The typical behavior of the parton

[2]See appendix C for a short description on this.

distribution functions of the proton is shown in the right panel of the Fig.2.1. All PDFs decrease at large x. At small x the valence quark densities vanish and the $q\bar{q}$ sea and the gluon density dominates. The sea-quark densities increase at small x because they are driven by the strong rise of the gluon density and the splitting of gluons in $q\bar{q}$ pairs.

At present it is not possible to calculate PDFs in QCD and their values are determined from experimental results. The method of extracting the PDFs from experimental data is well established in the case of the free proton: the initial non-perturbative distributions are parameterized at some Q_0^2 initial scale[3] and evolved to higher scales according to the Dokshitzer-Gribov-Lipatov-Altarelli-Parisi (DGLAP) equations [103, 104, 105]. Comparison with the data is made in various regions of the (x, Q^2)-plane. The parameters of the initial PDF distributions are fixed when the best global fit is found. The sum rules for momentum, charge and baryon number give further constraints. In this way, through the global DGLAP fits, groups like MRST [106], CTEQ [107] or GRV [108] obtain their sets of the free proton PDFs.

Although both structure functions and parton distribution functions (PDFs) describe how quarks are distributed inside a nucleon, they are not quite the same. The relationship between the measured structure functions and the parton distributions is not straightforward since the evolved parton distributions must be convoluted with coefficient functions and all types of partons may contribute to a particular structure function through the evolution. The structure functions are process dependent and can be determined by comparison with experimental measurements for each process. Parton distributions are universally defined and in principle, independent of any specific physical process. However, unlike the structure functions, parton distributions are not direct physical observables.

2.1.2 Fragmentation functions

The fragmentation functions (FFs), $D_{h/c}(z_c, Q^2)$, describe how a hadron is produced in the final state from a parent quark, antiquark, or gluon (quantify the probability that the parton c forms a jet that includes the hadron h with momentum fraction z_c).

The fragmentation of quarks and gluons into hadrons was studied in the annihilation processes $e^+e^- \to (\gamma, Z) \to hX$, where h may either refer to a specific hadron species (pion, kaon or proton), or to the sum over all charged-hadron species. The fragmentation process occurs from primary quarks, antiquarks, and gluons, so that the function is expressed by their contributions:

$$F^h(z, Q^2) = \sum_i C_i(z, \alpha_s) \otimes D_i^h(z, Q^2) \tag{2.2}$$

where $D_i^h(z, Q^2)$ is a fragmentation function of the hadron h from a parton $i(= u, d, s, ...)$, z is the fraction of parton momentum carried by the hadron, $C_i(z, \alpha_s)$ is a coefficient function, and $\otimes$ indicates a convolution integral[4] [109].

Hadronization occurs at the energy scale ~ 1 GeV, which is too small for the perturbative treatment to be valid. An approach, very similar to that developed for the PDFs (computation of evolution), applies to the fragmentation functions as well. Given the z dependence at some scale Q_0^2, the evolution of the fragmentation functions with Q^2 can be calculated perturbatively and is determined by the DGLAP equations.

Typically, the z dependence of the fragmentation functions at Q_0^2 is parameterized as $D(z, Q_0^2) = Nz^\alpha(1-z)^\beta$, where parameters N, α, and β are determined from fits to the experimental data [109]. Then the FFs at Q^2 can be calculated perturbatively from those at Q_0 and are obtained by solving the DGLAP equation. Furthermore, the fragmentation functions are universal in a sense that they are independent of the process in which they have been determined.

[3] This starting point Q_0^2 is arbitrary, but should be large enough to ensure that $\alpha_s(Q_0^2)$ is small enough for perturbative calculations to be applicable.

[4] $(f \otimes g)(x) = \int_0^1 dydv f(y)g(v)\delta(yv - x)$

Thus, both PDFs and FFs from Eq.2.1 are obtained from global fits to experimental data: an initial condition containing all the non-perturbative information is evolved, by DGLAP equations and then fitted, in a recursive procedure, to available data.

In the case of heavy-ion collisions, both the initial and, possibly, the final states are different from the p+p collisions. The nuclear parton distributions are different from those in free protons and the eventually produced medium would modify the fragmentation. Thus, for proton-nucleus or nucleus-nucleus collisions, the generalization of Eq.2.1 to p+A or A+A collisions needs of nuclear PDF and medium-modified FF. This medium that modifies the parton fragmentation could be the nucleus itself (cold nuclear matter) in both p+A and A+A collisions and/or eventually the high density final state produced in A+A collisions.

2.2 Nuclear effects

The perturbative QCD (pQCD) treatment of the hard parton scattering makes the standard factorization assumption that the cross section for producing a given final-state high-p_T hadron can be written as the product of suitable initial-state parton densities, pQCD hard-scattering cross section, and final-state fragmentation functions for the scattered partons. Nuclear modifications must be expected for the initial parton distribution functions as well as for the fragmentation functions. The nuclear effects are usually divided in two classes:

- *Initial*-state effects = effects acting on the hard cross section in a way that depends on the size and energy of the colliding nuclei, but not on the medium formed in the collision, such as Cronin effect, nuclear shadowing and gluon saturation.

- *Final*-state effects = effects induced by the created medium that influence the yields and the kinematic distributions of the produced hard partons, such as partonic energy loss. Final-state effects are not correlated to initial-state effects; they depend strongly on the properties of the medium (gluon density, temperature and volume). Therefore, they provide information on these properties.

2.2.1 Initial effects

Nuclear modification of the PDF refers to the fact that the PDF for nucleons bound in a nucleus are different from the PDF for free nucleons, such as protons. The nuclear modification of the parton distribution of the nucleons comes from the fact that when the nucleons are bound together, there are interactions between partons from different nucleons. Therefore, the parton distributions may change due to such interactions. In general, the heavier the nucleus is, the bigger these effects are.

The nuclear effects are often categorized according to those observed in the ratio of the structure functions of nuclei relative to deuterium, $R^A_{F_2} = \frac{\frac{1}{A}F_2^A}{\frac{1}{2}F_2^D}$, assuming nuclear effects in deuterium to be negligible (see Fig.2.2). The nuclear effects in the ratio $R^A_{F_2}$ directly translate into nuclear effects in the parton distributions, $f_{i/A} \neq f_{i/p}$ ($f_{i/A}$ is the parton distribution of a flavor i in a bound proton of a nucleus A, and $f_{i/p}$ is the corresponding distribution in the free proton), such as

- "shadowing": a depletion $R^A_{F_2} \leq 1$ at 0.05≤x≤0.1,
- "anti-shadowing": an excess $R^A_{F_2} \geq 1$ at 0.1≤x≤0.3,

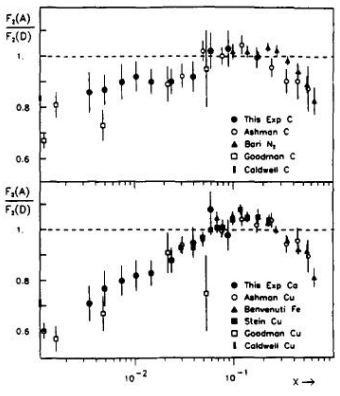

Figure 2.2: The EMC NA28 results for F_2^C/F_2^D and F_2^{Ca}/F_2^D together with a compilation of other experiments. Figure taken from [110].

- "EMC[5] effect": a depletion $R_{F_2}^A \leq 1$ at 0.3≤x≤0.8,
- "Fermi motion": an excess $R_{F_2}^A \geq 1$ towards x→1.

There is no unique theoretical description of these effects. It is believed that different mechanisms are responsible for them in different kinematic regions [110].

Nuclear shadowing

In the region of small x, partonic distributions are dominated by sea quarks and gluons. Nuclear shadowing refers to the depletion of low (x <0.1) partons within a nucleus compared to a free nucleon leading to a reduction in the high p_T hadron yield.

Several explanations of this shadowing have been proposed. There are the generalized vector meson dominance (GVMD) models in which the virtual photon is described as fluctuating from a bare photon state to a superposition of vector mesons (quark anti-quark pairs). These vector mesons interact hadronically with the nucleus (multiple scattering of the hadronic intermediate state on different nucleons inside the nucleus) and are absorbed mainly by the nucleons on the surface of the nucleus. The inner nucleons are thus "shadowed" by the surface ones and the measured cross section per nucleon is reduced with respect to the free nucleon one [111, 112].

Equivalently, there are the partonic models in which shadowing is described by the fact that low x partons, because of the uncertainty principle, spread over a large longitudinal distance (in the frame in which the nucleus is moving fast). Partons of different nucleons may thus overlap in space and fuse, thereby reducing the density of low momentum partons and increasing that of higher momentum ones. Since in DIS the cross section is proportional to the parton distribution functions, the depletion of low x partons causes a depletion in the nuclear structure functions. Similarly the enhancement in the parton density determines an increase - "anti-shadowing" - of the bound nucleon structure functions with respect to the free nucleon ones [110, 113].

On the other hand, other approaches (EKS98, HKM) do not address the origin of shadowing but only its evolution with $\ln Q^2$: parton densities inside the nucleus (nPDFs) are parameterized at some scale Q_0^2 and then evolved using the DGLAP evolution equations, similar to the case of the free proton PDFs. The differences in the approaches come mainly from the sets of data used (e.g. the use of Drell-Yan data or not) to constrain the parton distributions. Currently, there are two sets of nPDFs available which are based on the global DGLAP fits to the data: (i) EKS98 (Eskola, Kolhinen and Salgado) [114] and (ii) HKM (Hirai, Kumano and Miyama) [115]. The HKM analysis uses only the DIS data, whereas EKS98 includes also the Drell-Yan data from pA collisions[6].

In the EKS98 approach the parton distributions of the bound protons in the nucleus A, $f_i^{p/A}$, are defined through the modifications of the corresponding distributions in the free proton,

$$R_i(x, Q_0^2) = \frac{f_i^{p/A}(x, Q_0^2)}{f_i^p(x, Q_0^2)} \tag{2.3}$$

where $i = u, \bar{u}, d, \bar{d}, ..., g$ and f_i^p is the known free proton PDF (such as CTEQ, MRST or GRV). In this way, all nuclear effects on parton densities are included in the parameterization at Q_0^2=2.25 GeV^2, which is obtained from a fit to experimental data. Further constraints which are used are momentum and baryon number sum rules. Details of the EKS98 analysis can be found in [114].

The definition of the nPDF in the HKM analysis differs slightly from that in EKS98. Instead of the PDF of the bound protons, HKM define the nPDF as the average distributions of each flavor i in a nucleus A: $f_i^A(x, Q^2) = (Z/A) f_i^{p/A}(x, Q^2) + (1 - Z/A) f_i^{n/A}(x, Q^2)$. The HKM nuclear modifications

[5]EMC stands for European Muon Collaboration at CERN. The EMC experiment is a DIS experiment using muons scattering off nuclei.

[6]The DY data are very important in the EKS98 analysis in fixing the relative modifications of valence and sea quarks at intermediate x.

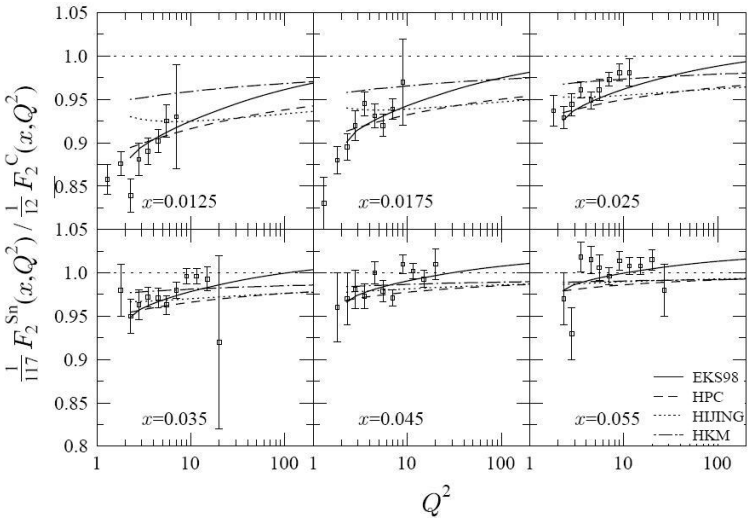

Figure 2.3: Comparison of the calculated and measured Q^2 dependence of the ratio F_2^{Sn}/F_2^C. The NMC data are shown with statistical errors only. The results are for EKS98 (solid lines), HKM (dotted-dashed), HPC (dashed) and HIJING (dotted). Figure taken from [116].

at the initial scale $Q_0^2 = 1$ GeV^2 are then defined through

$$f_i^A(x,Q_0^2) = w_i(x,A,Z)\left[\frac{Z}{A}f_i^p(x,Q_0^2) + (1-\frac{Z}{A})f_i^n(x,Q_0^2)\right] \tag{2.4}$$

where $w_i(x,A,Z)$ are the initial modifications obtained through a minimum χ^2 fit to DIS data [115].

The effect of nuclear shadowing was phenomenologically implemented in HIJING assuming the parton a distribution function inside nucleus A to be factorizable into the parton distribution in a nucleon $f_{a/N}(x,Q^2)$ and the impact-parameter dependent nuclear modification factor $S_{a/A}(x,b)$, which accounts for the nuclear shadowing and antishadowing effects. In the parameterization, the quark sector is fitted to DIS data, while the gluon sector, especially shadowing and antishadowing are constrained by the requirement that HIJING reproduces the measured charged-particle multiplicities in Au+Au collisions at RHIC[7]. The HIJING parameterization does not have any scale dependence [117].

In the Fig.2.3 are shown the NMC (New Muon Collaboration at NA37/CERN) data and the calculated results for the ratio F_2^{Sn}/F_2^C. The experimental data are well reproduced by the EKS98 parameterization. The HKM results do not describe the data well. Also, at small scales, the data suggest faster evolution than that in HKM. The HIJING parameterization results in a negative Q^2 slope for the ratio F_2^{Sn}/F_2^C at small values of x and Q^2, in contradiction with the data. This behavior is caused by the strong gluon shadowing at small x [116].

Cronin effect

One experimental observation, when comparing elementary p+p collisions to p+A reactions, is that the cross section does not simply scale with the number of target nucleons A in a p+A collision. It was first observed by Cronin et al., in 1975 at Fermilab that there is an enhancement in the production cross section of hadrons in p+A collisions compared to the p+p reactions in the $p_T > 2$ GeV/c region [120]. This effect is called "Cronin effect". The cross section of produced hadrons in

[7]In the case that the dominant contribution to total multiplicities comes from jets or minijets, the measurements of N_{ch} done at RHIC give direct information about the initial gluon distributions in nuclei. This has been used to parameterize the gluon distribution function in the HIJING model. As a result, a strong gluon shadowing has been proposed in order to reproduce the multiplicity.

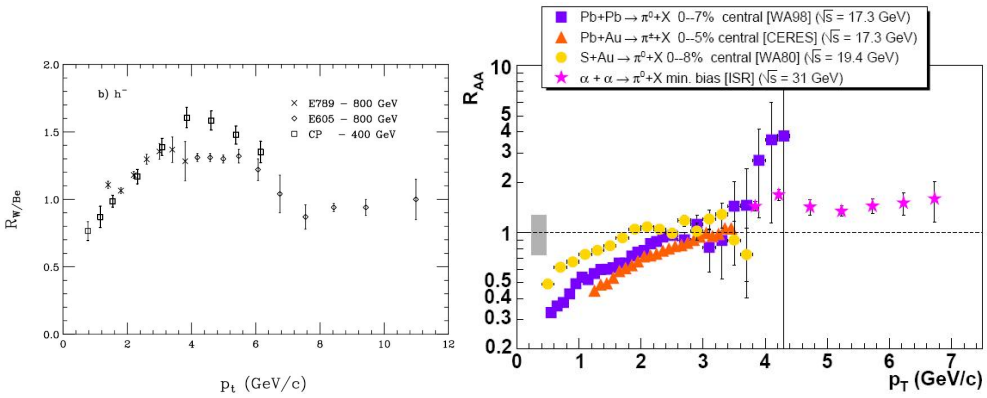

Figure 2.4: Left: Cronin effect at fixed target energies expressed as $R_{W/Be}$, the ratio of the cross sections in p+W and p+Be collisions vs. p_T. Right: Nuclear modification factors for pion production at CERN-SPS in central Pb+Pb, Pb+Au, and S+Au reactions at $\sqrt{s_{NN}} \approx 20$ GeV, and at ISR in minimum bias α+α reactions at $\sqrt{s_{NN}} = 31$ GeV. Figures taken from [118, 119].

p+A collision is represented by

$$E\frac{d^3\sigma^{pA}}{dp^3} = A^{\alpha(p_T)} E\frac{d^3\sigma^{pp}}{dp^3} \tag{2.5}$$

with α >1 for transverse momenta larger than 2 GeV/c (α=1 for binary scaling). Left panel of Fig.2.4 shows the pW-to-pBe ratio of cross sections for charged hadron particle production obtained at Fermilab in collisions of 800 GeV protons with the fixed tungsten(W) and beryllium(Be) targets. The ratios are less than one for $p_T < 2$ GeV/c and greater than one for $2 < p_T < 7$ GeV/c revealing the Cronin effect [118].

The Cronin effect has also been observed in heavy ion collisions. The nuclear modifications factors for the high p_T data from the CERN-SPS: π^0 and $\pi^{\pm}$ at $\sqrt{s_{NN}} = 17.3$ GeV from Pb+Pb (WA98) and Pb+Au (CERES/NA45) respectively, and π^0 from S+Au at $\sqrt{s_{NN}} = 19.4$ GeV (WA80) are plotted in right panel of Fig.2.4 [119]. These results indicate that high-p_T hadron production at $\sqrt{s_{NN}} \sim 20$ GeV is not enhanced in central nucleus-nucleus reactions and, within errors, is consistent with scaling with the number of NN collisions. However, in ref. [121] is shown that the high p_T pion production in peripheral Pb+Pb reactions at SPS is enhanced by as much as by a factor of ~ 2 compared to the N_{coll} scaling expectation. This fact indicates that there must exist a mechanism in central A+A that "neutralizes" the Cronin enhancement down to values consistent with $R_{AA} \approx 1$. The Cronin effect is clearly seen for α+α reactions at $\sqrt{s_{NN}} = 31$ GeV.

The Cronin effect is believed to be due to the initial state multiple scattering of the incident partons while passing through the nucleus A, prior to the hard scattering. These scatterings increase the transverse momentum of the partons leading to an effective broadening of the transverse momentum k_T of the colliding partons. Thus, the Cronin effect provides an additional k_T kick, leading to nuclear k_T broadening, $\langle \Delta k_T^2 \rangle_A$. Therefore, the initial parton k_T distribution inside a projectile nucleon going through the target nucleon becomes

$$g_A(k_T) = \frac{1}{\pi \langle k_T^2 \rangle_A} e^{-k_T^2/\langle k_T^2 \rangle_A} \tag{2.6}$$

with a broadened width $\langle k_T^2 \rangle_A = \langle k_T^2 \rangle + \langle \Delta k_T^2 \rangle_A$. The broadening is assumed to be proportional to the mean number of scatterings the projectile suffers inside the nucleus. The nuclear size gives the possibility to control the amount of multiple scattering at given values of momentum fraction x and scale Q. The generalized parton distributions in Eq.2.1 are approximated as

$$f_{a/A}(x, k_T, Q^2) = f_{a/A}(x, Q^2) g_A(k_T) \tag{2.7}$$

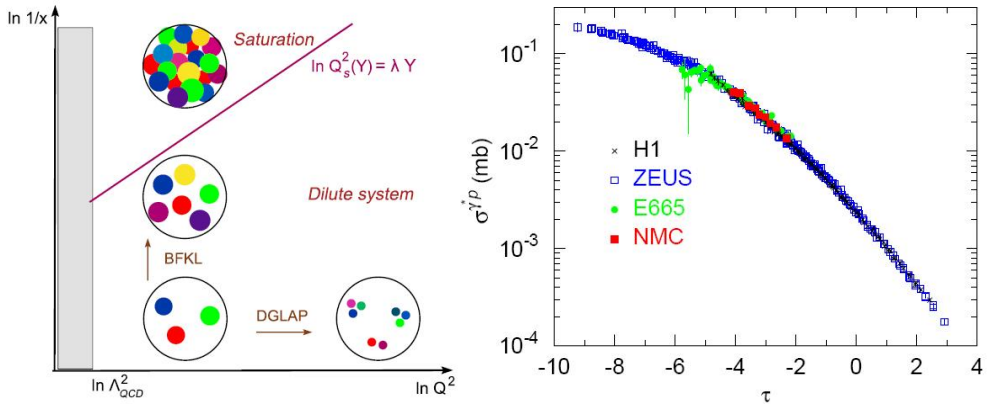

Figure 2.5: Left: The "phase-diagram" for QCD evolution suggested by the HERA data; each colored blob represents a parton with transverse area $\Delta x_\perp \sim 1/Q^2$ and fraction x of the hadron momentum. Right: Geometrical scaling in the γ^*-proton cross-section $\sigma_{\gamma^* p}(x, Q^2) \sim \frac{\alpha_s}{Q^2} xG(x, Q^2)$ at HERA. Figures taken from [122, 123].

Gluon saturation

As can be seen in the HERA data shown in Fig.2.1, the gluon density $xg(x, Q^2)$ rises very fast when decreasing Bjorken x at fixed Q^2 (roughly, as a power of $1/x$), and also when increasing Q^2 at a fixed value of x. For sufficiently small values of x and/or of Q^2, this sharp growth of gluon distribution function is expected to slow down eventually due to mutual interactions between gluons when they start to spatially overlap ($g+g \rightarrow g$ fusion). This is usually referred to as gluon density saturation and will happen when the probability of two gluons recombining into one is as large as the probability for a gluon to split into two gluons. The gluon recombination prevents further growth of parton densities and generate instead the gluon saturation described by a saturation scale[8], Q_s [122, 123].

The left panel of Fig.2.5 schematically shows the different evolution regimes of partons in the transverse plane as a function of lnQ^2 and $Y = ln(1/x)$. The number of partons increases both with increasing Q^2 and with decreasing x, but whereas in the first case (increasing Q^2) the transverse area $\sim 1/Q^2$ occupied by every parton decreases very fast and more than compensates for the increase in their number (so, the proton is driven towards a regime which is more and more dilute), in the second case (decreasing x) the partons produced by the evolution have roughly the same transverse area, hence their density is necessarily increasing.

Since $xg(x, Q^2)$ can be interpreted as the number of gluons in the hadron wavefunction which are localized within an area $\sim 1/Q^2$ in the transverse plane, an increase of Q^2 effectively diminishes the "size" of each parton, partially compensating for the growth in their number (i.e. the higher Q^2 is, the smaller the x at which saturation sets in). Saturation effects are, thus, expected to occur when the size occupied by the partons becomes similar to the size of the hadron, πR^2. In the case of nuclear targets with A nucleons (i.e. with gluon density $xG(x, Q^2) = A \cdot xg(x, Q^2)$), this condition provides a definition for the saturation scale:

$$Q_s^2(x) \cong \alpha_s \frac{1}{\pi R^2} xG(x, Q^2) \sim A^{1/3} x^{-\delta} \sim A^{1/3} e^{\delta y} \tag{2.8}$$

($\delta \sim$0.3 at HERA) and determines the critical values of the momentum transfer, at which the parton system becomes dense and recombination frequently happens. The nucleon number dependence implies that, at equivalent energies, saturation effects will be enhanced by factor $A^{1/3}$ ($\sim$6 for A_{Pb}=208) compared with protons. The dependence of the saturation scale Q_s on the rapidity suggests that saturation effects can be studied at RHIC[9] with heavy nuclei at large rapidities.

[8] The "saturation scale" Q_s is defined such that saturation is expected to occur at Q-values below Q_s.

[9] At RHIC energies and at midrapidity the saturation scale for Au ions is expected to be $Q_s^2 \approx$2 GeV^2.

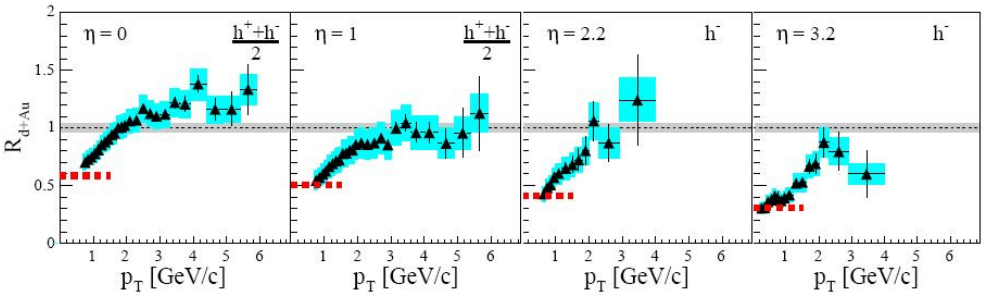

Figure 2.6: Forward suppression observed by BRAHMS. Figure taken from [126].

The first evidence of QCD saturation regime comes from the "geometrical scaling" observed in DIS at HERA [124, 125]. The measured virtual photon-proton γ^*p cross-section at $x \leq 0.01$, which in principle depends on both variables x and Q^2, was found to depend only on the combination $\tau = Q^2/Q_s^2(x)$ (see the right panel of Fig.2.5), $\sigma_{\gamma^* p}(x, Q^2) = \sigma_{\gamma^* p}(\tau)$. Therefore, in its essence geometric scaling is a manifestation of the existence of the saturation scale characterizing a dense partonic system.

In nucleus-nucleus collisions at RHIC and LHC energies, the CGC [41] is proposed to be the appropriate framework for describing the early stages of the collision, because most of the particles are produced from low x gluons. The CGC approach reproduces well not only the measured hadron multiplicities but also the centrality and energy dependences of the bulk AA hadron production [127, 128, 129]. The observation of the suppression of hadron spectra at high p_T and forward rapidity in d+Au collisions at RHIC provides further information on the onset of saturation.

The fact that the nuclear modification factor R_{dA} is larger than unity at midrapidity is believed to be an effect of multiple scatterings (Cronin effect). The evolution of the R_{dAu} with rapidity and centrality is consistent with the Au target description where the rate of gluon fusion becomes comparable with that of gluon emission as the rapidity increases and it slows down the overall growth of the gluon density. The measured nuclear modification factor compares the slowed down growth of the gluon density in the Au target to a sum of incoherent p+p collisions, considered as dilute systems, whose gluon densities grow faster with rapidity because of the absence of gluon fusion, leading to the observed suppression (see Fig.2.6) [126].

2.2.2 Final state effects. Parton energy loss. Jet quenching

Bjorken predicted that high energy partons propagating through the QGP suffer differential energy loss due to elastic scattering with the quarks and gluons in the plasma and he pointed out that events may be observed, in which the hard collisions may occur such that one jet is escaping without absorption, whereas the other is fully absorbed in the medium. The resulting "ionization" loss was estimated to be $-dE/dz \sim \alpha_s^2\sqrt{\epsilon}$, where ϵ is the energy density of the (ideal) QGP [130].

Bremsstrahlung is another important source of energy loss. The size of this effect depends on the density and nature of the medium and may be significantly enhanced in a deconfined partonic medium [131]. Due to multiple inelastic scattering and induced gluon radiation high-momentum jets and high-p_T leading hadrons may become depleted, quenched or even extinct.

In contrast with the QED energy loss of electrons in matter, the QCD energy loss of partons cannot be measured directly because partons are not final, experimentally observed particles. Instead, studies of partonic energy loss must exploit the modifications of the fragmentation functions $D_{h/c}(z)$ which can be directly related to the energy loss of the leading parton. Medium-modified fragmentation functions have been studied in lepton-nucleus and nucleus-nucleus collisions. Ideally one should perform a new global fit for these medium-FF using modified DGLAP evolution equations. These modified evolution equations take care of the evolution, in the medium, of the parton to the final

hadrons. The idea is to compare them in order to obtain information about the relative densities of the media and the effect of the energy loss on the p_T spectra.

The medium-induced distribution of gluons radiated off an initial hard parton has been computed by two approximations: the multiple soft scattering approximation and the opacity expansion [130]. In the first approximation, the medium-dependence results from the multiple soft scattering of the projectile in the spatially extended matter. The opacity expansion can be related to an expansion in the effective number of scatterings and allows for hard momentum transfers from the medium.

Multiple soft scattering

Consider a medium-dependence introduced by arbitrary many soft scattering centers. In such a medium the parton projectile undergoes a Brownian motion in the transverse plane due to multiple soft scattering and the in-medium path length, L, is larger than the mean free path[10], λ ($L \gg \lambda$). The transverse position of the parton projectile in configuration space changes rather smoothly. This is the approximation used by the Baier-Dokshitzer-Mueller-Peigne-Schiff group and Zakharov (BDMPS-Z formalism) [132].

In this approximation, the transport coefficient, $\hat{q}$, characterizes the transverse momentum squared q_T^2 transferred from the medium to the projectile parton per mean free path λ. For a static medium, it is time-independent, $\hat{q} = \langle q_T^2 \rangle / \lambda$.

BDMPS established that the dominant contribution to the energy loss in a dense medium comes from the rescattering of the emitted gluon with the colored plasma constituents. In the limit of a thick quark-gluon plasma, the authors found that the average energy loss of the parton due to the gluon radiation shows a quadratic L^2 dependence on the in-medium path length,

$$\langle \Delta E \rangle \sim \alpha_s C_R \hat{q} L^2 \tag{2.9}$$

where C_R is the QCD coupling factor (Casimir factor), equal to 4/3 for quark-gluon coupling and 3 for gluon-gluon coupling. BDMS average energy loss is proportional with $\alpha_s C_R$ and thus, larger by a factor 9/4=2.25 for gluons than for quarks, proportional to the transport coefficient of the medium, proportional to square of the path length and independent of the initial parton energy E.

In the multiple soft scattering approximation, the BDMPS transport coefficient $\hat{q}$ and the in-medium path length L are the only informations about the properties of the medium which enter the gluon radiation spectrum. The transport coefficient can be related to the density ρ of the scattering centers and to the typical momentum transfer in the gluon scattering off these centers, $\hat{q} = \rho \int q^2 d\sigma / dq^2$. For cold nuclear matter

$$\hat{q}_{cold} \cong 0.05 \; GeV^2/fm \tag{2.10}$$

has been obtained using the nuclear density $\rho_0 = 0.17$ fm^{-3}, the gluon PDF of the nucleon $xG(x, Q^2) \sim 1$ and $\alpha_s = 0.5$. The estimation for a hot medium

$$\hat{q}_{hot} \cong 1 \; GeV^2/fm \cong 20 \hat{q}_{cold} \tag{2.11}$$

based on perturbative treatment ($\alpha_s = 0.3$) of gluon scattering in an ideal QGP with a temperature of $T \sim 250$ MeV resulted in the value of the transport coefficient of about a factor twenty larger than for cold matter.

Single hard scattering (opacity expansion)

The single hard scattering limit consists in a series expansion (opacity expansion) of the gluon radiation spectrum in $[n(\xi)\sigma(r)]^N$ terms, where $\sigma(r)$ is modeled by a Yukawa potential with Debye

[10]The distance between the production point of the hard parton in space-time and the position of a secondary scattering introduces this microscopic length scale, i.e. mean free path.

screening mass μ and N is the number of scattering centers. This is the approximation used by the Gyulassy-Levai-Vitev (GLV) group ("single hard scattering" denotes the first term N = 1 in the this expansion).

In this limiting case, the radiation pattern results from an incoherent superposition of very few single hard scattering processes positioned within path length L. In the first order in the opacity expansion of the gluon energy distribution, the entire medium dependence comes from the interaction of the hard parton with a single static scattering center, multiplied by the number $n_0 L = L/\lambda$ of scattering centers along the path. In the single hard scattering, the Debye screening mass μ denotes the average transverse momentum transfer per scattering center and the single scatterer is modeled by a Yukawa potential. It will result again a quadratic L-dependence of the average energy loss.

In the opacity approximation, one specifies both the average transverse momentum squared μ^2 transferred to the projectile and the average number $n_0 L$ of scattering centers involved in this momentum transfer. This is in contrast to the multiple soft scattering approximation which specifies the average transverse momentum squared transferred to the projectile irrespective of the number of scattering centers involved. Thus, the single hard scattering approximation contains one additional model parameter, the opacity $n_0 L = L/\lambda$.

The hard scattering approximation is dominated by the hard region of the gluon energy distribution while the multiple soft scattering approximation is dominated by the soft region. Despite this difference, both approximations lead to quantitatively comparable results if comparable sets of model parameters are used [130].

2.2.3 Gyulassy-Levai-Vitev model

The Gyulassy-Levai-Vitev (GLV) approach [133, 134] to the parton energy loss relies on a systematic expansion of induced gluon radiation associated with jet production inside a hot and dense nuclear medium in terms of correlations between multiple scattering centers. Analytic expressions for the induced gluon transverse momentum distributions are derived to all orders in powers of the opacity of the medium, $\chi = L/\lambda$. The GLV approach is build around the Gyulassy-Wang (GW) model [131, 63] of multiple scattering in a plasma. In this model, the authors consider sequential elastic scattering of a high energy parton in a random color field produced by an ensemble of static partons and assume a Debye screened potential for each target parton.

For thin plasma, the GLV approach found an important dependence of the energy loss ΔE on the energy E of the fast parton and on the path length. At large jet energies (in the limit $2E/\mu^2 L \gg 1$), the behavior of the energy loss as a function of the density and the size of the system can be summarized to the first order in opacity as follows:

$$\frac{\Delta E}{E} \approx \frac{9 C_R \pi \alpha_s^3}{8} \rho^g L^2 ln \frac{2E}{\mu^2 L}, \qquad static \tag{2.12}$$

$$\frac{\Delta E}{E} \approx \frac{9 C_R \pi \alpha_s^3}{4} \frac{1}{A_\perp} \frac{dN^g}{dy} L \; ln \frac{2E}{\mu^2 L}, \qquad (1+1D) \tag{2.13}$$

where L is the jet path length in the medium, $A_\perp$ is the transverse size of nuclear matter, e.g. $A_\perp = \pi R^2$ for central nucleus-nucleus collisions. C_R=4/3(3) for quarks (gluons), respectively, is the Casimir factor in the fundamental representation of SU(3). For static media $\Delta E/E$ depends quadratically on the size of the plasma. The path dependence is changed if the medium is expanding. The medium induced radiative energy loss is proportional to the density of the scattering centers in the medium and for the case of a longitudinal (1+1D) Bjorken expansion is sensitive to the initial parton (gluon) rapidity density dN^g/dy, since the gluon rapidity density can be related to the hadron multiplicities and the number of participants in A+A collisions. For this case the energy loss dependence on the size of the medium is reduced to a linear dependence [135].

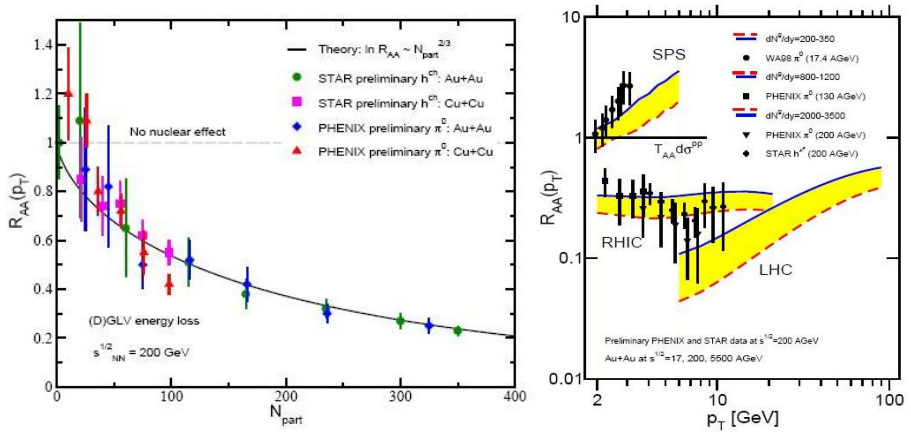

Figure 2.7: Left: Comparison of the GLV model to the centrality dependent quenching in Cu+Cu and Au+Au reactions measured by STAR and PHENIX. Right: suppression/enhancement ratio $R_{AA}(p_T)$ for neutral pions at $\sqrt{s_{NN}}$ = 17, 200, 5500 GeV. Solid (dashed) lines correspond to the smaller (larger) effective initial gluon rapidity densities at given $\sqrt{s}$ that drive parton energy loss. Figures taken from [135, 134].

The key to understanding the dependence of jet quenching on the nuclear species is the A or N_{part} dependence of the characteristic parameters in Eq.2.13

$$dN^g/dy \propto dN^h/dy \propto A \propto N_{part}, \tag{2.14}$$

$$L \propto A^{1/3} \propto N_{part}^{1/3},\ A_\perp \propto A^{2/3} \propto N_{part}^{2/3} \tag{2.15}$$

Therefore, the fractional energy loss scales as $\epsilon = \Delta E/E \propto A^{2/3} \propto N_{part}^{2/3}$. The authors predict that the logarithm of nuclear suppression has simple power law dependence on the system size, $lnR_{AA} = -kN_{part}^{2/3}$. The left panel of Fig.2.7 confronts the predicted N_{part} dependence of jet quenching with preliminary STAR and PHENIX measurements in Au+Au and Cu+Cu collisions at $\sqrt{s_{NN}}$= 200 GeV. Within the systematic uncertainty, this is a good description of the centrality dependence of jet quenching.

Jet tomography consists of determining the effective initial gluon rapidity density dN^g/dy that best reproduce the quenching pattern of the data. The right panel of Fig.2.7 shows the predicted nuclear modification as a function of $\sqrt{s_{NN}}$ at SPS, RHIC and the LHC as a function of the density of the quark-gluon plasma. The authors consider that the p_T dependence of R_{AA} is a result of the interplay of the Cronin effect, jet quenching and nuclear shadowing. At SPS, the large Cronin enhancement is reduced by a factor of two with $dN^g/dy = 350$ but the data are more consistent with a smaller gluon density ≤ 200. At RHIC, for $p_T > 2$ GeV jet quenching dominates, but surprisingly the rate of variation with p_T of the Cronin enhancement and jet quenching produce an approximately constant suppression pattern with magnitude dependent only on the initial dN^g/dy.

In a deconfined medium of high color charge density $\rho \sim dN^g/dy/\tau A_\perp$ if a fast parton loses ϵE of its initial energy prior to fragmentation its momentum fraction z is modified to $z \rightarrow z^* = p_h/p_c(1-\epsilon) = z/(1-\epsilon)$. The modification of inclusive hadron production from final state radiative energy loss can be computed from Eq.2.1 with the medium-modified fragmentation function

$$D_{h/c}(z) \Rightarrow \int_0^{1-z} d\epsilon P(\epsilon) \frac{1}{1-\epsilon} D_{h/c}(\frac{z}{1-\epsilon}) + \int_z^1 d\epsilon \frac{dN^g}{d\epsilon}(\epsilon) \frac{1}{\epsilon} D_{h/g}(\frac{z}{\epsilon}) \tag{2.16}$$

where $z = p_h/p_c$ is the unmodified momentum fraction in the vacuum and $P(\epsilon)$ is the probability for fractional energy loss $\epsilon = \Delta E/E = \sum_i \omega_i/E$ due to multiple gluon emission. The first term is the FF of the jet c after losing energy due to medium-induced gluon radiation and the second term is the

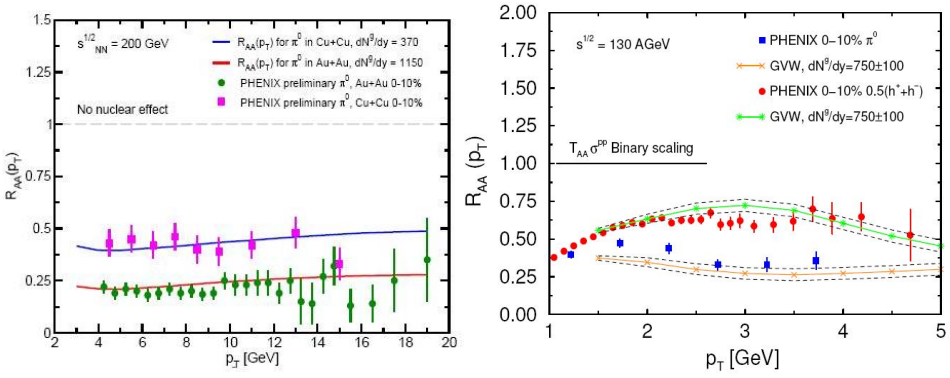

Figure 2.8: Left: Comparison of the preliminary π^0 production in 0-10% central Au+Au and Cu+Cu data from PHENIX to the energy loss calculations with $dN^g/dy = 1150$ and 370, respectively. Right: Suppression of neutral pions and inclusive charged hadrons in central Au+Au at $\sqrt{s_{NN}}$=130 GeV relative to the binary collision scaled p+p result. Figures taken from [136, 137].

feedback due to the fragmentation of the $N^g = \int_0^1 d\epsilon \frac{dN^g}{d\epsilon}(\epsilon)$ radiated gluons. For the single inclusive particle production at RHIC the first term in Eq.2.16 dominates. The second term in Eq.2.16 which reflects the gluon feedback contribution, becomes important for single inclusive measurements only at the LHC. The authors found that, at RHIC the redistribution of the lost energy leads to small, $\sim$ 25% modification of the neutral pion cross section in the low and moderate p_T in contrast to LHC where the fragmentation of medium-induced gluons is shown to alter the $p_T \leq 15$ GeV/c π^0 cross section in central Pb+Pb reactions by as much as a factor of two [135].

The left panel of Fig.2.8 shows the predicted transverse momentum dependence of $R_{AA}(p_T)$ for central Au+Au and Cu+Cu collisions at the top RHIC energy. The GLV description for the energy parton loss predicted the flat p_T dependence of R_{AA} over the high p_T range covered by RHIC data. The authors make the important observation that for similar densities and system sizes, for example $dN^g/dy = 410$ in mid-central Au+Au and $dN^g/dy = 370$ in central Cu+Cu, the magnitude of the predicted pion suppression is similar [136].

In the ref. [137], the GLV energy loss was combined with a non-perturbative baryon production and transport mechanism to gain insight into the meson/baryon behavior at RHIC. The right panel of the Fig.2.8 shows the R_{AA} for inclusive charged hadrons and neutral pions; the authors obtain agreement with the data if the jet energy loss is driven by initial gluon rapidity density $dN^g/dy \cong$800. The difference in the suppression factor of π^0 and $(h^+ + h^-)/2$ is understood through the possibly different baryon and meson production mechanisms in the moderate high $2 \leq p_T \leq 5$ window. In the calculation, pion production becomes pQCD dominated for $p_T > 2$ GeV/c and correspondingly suppressed by the jet energy loss. In contrast, baryon production is dominated through the junction mechanism[11] by baryon transport in rapidity and moderate p_T. This accounts for different suppression for neutral pions and inclusive charged hadrons as seen in the Fig.2.8. At $p_T > 5$ GeV/c baryon production also becomes perturbative, leading to a suppression.

[11] Baryons are considered as "Y" shape configurations consisting of three strings attached to three valence quarks and connected in a point called "baryon junction". Thus, the baryon junction is the vertex where the three color flux tubes link the three valence quarks. In a highly excited baryonic state, when these strings fragment via $q\bar{q}$ production, the resulting baryon will be composed of the three sea quarks which are linked to the junction while the original valence quarks will emerge as constituents of three leading mesons. Being a purely gluonic configuration, the junction may be easily transported into the mid-rapidity region. One prediction of this mechanism is that fragmentation of the valence quarks down to the junction is expected to enhance hyperon production by a factor of 3 just from the random combinatorics of s vs u, d pair production. In addition, from the random addition of three sea quarks, the transverse momentum of the final baryon is automatically enhanced by a factor of $\sqrt{3}$.

2.2.4 Quenching weights

It has been proposed by K.J. Eskola, H. Honkanen, C.A. Salgado and U.A. Wiedemann [138, 139] that in the presence of a spatially extended medium, the additional medium-induced energy degradation of the leading parton can be described by a probability $P(\Delta E)$, the so-called quenching weight. The authors calculate the quenching probabilities (weights) for light quarks and gluons corresponding to two limits which emphasize the role of multiple soft and single hard medium-induced scatterings, respectively.

The medium-induced gluon radiation spectrum depends on the length of the medium L and the transport coefficient $\hat{q}$. Formally, the $\hat{q}$ parameter enters via an integral over the spectrum of emitted gluons, which is related to the medium density of color charges. Considering the independent gluon emission approximation, the probability that a parton loses an additional energy ΔE of its energy by medium-induced gluon radiation is given by the quenching weight, $P(\Delta E)$, and the medium-modified fragmentation functions are modeled by the convolution $D^{med}_{k\to h} = P(\Delta E) \otimes D_{k\to h}$. Then the medium-modified function are used to compute the cross-section for the production of a hadron h through the expression

$$\frac{d\sigma^{AA\to h+X}}{dp_T} \sim f_{i/A}(x_1, Q^2) \otimes f_{j/A}(x_2, Q^2) \otimes \sigma^{ij\to k} \otimes D^{med}_{k\to h}(z, Q^2) \tag{2.17}$$

where $f_{i/A}(x, Q^2)$ are the nuclear PDF and $\sigma^{ij\to h}$ the perturbatively calculable partonic cross-section. The strategy is then to fit the best value of $\hat{q}$ that reproduces the experimental suppression measured by the nuclear modification factor $R_{AA}(p_T)$. $\hat{q}$ is proportional to the medium density. Thus, comparing the different $\hat{q}$ obtained by applying this procedure to different systems, information about the density of the media is obtained.

In general, in nucleus-nucleus collisions at collider energies, the produced hard partons propagate through a rapidly expanding medium. Hence, the transport coefficient is time-dependent, decreases with time - this translates into a dependence $\hat{q} = \hat{q_0}(\frac{\tau_0}{\tau})^\alpha$, where $\alpha = 0$ characterizes a static medium and α=1 a one-dimensional, boost invariant longitudinal expansion. The maximal value $\hat{q_0}$ of the transport coefficient is reached at the time of highest density of the system which is the formation time, τ_0. It has been observed a scaling law which relates the time-dependent transport coefficient to an equivalent static transport coefficient $\bar{\hat{q}} = \frac{2}{L^2}\int_{\tau_0}^{\tau_0+L} d\tau(\tau - \tau_0)\hat{q}(\tau)$. The gluon energy distribution for a time-dependent transport coefficient $\hat{q}$ agrees with the energy distribution obtained for an equivalent static averaged transport coefficient $\bar{\hat{q}}$. This allows to use for the analysis the static scenario and translate afterwards the values for the time-averaged transport coefficients into time-dependent transport coefficients.

The left panel of the Fig.2.9 compares data from RHIC with the R_{AA} calculated with different values of the transport coefficient $\hat{q}$. As the density of the medium (or equivalently the transport coefficient) is increased, the nuclear modification factor is reduced further. This is caused by parton energy loss in the final state. Interestingly, the resulting nuclear modification factor R_{AA} is almost p_T-independent and its dependence on $\hat{q}$ becomes weaker as $\hat{q}$ increases. Partons which traverse a larger in-medium pathlength tend to lose more energy. As long as the density of the medium is sufficiently high, R_{AA} approaches a factor 5 suppression for central Au+Au collisions. Even if one increases the density further, the suppression increases only slightly, since an essentially fixed fraction of the hard partons is produced in the outer "skin" of the two-dimensional transverse overlap of the colliding nuclei and thus remains almost unaffected due to a negligible in-medium path-length. The dominance of surface-emission appears to limit the sensitivity of R_{AA} on the density of the medium. The authors find that the nuclear modification factor is sensitive to the density of the medium up to $\hat{q} \leq$4 GeV^2/fm, but it loses this sensitivity for higher values of $\hat{q}$. The best fits to the data is for $\hat{q}$ between 5 and 15 GeV^2/fm. This implies that the sensitivity of single inclusive spectra to the properties of the medium is rather limited: they provide only a lower bound on the produced density.

Another illustration of surface-dominated leading hadron production in nucleus-nucleus collision is to compare R_{AA} calculated for several fixed in-medium pathlengths L = 1,..., 6 fm, see Fig.2.9

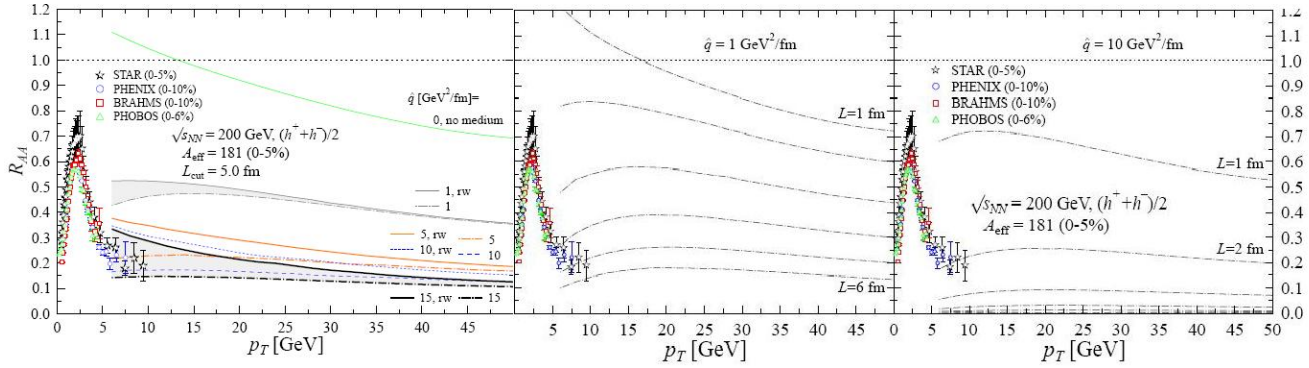

Figure 2.9: Left: Nuclear modification factor R_{AA} for charged particles in central Au+Au collisions at $\sqrt{s_{NN}}$=200GeV compared with theoretical curves for different values of $\hat{q}$. This figure is for a medium which exists for at most $\tau \sim L_{cut} = 5$ fm in the dense partonic phase. Differences between solid and dash-dotted curves indicate uncertainties related to finite energy corrections. Middle: The R_{AA} results at RHIC computed using constant in-medium path length L for $\hat{q}$ = 1 GeV^2/fm and $\hat{q}$ = 10 GeV^2/fm (right panel). Figure taken from [138].

middle. For a small transport coefficient, $\hat{q}$ = 1 GeV^2/fm, R_{AA} decreases significantly even for L = 4, 5, 6 fm, indicating that leading hadrons can originate from partons with significant in-medium pathlength. If the transport coefficient is increased to $\hat{q}$ = 10 GeV^2/fm, partons with in-medium pathlength more than 3 fm make a negligible contribution to R_{AA}, see Fig.2.9 right. Effectively, with $\hat{q}$ = 10 GeV^2/fm the results from RHIC can be reproduced with a fixed path length $L \sim 2$ fm, which is clearly smaller than geometrical path length (5-6 fm).

2.2.5 Parton Quenching Model (PQM)

In the Monte Carlo program Parton Quenching Model (PQM) [140, 141, 142] the authors combine a calculation of parton energy loss with a realistic description of the collision geometry given by the Glauber model. The model has one single parameter that sets the scale of the energy loss. Once the parameter is fixed on the basis of the data at $\sqrt{s_{NN}}$ = 200 GeV, it is scaled to different energies assuming its proportionality to the expected volume-density of gluons and then apply the same approach to calculate the nuclear modification factors at different energies. Since the model do not include initial-state effects, such as nuclear modification of the parton distribution functions and parton intrinsic transverse-momentum broadening, it is restricted the study to the high-p_T region, (above 4-5 GeV at RHIC energies), where these effects are expected to be small (less than 10% on R_{AA}). The modification with respect to the pp (vacuum) case is given by the energy-loss probability, $P(\Delta E_j)$, for the parton j, which is calculated in the multiple soft scattering approximation, in the framework of the BDMPS formalism.

In PQM the authors use Monte Carlo techniques based on a parton-by-parton basis: for a given centrality, the (transverse) density profile of the matter is computed and for each produced parton in the collision its path (azimuthal direction and length) through the matter determined. Thus, the fixed values of $\hat{q}$ and L are replaced with their respective distributions as "seen" by the partons on the way out. The collision geometry is incorporated in the calculation of parton energy loss via the "local", space-point dependent, transport coefficient, $\hat{q}(\xi)$. Details on the quenching procedure and its application to high-p_T data can be found in ref. [140, 141, 142].

Using the parton-by-parton approach in PQM, for the most central collisions, the result obtained with the $\bar{\hat{q}}$=14 GeV^2/fm (where the average is done over all produced hard partons) matches the data. Then, keeping the same value of $\bar{\hat{q}}$ the centrality is changed by using dependence of the local transport coefficient. The PQM parton-by-parton calculation is shown in Fig.2.10. The results follow the increase of the measured R_{AA} with decreasing centrality. Numerically, the PQM value of $\hat{q}$=14

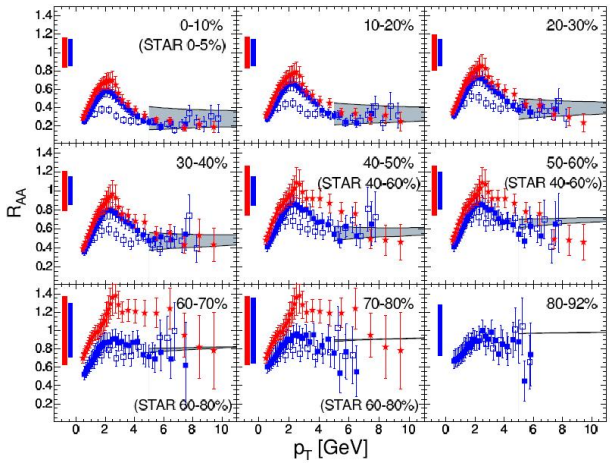

Figure 2.10: R_{AA} in the PQM parton-by-parton approach at midrapidity for different centralities in AuAu collisions at $\sqrt{s_{NN}}$=200 GeV. The measured points are for charged hadrons (stars, closed squares) and neutral pions (open squares). The gray band is the PQM quenching weights calculation using the $\bar{\hat{q}}$=14 GeV^2/fm for the most central collisions. Figure taken from [141].

GeV^2/fm is larger than $\hat{q}$=10 GeV^2/fm found by Eskola et al. for central collisions. However, this is not an inconsistency. The value of α_s used in the calculation of the quenching weights is $\alpha_s = 1/3$ here and $\alpha_s = 1/2$ there. Since the scale of the energy loss is set by the product $\alpha_s\hat{q}$ ($\langle\Delta E\rangle \propto \alpha_s C_R \hat{q} L^2$), the product is about the same for both calculations. The authors find that the partons yielding hadrons with $p_T > 5$ GeV are, on average, emitted from a depth of about 1.7 fm and suffer an energy loss of less than 0.3 GeV/fm.

2.2.6 pQCD Model

To characterize medium-modifications to the high p_T particle production in nucleus-nucleus collisions and to relate them to the properties of hot and dense QCD matter produced in collision, knowledge about the multiple scatterings which a hard parton undergoes while propagating through cold nuclear matter is a very important baseline. The GLV approach cannot be applied directly to multiple parton scattering in a cold nuclear medium because it applies mainly to a medium where colors are screened and deconfined.

X.N. Wang et al. [144, 145] calculated the parton energy loss in cold and hot nuclei and the modification modification of the fragmentation functions due to multiple scattering and induced gluon bremsstrahlung. The authors elaborate a general twist-expansion[12] of multiple parton scattering and can calculate explicitly the modified parton fragmentation functions. The parton matrix elements

[12]In the pQCD the leading twist approximation is widely used to describe a large class of phenomena. Factorization theorem enable us to shift non-perturbative physics into a set of well-defined, gauge-invariant (i.e. observable) and universal (i.e. process independent) quantities. These quantities can be expressed by matrix elements of parton operators between hadron states. It is possible to establish a hierarchy between the matrix elements in terms of an expansion in inverse powers of the momentum transfer. The expansion parameter is λ^2/Q^2, where Q is the perturbative hard scale and λ is some non-perturbative scale. The leading contribution in this expansion is called leading twist and always consists of one hard scattering on the parton level.

In the simple example of DIS the hard scattering takes place between the virtual photon and a quark from the target. The non-perturbative part is described by a matrix element defining the parton distributions for quarks and gluons respectively. In a nuclear environment (AA collisions), the picture of a dominant single hard scattering process is doubtful. From the point of view of the twist expansion, the matrix elements which are factors in front of the expansion parameter λ^2/Q^2, can be numerically larger compared to the case of the same observable in p+p collisions. The parton distributions are expected to scale roughly with the mass number A of the nucleus, when we neglect shadowing corrections. However it can happen that some higher twist matrix elements scale more strongly with the nuclear size. They have to contain more operators of parton fields, corresponding to more partons that enter the hard scattering [130].

replace the Debye screened interactions used in the GLV approach. This higher twist formalism is presented in detail in ref. [144].

The authors calculate the cross section for the DIS process, where the lepton imparts a large momentum transfer (Q^2) to one of the quarks in the incoming nucleus via single photon exchange. The struck quark then will have to propagate through the rest of the nucleus and possibly experience additional scatterings with other partons from the nucleus. The rescatterings may induce additional gluon radiation and cause the leading quark to lose energy before it fragments into hadrons. Such induced gluon radiations will effectively give rise to additional terms in the DGLAP evolution equations leading to the modification of the fragmentation functions in a medium. Shown in the Fig.2.11 are the calculated nuclear modification factor of the fragmentation functions for the N^{14} and Kr^{84} targets

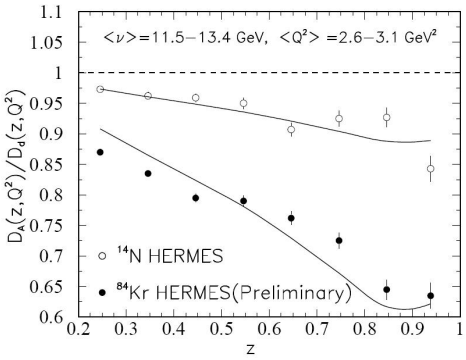

Figure 2.11: Ratios of medium-induced FF over those for a deuterium target. The solid lines are the model calculations based on a modified fragmentation function in a (cold) nucleus. Figure taken from [143].

$$R_A^h(z,\nu) = \frac{d\sigma_A^h(z,\nu)/d\nu dz}{d\sigma_D^h(z,\nu)/d\nu dz} \sim \frac{D_q^h(z,Q^2,A)}{D_q^h(z,Q^2,D)} \quad (2.18)$$

compared to HERMES data [146]. The model can predict the z, energy and a quadratic $A^{2/3}$ nuclear size dependence of the suppression. Using the determined values of the calculation parameters for the HERMES data, one gets the quark energy loss $dE/dL \approx$ 0.5 GeV/fm inside a cold Au nucleus.

Working in the same framework of twist expansion in the pQCD model, the author extends the study of modified fragmentation functions to jets in heavy ion collisions. The dense medium created in high energy heavy ion collisions is not static, instead is rapidly expanding which should affect the total parton energy loss. Assuming one-dimensional longitudinal expansion, the energy loss is calculated as

$$\Delta E(b,r,\phi) \approx \left\langle \frac{dE}{dL} \right\rangle_{1d} \int_{\tau_0}^{\Delta L} d\tau \frac{\tau-\tau_0}{\tau_0\rho_0} \rho_g(\tau, b, \vec{r}+\vec{n}\tau) \quad (2.19)$$

where $\Delta L(b,\vec{r},\phi)$ is the path length in matter for a jet produced at $\vec{r}$ and traveling in direction $\vec{n}$ with azimuthal angle ϕ relative to reaction plane, in a collision with impact parameter b. ρ_0 is the averaged initial gluon density at τ_0 in a central collision and $\left\langle \frac{dE}{dL} \right\rangle_{1d}$ is the average parton energy loss over a distance R_A in a 1-D expanding medium with an initial uniform gluon density ρ_0. The energy dependence is parameterized as

$$\left\langle \frac{dE}{dL} \right\rangle_{1d} = \epsilon_0 (E/\mu - 1.6)^{1.2}/(7.5 + E/\mu) \quad (2.20)$$

according to a study of parton energy loss that includes both bremsstrahlung and thermal absorption of gluons. A fit to the most central Au+Au collisions at $\sqrt{s_{NN}}$ =200 GeV results in ϵ_0=1.07 GeV/fm, μ= 1.5 GeV and $\lambda_0 = 1/\sigma\rho_0$=0.3 fm. The corresponding energy loss in a static medium with parton density ρ_0 over a distance R_A is $dE_0/dL = (R_A/2\tau_0)\langle dE/dL\rangle_{1d} \approx$14 GeV/fm. This is about 30 times higher than the parton energy loss in a cold nucleus. Since the parton energy loss in the thin plasma limit is proportional to the gluon number density, one can conclude that the initial gluon density reached in central Au+Au collisions at 200 GeV should be about 30 times higher than the gluon density in a cold Au nucleus.

Since parton behavior in medium depends both on the local gluon density and the propagation length, the centrality dependence of the single inclusive hadron suppression reflects a combination of these two dependencies. One can extend the study of the density and length dependence by varying

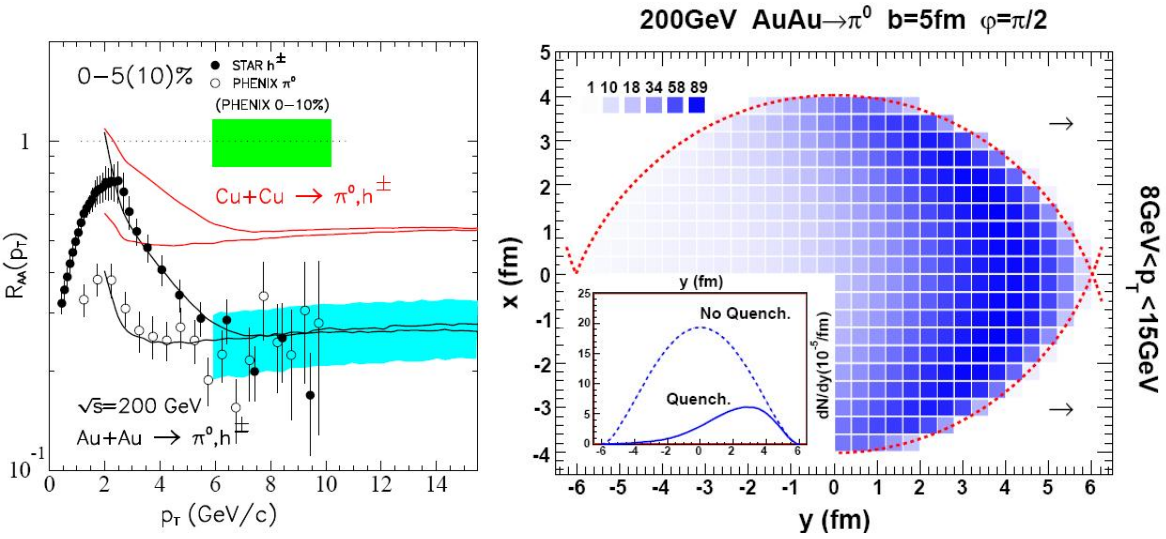

Figure 2.12: Left:Hadron suppression factor $R_{AA}(p_T)$ for the most central (0-10%) Au+Au and Cu+Cu collisions at 200 GeV. Right: Spatial transverse distribution (arbitrary normalization) of the initial parton production points that contribute to the final π^0 at $8 < p_T < 15$ GeV along $\phi = \pi/2$. The insert is the same distribution projected onto the y-axis. Figures taken from [145, 147].

the nuclear size at a fixed energy. Shown in the left panel of Fig.2.12 are the parton model calculations of the suppression factor $R_{AA}(p_T)$ for the most 0-10% central Cu+Cu collisions at $\sqrt{s_{NN}}$=200 GeV together with the calculation and experimental data of central Au+Au collisions. As expected, the high p_T suppression is stronger in Au + Au collisions than in Cu+Cu collisions.

Because of jet quenching, the dominant contribution to the measured single hadron spectra at large p_T comes from those jets that are initially produced in the outer part of the overlap region toward the direction of the detected hadron. This is illustrated in the right panel of Fig.2.12 by the spatial distribution of the production points of those jets that have survived the interaction with the medium and contribute to the measured spectra. Jets produced in the region away from the detected hadron are severely suppressed due to their large energy loss and don't contribute much to the final hadron spectra. However, high-p_T hadron yield via such surface emission should be proportional to the thickness of the outer corona which decreases with the initial gluon density. Therefore, the suppression factor for single hadron spectra should never saturate but continue to decrease with the initial gluon density [147].

2.2.7 High p_T particle production in A+B collisions

In the absence of initial and final state interactions, QCD factorization implies that the inclusive A+B cross-section for hard processes should scale as $Ed\sigma_{AB\to h}/d^3p = A \cdot B \cdot Ed\sigma_{pp\to h}/d^3p$. For a given centrality class f or impact parameter b in a nucleus-nucleus collision, the scaling is proportional to $T_{AB}(b)$, the nuclear thickness function averaged over the centrality class[13]. Since N_{bin} is the number of binary nucleon-nucleon inelastic collisions, with cross section σ_{pp}^{inel}, in the centrality class f: $\langle N_{bin}\rangle_f = \langle T_{AB}\rangle_f \cdot \sigma_{pp}^{inel}$, one can write $EdN_{AB\to h}/d^3p = \langle N_{bin}\rangle_f \cdot EdN_{pp\to h}/d^3p$.

However, for an accurate description of hadron production in A+A collisions, the initial and

[13] $T_{AB}(b)$ is normalized so that integrating over all impact parameters one gets: $\int d^2bT_{AB}(b) = AB$. The nuclear thickness function $\langle T_{AB}\rangle_f$ averaged over the centrality class f is:

$$\langle T_{AB}\rangle_f = \frac{\int_f d^2bT_{AB}(b)}{\int_f d^2b(1-e^{-\sigma_{NN}T_{AB}(b)})} = \frac{\langle N_{coll}\rangle_f}{\sigma_{NN}} \tag{2.21}$$

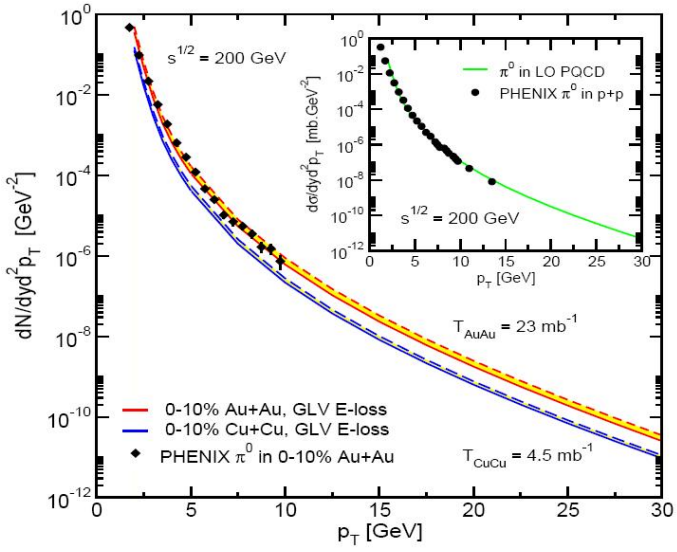

Figure 2.13: The predicted invariant multiplicity distribution of π^0 in central Au+Au collisions at 200 GeV for medium density dN_g/dy = 800-1175 and T_{AuAu} = 23 mb$^-$1 and for Cu+Cu collisions with dN_g/dy = 255-370 and T_{CuCu} = 4.5 mb$^-$1. The insert shows the cross section for π^0 production in p+p collisions to LO pQCD. Figure taken from [135].

final nuclear effects must be incorporate: nuclear modification of the parton distribution functions, nuclear k_T broadening (both arising as a consequence of multiple scattering) and the parton energy loss causing the suppression of high p_T particle production.

The inclusive hadron spectrum in nucleus-nucleus (A+B) collisions can be calculated using the pQCD model,

$$\frac{d\sigma^{AB}}{d\eta d^2p_T} = K\sum_{abcd}\int d^2bd^2rdx_adx_bd^2k_{aT}d^2k_{bT}t_A(r)t_B(|\mathbf{b}-\mathbf{r}|)g_A(k_{aT},r)g_B(k_{bT},|\mathbf{b}-\mathbf{r}|) \\ f_{a/A}(x_a,Q^2,r)f_{b/B}(x_b,Q^2,|\mathbf{b}-\mathbf{r}|)\frac{d\sigma}{d\widehat{t}}(ab\to cd)\frac{D'_{h/c}(z_c,Q^2,\Delta L)}{\pi z_c^2} \tag{2.22}$$

where the fractional momentum is defined by $z_c = p_T/p_{Tc}$, $T_{AB}(b) = \int d^2rt_A(\mathbf{r})\mathbf{t_B}(|\mathbf{b}-\mathbf{r}|)$ is the nuclear thickness function, $D'_{h/c}(z_c,Q^2)$ is the medium modified fragmentation function for produced parton c. The K $\approx$ 1.5 - 4 factor is used to account for higher order pQCD corrections. Since partons from projectile and target beam both suffer multiple scattering before the hard process, their initial transverse momentum distributions are broadened as given by Eq.2.6. For the nuclear PDFs inside the colliding nuclei can be used different parameterizations, EKS98, HIJING (see section 2.2.1). Figure 2.13 shows the calculated invariant π^0 spectrum based on the Eq.2.22 compared with PHENIX data obtained in central Au+Au and Cu+Cu reactions at $\sqrt{s_{NN}}$ = 200 GeV.

2.3 Rapidity dependence of the high p_T suppression

Most studies focus on the suppression of p_T spectra at mid-rapidity in nucleus-nucleus collisions compared with the peripheral ones or the proton-proton case at the same energy. Although one can study the dependence on the medium density by varying the impact parameter/collision centrality for nucleus-nucleus collisions, also different rapidities provide different densities of the medium, through which the high momentum jet travels.

When a high energy jet travels through the quark-gluon plasma produced at the early stage of nucleus-nucleus collisions, the medium density is much larger at mid-rapidity than in the forward or

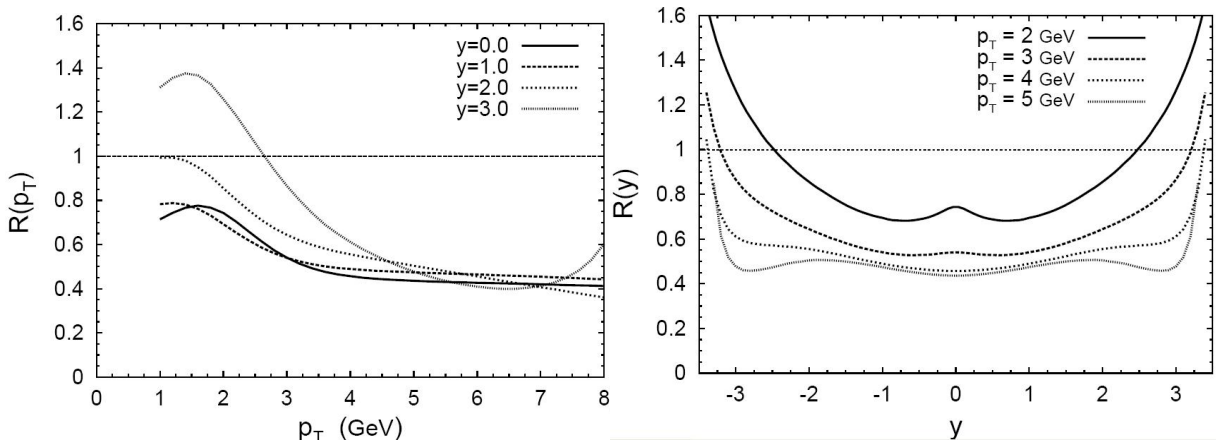

Figure 2.14: Left: Transverse momentum dependence of the R_{AA} in Au+Au collisions at $\sqrt{s_{NN}}$ = 200 GeV with respect to the pp case, for different rapidity values. Right: Rapidity dependence of the R_{AB} for Au+Au collisions at $\sqrt{s_{NN}} = 200$ GeV with respect to the p+p case, for different transverse momentum values. Figures taken from [148].

backward directions (large rapidity). Because jet energy loss is proportional to the density of the local medium, at different rapidities the energy loss of the fixed p_T jet will be different, and the high p_T hadron spectrum from jet fragmentation will also have different behavior. Therefore, by scanning the rapidity of hadrons produced in central nucleus-nucleus collisions, one can observe the variation of energy loss effects and its influence on the high p_T spectrum of charged hadrons. The analysis of high rapidity data offers a unique possibility to extract information about the properties of the dense matter in the longitudinal direction in the very early stage of the heavy ion collisions.

2.3.1 Polleri-Yuan Model

In their model [148], Pollery and Yuan used the GRV94 parameterization [108] for the PDFs, the KKP parameterization [149] for the FFs and the EKS98 parameterization [114] for the nuclear modification of the PDFs. In their calculations, they also take into account the broadening effects to the final jet spectrum prior to fragmentation.

The authors make a simple parameterization. If a jet is produced at midrapidity, it will encounter a dense medium and the energy loss will be large. The authors argue that at larger rapidity, the energy loss effect diminishes due to the lower medium density. Therefore they assume that the parton c energy loss due to gluon radiation induced by the medium is proportional to the parton energy E_c and the rapidity density of the medium dn/dy,

$$\Delta E_c(y, E_c) = q_c E_c \frac{dn}{dy} \tag{2.23}$$

where q_c is the average value of energy loss which implicitly also includes the size of the medium (model parameter).

For the medium density dn/dy, it is further assumed for simplicity that the plasma density at the early stage is proportional to the measured rapidity density of charged hadrons, therefore including both soft and hard produced particles. The model do not take into account the time evolution of the plasma which, due to geometric and dynamical effects, requires a more detailed study of its properties.

Left panel of Fig.2.14 shows the p_T dependence of the nuclear modification factor R_{AA} for Au+Au collisions at $\sqrt{s_{NN}} = 200$ GeV at different rapidities. We see that for different rapidities the ratios have different behaviors. In general, at larger y, the suppression is reduced due to the decrease in the medium density. Especially, at very large rapidity one can really observe the Cronin effect.

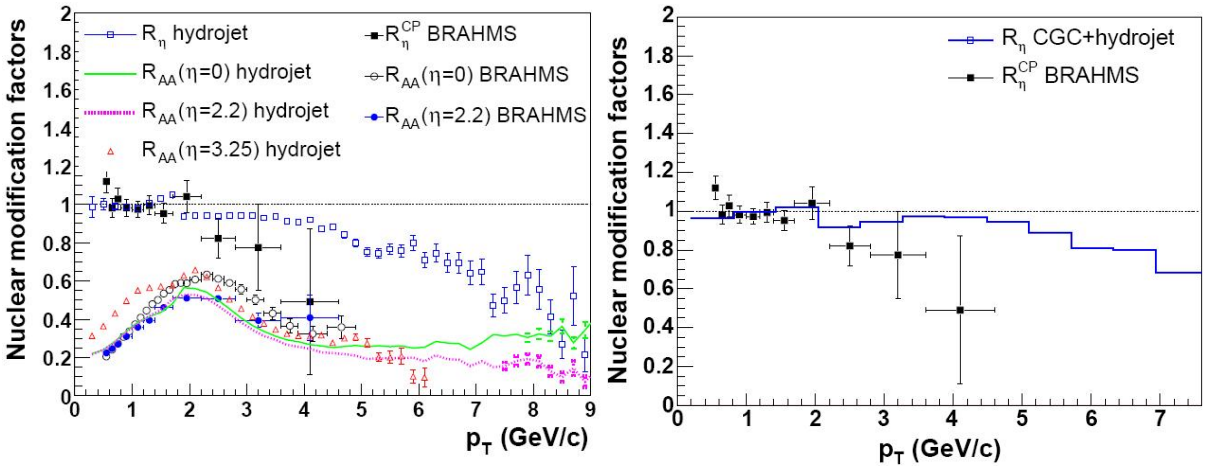

Figure 2.15: Left: Nuclear modification factors compared to the BRAHMS data in Au+Au collisions at $\sqrt{s_{NN}} = 200$ GeV. Right: CGC + hydrojet result is compared with the BRAHMS data on $R_\eta = R_{CP}(\eta = 2.2)/R_{CP}(\eta = 0)$. Figures taken from [152, 129].

The right panel of Fig.2.14 shows the R_{AA} for Au+Au collisions at $\sqrt{s_{NN}} = 200$ GeV as a function of rapidity at different p_T values. At midrapidity, because of the high density of the medium, the largest energy loss produces the strongest suppression. As rapidity increases, the energy loss effect reduces and the R_{AA} increases. The energy loss coefficient used is $q_c = 0.27$ with which the suppression of the charged hadron spectrum in central collisions observed at $\sqrt{s_{NN}} = 130$ GeV was reproduced.

2.3.2 Hirano-Nara Model

The authors developed a unified model (CGC+Hydro+Jet model) [129, 150] in which CGC initial conditions, hydrodynamic evolution and the production and propagation of high p_T partons are combined. The model is mainly composed of two models with CGC as initial conditions. One is a full three dimensional hydrodynamic model which describes the space-time evolution of thermalized partonic/hadronic matter. The other describes the dynamics (production, propagation, and fragmentation) of high p_T partons which interact with thermalized partonic matter through a phenomenological model for parton energy loss.

The authors assume that the origin of thermalized partonic matter is the CGC in high energy heavy ion collisions, and use it as an initial condition in the hydro+jet model. They assume that the system of initially produced gluons reach local thermal equilibrium a very rapid time scale. They further assume that during thermalization, the shape of the rapidity distribution is not changed.

For the high momentum processes, the spectrum of hard partons is generated with PYTHIA [151]. The jets are calculated from the pQCD parton model. The parton distribution functions are taken to be CTEQ5 leading order [107]. The model uses EKS98 nuclear shadowing [114] and take into account the multiple initial state scatterings, assuming a Gaussian distribution function for primordial transverse momentum k_T with the width of $\langle k_T^2 \rangle = 1$ GeV^2/c^2. In order to convert hard partons into hadrons, they use an independent fragmentation model using PYTHIA after hydro-simulations. The independent fragmentation is not applicable for the low p_T transverse momentum range and for p+p reference and hence the Lund string fragmentation model is used.

In their model, high p_T jets suffer interaction with the local parton density which is governed by hydrodynamic evolution with the CGC initial conditions. They only take into account parton energy loss in deconfined matter $T \geq T_c$. Jets lose their energies through gluon emission induced by the dense medium. The Gyulassy-Levai-Vitev (GLV) energy loss formula, based on an opacity expansion approach, is used.

Hydro+jet model [152] calculation (no CGC) for the nuclear modification factors R_{AA} for charged

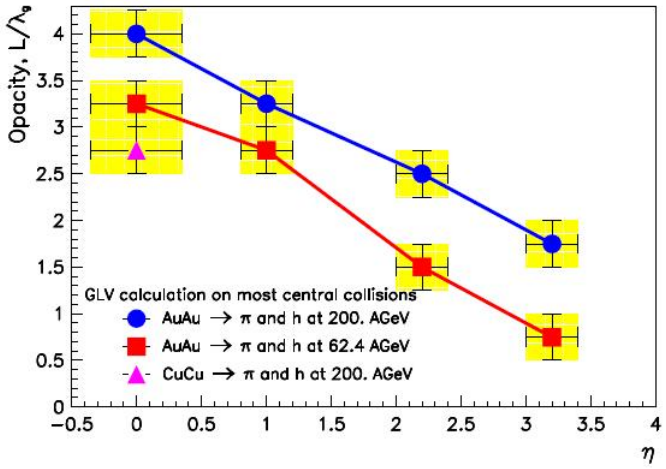

Figure 2.16: The pseudorapidity dependence of the opacity, L/λ, for forward pion production in the most central Au+Au collisions at energies $\sqrt{s_{NN}}$ = 62.4, 200 AGeV, and Cu+Cu collisions at energies $\sqrt{s_{NN}}$ = 200 AGeV. Figure taken from [153].

hadrons at $\eta = 0$, 2.2 and 3.25 in Au+Au collisions at RHIC are shown in left panel of Fig.2.15. The nuclear modification factor R_{AA} in low p_T region ($p_T \leq 2$ GeV/c), where the hydrodynamic component dominates, at $\eta = 0$ and 2.2 are almost identical. The rapidity dependence of the initial parton density was assumed to be flat in $|\eta| < 2$, the dynamical evolution at midrapidity was almost the same as at $\eta = 2$ and $R_\eta < 1$ came from purely the difference of p_T slope between midrapidity and forward rapidity (a steeper slope at $\eta = 2.2$ compared to the slope at $\eta = 0$). When the p_T slope is steep, the nuclear modification factor becomes sensitive to nuclear effects: a small shift of a spectrum is likely to produce a large effect on the ratio of the shifted spectrum to the original one. $R_{AA}(\eta = 3.25)$ becomes smaller than the one for $\eta = 0$ or 2.2 in high p_T region. This is due to the much steeper slope at high p_T.

In the CGC+hydrojet model, the initial parton density from the CGC has no flat region and is slightly larger at midrapidity than at $\eta = 2$. Therefore, the "slope" effect is compensated by the dynamical effect. The CGC+hydrojet [129] result for charged hadrons is compared with the BRAHMS data in right panel of Fig.2.15. $R_\eta \sim 1$ in the soft region $p_T \leq 2$ GeV/c, which is dominated by the hydrodynamic component. The model result starts to deviate from unity at $p_T \sim 5$ GeV/c since the slope in p_T from pQCD hard collisions becomes much steeper for larger rapidity. This result indicates that p_T spectrum in forward rapidity region is already suppressed by the initial state effect and suggests that the small-x evolution will be necessary for the calculation of particle spectra at forward rapidities at RHIC.

2.3.3 Barnafoldi-Levai-Papp-Fai Model

The authors apply a perturbative QCD parton model to describe hadron production at high p_T [153, 154]. The collision geometry and the superposition of the nucleon-nucleon collisions is included by the Glauber-Gribov model. In the model, the MRST parameterization [106] for the PDFs is used, the nuclear shadowing parameterization was taken from HIJING [155], the KKP parameterization [149] is used for fragmentation functions and nuclear multiscattering (Cronin effect) are also included.

The parton energy loss is calculated by the GLV-method (Eq.2.13) and the opacity of the dense matter is extracted in different rapidity regions, i.e. for different parton momentum directions. The effect of jet energy loss on the final hadron spectra is introduced via modifying the momentum fraction of the outgoing parton $z_c^* = z_c/(1 - \Delta E/p_c)$ before the fragmentation and therefore the argument of the fragmentation functions will be modified.

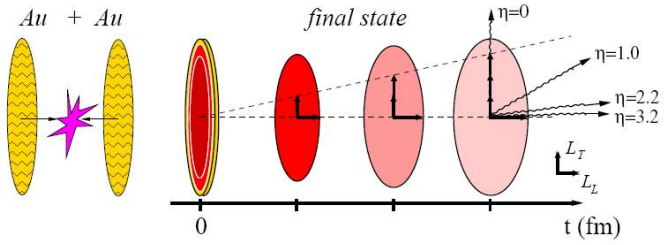

Figure 2.17: Time evolution of the quark or gluon jet traveling through the expanding hot dense matter into the transverse and longitudinal direction. Figure taken from [153].

The authors assume the presence of a possible asymmetry between transverse and longitudinal directions seen by the particles produced in different rapidities. Since the produced hot dense matter is characterized by different dynamical behavior in transverse and longitudinal direction, it is possible to see differences during the analysis of available data at different rapidities. Therefore, the authors analyze the hadron production in forward rapidity region. They assume that the suppression factors at different rapidities are approximately the same in the high p_T region and perform the model calculations in this manner.

The opacity parameter, L/λ, is determined by finding the best fit for energy loss and comparing the theoretical results to the data points on the nuclear modification factor. L is the path length of the parton in the medium and λ is the mean free path. The pseudorapidity dependence of the L/λ opacity for the most central Au+Au collisions at energies $\sqrt{s_{NN}}$ = 62.4, 200 AGeV, and Cu+Cu collisions at energies $\sqrt{s_{NN}}$ = 200 AGeV is presented in the Fig. 2.16. For the Au+Au collisions at the top RHIC energy the opacity parameter is decreasing with increasing rapidity. Comparing the extracted opacity values in the mid-rapidity and in the most forward rapidity, one can see a factor of 3 difference at both energies, 62.4 AGeV and 200 AGeV. The above results indicates that longitudinally traveling partons see less colored matter than those traveling in the transverse direction.

In the Fig.2.17 is presented a schematic picture for the time evolution of the formed hot dense matter and the outcoming jets. A jet, created in the central region of the collision and producing mostly mid-rapidity hadrons, is traveling transversally through an $L_T \sim 4$ fm length. This jet looses a large portion of its energy and indicates an opacity $L_T/\lambda = 4$. Hadrons in the forward rapidities are produced from forward jets. These jets are moving mostly longitudinally and after passing a (contracted) thin region of the compressed matter (characterized by an effective length of $L_L \sim 1.5$ fm) they reach very quickly the longitudinally expanding surface. Both jet and expansion surface are moving with speed of light, thus the comoving jet does not loose more energy and an opacity L_L/λ = 1.5 can be extracted at the highest rapidities.

The authors conclude that in their investigation on hadron production in forward rapidities, the suppression pattern indicated the formation of a longitudinally contracted dense deconfined zone in the most central heavy ion collisions. They consider that at large forward rapidities the interplay between a stronger shadowing and weaker quenching effects is able to maintain a rapidity independent nuclear modification factor.

2.4 Recombination models

In the past few years, several features of the high-p_T data obtained by the experiments from RHIC are puzzling, and may be taken as anomalies according to the "standard" approach regarding the treatment of hadron production at high p_T, namely: a hard scattering of partons, followed by a fragmentation process that leads to the detected hadron. The ratio of produced hadrons should depend only on the ratio of the fragmentation functions (FF), $D(z)$. Given a parton, whether a

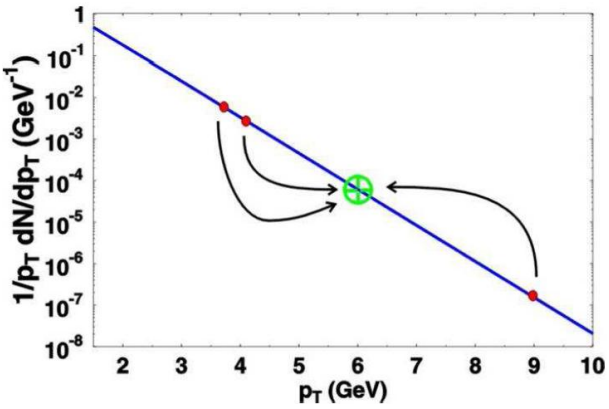

Figure 2.18: Recombination and fragmentation for a meson at $p_T \approx 6$ GeV/c, starting from a parton spectrum with steep slope (solid line). Fragmentation requires a single parton with transverse momentum larger than p_T^h to start with, while recombination is possible with two partons that have roughly $p_T^h/2$ each. The competition between both processes is decided by slope and normalization of the parton spectrum. Figure taken from [56].

quark or a gluon, its FF for the production of a proton $D_p(z)$ is much smaller than that for a pion $D_\pi(z)$. The observed data reveal several anomalies according to that picture. The ratio of proton to pion, $R_{p/\pi}$, in Au+Au collisions at $\sqrt{s_{NN}}$=200 GeV is approximately 1 between 2 GeV/c and 4 GeV/c [37]. The central-to-peripheral factor R_{CP}, in d+Au collisions at $\sqrt{s_{NN}}$=200 GeV is greater for p than for π at $p_T > 2.5$ GeV/c for $|y| < 1.0$ [156]. The azimuthal anisotropy parameter v_2 is larger for baryons than for mesons for $p_T > 2$ GeV/c in Au+Au collisions at at $\sqrt{s_{NN}}$=200 GeV (the data from RHIC show also that the elliptic flow and nuclear modification factor for the ϕ mesons, though are as heavy as protons, are very similar to those for kaons) [157, 158]. Thus, the meson vs baryon signatures at intermediate p_T are very robust and can neither be explained by an extrapolation of hydrodynamics nor by perturbative jet production and fragmentation.

All those anomalies can be resolved when the process of hard parton fragmentation is replaced by the recombination of partons. When a multi-parton state is to hadronize, it is far more efficient for a quark q and an antiquark $\bar{q}$ to recombine than for a higher momentum quark q to fragment, assuming that the parton distribution is falling rapidly in momentum. That is simply because recombination involves the addition of a q and $\bar{q}$ of lower momenta as illustrated in Figure 2.18, where the densities are higher, whereas fragmentation involves first the creation of a parton at higher momentum (at a cost in yield), and then the production of a hadron at some momentum fraction at the cost of another factor of suppression[14]. Baryon production is enhanced because of the extra quark compared with the mesons. The comparison is meaningful only when there are many soft partons moving collinearly with a hard parton, which is the case for heavy-ion collisions, but not for leptonic and hadronic collisions.

Hadron production by recombination is expected to dominate over fragmentation as long as the parton p_T spectra are exponential. With an exponential p_T spectrum lower p_T quarks are much more abundant than high p_T quarks and the probability for lower p_T quarks to recombine is much higher than the probability for a higher p_T quark from a hard scattering to fragment into the final state hadron.

[14]The hadrons originating from fragmentation process of a parton with transverse momentum p_T, is believed to have less transverse momentum $p_T^h = z \cdot p_T$. The average value z is about 0.5 for pions in p+p collisions. In other words the production of a 5 GeV/c pion has to start with a 10 GeV/c parton in average, which are rare to find due to the steeply falling parton spectrum. Jet quenching even enhances the lack of high p_T partons. On the other hand, the 5 GeV/c pion could be produced by the recombination of a quark and an antiquark with about 2.5 GeV/c each in average. 2.5 GeV/c and 10 GeV/c are separated by orders of magnitude in the parton spectrum. In central heavy ion collisions at RHIC is created a densely populated phase space where we expect to exist a thermalized quark gluon plasma.

Parton recombination in heavy-ion collisions was investigated first by R. Hwa and was later studied in detail in terms of coalescence or recombination models [54, 55, 56]. These models generally assume two components of high p_T hadron production in heavy-ion collisions. The recombination of partons from the bulk medium dominates the production of low and intermediate p_T hadrons, while high p_T hadrons result mainly from the fragmentation of parton jets after propagating through the bulk medium and losing energy.

R. Hwa and C.B. Yang in their recombination model[159, 160] assume that in high-energy nuclear collisions, the hadronization processes take place always in the environment of soft partons. They introduce the notion of semi-hard shower partons which are initiated by a hard parton; these shower partons can either recombine among themselves or recombine with soft partons in the environment. In the former case the fragmentation function is reproduced and the final state hadrons originating from the shower-shower recombination are regarded as the products of the fragmentation process. It is the latter case that authors consider that should be an important hadronization process in the intermediate p_T region and stands between the recombination of soft thermal partons at lower p_T and the fragmentation of hard partons at higher p_T.

The invariant inclusive distribution for a produced meson with momentum p is written in the Hwa recombination model as

$$p\frac{dN_M}{dp} = \int \frac{dp_1}{p_1}\frac{dp_2}{p_2} F_{q\bar{q}'}(p_1, p_2) R_M(p_1, p_2, p) \tag{2.24}$$

where $F_{q\bar{q}'}(p_1, p_2)$ is the joint distribution of a quark q and an antiquark $\bar{q}$ with momenta p_1 and p_2 and $R_M(p_1, p_2, p)$ is the recombination function, which specifies the probability that those two quarks recombine to form a meson with momentum p: $R_\pi(p_1, p_2, p) = (p_1 p_2/p)\delta(p_1 + p_2 - p)$. The pion production can be written as

$$\frac{dN_\pi}{dp} = \frac{1}{p^3}\int_0^p dp_1 F_{q\bar{q}'}(p_1, p - p_1) \tag{2.25}$$

The produced mesons are either, "thermal-thermal" coming from the recombination of two thermal quark-antiquark (those coming from the thermal source), "shower-thermal" in which one quark is from the thermal source and the other is from a hard scattering and "shower-shower" originating from the recombination of the quarks and anti-quarks associated with a hard scattering. Thus, the $q\bar{q}^{'}$ distribution has four components

$$F_{q\bar{q}'} = TT + TS + SS + (SS)_2 \tag{2.26}$$

where T denotes thermal partons and S shower partons. The SS represents the quarks and antiquarks arising from one hard parton (hence within one jet) and $(SS)_2$ signifies two shower partons that are from two separate but nearby hard partons, and are therefore associated with two overlapping jets. $(SS)_2$ is not expected to be important unless the density of hard partons is extremely high (at LHC). At low p_T the observed pion distribution is exponential, which suggest the form

$$T(p_1) = p_1\frac{dN_q^T}{dp_1} = Cp_1 \cdot exp(-p_1/T) \tag{2.27}$$

so that the TT component yields

$$\frac{dN_\pi^{TT}}{pdp} = \frac{C^2}{6} \cdot exp(-p/T) \tag{2.28}$$

where C and T are model parameters obtained from fits to the low-p_T data. The distribution S is a convolution of the hard parton distribution $f_i(k)$ and the shower parton distribution (SPD) $S_i^j(z)$ from hard parton i to semi-hard parton j

$$S_j(p_1) = \xi \sum_i \int_{k_{min}} dk k f_i(k) S_i^j(p_1/k) \tag{2.29}$$

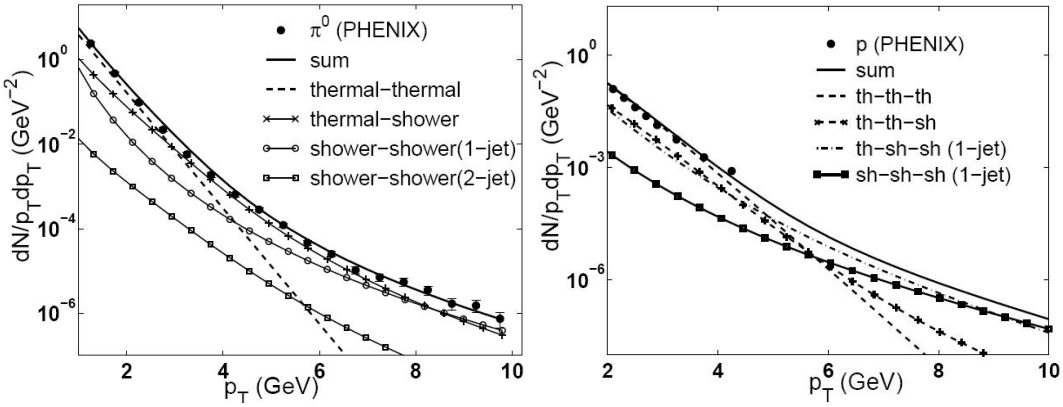

Figure 2.19: Transverse momentum distributions of π^0 and p in Au+Au collisions from PHENIX. Left: The solid line is the sum of four contributions to the recombination of partons. Thermal-thermal represents the soft contribution. Thermal-shower represents the contribution from the interplay between soft and hard components. Shower-shower represents the hard contribution. Right: The solid line is the sum of four contributions to the recombination of partons: *TTT*, *TTS*, *TSS* (one thermal parton with two shower partons in one jet) and *SSS* (three shower partons from one jet). Figures taken from[159].

where $f_i(k)$ is the probability of producing a hard parton of specie i that initiates the shower of partons at transverse momentum k, k_{min} is set to 3 GeV/c, below which the pQCD derivation of $f_i(k)$ is invalid. ξ is the average fraction of hard partons that can get out from the dense medium to produce showers and parameterizes the energy loss effect. Thus, S and SS are proportional to ξ, but not T. For each i, $f_i(k)$ depends on the parton distribution functions, nuclear shadowing and hard scattering cross sections. The SPDs are obtained from the FFs and can be found in Ref.[161]. The contribution to the pion spectrum from thermal-shower recombination is

$$\frac{dN_\pi^{TS}}{pdp} = \frac{1}{p^3}\int_0^p dp_1\, T(p_1)S(p-p_1) \tag{2.30}$$

and from shower-shower recombination is

$$\frac{dN_\pi^{SS}}{pdp} = \frac{\xi}{p}\sum_i \int dk k f_i(k)\frac{p}{k}D_i^\pi(\frac{p}{k}) \tag{2.31}$$

where $D_i^\pi(p/k)$ is the fragmentation function of parton i into a pion. When all three terms in $F_{q\bar{q}'}$ and the R_π are substituted into Eq.2.24, we obtain the basic formula for the inclusive distribution of pion

$$\frac{dN_\pi}{pdp} = \frac{C^2}{6}\cdot e^{-p/T} + \frac{\xi}{p}\sum_{ij}\int dk k f_i(k)\left[\frac{1}{k}D_i^\pi(\frac{p}{k}) + \frac{C}{p^2}\int dp_1 S_i^j(\frac{p_1}{k})(p-p_1)e^{-(p-p_1)/T}\right] \tag{2.32}$$

where the hard parton i is summed over all relevant species, while j is summed over the two possible constituent quark species of the pion.

The left panel of Fig.2.19 shows the π^0 spectrum for central Au+Au collisions calculated in the recombination model compared with the data from PHENIX. At low p_T (p_T <3 GeV/c) thermal-thermal recombination dominates. The thermal-shower component dominates over other components in the region $3 < p_T < 8$ GeV/c. The shower-shower (1 jet) component (SS) is the usual fragmentation and is not important until $p_T > 8$ GeV/c. The shower-shower (2 jet) component (SS_2) has no important contribution to particle production. The model calculation agrees well with the data.

It is important to emphasize that because of the dominance of the *TS* recombination, the jet structure in AA collisions is not the same as that in pp collisions, since there are no thermal soft partons and the *SS* recombination gives rise to the usual fragmentation.

The baryon production in the recombination model occurs the same as for mesons, from shower and thermal quarks or antiquarks recombinations.

$$p\frac{dN_B}{dp} = \int \frac{dp_1}{p_1}\frac{dp_2}{p_2}\frac{dp_3}{p_3}F(p_1,p_2,p_3)R_B(p_1,p_2,p_3,p) \tag{2.33}$$

where $F(p_1,p_2,p_3)$ is the joint distribution of three relevant quarks to form the baryon B and $R_B(p_1,p_2,p_3,p)$ is the recombination function for a baryon with momentum p. There are more terms in the various possible contributions from the thermal and shower partons than in meson production. Schematically, it takes the form

$$F_{qq'q''} = TTT + TTS + T(SS)_1 + (SSS)_1 \tag{2.34}$$

Right panel of Fig.2.19 shows the recombination model calculations for the proton spectra in central Au+Au collisions compared with PHENIX data. The various contributions to the proton yield are shown with different lines. Their sum is shown as solid line, and agrees well with the data. The recombination of three thermal quarks is expected to dominate until p_T <5 GeV/c. At higher p_T the recombination of one thermal quark with two shower quarks from one jet, *TSS* component, dominates until $p_T > 9$ GeV/c where the *SSS* component takes over.

2.4.1 Rapidity dependence of the recombination

The authors assume that at forward rapidity in Au+Au collisions at $\sqrt{s_{NN}}$=62.4 GeV there are only thermal partons that recombine to form hadrons[162]. For larger values of y the spectra are increasingly suppressed at high k_T, because of the phase space boundary that requires $k_T < k_0(y)$. The kinematic limit is given by $k_0(y) = \sqrt{s}/(2cosh(y))$ and takes the values 12.23 GeV/c and 4.54 GeV/c for y=2.2 and 3.2 respectively. Therefore the authors consider that no shower partons are involved in the recombination process because hard partons are suppressed in the forward region[15]. Thus for pion production one has *TT* recombination, while for the proton one has *TTT* recombination, where *T* represents the thermal parton distribution. The invariant distributions of produced pions and protons due to thermal-parton recombination are

$$\frac{dN_\pi^{TT}}{p_T dp_T} \propto C_q C_{\bar{q}} \cdot exp(-p_T/T) \tag{2.35}$$

$$\frac{dN_p^{TTT}}{p_T dp_T} \propto C_q^3 p_T \cdot exp(-p_T/T) \tag{2.36}$$

The exponential factors in the above equations give the characteristic behavior of hadrons produced by recombination of thermal partons. Since the particles are produced by the recombination of thermal partons only, there can be no jet structure associated with any hadron at any p_T, yet there are high p_T particles.

The authors have shown that the BRAHMS data from Au+Au collisions at $\sqrt{s_{NN}}$=62.4 GeV at forward pseudorapidity η=3.2 can be well reproduced by the recombination model calculations for all p_T with the above assumptions. For p_T up to 2.2 GeV/c, the charged particle spectrum shows

[15]In the forward region the authors refer specifically to hadrons produced at $x > 0.5$, with the fragmentation region (FR) being $0.5 < x < 1$ and trans-fragmentation region (TFR) being $x > 1$. Any hadron produced in the TFR cannot be due to the fragmentation of any parton because of momentum conservation, since no parton can have momentum fraction > 1. In the FR hadrons with any p_T that are kinematically allowed can, in principle, arise from the fragmentation of hard partons; however, the momenta of those hard partons must be even higher than the detected hadrons in the FR, and the probability of hard scattering into the region near the kinematical boundary is severely suppressed.

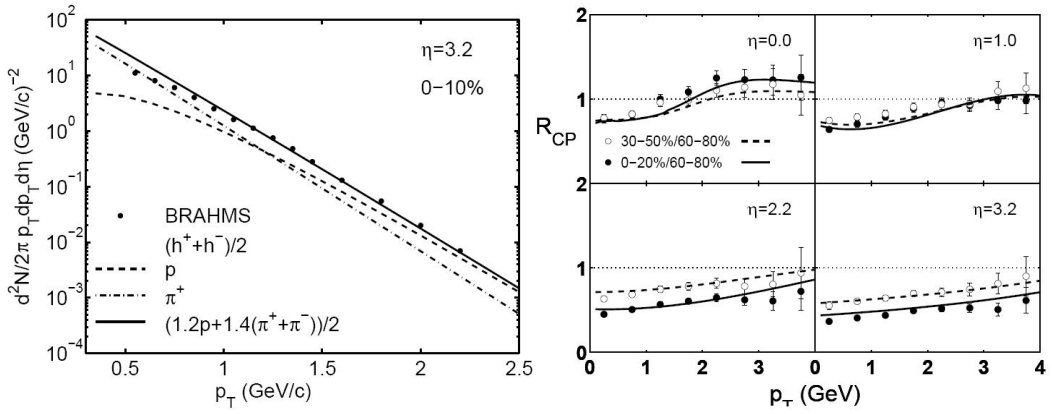

Figure 2.20: Left: The p_T distribution for charged hadrons produced in Au+Au collisions at $\sqrt{s_{NN}}$=62.4 GeV in forward region. Data from BRAHMS[163]; lines are model calculation. Right: R_{CP} in d+Au collisions at $\sqrt{s_{NN}}$=200 GeV for four pseudorapidities. Data from BRAHMS[126]; lines are the recombination model calculations. Figures taken from[162].

exponential behavior reflecting the thermal origin of the partons. The charged particles produced are predominantly protons[16]. The authors assume $[1.2p + 1.4(\pi^+ + \pi^-)]/2$ (solid line) to fit the charged hadron BRAHMS data $(h^+ + h^-)/2$, based on p and π distribution determined by thermal recombination only.

The RHIC data from d+Au collisions at $\sqrt{s_{NN}}$=200 GeV are in agreement with the expectation from parton recombination at all η and p_T [160]. Although there are no thermal partons in d+Au collisions as in Au+Au collisions, there are soft partons with low transverse momentum k_T that play the same role. Since the density of soft partons depends on the number of participants even in d+Au collisions, the hadron spectra at moderate p_T depend on centrality, when those soft partons recombine with the shower partons. The authors consider that at midrapidity the *TS* contribution to the spectra is what accounts for the Cronin enhancement at intermediate p_T in more central collisions and is a final-state effect, in contrast to the usual explanation in terms of initial-state parton multiple scattering.

At forward rapidity, in the recombination model the R_{CP} suppression at η >1 is mainly due to the reduction of the density of soft partons that recombine either among themselves or with the semi-hard shower partons. Also, the hard parton distributions are suppressed at high k_T (for η=3.2 the kinematical limit is k_T=8.13 GeV/c). At η=3.2 there are so few hard partons that most hadrons are the result of soft-soft recombination. The authors found that the *TS* and *SS* components are much smaller than *TT* component, so that the soft component has the dominant contribution to the overall distribution for p_T up to 3 GeV/c.

The authors conclude that the hard partons are suppressed at high η and one should not neglect the soft background, which is more important than fragmentation at intermediate-high p_T.

[16]For a proton to be produced at momentum fraction x ∼1, it is rather easy to find three nucleons in A each contributing a quark at ∼ 1/3 to form the proton. For a pion with x ∼1, it is hard to find any antiquark at, for example, ∼ 1/3 to help a quark at ∼ 2/3 to make up the pion due to the scarcity of antiquarks in the forward regions.

Chapter 3

The BRAHMS Experiment

In this chapter we will present an overview of the Relativistic Heavy Ion Collider (RHIC) and the BRAHMS detector alongwith the subsystems that were used for measuring the particle production in Au+Au collisions at $\sqrt{s_{NN}}$=200 GeV in run04.

3.1 The Relativistic Heavy Ion Collider

The Relativistic Heavy Ion Collider (RHIC) is located at Brookhaven National Laboratory (BNL) and is designed to accelerate and collide a variety of nuclei and ions from protons to Au ions in a wide range of beam energies. The top energy for heavy ion beams (e.g., for Au ions) is 100 GeV per nucleon and that for protons is 250GeV.

The schematic diagram of the RHIC collider facility is shown in Fig.3.1. Procedure of the RHIC acceleration for Au ion beams is as follow. The negative gold ions (-1 charge) generated by pulsed sputter ion source are accelerated in the Tandem Van de Graaff facility. The ions are partially stripped off their electrons with a foil (13 electrons removed) at the Tandems high voltage terminal and then accelerated. For the gold beams, the ions exit the Tandem at the energy of 1 MeV per nucleon and with Q = +12 charge state. Exiting from the Van de Graaff, the ions are further stripped to charge state +32. The Au beam of 1 MeV/u energy is transferred to the Booster Synchrotron where it is accelerated to 95 MeV/u. In the Booster-to-AGS (BtA) transfer line, the ions are stripped once again to charge state +77 (only the two most tightly bound K-shell electrons remaining) and then enter the AGS. The AGS accelerates the Au beams to the RHIC injection energy of 10.8 GeV per nucleon. Finally, the ions are transferred to the RHIC rings via the AGS-to-RHIC (AtR) transfer line. A final stripping from +77 to +79 takes place at the exit from the AGS. A total of 60 bunches[1], each bunch containing 1×10^9 ions, are injected into each collider ring.

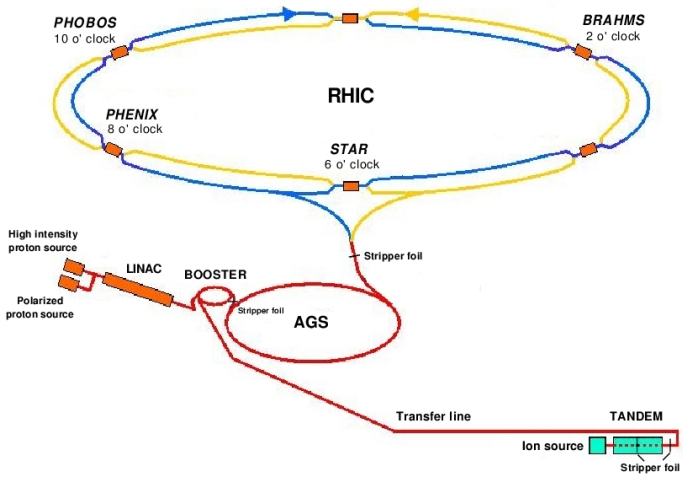

Figure 3.1: The Relativistic Heavy Ion Collider (RHIC) accelerator complex at Brookhaven National Laboratory (BNL).

The two concentric accelerator/storage rings with a 3.8 km circumference on a horizontal plane are one for clockwise (the "Blue Ring") and the other for counter-clockwise (the "Yellow Ring") beams. The RHIC facility consists of two concentric rings of super-conducting magnets that focus

[1]The main reason for storing the ions in discrete bunches is to allow an optimized acceleration in the RF cavities.

and guide the beams and a radio frequency (RF) system that captures, accelerates and stores the beams. The total number of superconducting magnets is 1740 used to bend and focus the ion beams. The magnets are cooled by circulating liquid helium to a temperature of less than 4.6 K. Extremely good vacuum inside the beam pipes is necessary to minimize beam losses and radiation background (10^{-11} - 10^{-10} mbar). More details about RHIC can be found in [164].

RHIC provides particle collisions at 6 intersection regions located around the collider rings, which are conveniently identified by their clock positions as 2-, 4-, 6-, 8-, 10-, and 12-o'clock. Four of them are occupied by the experiments (BRAHMS, PHENIX, PHOBOS and STAR). Collisions are made by steering each of the counter rotating beams into a common beam pipe, by using a "kicker" magnet (DX magnet). The beams are diverted back into their own respective rings by another kicker magnet, at the opposite end of the beam pipe.

The beam luminosity L, which states the number of interactions per unit time per unit cross-section, is calculated as

$$L = \frac{f_r \times n_{bunch} \times N_{blue} \times N_{yellow}}{4\pi\sigma_x\sigma_y} \tag{3.1}$$

$A = 4\pi\sigma_x\sigma_y$ is the beam cross section at the collision point for a gaussian distribution of the beam particles around the beam center (with horizontal and vertical standard deviations σ_x and σ_y, respectively). To achieve a high luminosity, the beam must be focused at the interaction point into the smallest possible cross-sectional area possible. f_r=80kHz is the revolution frequency, $n_{bunch} \sim 60$ is the number of bunches in one beam in the storage ring and $N_{blue(yellow)}$ is the number of ions in each beam ($\sim 1\times10^9$ for Au beam and $\sim 1\times10^{11}$ for proton beam). The stored beam lifetime for gold ions is approximately 10 hours and the average luminosity is $L \approx 2 \times 10^{26}$ cm^{-2}s^{-1} for $\sqrt{s_{NN}}$=200GeV Au+Au collisions. The expected collision rate[2] at RHIC is estimated from $R = L \cdot \sigma$, where σ is the total nuclear interaction cross section. Since $\sigma \sim$7.2 barn for Au+Au collisions, the expected collision rate is $\sim$ 1.4kHz.

The Au+Au data, which are the subject of this analysis, were taken in RHIC Run IV, between December 2003 and April 2004, with the BRAHMS detector, which will be presented next.

3.2 The BRAHMS Experiment

The BRAHMS (Broad RAnge Hadron Magnetic Spectrometers) [165] is one of the four heavy ion experiments running at the RHIC. This experiment covers the widest possible range in polar angle relative to the beam direction with precise momentum determination and good particle identification (PID). In this way, the BRAHMS measurements are complementary to the other three RHIC experiments that analyze the collisions in the mid-rapidity region, providing unique results regarding the forward particle production from colliding systems as varied as p+p, d+Au, Cu+Cu and Au+Au.

BRAHMS experiment contains a set of global detectors for event characterization and two separate spectrometers, one spectrometer called Forward Spectrometer (FS), which measures high momentum charged particles at angles with respect to the colliding beams that range from 2.3° to 30°, and the other called Midrapidity Spectrometer (MRS), that covers angles from 30° to 90°. Fig.3.2 shows a schematic view of the setup.

The global detectors (the Multiplicity Array - MA, the Beam-Beam Counters - BBC, and the Zero-Degree Calorimeters - ZDC) enable event characterization by the observation of overall features of each detected collision, such as charged particle multiplicity, the collision centrality and the location of the interaction vertex. Some of the detectors also provide signals for the first level triggers.

[2] the number of reactions which can be observed in a given reaction time

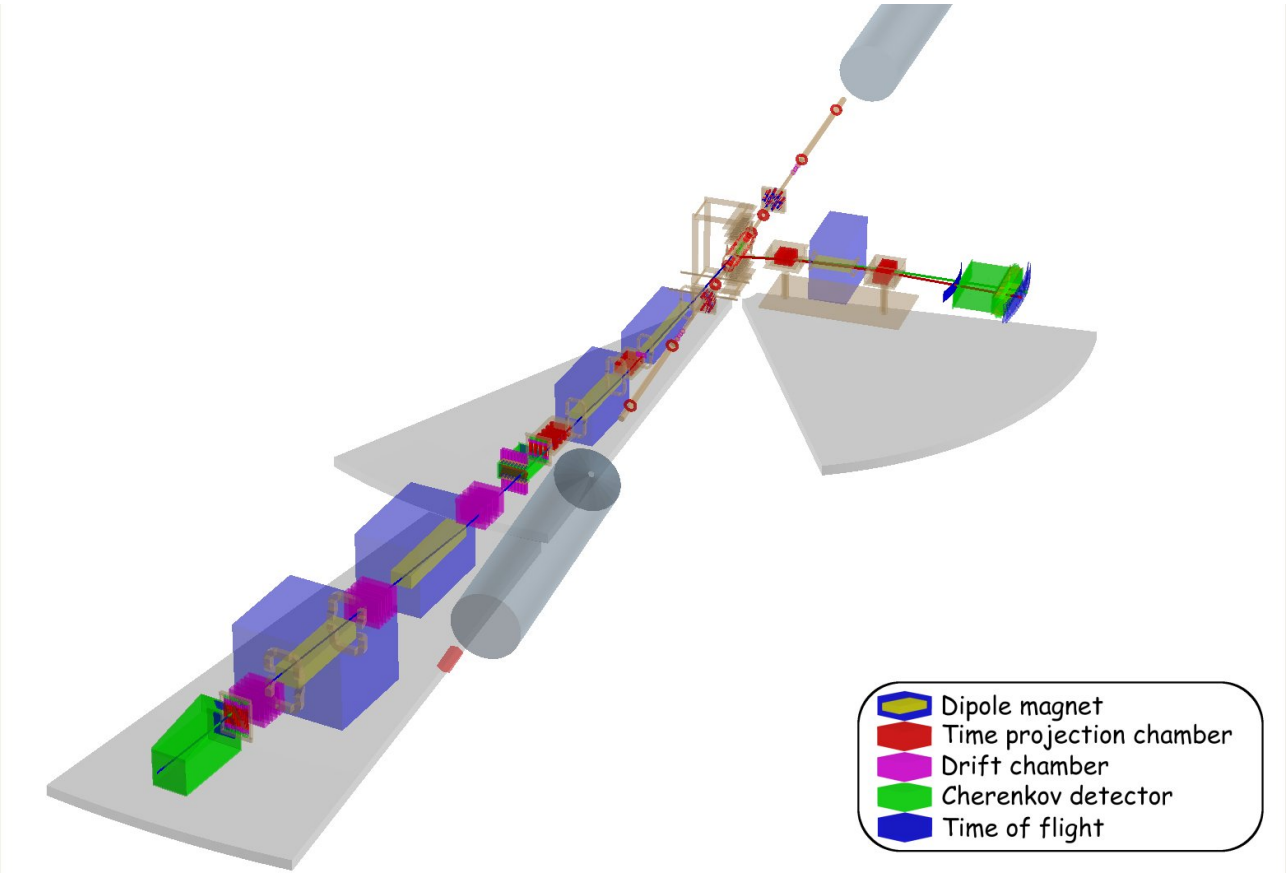

Figure 3.2: The BRAHMS experiment.

3.2.1 Midrapidity Spectrometer

MidRapidity Spectrometer consists a dipole magnet D5 placed between two time projection chambers (TPM1 and TPM2), two time-of-flight wall detectors (TOFW and TFW2) and a Cherenkov detector (C4). Matching tracks in TPM1 and TPM2 through D5 magnet allows the particle momenta to be determinated. Particle identification is made based on time-of-flight measurements. The TOFW is located at a distance of 4.3 m from the nominal IP and provides π/K separation to the momenta of 2 GeV/c and K/p separation to the momenta of 3 GeV/c. TFW2 extend the particle identification to 2.5 for π/K separation and 4 GeV/c for K/p separation. C4 provides additional information for PID. The TPM1 can measures the vertex position by the projection of the tracks inside the chamber to the vertical plane containing the beam pipe. For the present analysis, the MRS spectrometer was positioned at 90°, 45° and 40° degrees relative to the beam axis, and measured produced particles in the rapidity ranges of [-0.2, 0.2] and [0.7, 1.1].

3.2.2 Forward Spectrometer

The FS contains four dipole magnets (D1-D4), five tracking detectors - the first two are time projection chambers (T1 and T2) and the last three are drift chambers (T3, T4 and T5), two TOF hodoscopes (H1 and H2) and two Cherenkov detectors (C1 and ring imaging Cherenkov detector - RICH).

The spectrometer can be operated in two configurations: one for intermediate momenta and one for the highest momenta. The front part of the spectrometer, Front Forward Spectrometer (FFS), which constitutes the intermediate momentum configuration, is mounted on a platform that can

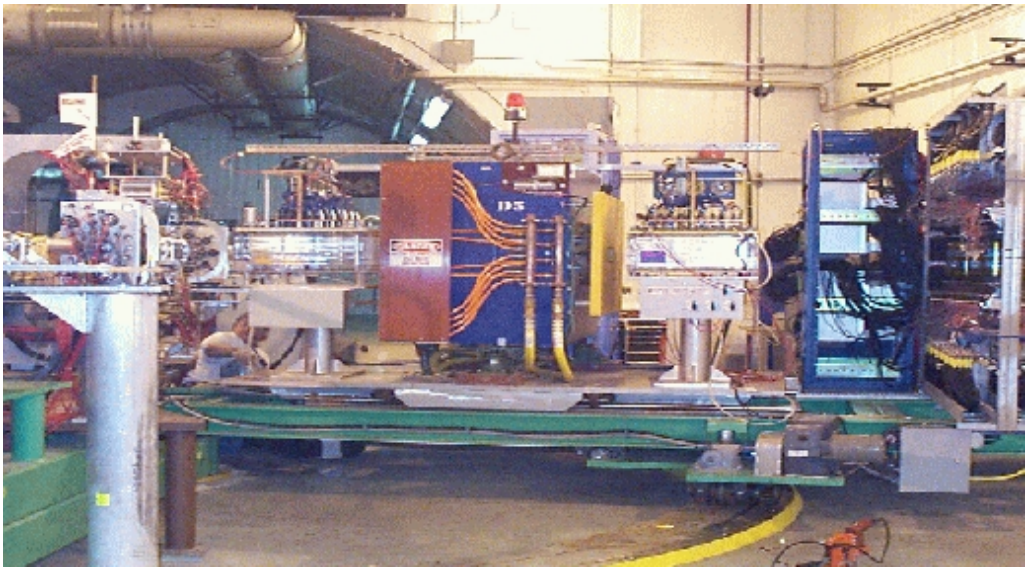

Figure 3.3: Mid-Rapidity Spectrometer (MRS).

rotate from 2.3° to 30°. In the FFS, the particles are tracked by T1 and T2 and the momenta are determined using the field setting of D2.

The back part of the FS spectrometer, BFS, is located on a rotating platform that covers the range 2.3° to 15°. In this high momentum configuration, the particles are deflected by the dipoles D1 and D2 into the back end of the spectrometer where the tracking is performed by T2 and the DCs, and the momenta are determined by combining the tracking and the fields of dipole magnets D3 and D4.

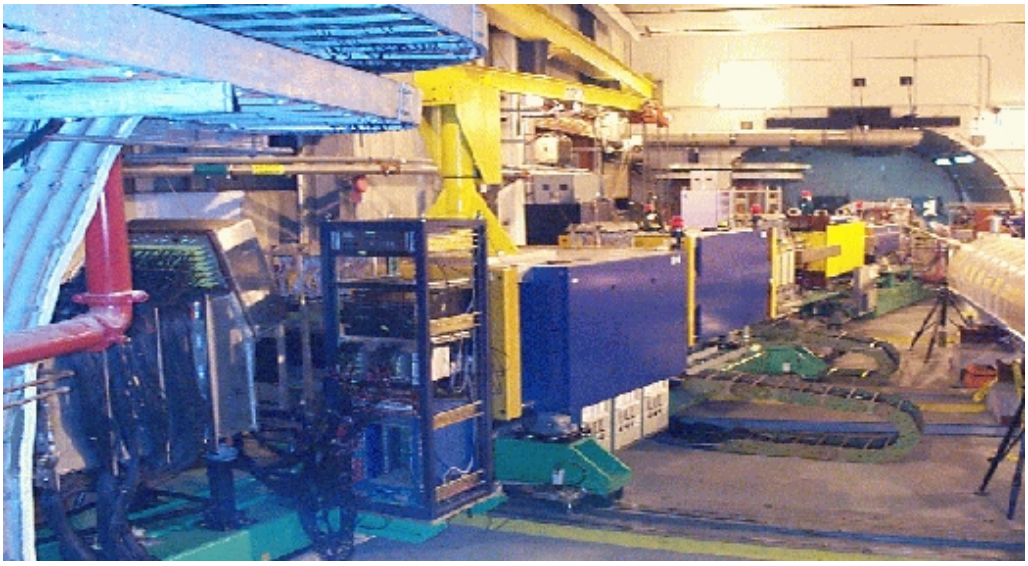

Figure 3.4: Forward Spectrometer (FS).

The TOF hodoscopes, H1 and H2, consist of 40 and 32 plastic scintillator slats, respectively and are positioned at 8.6m and 19m, respectively from the nominal vertex. They provide π/K and K/p separation up to momenta of 3.3 and 5.7 GeV/c, respectively, for H1 and to 5.8 and 8.5 GeV/c, respectively, for H2. The threshold Cherenkov detector, C1 extends the π/K/p identification behind

H1 to 9 GeV/c, while the RICH detector allows π/K/p separation in the high momentum configuration up to ∼25 GeV/c.

The data presented in thesis were taken with the FS spectrometer placed at six different angles, 10°, 8°, 6°, 4°, 3° and 2.3°, corresponding to the rapidity range of [2.2, 4.0].

3.3 Global Detectors

BRAHMS global detectors are the multiplicity array detector (MA), the Beam-Beam Counters (BBCs) and the Zero Degree Calorimeters (ZDCs). For d+Au and p+p runs, Inelastic Counters (INEL) were used as minimum-bias trigger and to provide the vertex position.

3.3.1 Multiplicity Array

The BRAHMS multiplicity array detector (MA) consists of an inner array of silicon strip detectors, and an outer array of plastic scintilator tiles located concentric with the beam line (see figure4.5). The inner barrel is made of 25 silicon wafers, located 5.3 cm from the beam (SiMA). The outer barrel is made of 38 scintillator tiles at 13.7 cm from the beam (TMA). Both hexagonal barrels cover the pseudo-rapidity range -2.2< η <2.2.

The MA detector measures the energy loss of produced particles that traverse the detector elements. The particle multiplicity is determined by dividing the total measured energy by the predicted average energy loss for a single particle as obtained from GEANT simulations. The final determination of charged particle multiplicity is made as the average between the SiMA and TMA measurements. The collision centrality is deduced from the measured multiplicity using the model calculations and simulations of the array response. The MA detector is described in detail in [166].

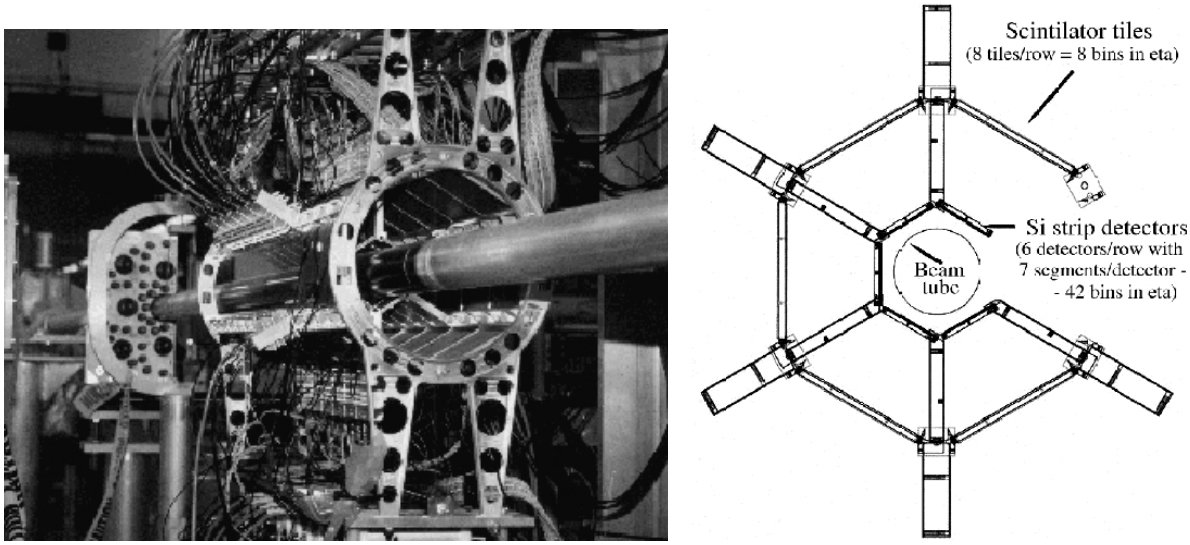

Figure 3.5: Multiplicity Detector

3.3.2 Beam-Beam Counter Arrays

The Beam-Beam Counter Arrays consists a set of Cherenkov radiators coupled with photomultiplier tubes (PTMs). The BBCs are located on either side of the interaction vertex at 220 cm along the beam axis. The BBCs measure the charged particle multiplicity at large pseudo-rapidity (3.0< $|\eta|$ <4.2), complementary to the SiMA and TMA measurements. In addition, they provide the vertex position and the start time for the time-of-flight measurements.

Because are placed in a high particle density region, which can compromise the ability to provide a good timing, two kinds of detector elements are used: small tubes and big tubes. The small tubes have a reduced geometrical solid angle so that the probability for multiple hits is small even for central collisions. The big tubes have a much larger solid angle so that the probability of receiving at least one hit is large even for peripheral events. The left array (BBL) consists of 44 radiators made up of 36 small tubes and 8 big tubes, while the right array (BBR) has 35 radiators, with 30 small tubes and 5 big tubes (see figure3.6). The BBR has reduced azimuthal coverage because the D1 magnet moves to within a few cm of the beam pipe when placed at most forward angle. This reduced coverage is partially compensate by higher spatial density of modules in the array. More details can be found in [167].

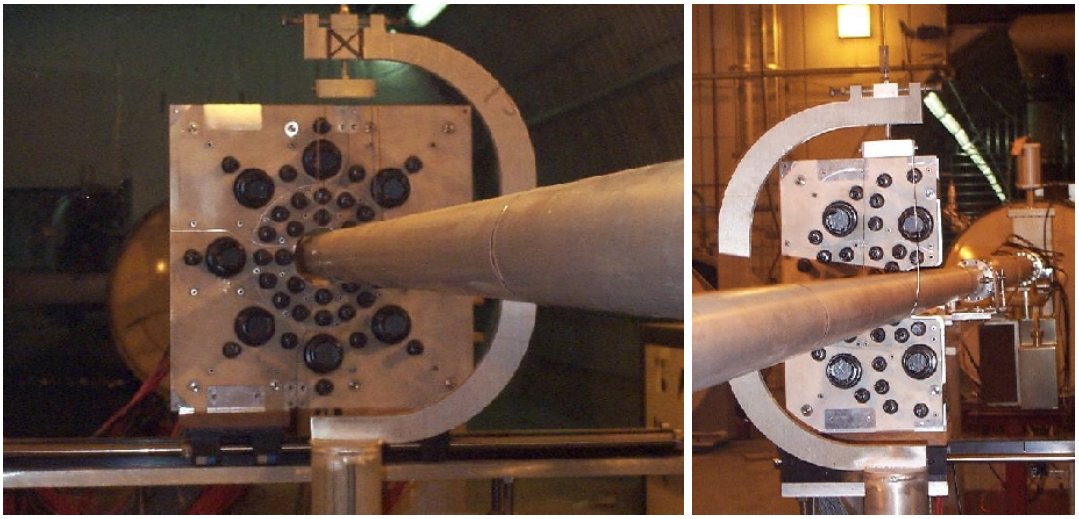

Figure 3.6: BBCs.

3.3.3 Zero Degree Calorimeters

The Zero Degree Calorimeters are located on each side of the vertex location at a distance of 18 m, behind the DX magnets. Each calorimeter is divided into three modules with alternative absorber and Cherenkov radiator. ZDCs measure the energy of the spectator neutrons that travel along the beam axis in a solid angle of 2mrad. The neutron multiplicity is related with event geometry and may be used together with the data from the MA and BBCs to determine the collision centrality. The difference in flight time from the vertex to each ZDC can be used to measure the vertex position while the average of the two times can be used as a time zero signal. Also, ZDCs serve as minimum-bias trigger detectors for run04.

They are the only common detectors between the four RHIC experiments and can be used for monitoring of the collider performance (the luminosity of the colliding beams). More details can be found in [165].

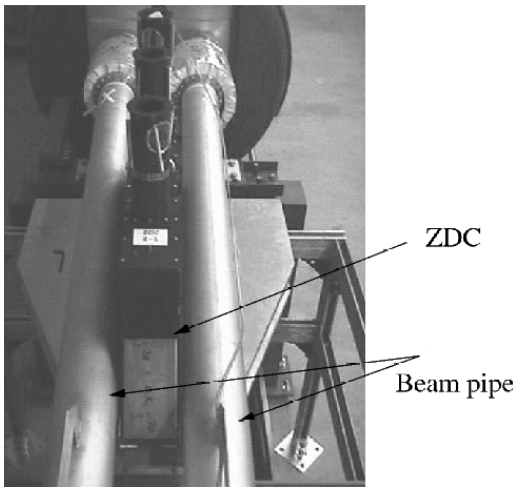

Figure 3.7: ZDC

3.4 Tracking Detectors

BRAHMS has two types of tracking devices: Time Projection Chambers and Drift Chambers in order to reconstruct the charged particle trajectories through the spectrometers.

3.4.1 Time Projection Chambers

The Time Projection Chambers provide three-dimensional particle trajectories measurements with an intrinsic position resolution less than 400μm and a two-track resolution smaller than 15 mm. Two TPCs are located in front (TPM1) and behind (TPM2) the D5 magnet in the MRS and the other two in front (T1) and behind (T2) the D2 magnet in the FS. As the TPCs are placed outside magnetic fields, the tracks are straight lines.

In the TPC, electrons and positive ions are created from ionization by a charged particle passing through the 90% Ar+10% CO_2 gas-filled volume. The primary ionization electrons drift in the electrical field inside the TPC volume towards the readout system situated at the top of the TPC. When the electrons drift towards the anode wires (sense wires) held at a positive potential of +1200V they accelerate and initiate an avalanche leaving a cloud of positively charged ions around the anode wires. Image charges are induced on an array of pads located 4.5mm above the anode wires.

In order to have a TPC active only during well-defined collision events, a gating grid is installed between the cathode grid and the drift region. In its closed state, the gating grid prevents positive ion feedback from the avalanche region near the anode wires into the drift volume. When the gating grid is opened, all gating grid wires are at the same potential (-180 V). The closed state is obtained by applying different voltages to adjacent wires (-100 and -260 V), thereby creating an electrostatic field that renders the gate opaque to the passage of charged particles.

When the velocity of the drifting electrons (drift velocity) is constant, the drift time is proportional to the drift distance. Thus, for each track segment, the drift time provides the y-coordinate, while the position and amplitude of the induced signals on the pad rows are used to extract the x- and z-coordinate. Details about TPCs can be found in [165, 35].

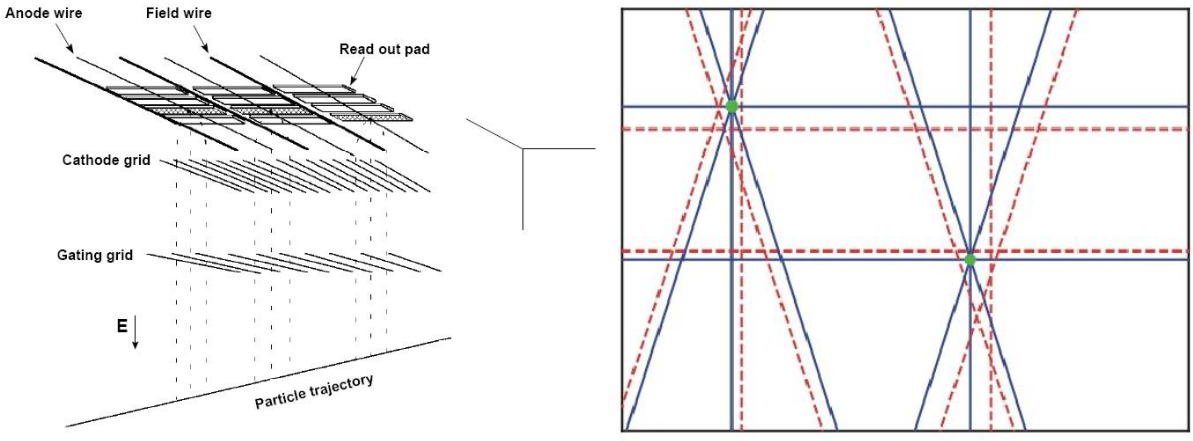

Figure 3.8: Schemetic figure of the TPC. DC is shown from its front and views are x, y, u and v (intermediate angles). Each hit gives rise to two lines before the left/right ambiguity is solved. The solid lines are the true ones. The two tracks are defined by the intersection of the solid lines (green dots).

3.4.2 Drift Chambers

BRAHMS has three drift chambers in the FS spectrometer located at at 10.5, 14.5 and 18.4 m, respectively, from the nominal vertex. Each DC consists of three modules with 8-10 detection planes arranged in different orientations or "views". The sense wires are spaced 1.0 cm apart in T3 and 2.2 cm apart in T4 and T5. The wire directions are x, y, u, v, where the first two correspond to the x and y directions, where x is in the horizontal direction and y is in the vertical direction, while u and v are + and -18° relative to the y direction. Each x and y plane is followed by another plane with the same wire orientation, but shifted by a quarter cell width, to remove right-left ambiguities.

The electrons created when a charged particle pass through the DC are attracted by the anode wires. When the correspondence between drift time and drift distance to the wire has been established, each hit in a view gives a line parallel with the view direction (wires). However, at least two planes with the same view are needed to resolve the hit ambiguity, i.e. on which side of the wire the charge particle passed. By combining the different views one obtains the tracks as the intersection of the wires that were hit, see figure3.8. Details about DCs can be found in [165, 35].

3.5 Magnets

BRAHMS has five dipole magnets, D1-D5, designed to bend the particles in the horizontal plane and to provide momentum determination for the charged particles produced in the collisions. D1 is the most forward magnet and it is closest to the beam line. The magnet was designed to fit into the space near the beam pipe when FS is placed at the most forward angle of 2.3°. The D1 field delivered is up to 1.3 T to give sufficient bending power to particles with momenta up to 25 GeV/c. The D2-D5 magnets are located between the tracking detectors.

Inside the magnet gaps, the magnetic field is vertical and deflects particles only in the x direction. The field is determined by two parameters: the current intensity and the current polarity. The orientation of the magnetic field depends on the polarity, A or B. In the FS, an A(B) polarity field corresponds to negatively (positively) charged particle detection. In the MRS, particles with both charge signs are detected in a single polarity setting because is only one magnet and the detectors behind it are large enough to detect the particles.

The magnet field settings are fully determined by their polarity and the fraction of the maximum current used during data taking. The Au+Au data at $\sqrt{s_{NN}}$=200 GeV taken in run04 were using high magnetic fields (half field, full field) because the primary BRAHMS goal was high p_T particle production study.

3.6 PID Detectors

The particle identification (PID) both in the MRS and FS spectrometers is based on time-of-flight measurements and Cherenkov radiation detection.

3.6.1 TOF

There are four TOF detectors in BRAHMS, two in the MRS (TOFW and TFW2) and two in the FS (H1 and H2). All detectors are built of a number of vertical plastic scintillator "slats" read out by two PMTs placed at either end of each slat. In order to extract a good PID from the TOF information, one must determine the location of the collision vertex as well as define a start time. For the Au+Au run04, they are determined by the beam-beam arrays.

Particle identification is achieved by the use of the momentum measurement obtained with the tracking through two TPCs with a dipole magnet in between and the data from the TOF arrays

located behind the tracking detectors. The particle mass squared is calculated as:

$$m^2 = p^2(\frac{1}{\beta^2} - 1) = p^2[(ct/l)^2 - 1] \tag{3.2}$$

where l is the path length of the particle, t is the time-of-flight and p is the particle momentum.

3.6.2 Cherenkov Detectors

Cherenkov radiation arises when a charged particle in a material medium moves faster than the speed of light in that same medium. This speed is given by $v = \beta \cdot c = c/n$, where n is the index of refraction and c is the speed of light in vacuum. A particle emitting Cherenkov radiation must therefore have a velocity $v_{part} > c/n$. In such a case, a Cherenkov radiation is emitted at an angle

$$cos\theta_c = \frac{c}{v \cdot n} = \frac{c}{n \cdot \beta \cdot c} = \frac{1}{\beta \cdot n} \tag{3.3}$$

with respect to the trajectory of the particle. Due to different thresholds for pions, kaons and protons to generate Cherenkov radiation, the Cherenkov detectors provides good separation of the particle species. BRAHMS has three Cherenkov detectors, two threshold Cherenkov detectors (C1 and C4), one in FS and another in MRS, and a rich imaging Cherenkov detector (RHIC) in FS.

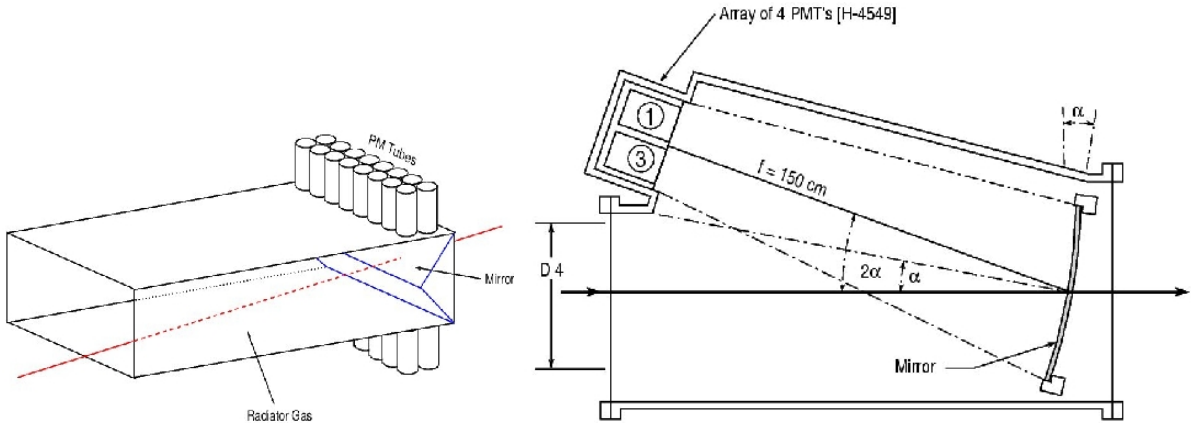

Figure 3.9: Cherenkov detector C1 (left) and ring imaging Cherenkov detector RICH (right).

C1

C1 is a threshold Cherenkov detector installed in the front FS to extend the particle identification obtained by H1. The detector has the pion threshold set at 2.6 GeV/c and it can discriminate between pions and kaons up to the kaon threshold at 9.3 GeV/c. The pions in the energy range $3< p <9$ GeV/c give a significant signal in the C1 while the kaons and protons do not.

The radiator volume is 75 cm long, 50 cm wide and 40 cm tall and is filled with C_4F_{10} gas at atmospheric pressure. Cherenkov light produced by charged particles with momenta above threshold is reflected from two flat mirrors onto two photon detector planes above and below the radiator volume. The photon detectors are arrays of photomultipliers arranged in two rows of eight phototubes each. Light reflected by the flat mirrors is funneled into the active area of the PMTs by a set of glass mirrors arranged in the shape of a truncated pyramid.

C4

C4 is a gas threshold Cherenkov detector installed in run03 behind the time-of-flight wall (TOFW) in the MRS to extend the particle identification obtained by TOFW. Cherenkov light is reflected off of large back mirrors into 16 light-collector mirror pyramids, 8 top and 8 bottom, which directs light into PMTs. C4 radiator gas is C_4F_{10} with an index of refraction n=1.00138. C4 has the pion threshold at 2.8 GeV/c and it can discriminate between pions and kaons up to the kaon threshold at 9.5 GeV/c.

In MRS, for lower p_T values, time-of-flight identification with TOFW and TFW2 is used. Once π/K identification is no longer possible using TOFW and TFW2, the presence of Cherenkov radiation for the pions and lack of the radiation for the kaons and protons in the C4 volume is used.

RICH

The RICH detector is situated at the end of FS spectrometer in a low multiplicity environment of one or two tracks per event. The combination of momentum and ring radius measurement provides particle identification for pions with momenta starting at 2.5 GeV/c. Above 20 GeV/c, the ring radii of pions and kaons cannot be differentiated. Protons can be identified well above 35 GeV/c.

The RICH detector has a gas radiator volume filled with a mixture of C_4F_{10} and C_5F_{12} with an index of refraction 1.001850, at a pressure of 1.25 atm. The Cherenkov light is focused onto a photon detector by a spherical mirror with a 3m radius of curvature. The photon detector is an array of 80 photomultipliers mounted in four bases that contain 20 tubes each. The spherical mirror is rotated by 8° with respect to the spectrometer axis to focus the light onto the photon detector whose center is 16° off the axis [165, 168]. The focused light form a ring with the radius dependent on the momentum and mass of the particle. Tracks reconstructed with the FS spectrometer tracking system are used to find the center of rings.

Figure 3.10 shows the y-p_T coverage for the π, K and p identified using the BRAHMS PID detector systems. For the data used in the present analysis, the PID in MRS was done with both TOFW and TFW2 and in the FS was done only with RICH.

3.7 Triggers

Data presented in this thesis were taken in run04 Au+Au collisions at $\sqrt{s_{NN}}$=200 GeV and in run 05 p+p collisions at $\sqrt{s_{NN}}$=200 GeV using the next trigger system (table3.1).

Trigger	1	2	3	4	5	6	7	8
$Au+Au$	BB	FS	MRS	$ZDC(MB)$	$ZDCwide(MB)$	FFS	$Pulser$	$Sync.$
$p+p$	–	FS	MRS	–	$CC(MB)$	FFS	$Pulser$	$Sync.$

Table 3.1: Triggers used for data acquisition in run04 and run05.

The DAQ records events based on the signals coming from the trigger box. The trigger box can be set up to scaledown any of the triggers. This way, only events with required trigger and scaldown are recorded. The scaledown factors are stored in the raw data, and therefore the proper normalization can be retrieved at the analysis stage. The scaledown system makes sure that the event rate does not exceed the limit of $\sim$ 150 events/sec, due to limits of the bandwidth and storage space.

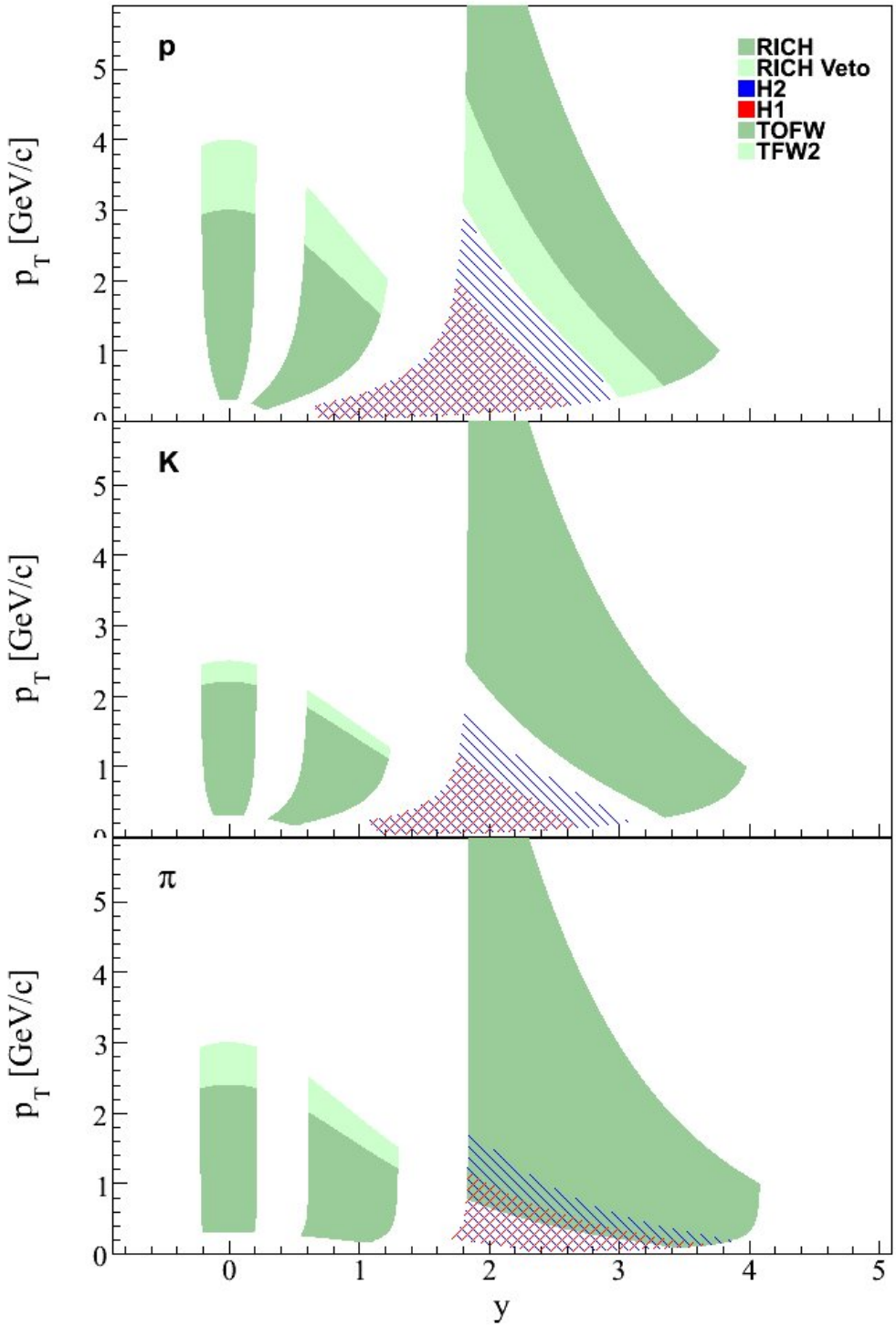

Figure 3.10: The π, K and p acceptance maps for different spectrometer settings, generated with 5 cm vertex bins in the [-15, 15] vertex range. The green color regions are showing the acceptance for the data used in this analysis.

Chapter 4

Data Analysis

4.1 Vertex measurements

There is one specific feature for a collider experiment, namely the variable point where the two ions collide. The beams are tuned to produce collisions at the nominal interaction point (IP). Beam crossings occur within 1m of this point, in a region referred to as the interaction diamond. The interaction vertex of the collision is defined with respect to the nominal interaction point (IP) along the beam axis (z direction). The vertex distribution usually seen by BRAHMS is shown in the Figure 4.3. FWHM of the vertex distribution for AuAu and pp collisions are ∼20 cm and ∼50 cm, respectively.

Vertex measurement is important for the BRAHMS experiment. The event selection for the analysis is done based on the vertex position - outside a certain vertex range, the ability of the spectrometers to reconstruct tracks decreases. Global measurement of event centrality requires a rough 5 cm precision for the vertex, as the event multiplicity is corrected for the vertex position. Particle identification uses the path length of the track, where the vertex position is also used, along with the momentum determined from bending inside the magnets.

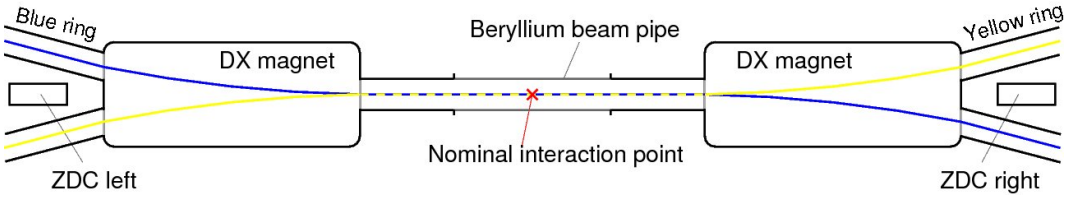

Figure 4.1: Schematic view of the interaction region. The red cross indicates the nominal interaction point.

At BRAHMS, several methods and detectors are used to determine the collision vertex. They differ by the inner details of each method, and result in providing the vertex position with a specific resolution and efficiency of finding the vertex for a certain event centrality.

The vertex measurement is done in detectors placed left and right to the IP, in the forward direction by measuring the time-of-flight for fast charged particles ($\beta \sim 1$) in the BBC, or for spectator neutrons in the ZDC. Additionally, the BBC detector array also provides the start time for the TDC units.

$$z_{vtx} = \frac{c}{2}\left[\langle t_L \rangle - \langle t_R \rangle\right] - z_{off} \tag{4.1}$$

$$t_{start} = \frac{c}{2}\left[\left(\frac{D - z_{off}}{c}\right) - \langle t_L \rangle - \langle t_R \rangle\right] \tag{4.2}$$

where $\langle t_{L,R} \rangle$ are the averaged (calibrated) times measured in the left and right arrays respectively, z_{off} is the overall vertex offset and D is the distance between the left/right arrays.

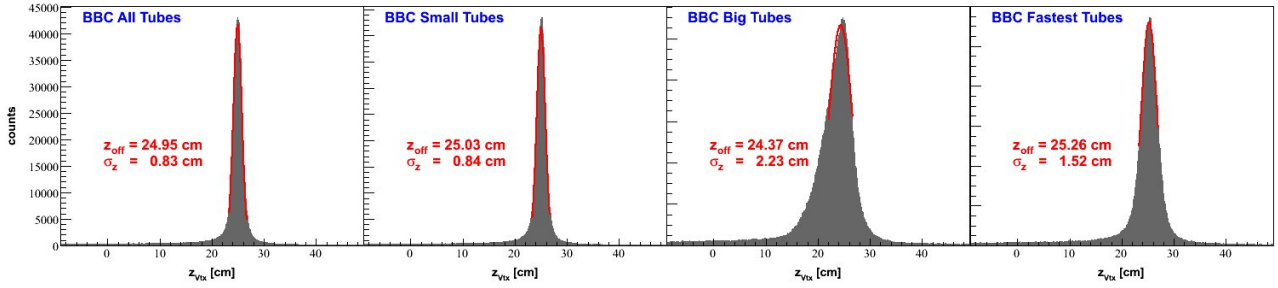

Figure 4.2: BBC vertex offset and the vertex resolution determined by all tubes, small tubes, big tubes and fastest tubes.

The BBC geometry allows us the use four different methods to estimate the vertex position, by using: (1) all tubes (2) small tubes (3) big tubes and (4) fastest tubes. Time measurements are averaged over all tubes that have been hit, in order to make the measurement more precise. The farthest tubes in time with respect to average time are disregarded. The BBC methods above have been indexed by the order of choosing the event vertex at the reconstruction stage. The small and all tubes methods give the most precise vertex measurement but they require a large number of hits in both arrays in the same event. As the number of hits decreases, as for example for a peripheral event, the big tubes have larger probabilities of being hit and therefore the fraction of vertices found by big tubes increases.

BBC tubes are calibrated for slewing effects - timing differences induced by different energy of particles. The time calibrations of the BBC tubes align in time all the tubes with respect to a given big tube in each array. Therefore, the vertex shows an offset with respect to the real vertex, given by the time delays of the reference tubes. This offset is corrected by comparison with the tracks projected from TPM1 to the beam axis. The BBC vertex resolution is shown in Figure 4.2, and ranges from ∼0.8 cm for small tubes to ∼2.5 cm for big tubes. The resolutions presented in figure 4.2 contain the uncertainty in projecting TPM1 tracks forward to the beam line.

ZDC detectors employ the same principle of finding the vertex by the use of 3 modules in each of the left/right arrays with a resolution of the order of 2-3 cm.

The 3rd method consists in projecting either tracks or fits to the TPC clusters back to the beam axis. Detector tracks in the TPM1 can be used to reconstruct the collision vertex with an accuracy better than 0.5 cm. Other tracking devices are either too far, or badly placed, to allow good vertex resolution along the z direction. The pointing to the beam axis is affected by momentum and angle resolutions and also by the detector occupancy.

In the case of elementary collisions, the BBC are not able to reconstruct the interaction vertex for all the events. The pp vertex measurement is done with a set of Cherenkov radiators (CC) placed symmetrically with respect to the nominal interaction point and covering pseudo-rapidities that range in absolute value from 3.26 to 5.25.

4.1.1 Vertex selection

The analysis has to include a wide enough vertex selection to maximize track statistics and event selection, yet narrow enough to allow for a good analysis. The centrality measurement becomes less certain for events with vertex close to the edges of multiplicity array acceptance. Track reconstruction in the MRS TPC is worse for tracks well outside the IP. In the FS, track reconstruction is less affected, due to smaller polar angles. Figure 4.3 shows vertex distributions from Au+Au collisions, using the BBC, and from p+p collisions, using the CC. The accepted vertex for the MRS AuAu and pp analyzes is [-15, 15] cm and [-30, 30] cm, respectively. For the AuAu and pp FS analyzes, selected events have the vertex inside [-20, 20] cm and [-30, 30] cm, respectively. Wider vertex selection for the pp system was chosen due to wider vertex distribution.

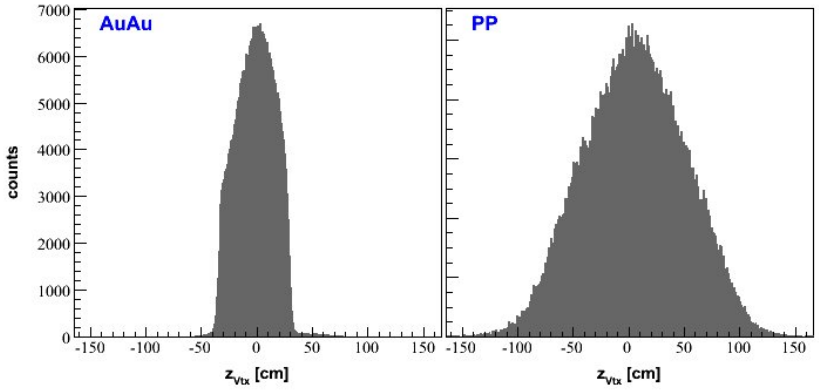

Figure 4.3: The distribution of collision vertex for Au+Au collisions and p+p collisions at $\sqrt{s_{NN}}$=200 GeV.

4.2 Centrality measurements

For the heavy ion collisions, one important criterium of selecting events is the centrality of the collision. The collision centrality is defined by the impact parameter b (see section 1.3.1). Smaller b corresponds to more central collisions and larger b to more peripheral collisions. However, we cannot measure the impact parameter experimentally, so we must rely on some other experimental observable that correlates with the impact parameter. For this analysis, we use a simple measured quantity, the multiplicity of the charged particles produced in the collision. Central collisions produce the largest particle multiplicities.

Most central collisions, because they have the most participants, produce the largest number of charged particles N_{ch}, which are then detected. The centrality is determined as percent of cross-section of all the collisions based on the number of N_{ch} particles produced.

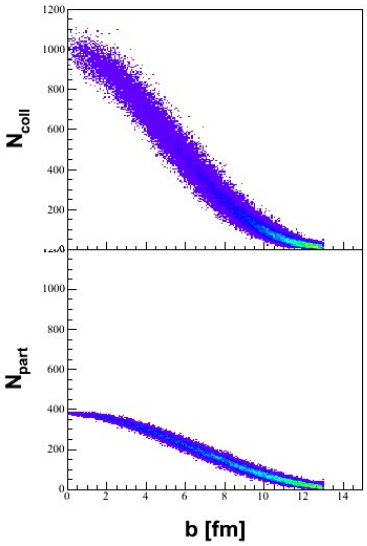

Figure 4.4: The number of participants N_{part} and the number of binary collisions N_{bin} as a function of impact parameter b, in a Au+Au collision at 200 GeV.

Two quantities correlated with the impact parameter are the number of participants, N_{part}, and the number of binary collisions, N_{bin} (see section 1.3.1). Both N_{part} and N_{bin} are not experimentally measurable quantities and it is necessary to rely on model calculations to determine the values. For BRAHMS data, the estimations are done using the HIJING events as input to a BRAG (BRAHMS GEANT) simulation with the same centrality cuts as in the analysis of real data, and with the same acceptance cuts as the global detectors.

Details about the calculation of N_{part} and N_{bin} can be found in [28]. Figure 4.4 shows the dependence of N_{part} and N_{bin} as a function of impact parameter, in Au+Au collisions at 200 GeV. N_{bin} and N_{part} for different collision centralities used in this analysis are presented in the Table 4.2.

In order to estimate the centrality from the multiplicity distribution detectors with solid angles close to 4π are required. The missing part must be corrected for. BRAHMS uses the MA (multiplicity array) to estimate the event multiplicity. This overall quantity is inferred as an average of the two components of the detector, Tile array and Si array. The Tile array has a larger solid angle, but the Si array is highly segmented. MA covers only the pseudorapidity range [-2.2, 2.2], and therefore the rest of the multiplicity distribution is estimated by the BBC detectors. Figure 4.5 presents the

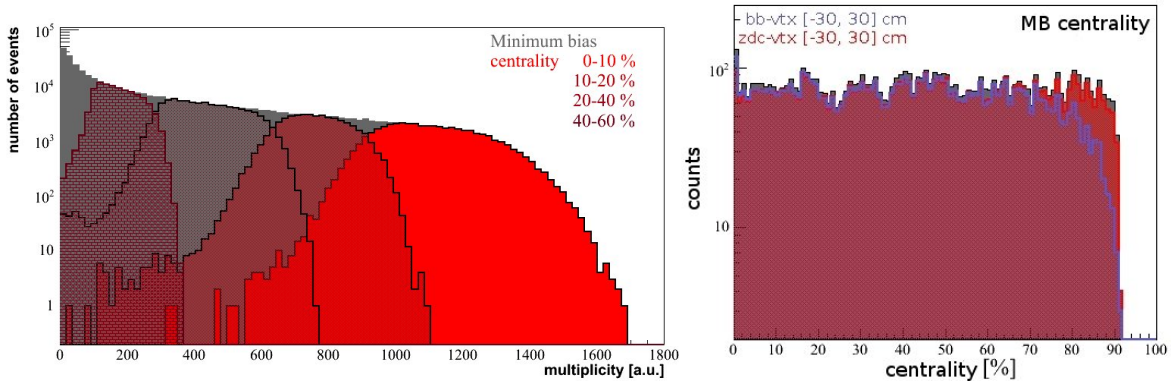

Figure 4.5: Left: Multiplicity distribution with different centrality selections, measured using the minimum bias trigger. Right: Minimum bias centrality distribution for events with good BBC/ZDC vertex. Selected vertex range is ±30 cm.

charged particle multiplicity distribution measured by BRAHMS in 200 GeV Au+Au collisions.

The variable position of the event vertex has to be taken into account when dividing the data sample into centrality classes. Therefore, the size of MA detector along the beam axis restricts the event selection to [-50, 50] cm in vertex. Event centrality is calculated from the corrected multiplicity distribution and from MC simulation. The segmentation of MA determines the associated uncertainty in the centrality calculation. The MA is able to provide four to six centrality windows for the analysis.

$Centrality[\%]$	N_{bin}	N_{part}	$b[fm]$
$0-10$	$886.8^{+96.7}_{-123.9}$	$328.6^{+3.4}_{-5.8}$	$3.2^{+0.2}_{-0.1}$
$10-20$	$534.3^{+71.4}_{-85.2}$	$233.3^{+8.0}_{-8.5}$	$6.0^{+0.3}_{-0.3}$
$20-40$	$244.2^{+44.3}_{-47.5}$	$134.2^{+9.0}_{-8.6}$	$8.5^{+0.5}_{-0.4}$
$40-60$	$71.2^{+19.7}_{-17.8}$	$56.1^{+7.8}_{-6.5}$	$10.9^{+0.6}_{-0.5}$

Table 4.1: Number of participants and number of binary collisions for different centrality classes in Au + Au collisions at $\sqrt{s_{NN}} = 200$ GeV.

The same approach may be applied also to BBC and ZDC measurements. Given the detectors' geometries, various combinations between the total energy deposited in the ZDC, total multiplicities measured by the BBC and integrated multiplicities from MA may be used to extract the event centrality. However, MA efficiency decreases for both very central or very peripheral collisions, as it can be observed in the right panel of figure 4.5.

4.3 Tracking

Charged particle trajectories are reconstructed in the tracking devices, TPCs and DCs. Each of the detectors reconstructs local tracks from matching hit positions. Then local tracks are projected to the mid plane of a dipole magnet. The local tracks from the detectors on either side of the magnet are then compared and if the tracks "match" within predefined parameters they are considered to form a global track. The momentum associated to each track is calculated from the bending radius inside the magnets. Additionally, FFS and BFS tracks are also matched to obtain full FS tracks. Finally, global tracks are projected toward the beam pipe where the vertex position is checked and primary particles can be selected. The match of global tracks and time of flight information results in an identified particle (PID).

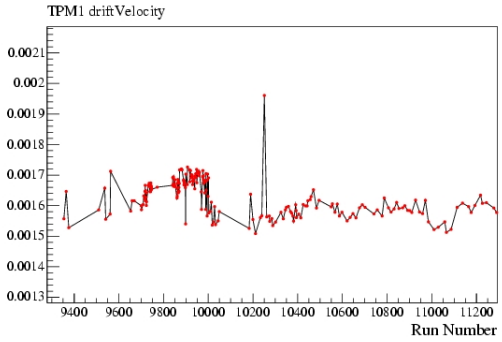

Figure 4.6: TPM1 drift velocity as a function of run number during the run04 Au+Au data acquisition. The fluctuations are due to the changes in the TPC gas pressure.

4.3.1 Local tracking

Charged particles passing through detector volume ionize the gas along its trajectory. Electrons are collected and give electric signals from which the position of the "hit" can be calculated. For each event, hits in the last detection plane are used as the starting point for finding local tracks using the procedure described in [35].

Calibrations of the tracking detectors are required in order to minimize the variations of the matching parameters. The event vertex depends also good tracking in the TPM1.

TPC calibration takes place in 3 steps. (1) Pads that did not provide standard signals are identified and ignored subsequently. (2) The drift velocity for the pad-rows placed to the sides of the TPC show nonlinearities which must be corrected. (3) The calibration of the drift velocity inside the detector against changes of gas pressure in time. Such a calibration is shown in Figure 4.6.

4.3.2 Global tracking and momentum measurements

Momentum measurements are made by units of two tracking devices with a magnet placed in the middle. There are 4 places where this takes place, TPM1-D5-TPM2 in MRS, and T1-D2-T2, T3-D3-T4, T4-D4-T5 in the FS. The actual geometry is illustrated in Figure 4.7. BRAHMS uses the effective edge approximation algorithm, where the magnetic field is constant along the y direction, such that the bending takes place only in the xz plane. The movement of particles is therefore an helix inside the gap region of the magnet. The Figure 4.7 shows the top view of the tracking detector and the middle magnet.

Momentum of the track in the x-z plane is given by $p_{xz} = qB\rho$, where q is the charge of the particle, B is the magnetic field and ρ is the radius of the helix in the magnetic field.

Following simple calculations, p_{xz} is:

$$p_{xz} = \frac{qB\Delta L}{sin\theta_f - sin\theta_b} \tag{4.3}$$

Taking into account that on the the vertical direction there is no bending, the final momentum of the particle can be computed as:

$$p = \frac{qB\Delta L}{sin\theta_f - sin\theta_b} \frac{1}{\sqrt{1-\alpha_y^2}} \tag{4.4}$$

where α_y is the y-slope of the track.

Matched local tracks should have $\Delta y = 0$ in the matching plane and $\Delta\Psi = \Psi_b - \Psi_f = 0$. Because of the finite resolution of the tracking devices, multiple scatterings through the material and the approximations used by the effective edge method, there are slight deviations of the matching parameters Δy, $\Delta\alpha_y$ and $\Delta\Psi$.

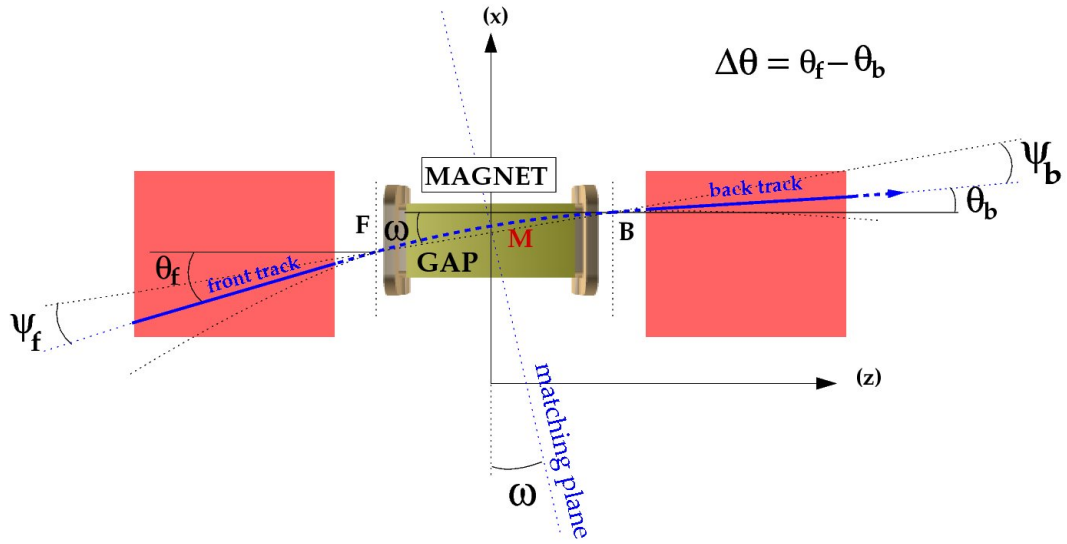

Figure 4.7: Top view of a charged particle trajectory through the spectrometer (tracking detector - magnet - tracking detector).

Spectrometer tracks

Tracks reconstructed in the full spectrometer are called global tracks. Spectrometer tracks have a track vertex and a track path length. Track path length is used with TOF information to determine particle identification.

In the MRS, the front part of the global track is projected to the z-y plane containing the beam pipe. The intersection with the plane gives the track vertex. The back part of the track is projected to either TOFW, or TFW2 in order to estimate the path length from track vertex to the PID detector.

Since the determination of event vertex offset is done by comparing to the track vertex, the distribution of points $(z - z_{track}, y_{track})$ should be centered on (0,0). However, the calibrations are done every few runs, therefore small offsets might be still visible. At the analysis level, the offsets are extracted and a 2 dimensional fit is done. Selecting tracks within 4σ of the mean vertex position make sure that only primary tracks are selected. Figure 4.8 shows track vertex distribution along with the applied cut.

For the FFS spectrometer track, the tracks from T1 are projected thorough D1 magnet, where the D1 track's helix is determined using the D2 calculated momentum. Therefore, the projection of the track can be done, in the x-y plane perpendicular to the beam pipe in the global vertex point. Like for the MRS tracks, the distribution is corrected for the offsets and fitted with gauss functions in order to select primary particles. Figure 4.8 shows this selection.

FS tracks are obtained by matching FFS tracks with BFS tracks. T3-D3-T4 track and T4-D4-T5 tracks are matched to obtain the BFS track. Since both tracks share the same local track in T4, the matching is done simply by comparing T4 track identification. Therefore, BFS tracks are made of T3-D3-T4-D4-T5 tracks, or T2-D3-T4-D4-T5 when there was no T3 track and T2 was used for the BFS track. The matching between T2-T3 tracks is made without a magnet, using as matching parameters Δx, $\Delta\alpha_x$, Δy and $\Delta\alpha_y$.

MRS details for the AuAu data

During the AuAu run4, the back TPC of the MRS had many dead pads close to its back plane. TPM2 ability to reconstruct local tracks lowered into that region. This situation required modifications to the acceptance of the spectrometer. MRS tracks that project outside [-19, 23] cm on the x axis of the back plane of TPM2 are disregarded, both in the acceptance and in the data selection because of the

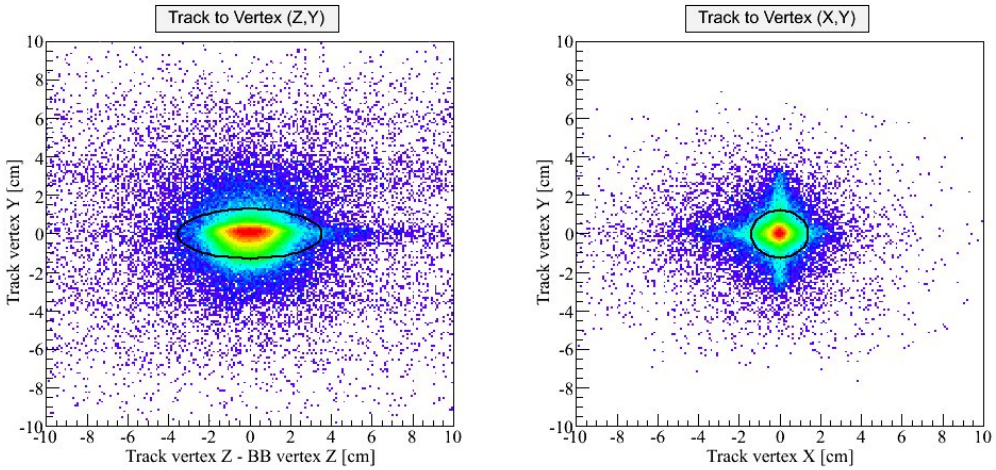

Figure 4.8: Intersection of particle tracks with primary vertex plane, in the MRS (left) and FS (right). Tracks are distributed around the collision point with a maximum at the primary vertex location. The line is the 4σ cut (elliptic cut) used in the present analysis.

reduced TPM2 efficiency.

Hit correction in the FS

Slight adjustments were necessary to the T1 and T2 positions in the geometry. The alignment of the detectors is done with small imprecision that is found by analyzing certain runs. The magnetic field is switched off allowing the determination of offsets to the data recorded by the tracking devices. Momentum of the particles can not be determined for such runs.

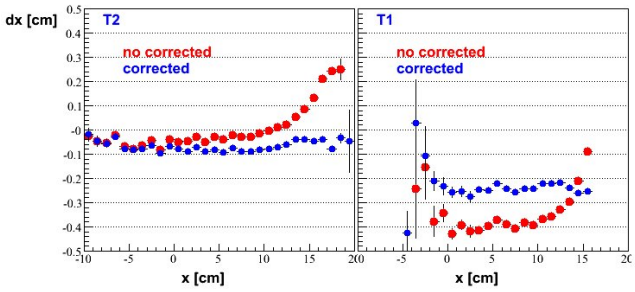

Figure 4.9: The difference between the T1 and T2 hits and the projected T3 tracks (red points). The blue points show the corrected hit distribution.

An analysis was done in order to test the performance of the front tracking detectors in the FS, T1 and T2. Track from T3 are projected through T2 and T1. Figure 4.9 shows the difference between the hits in T2, T1 and the projected T3 tracks. The overall offset is due to misalignment of the detectors and the geometries of T1 and T2 were modified in order to minimize this offset. Additionally, it was found that serious corrections were necessary for the hits at the edges of the TPCs. The effect seen from Figure 4.9 was parameterized and the hits were corrected. Both AuAu and pp data were investigated and corrected.

4.3.3 Momentum resolution

Momentum resolution depends on the resolutions of the tracking detectors, the bending angle resolution and the effects of the multiple scattering in the spectrometers. This can be expressed as:

$$\left(\frac{\delta p}{p}\right)^2 = (\sigma_{ang} p)^2 + \left(\frac{\sigma_{ms}}{\beta}\right)^2 = (\sigma_{ang} p)^2 + \left(1 + \frac{m^2}{p^2}\right)\sigma_{ms}^2 \tag{4.5}$$

It can be seen that momentum resolution is also inversly proportional to the magnetic field strength. Momentum resolution changes from setting to setting because of σ_{ang}.

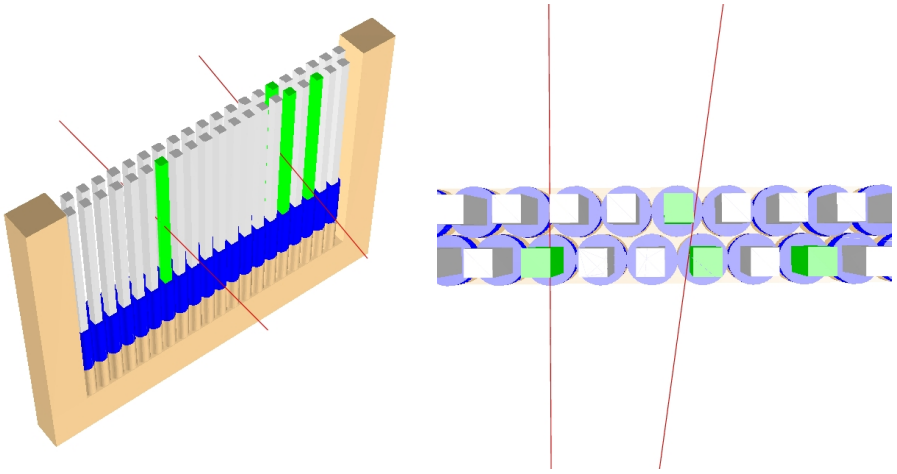

Figure 4.10: The hodoscope H1 in the FS. The red lines are the particle tracks intersecting the scintillator slats of H1.

Momentum resolution is improved by using the global refitted module, which takes the local tracks, vertex position and momentum measurements through the magnets and estimates the best momentum and track theta angle from minimization algorithm. Momentum resolution can be determined from full GEANT simulation. In the absence of multiple scatterings, it is 0.5% and ranges between 2-8% in the FS spectrometer at half field in D1, with all physics options turned on. Tracks with bad global χ^2 are removed both in the simulation and the data analysis.

Transverse momentum ($p_T = p\sin\theta$) resolution can be calculated as

$$\sigma^2_{p_T} = (sin\theta)^2\sigma^2_p + p^2(cos\theta)^2\sigma^2_\theta \tag{4.6}$$

Particle identification results and p_T measurements rely on the momentum and angle resolutions.

4.4 PID

In BRAHMS, there are two distinct methods to achieve particle identification, by using time of flight detectors - TOFW/TFW2 in the MRS, H1/H2 in the FS, and the second method, by using Cherenkov detectors - C4 in MRS, C1/RICH in the FS, respectively. For the present analysis, TOFW, TFW2 and RICH are used.

4.4.1 TOF

A particle passing through the spectrometers reaches the time of flight detector. The information on a TOF hit contains the stop time for the particle, the hit slat and the y position of the hit. Since we know the vertex location and the start time - when and where the particle was produced - the time it took the particle to pass through the detector is $t = t_{TOF} - t_{start}$. The track length L and momentum p are known from the tracking of the particle and from the matching of local tracks inside the magnets. Therefore we assign the velocity β and the mass for the particle as:

$$\beta = L/t \tag{4.7}$$

$$m^2 = p^2\left(\frac{1}{\beta^2} - 1\right) \tag{4.8}$$

Due to time resolution, velocities may be greater than the speed of light ($\beta > 1$), resulting in a negative squared mass. There are several conditions to select good hits in the TOF detector: (1)

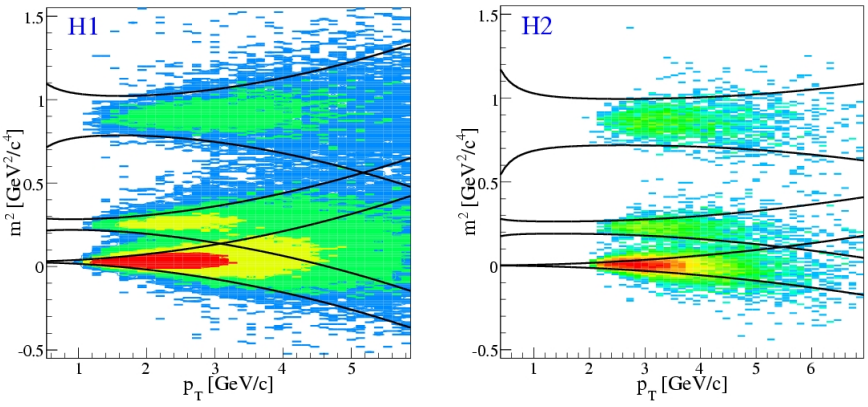

Figure 4.11: Pions, kaons and protons selection in the FS, with H1 and H2. The momentum dependent curves are obtained by a simultaneous fit using Eq. 4.11 and delimit a 2σ area around the mean mass squared.

multiple hits are rejected; (2) hit slat can be different from the track pointed slat by no more than ± 1, and (3) $\Delta y = y_{hit} - y_{track} < 3\sigma_y$.

Projection of a track to the TOF volume might fall in the space between the slats. This situation regards the TOF efficiency, which is corrected by applying the PID efficiency. There are also rare cases when more than one hit slat matches the same track. Figure 4.10 shows such cases. Multiple hits are removed from the analysis.

The separation of the particles is done based on mass squared distribution dependence on momentum. From equation 4.8 it follows by using the error propagation:

$$\left(\frac{\sigma_{m^2}}{m^2}\right)^2 = 4\frac{\sigma_p^2}{p^2} + 4\gamma^4\frac{\sigma_\beta^2}{\beta^2} \tag{4.9}$$

Momentum resolution is written as $\sigma_p^2/p^2 = p^2\sigma_{ang}^2 + \left(1 + m^2/p^2\right)\sigma_{mult}^2$ where σ_{ang} depends on the track angle resolution and intensity of the magnetic field, and σ_{mult} takes into account multiple scattering. Using $\beta = L/(ct_{TOF})$, we can write the β resolution as:

$$\frac{\sigma_\beta^2}{\beta^2} = \frac{\sigma_{t_{TOF}}^2}{t_{TOF}^2} + \frac{\sigma_L^2}{L^2} \approx \frac{\sigma_{t_{TOF}}^2}{t_{TOF}^2} \tag{4.10}$$

Finally, from equation 4.9 and $\gamma = E/m$:

$$\sigma_{m^2}^2 = 4\left[m^4p^2\sigma_{ang}^2 + m^4\left(1 + \frac{m^2}{p^2}\right)\sigma_{mult}^2 + \left(m^2 + p^2\right)p^2\sigma_t^2\right] \tag{4.11}$$

where $\sigma_t = c\sigma_{TOF}/L$.

Mass squared versus p distributions are sliced in narrow intervals in momentum which are fitted by gauss functions. The experimental widths and means are extracted and fitted simultaneously for π, K and p with relation 4.11 (Figure 4.11). The K/π and K/p separation ranges are extracted for 2σ or 3σ separation level. Table 4.3 lists 2σ and 3σ momentum separation parameters for the TOF detectors used for the analysis.

Time of flight distributions versus p may be used to find the separation parameters. For any particle, we assume a certain PID, and then estimate the theoretical value, $1/\beta_{th}$. The widths and means of $1/\beta_{exp} - 1/\beta_{th}$ can be fitted in order to find $1/\beta$ resolution for π, K and p and then do the particle identification.

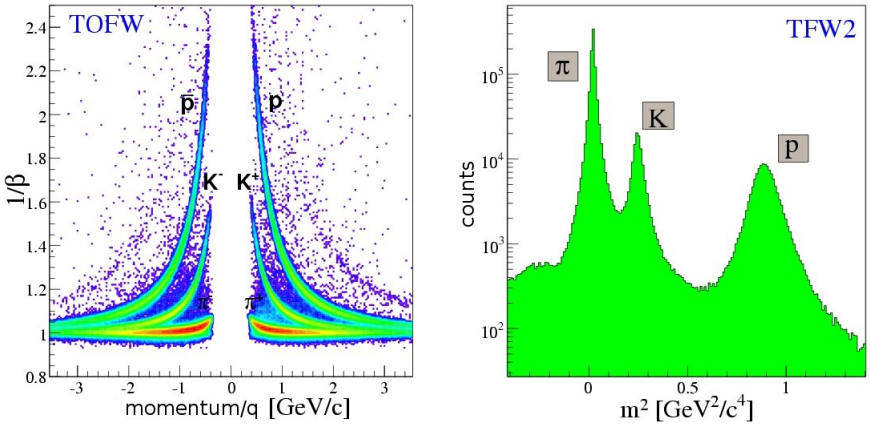

Figure 4.12: Left: Particle velocity as a function of momentum in the TOFW. Right: TFW2 mass squared distributions obtained from Au+Au data set.

The m^2 and $1/\beta$ methods are equivalent and they yield similar results (Figure 4.12). Even after the calibrations of TOF detectors, some small offsets of $\Delta\beta = 1/\beta_{exp} - 1/\beta_{th}$ were observed. These offsets are calculated on run by run basis and extracted from both m^2 and $1/\beta$ distributions, in order to improve the separation performance. The $1/\beta$ offsets are independent of the individual slat distributions.

There are bad slats which are disregarded in the analysis. Dead slats are identified at the calibration stage and their effect is taken into account at the level of the acceptance maps. The TOF detectors are the volumes which make the fiducial cut, and outer slats which have insufficient statistics are removed.

θ_{MRS}	90°1/2	90°1/1	45°1/2	45°1/1	40°1/2	40°1/1
A polarities						
$\sigma_{ang} \times 10^2$	1.3	0.3	1.6	-	1.2	0.1
$\sigma_{mult} \times 10^2$	1.3	0.9	0.7	-	1.3	1.0
$\sigma_t \times 10^3$	6.2	6.7	6.8	-	7.2	7.3
B polarities						
$\sigma_{ang} \times 10^2$	1.4	0.3	1.7	0.3	1.2	0.1
$\sigma_{mult} \times 10^2$	1.3	0.9	0.7	0.9	1.4	0.9
$\sigma_t \times 10^3$	6.0	6.5	6.6	6.4	7.1	7.2

Table 4.2: Simultaneous fit parameters for TOFW.

The analysis was made on AuAu data from 2004 and pp data from 2005. Data taking was done mainly for high magnetic field settings, in order to select mostly high p_T particles. For the MRS analysis we use the time measured in the TOFW and TFW2. For the FS analysis, high momentum particles can not be identified using the hodoscopes and therefore RICH was used for most of PID. H1 and H2 are used to identify protons and antiprotons for 8 and 10 degrees lower field settings, where RICH acceptance is too small for intermediate p_T particles.

4.4.2 Cherenkov PID

High p_T particles are identified in the FS with RICH detector. Inside the volume of RICH, Cherenkov radiation is emitted along the charged particle trajectory. The photons are reflected on the spherical

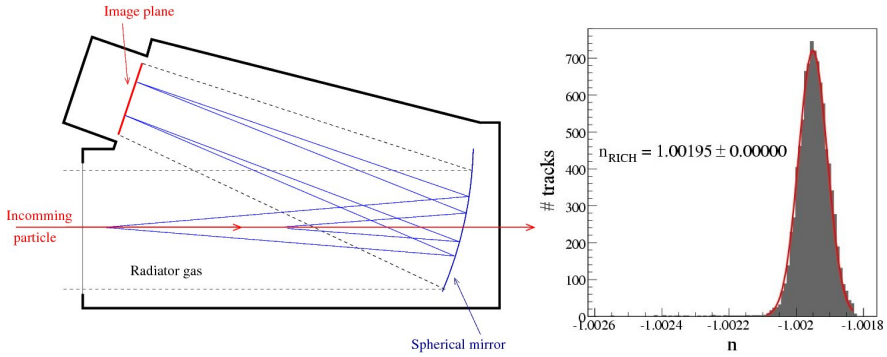

Figure 4.13: Left: Schematic side view of the RICH. A particle passing through detector is shown with the red line and the blue lines indicate the photon reflection on the mirror. Right: RICH refraction index.

mirror and get focused on the sensitive surface. All the photons produced at the same angle θ_C relative to the particle passage fall on certain angles on the spherical mirror and add hits to the same ring in the image plane. The center of the ring is fixed by the angle of the particle, known from tracking in the DC detectors. If the number of photons collected is smaller then the estimated number of photons for a certain particle β, the particle will not be identified. RICH inefficiency for finding the radius associated with a certain particle inside the RICH acceptance has been estimated to 3%. Figure 4.13 shows a side-view schematic of the detector and photon reflection on the mirror.

RICH calibration

RICH calibration consists in the precise determination of the refractive index n, due to the slight variations of gas pressure. The ring radius and the momentum threshold depend on the refactive index.

Refractive index calibration is done on a run by run basis, and consists in rough pion identification, based on an approximate value of n, followed by the exact determination of n from:

$$n = \frac{\sqrt{(r/L)^2 + 1}}{\beta} \tag{4.12}$$

Right panel of the Figure 4.13 shows the procedure to extract the value of n.

The ring radius is related to the Cherenkov angle as:

$$tan\theta_C = \frac{r}{L} \tag{4.13}$$

where $L = 150$ cm is the focal length of the spherical mirror. Therefore, particle mass is:

$$m^2 = p^2 \left(n^2 cos{\theta_C}^2 - 1\right) = p^2 \left(\frac{1}{\beta^2} - 1\right) = p^2 \left(\frac{n^2 L_{foc}^2}{L_{foc}^2 + r^2} - 1\right) \tag{4.14}$$

The uncertainty for m^2 can be extracted from the error propagation formula, where only r and p are measured quantities, L and n being constant.

$$\frac{\sigma_{m^2}^2}{m^2} = \left(\frac{\partial(m^2)}{\partial p}\sigma_p\right)^2 + \left(\frac{\partial(m^2)}{\partial r}\sigma_r\right)^2 = \left[2p\left(\frac{1}{\beta^2} - 1\right)\sigma_p\right]^2 + \left[2p^2\frac{L\sqrt{\beta^2 n^2 - 1}}{\beta^2}\sigma_r\right]^2 \tag{4.15}$$

Particle identification is done by extracting the 2 σ and 3 σ separation functions from m^2 versus p distributions, the same way it is done for the TOF detectors (Figure 4.14). The ring radius versus p distributions can also be used to identify particles.

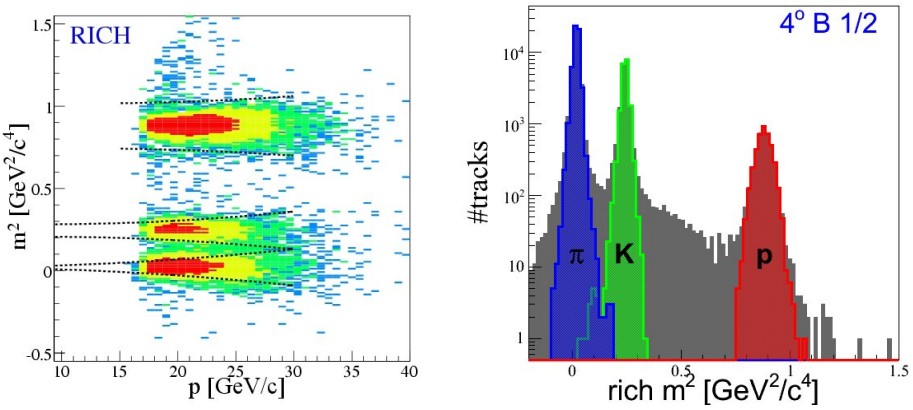

Figure 4.14: Left: Mass squared as function of momentum. The curves indicate a 2σ cut around the pions, kaons and protons. Right: PID selection in RICH at 4^o FS full field. The selected particles are restricted to the momentum dependent cut of 2σ around the mean mass squared.

		MRS		FS
Detector		*TOFW* p [GeV/c]	*TFW2* p [GeV/c]	*RICH* p [GeV/c]
2σ	π/K	2.2	2.4	26
	K/p	3.4	3.8	-
3σ	π/K	1.7	2.0	22
	K/p	2.7	3.0	-

Table 4.3: Particle separation in the MRS and FS.

4.4.3 PID contamination

PID contamination is studied above the K/π momentum separation limit for the time of flight detectors in the MRS and for RICH in the FS. Additionally for RICH, contamination of protons and antiprotons occurs in the region where RICH ring radius R=0 (in the region 10<p<16 GeV/c, above kaon threshold and below proton threshold).

The particle separation in the TFW2 is better than in the TOFW, due to longer flight path. With the 2σ separation in the TFW2, kaon and pion separation is achieved up to 2.4 GeV/c. Pion identification may be extended to slightly higher momenta (3 GeV/c in this analysis), because the K/π ratio is below 1 (0.2-0.3). Above the separation K/π momentum, the m^2 distribution is sliced in narrow momentum intervals (0.2 GeV/c) and the pion contamination due to kaon are extracted via double gauss fits. Figure 4.15 shows the quality of extraction these numbers at 90^0. Pion identification is extended up to 3 GeV/c with 2σ separation in the TFW2. Pion contamination at 3 GeV/c is about 10-15%. Kaon identification can be extended only up to 2.6 GeV/c. Above this limit the contamination grows fast. In the K/π overlap region, pion and kaon identification are done statistically, assuming the same K/π ratio as outside the overlap area.

The same method is applied for K/π identification with RICH (Figure 4.14), above the separation momentum. For low p and $\bar{p}$ momenta (the indirect RICH identification), p and $\bar{p}$ contamination from pions and kaons was estimated to be constant, 3% [35]. The correction is larger for antiprotons, due to smaller number of $\bar{p}$ then p. For the region with positive RICH radius identification, the RICH efficiency is constant, 97% for all the data.

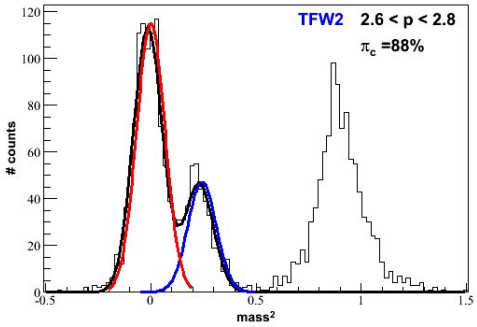

Figure 4.15: Pion and kaon $mass^2$ overlap above the K/π separation momentum, in the TFW2. Simultaneous double gauss fit is shown with black line, and the associated single gauss functions are shown with colored lines. For 2.6< p <2.8 GeV/c, estimated pion contamination is 12%.

4.5 Efficiencies

There are several corrections which directly affect our measurements. Most of them are related to the efficiency of the detectors - tracking efficiencies, pid efficiency, trigger efficiency. Other corrections are made in order to take into account effects related to interaction with the matter. In general, charged particles lose energy in the process of interaction with the detector, but there are also effects from other secondary reactions, like particle decays before reaching the detector, i.e. the time of flight detector. These are genericaly called "GEANT" corrections: decays, interaction with the beam pipe and gas - absorption, multiple scattering on the medium. Doing PID require the choose of 2 σ or 3 σ separation, which means that we ignore a certain percent of PIDs. Therefore, the results are corrected by 1% when using 3σ, and by 5% in the case of 2σ. The last correction relates to the finite solid angle covered by the spectrometers. In order to extract invariant yields we have to extrapolate the results to 2π coverage on the azimuthal angle. This is purely a geometrical correction.

4.5.1 Tracking efficiency

Tracking efficiencies have been evaluated using two different methods, the track embedding method and the reference track method.

Track embedding method. Simulated tracks with well known characteristics are embedded into real raw data, at the level of TPC clusters. Successful reconstruction of the fake track following normal data reduction is studied as a function of the number of hits in the TPC. The fake track has been found when there was more than 60% overlap with the cylinder built around a final track. The efficiency has been studied by changing the initial conditions - momentum, track angle, mass of the particle. More details can be found in [169]. The primary dependence was found on the occupancy of the TPC, i.e. the number/density of hits. The efficiency has an almost linear dependence and increases as the number of hits decreases. It shows slight dependency with particles' type and with the polar angle in the MRS. Therefore, in the case of AuAu collisions we use average efficiency curves shown in the Figure 4.16. This efficiency is applied independent of the event centrality. However, since the the number of hits is directly proportional with the event centrality (in the first approximation), the applied efficiency is still correlated with the centrality. Figure 4.17 shows the event centrality versus the number of hits in the MRS. The method could be extended in order to estimate TOF detector efficiency. Then an overall track efficiency could be used.

For the TPC in the FFS the efficiency is changing rapidly with the angle θ, because the track density changes rapidly, decreasing from smaller to larger spectrometer angles. Therefore, it's not possible to extract average efficiencies.

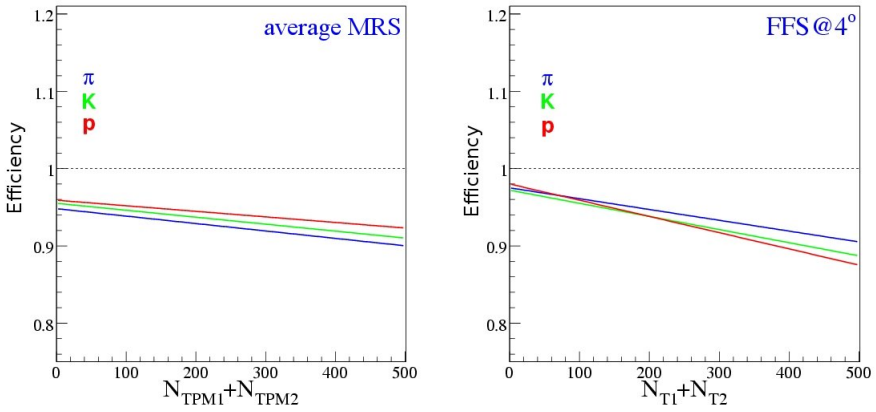

Figure 4.16: MRS tracking efficiency as a function of the number of hits in TPM1 and TPM2 (left) and FS tracking efficiency as a function of the number of hits in T1 and T2 (right), calculated using the track embedding method.

Reference track method. This method determines the efficiency of one tracking detector with respect to reference tracks obtained in other detectors, except the one under study. Using experimental data to extract the efficiency is the primary advantage of this method. The tracking efficiency is defined as:

$$Eff_{tracking} = \frac{N_{local}}{N_{reference}} \tag{4.16}$$

where $N_{reference}$ is the total number of reference tracks and N_{local} is the total number of local tracks found to match a reference track. By definition, $Eff_{tracking} < 1$ since $N_{local} < N_{reference}$. This method has been applied for the FS, where there are five tracking detectors. There are four different detectors left to define the reference track.

One reference track built from detectors standing forward and backward of the detector studied should have a matching local track. The comparison takes place in slope and projection on the horizontal plane, within a certain σ. The deviations of local tracks to the reference tracks for T1-T2, T2-T4, T3-T4 and T4-T5 have to be within 6σ, 4σ, 4σ and 4σ, respectively. The parameters have been chosen large enough, to avoid efficiency underestimations, but still narrow enough to reject the background combinations. The background combinations increase as we move forward with the FS. Tracks passing too close to the edges of the magnet are disregarded, because of the field nonlinearities.

Applying the efficiency resumes to simple multiplication of individual efficiencies, in the first approximation:

$$Eff_{FFS} = Eff_{T1} \cdot Eff_{T2} \tag{4.17}$$

$$Eff_{FS} = Eff_{T1} \cdot Eff_{T2} \cdot Eff_{T3} \cdot Eff_{T4} \cdot Eff_{T5} \tag{4.18}$$

The complications arise for T3 and T5 efficiencies. Being the first drift chambers, T3 operates in a large background, and this has lower efficiency. Despite the efforts to shield it from the beam pipe, the number of reconstructable local tracks in T3 is rather low. The global tracking algorithm is able to generate global tracks even without a matching T3 track (the so-called T3 enhancement), if there is an FFS track matching the one from T4-D4-T5. T5 is used in the enhancement mode similar to T3, in order to maximize the efficiency of finding rings in RICH.

Therefore, the efficiency estimations for T3 and T5 must take into account the correlation of measurements from the other detectors. The overall efficiency has been found as:

$$Eff_{FS} = Eff_{FS-T2} + Eff_{FS-Org} \tag{4.19}$$

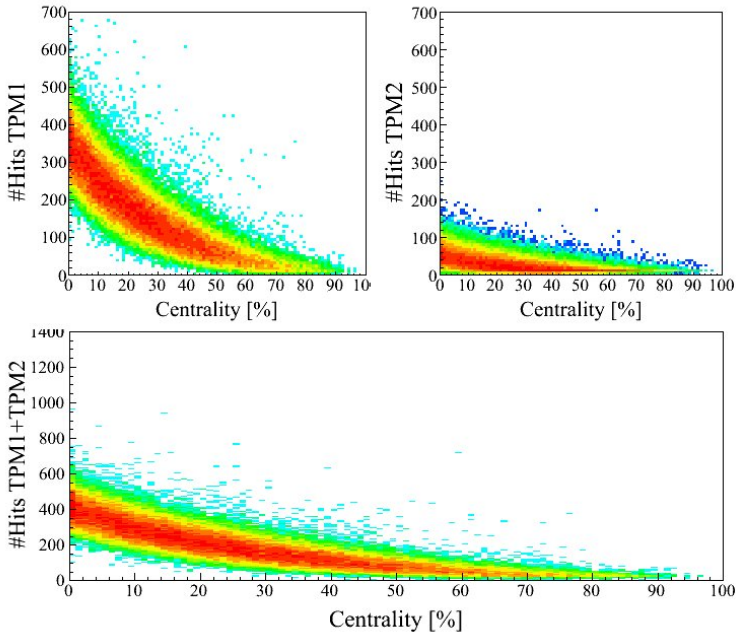

Figure 4.17: Number of hits in TPM1 and in TPM2 (upper panel) and the sum of them $N_{TPM1} + N_{TPM2}$ (lower panel) as a function of collisions centrality.

$$Eff_{FS-T2} = Eff_{T1} \cdot (Eff_{T2} \cdot (1 - Eff_{T3}) \cdot Eff_{T4} \cdot Eff_{T5}$$

$$Eff_{FS-Org} = Eff_{T1} \cdot Eff_{T2} \cdot Eff_{T3} \cdot Eff_{T4} \cdot Eff_{T5}$$

where $FS - T2$ denotes the fact that T2 track has been used to build the local track in T3 and $FS - Org$ for the case that a T3 local track existed. More details about efficiency calculations may be found in [170].

Different tracking efficiency dependencies have been studied - versus momentum, x, y positions, a_x, a_y slopes, centrality. Figure 4.18 shows FFS efficiency and full FS efficiency versus momentum, for different angles. For the FFS, in the most central 0-10% AuAu collisions, the tracking efficiency decreases with decreasing angle, from 95% at 12^o to 80% at 2.3^o, whereas for the pp collisions levels up at 98% for all angles. Full FS efficiency range from 85% at 10^o to 65% for the most forward angle. FS efficiency for pp is almost constant, ∼90% for all the angles. This reflects the dependence of the DC efficiency on the number of hits. As the spectrometer moves toward smaller angle, the detectors subtend a larger solid angle.

The main dependence was found on the centrality (and therefore on the number of hits) for AuAu system, the same as in the MRS case. The tracking efficiency is applied for each track from 2 dimensional histograms, in centrality and x position for the AuAu system, and x-slope and x-position for pp system.

Recently, the reference track method was applied in the MRS case, to estimate the MRS tracking efficiency for the pp collisions. Reference tracks for the TPCs could be built using vertex position and the hits from TOFW and TFW2. The efficiency is estimated as the ratio of rough matches between TOFW hits and TFW2 hits, from events with single hits in both TOF detectors. Figure 4.19 shows the result of this analysis. TPM1 and TPM2 efficiencies are constant with x position.

Constant efficiency of 90% has been used for the pp MRS analysis. It is difficult to use this method for the AuAu collisions because there are larger track densities and more than single hits in the TOF detectors. The reference track set might be overestimated, leading to low efficiency.

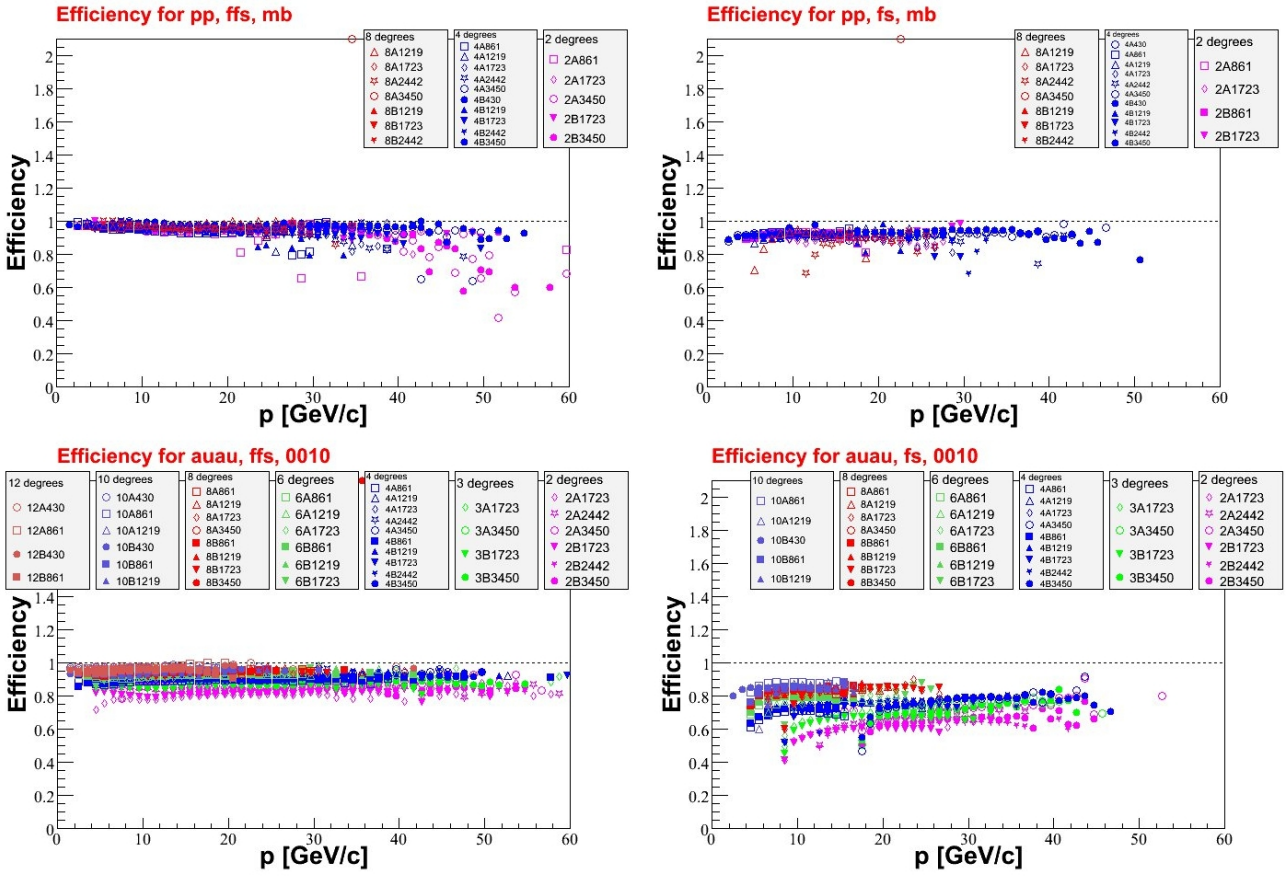

Figure 4.18: Tracking efficiency as a function of momentum, for the FFS (left panels) and full FS (right panels). Upper row shows the efficiency used for the pp system, for different angles and magnetic fields, as specified in the legends. Bottom row shows the efficiency extracted for AuAu most central 0-10% collisions, for all the data used in the analysis.

4.5.2 PID efficiency

TOF efficiency. PID efficiency in the case of TOF detectors depends only on the detector geometry. The slats in the TOFW are grouped in 4 panels. Such setup determines edge effects, i.e. traversing particles may deposit only small amounts of energy when only grazing the scintilators. It may happen that one particle miss completely a hit in TOF, passing through the space between the slats.

TOF efficiency decreases when the same hit matches 2 different tracks, i.e. multiple hits. Hit slat distributions change with different value of the magnetic field. Outer slats have in general fewer hits and its difficult to estimate their efficiency.

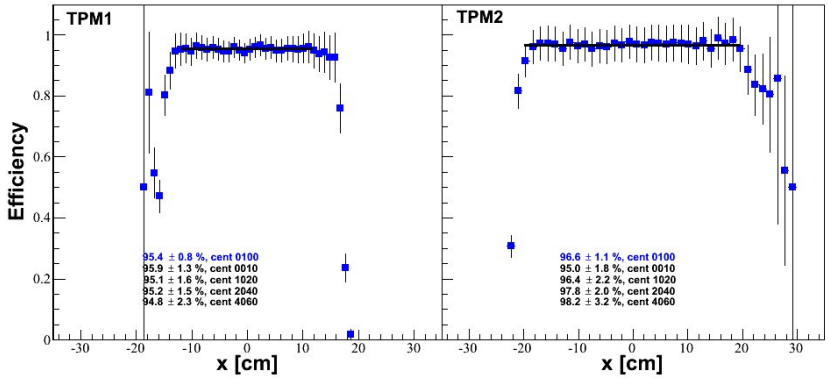

Figure 4.19: TPM1 and TPM2 tracking efficiencies as a function of local position in the TPCs, estimated with the reference track method, for the most central 0-10% events. The inserts list the numbers found for other centrality classes.

PID efficiency is calculated as the ratio between the number of valid hits recorded and the the number of projected tracks. It is studied as a function of the slat number. Figure 4.20 shows the efficiency, for two different angles in the MRS. Apart from the hits missed because of dead slats in TOF, the slat efficiency fluctuations are related to the statistics. Therefore, in this analysis the TOF efficiency is considered constant regardless the angle θ, 98%.

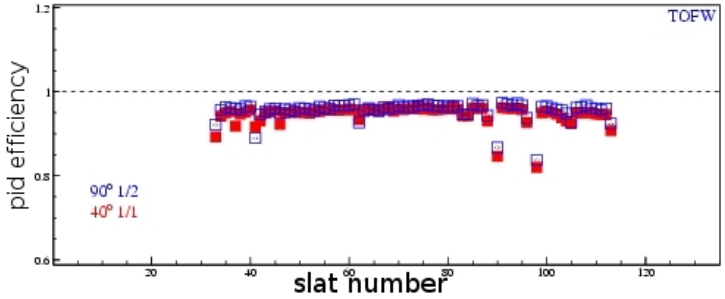

Figure 4.20: TOFW PID efficiency as a function of the slat number in the TOFW. Red symbols are used for MRS at 40^o and blue symbols for MRS at 90^o.

4.5.3 Corrections for secondary reactions

Particles passing through the spectrometers have interactions with the material (beam pipe, detectors, air) and lose energy. There are small changes in momentum and angle due to multiple scattering. Protons and anti-protons have large absorption cross-sections. Absorption processes occur also in the case of pion and kaons, at smaller level, yet still important to consider. Pions and kaons may decay prior to the detector that makes particle identification.

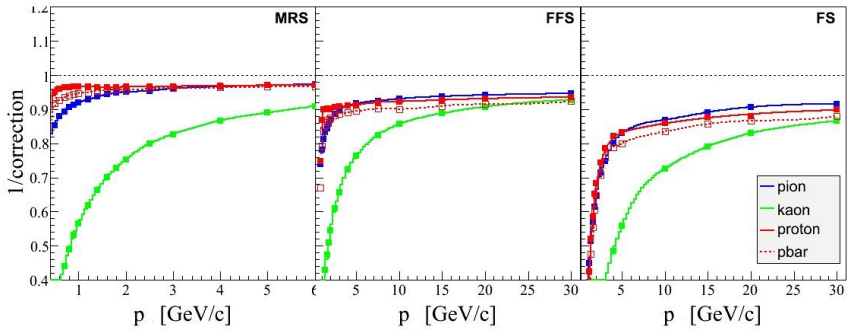

Figure 4.21: Decay, absorption and multiple scatterings corrections applied for pions, kaons and protons as a function of momentum in the MRS, FFS and FS.

The effects contribute to throwing good particles out of the acceptance and some other fraction of bad particles, which would be ignored otherwise, are considered in the final result.

All these procceses have to be taken into account and the results have to be corrected for them.

Full GEANT simulations are performed and the resulting particles are digitized and analyzed with the same tools used for real data. For each of the particles under study, a discrete set of same momentum particles are generated with GEANT. Then the momentum is scaled depending on the real magnetic field, in such a way that particles pass through the spectrometer in the middle of the acceptance, making sure there are no other effects like edges of magnets, acceptance effects, other non-linearities. The final ratio between the number of good reconstructed particles and the number of particles passing wide cuts is taken as the correction for the momentum considered.

This way, the correction is calculated separately from tracking efficiency and pid efficiency. In GEANT, the energy loss, decays, hadronic interactions and multiple scatterings are turned on. The main reason is related to the fact that the processes do not factorize. In general, the main effects on pions and kaons are from decays, whereas absorption for protons and anti-protons is important. The maximum effect for all particles has been found for low momentum.

Different cuts are studied in order to remove bad reconstructed tracks. Optimal cuts are selected and used for the analysis of the real data. The corrections are extracted per particle and per spectrometer angle. The most efficient methods to remove bad reconstructed tracks were identifed: target cut in the MRS, FFS and FS, plus the momentum dependent χ^2 cut in the FS and MRS (in the MRS, the χ^2 selection was found also to be PID dependent). Figure 4.21 shows the final corrections applied. The feed-down correction for protons and antiprotons was not considered for this analysis.

Charged hadrons. From the corrections above, one can estimate the correction on non-identified charged hadrons. The mixing of particles has to be estimated. This is done by counting each identified particle in small momentum intervals, for the pseudorapidity considered. The left panel in Figure 4.22 shows π, K and p in percents, as they enter into the yields for not-identified charged hadrons.

4.5.4 Trigger efficiencies

The results of the analysis are corrected for minimum bias and spectrometer trigger efficiency. The correction is significant for the pp collisions. For the 200 GeV pp collisions it was estimated from Pythia simulations that the CC counters measure only 70% of the inelastic cross-section (assuming $\sigma^{pp}_{inel} = 42$ mb). The probability that the event has a CC vertex associated with the track is 80%. Therefore, the overall correction factor is 0.87, reducing the measured yields.

For the AuAu collisions, the minimum bias trigger covers 93.6% of the total inelastic cross-section, and the spectrometer trigger is 100% efficient. The final AuAu results should be scaled downwards with this number. However, the correction to AuAu results is not applied for the analysis.

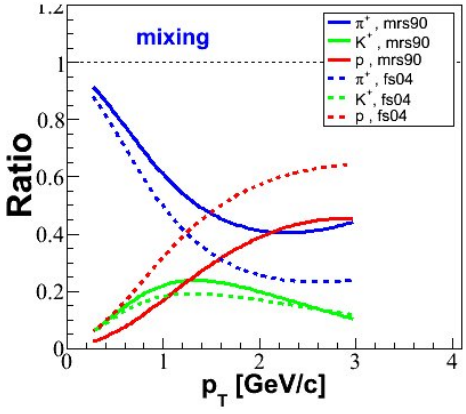

Figure 4.22: Ratios of positive particles with respect to the total number of positive charged particles, as functions of momentum, for the MRS at 90^o (full lines) and FS at 4^o (dashed lines). Blue lines are π^+ ratio, green for K^+ and red lines for protons.

4.6 Acceptance maps

Acceptance correction is done in order to remove the effect of finite solid angle of the spectrometers. It is a geometrical correction obtained by throwing a flat distribution of particles in p, θ and ϕ. Particles are tracked through the spectrometers, checking the detector geometry, magnetic field and fiducial cut through magnets. If the particle is able to be reconstructed by the final PID detector, the corresponding accepted (y, p_T) or (η, p_T) cell is filled. Finally, the accepted map is divided by the thrown particles' map:

$$ACC\,(y, p_T) = \frac{Accepted\,(y, p_T)}{Thrown\,(y, p_T)} \times \frac{\Delta\Phi}{2\pi} \tag{4.20}$$

The factor $\Delta\Phi/2\pi$ reflects the fact that particles cover only a fraction $\Delta\Phi$ of the full range 2π, due to the aperture of the spectrometer. θ and Φ ranges change depending on the vertex position, therefore the acceptance maps are generated in 5 cm steps in the vertex range used for the analysis ($\pm$15 cm for MRS and $\pm$20 cm for FS). The correction applied to the data is $1/ACC$.

The edges of the acceptance maps show large fluctuations, therefore they are removed. The (y, p_T) bins with content smaller than 50% of the average map value are removed.

Acceptance maps generated this way were also compared with a full GEANT simulation and they were found in agreement. Since the maps do not contain information about energy loss of particles, low momentum cut relies on the secondary reaction curves. For the FS analysis, it has been checked that tracking efficiency decreasing with the x position in the detector match the generated acceptance maps.

For the case when TOF detectors are used for PID (TOFW, TFW2 in the MRS), dead slats are also checked when generating the maps. Dead slats are showing in the acceptance maps as stripes with low acceptance.

Figure 4.23 shows the overlapping between the acceptance maps and the real data, before and after edges cut and Δy cut.

4.7 Making spectra

BRAHMS has developed two distinct methods to build the differential spectra, in the form $1/2\pi p_t d^2N/dydp_t$. The spectrum is expressed as:

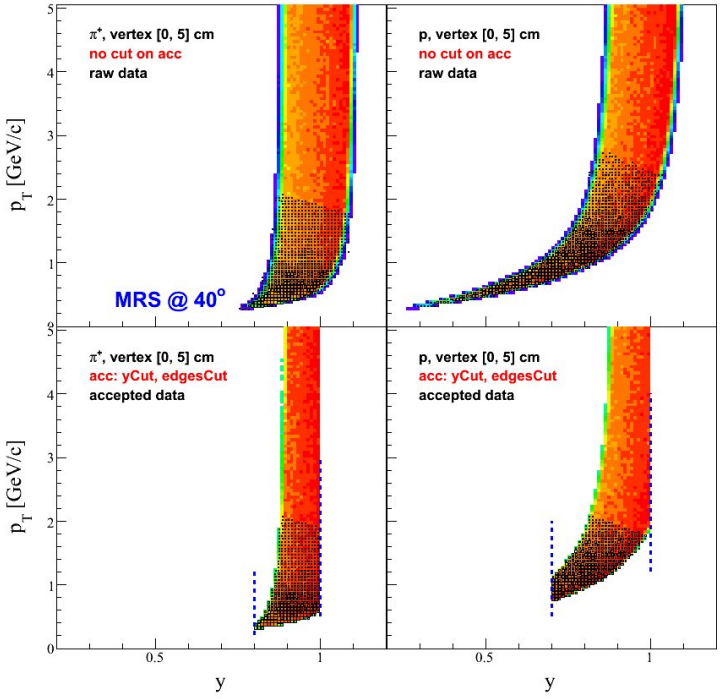

Figure 4.23: Acceptance and data overlap for [0, 5] cm vertex bin in the MRS at 40^o. Upper row shows raw acceptance maps (colored symbols) and raw scaled data (black boxes). Bottom row shows the acceptance maps after edges cut and δy cuts, together with the accepted data. Pion are shown in the left panels, and protons on the right side.

$$Spectrum(y, p_T) = \left(\sum_s Data(y, p_T) \right) \times \sum_s \left(\frac{1}{Correction(y, p_T)} \right)^{-1} \tag{4.21}$$

First method uses 2-dimensional representations of both data and corrections, in (y, p_T) [35]. The second method calculates the weight associated to each particle contribution to the final p_T bin [171]. Both methods have been used for this analysis, and the agreement found was inside few percents, once the event/track selections are the same. Figure 4.24 shows the comparison of the spectra obtained with the two methods.

Maximum likelyhood method The input to the yield calculation are histograms for (y, p_T) containing separately the counts and the corrections. The correction histogram includes tracking efficiency, correction for decays, multiple scatterings and absorption, the acceptance correction and the event normalization. There is an array of histograms for each of the vertex bins, and each of the settings. When different settings or different vertex bins overlap in a certain (y, p_T) cell, counts are added and proper weights are found from the correction histograms.

Therefore, the yields can be expressed as:

$$Spectrum(y, p_T) = \left(\sum_s Data(y, p_T; s) \right) \times \sum_s \left(\frac{1}{Correction(y, p_T; s)} \right)^{-1} \tag{4.22}$$

where the index s means either a certain vertex bin, or a different setting. Taking weights as $1/Correction$ gives the factorization of equation 4.21 into the final form 4.22. The p_T spectrum is constructed for narrow intervals in rapidity Δy by projection on the p_T axis.

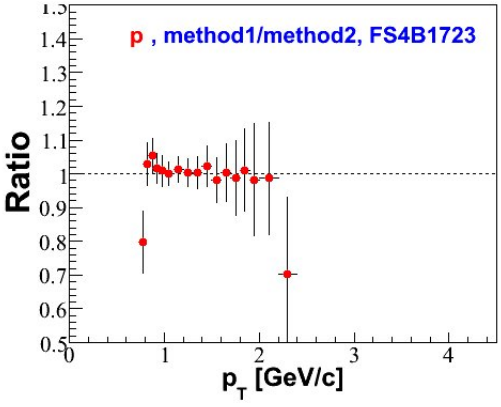

Figure 4.24: The ratio of the two methods used at BRAHMS to make the spectrum (setting 4B1723 is used).

Track by track method The sum in the equation 4.21 is taken over each of the tracks falling into the p_T bin range and Δy rapidity interval. The final spectrum is calculated as simple average over the vertex bins and different settings.

Table 4.4 summarizes the event selection used for the analysis.

Cut	$Au + Au$ (200 GeV)	$p + p$ (200 GeV)
Vtx (MRS/FS)	$< \pm 15$ cm/20 cm	$< \pm 30$ cm[a]
Track Trigger	MRS FFS FS	[b] MRS FFS FS
MB Trigger	ZDC(4)	CC(5)
Centrality (%)	0–10,10–20,20–40,40–60	MB[b]

Table 4.4: Event selection.

a. Due to the wider vertex distributions, larger vertex range has to be selected in order to increase track statistics.

b. The efficiency of minimum bias and spectrometer triggers lead to overestimation of the results. An 87.5% correction is applied to all pp results, independent of the p_T.

Track selection used for the present analysis:

- **Target cut** Tracks are required to project within 4σ elliptic cut in the zy plane in the MRS and xy plane in the FS, both for pp and AuAu.
- **Magnet cuts** For the MRS, fiducial distance in D5 $FidX > 1$cm on x, and $FidY > 0$cm on y directions. For the FFS and FS analysis, D1 fiducial cut on x $FidX > 1$cm and $FidY > 0$cm, $FidX > 0$cm and $FidY > 0$cm for all the other magnets. Additionally, swim status through D1 has to be 1.
- **Volume fiducial cuts** are set to volume sizes for all the tracking devices. For AuAu collisions, due to bad regions on the back of TPM2, there is a cut on the back plane of TPM2, at [-18, 23] cm on x direction. Last volume for each of the spectrometers sets up the final fiducial cut. Pointed slat in TOFW [32, 113] or [3, 38] in TFW2 AuAu for MRS. The size of H1 and H2 for

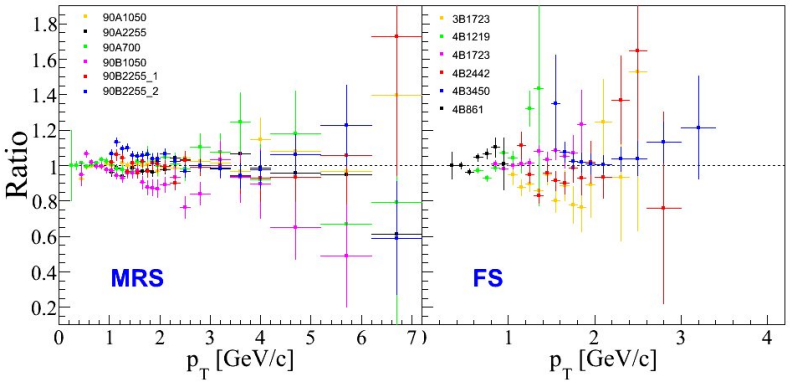

Figure 4.25: The ratios of yields obtained in single settings to the average final yields are shown. Charged hadrons produced in p+p collisions at $\sqrt{s_{NN}}$=200 GeV at midrapidity in the MRS are shown in the left panel and positive pions in Au+Au collisions at $\sqrt{s_{NN}}$=200 at rapidity y∼3 in the right panel.

charged hadrons in the FFS and FS respectively. Identified particles in the FS have to project inside [-20, 20] cm on x, and [-15, 15] cm on y directions. For the pp collisions in the MRS, pointed slat for PID is inside [9, 37] for TFW2. This is due to many bad slats in the TFW2 over the run5 data taking.

- χ^2 **cuts** 10σ in the MRS and 4σ in the FS. In the MRS, this selection is done separately for each type of particles, and therefore it is not applied for charged hadrons analysis.

- **PID cuts** 2σ separation in m^2 versus p for RICH, TOFW and TFW2. $p > 1.1 * p_{threshold}$ is required in RICH, in order to avoid efficiency fluctuations at the momentum thresholds. Accepted tracks in the MRS have matched hit within ±1slat of the pointed slat.

4.7.1 Systematic errors

A study of systematic uncertainties was done for this analysis. Systematic errors arise from various sources, related to the analysis methods and the cuts used. It is important to estimate the impact of systematic errors on a p_T basis (track selection, particle identification), as well as errors which are independent of p_T (vertex selection, centrality measurement, event normalization).

In BRAHMS, sets of data are taken by changing the magnetic field and the spectrometer angle, such that a an important area of the phase-space is covered. The systematic error can be estimated in the regions where different sets overlap and give contributions to the same p_T bin. Such an estimation is limited by the statistics in the high p_T regions. Different magnetic fields have different systematic deviations. Systematic errors are due to different momentum resolution and track angle resolution, acting on momentum measurement, time resolution and multiple scattering effect, acting on mass measurement and PID related cuts. The ratio of each individual setting spectrum to the final p_T spectrum gives an overall estimation of the systematic errors.

Figure 4.25 shows typical results from this analysis, for charged hadrons produced in p+p collisions at $\sqrt{s_{NN}}$=200 GeV at midrapidity in the MRS (left panel) and for positive pions in Au+Au collisions at $\sqrt{s_{NN}}$=200 at rapidity y∼3 (right panel). As seen from the figure, in the low p_T region, the systematic errors in the MRS are consistent with 10% deviations and 15% deviations for the FS. Similar deviations are observed in the high p_T regions, limited though by the statistics.

Another way to estimate systematic uncertainties on the p_T distribution is to generate various sets of p_T spectra where the cut parameters, including the event and track vertex windows, acceptance cuts and Δy ranges, are slightly changed from those used in the analysis. The absolutely normalized

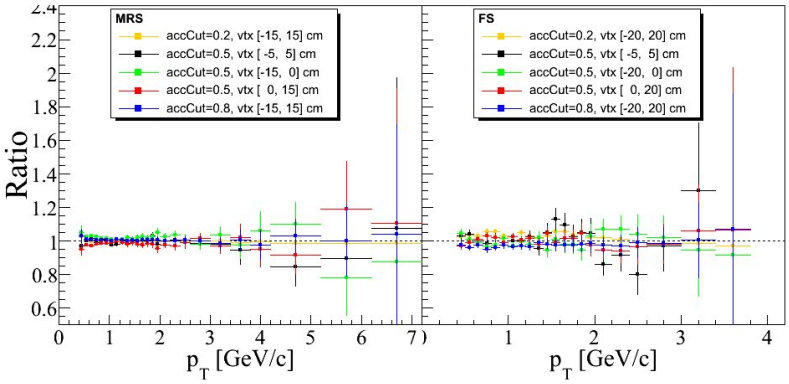

Figure 4.26: Ratios between the yields obtained with different analysis cuts and the final yields obtained with standard cuts (vertex [-15, 15] cm and acceptance cut = 0.5). Charged hadrons produced in p+p collisions at $\sqrt{s_{NN}}$=200 GeV at midrapidity in the MRS are shown in the left panel and positive pions in Au+Au collisions at $\sqrt{s_{NN}}$=200 at rapidity y∼3 in the right panel.

spectra with different cut conditions are divided by the spectra with the standard cut conditions, resulting in uncertainties associated with each cut condition.

Figure 4.26 shows the ratios between the spectra obtained with different analysis cuts and the final spectrum obtained with standard cuts (vertex [-15, 15] cm and acceptance cut = 0.5). The left panel shows the analysis in the MRS for charged hadrons produced in 200 GeV Au+Au collisions, whereas the right panel shows the positive pion spectra in the FS (the same data as for the previous figure). The associated systematic errors are consistent with 5% in the MRS and 10% in the FS.

PID cuts were tested by comparing 2σ and 3σ cuts in both TOFW and TFW2, for the MRS, and in RICH, for the FS. Ratios between the spectrum, generated using separate acceptance maps and PID efficiency, are found consistent within a few percents of the theoretical values. The systematic error associated with triggers, tracking efficiency calculation and GEANT corrections were estimated by comparison of FFS and FS spectrum. Systematic differences less than 10% were revealed by such an analysis.

The systematic error from the acceptance maps is 2-5% (including the edge effects). Systematic uncertainty from the tracking efficiency is estimated at 3-5%. Geant corrections add 2-6% to the systematic errors. However, the separate systematic errors may be correlated such that the final conservative estimation of the systematic error acting on the spectra is 10-15% in the MRS and 15-20% in the FS.

In the nuclear modification factor and central-to-peripheral ratio, one separate systematic error comes from the error in N_{bin} estimation. This error it is shown as a shaded box around unity in the R_{AA} and R_{CP} distributions. The systematic error associated with the p_T spectra are added in quadrature and shown for each p_T bin as boxes.

Chapter 5

Results

In this chapter we present the results obtained from run04 Au+Au collisions and run05 p+p collisions at $\sqrt{s_{NN}}$=200 GeV. The transverse momentum spectra for charged hadrons as well as for identified particles at different event centralities (minimum bias spectra for p+p) in narrow rapidity ranges ($\pm$ 0.1), from midrapidity to high rapidities (up to 3.8) are presented. Nuclear modification factor R_{AA} and central-to-peripheral ratio R_{CP} are shown and discussed. The results are compared with predictions of several of the theoretical models described in section 2.3.

5.1 Charged Hadrons

5.1.1 Transverse momentum spectra

For the Au+Au data at $\sqrt{s_{NN}}$=200 GeV which are presented in this analysis, the midrapidity spectrometer was positioned at 90^0, 45^0 and 40^0 relative to the beam axis, and measured charged particles in the pseudorapidity[1] ranges of [-0.2, 0.2] and [0.7, 1.2] respectively.

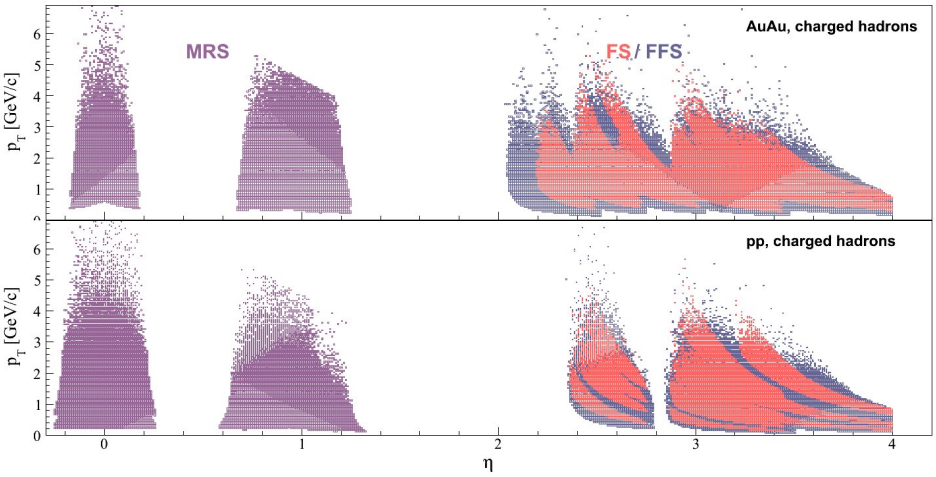

Figure 5.1: Charged hadrons from MRS, FFS and FS used in this analysis in the (η, p_T) phase-space. Top panel is for Au+Au collisions and bottom panel is for p+p collisions at $\sqrt{s_{NN}}$=200 GeV.

The forward spectrometer (FS) was placed at six different angles, from 10^0 down to 2.3^0 relative to the beam axis, corresponding to the rapidity range of [2.0, 4.0]. The phase space coverage of the FS data used in this analysis is shown in Figure 5.1.

[1]Pseudorapidity is $\eta = -ln(tan(\theta/2))$, where η is the angle of emission relative to the beam direction.

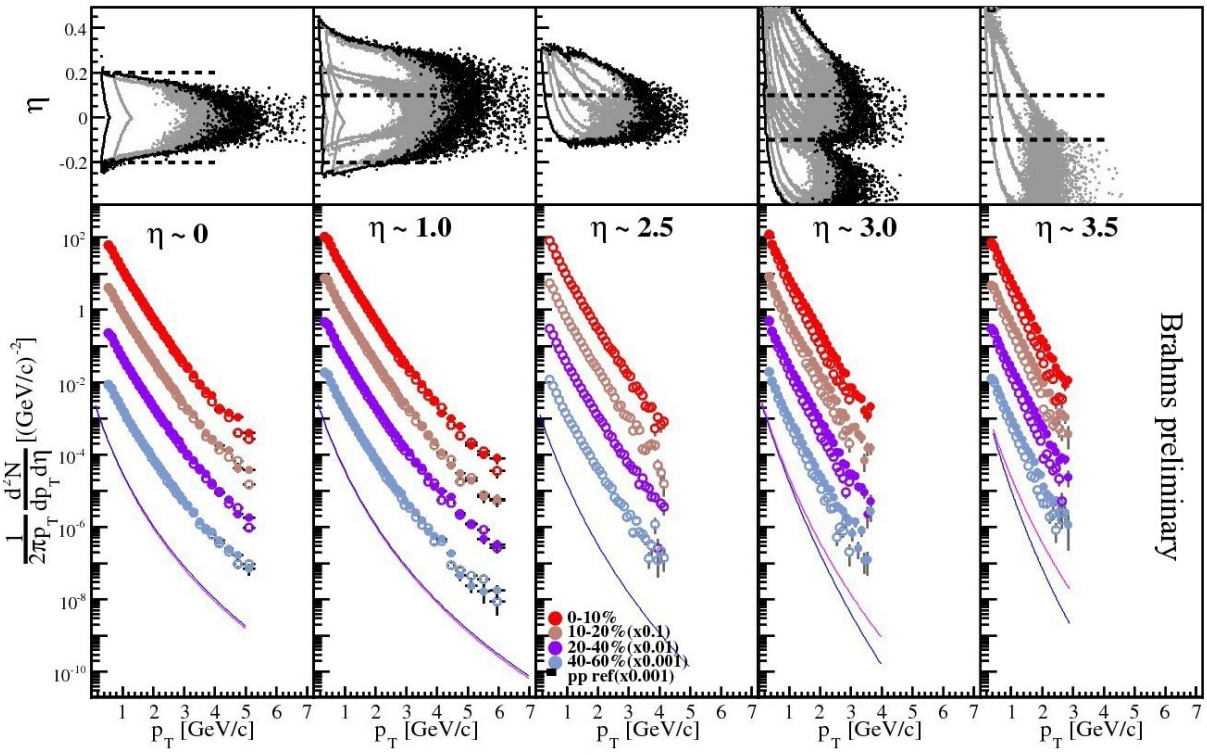

Figure 5.2: Top row: Population of data in $\eta - \langle\eta\rangle$ vs. p_T for each setting. Bottom row: Invariant p_T spectra for charged hadrons produced in Au+Au collisions at $\sqrt{s_{NN}}$ = 200 GeV at η = 0, 1.0, 2.5, 3.0 and 3.5. The p+p reference spectra used to make the R_{AA} are shown with lines. For clarity, non-central spectra have been scaled with the indicated factors. The errors shown are statistical.

Figure 5.2 shows the invariant transverse momentum p_T spectra for unidentified charged hadrons produced in Au+Au and p+p collisions at $\sqrt{s_{NN}}$ = 200 GeV in five narrow pseudorapidity ranges around η= 0, 1.0, 2.5 3.0 and 3.5. The Au+Au spectra are for collision centralities of 0-10%, 10-20%, 20-40% and 40-60%. The spectra shown as full lines are from p+p collisions. Each distribution is constructed from measurements at various magnetic fields (mostly high magnetic field chosen in order to increase the statistics at high p_T) in the corresponding acceptance of the spectrometers, as shown in the top panels of Figure 5.2. The spectra have been corrected for the geometrical acceptance of the spectrometers and for tracking efficiencies. The error bars reflect only the statistical uncertainties in the data.

The hadron yields in Au+Au collisions at $\sqrt{s_{NN}}$=200 GeV decrease rapidly with increasing p_T. At high p_T the charged hadron spectra have a power law shape that is characteristic of perturbative QCD hard-scattering processes. At higher pseudorapidities the hadron spectra are steeper than the corresponding spectra for midrapidity. Therefore, narrow rapidity bins are required to reduce the effects of rapidly changing cross sections, in particular at higher p_T.

5.1.2 Nuclear modification factors

The nuclear medium effects on hadron production in Au+Au collisions are measured through comparison to the p+p spectrum scaled by the number of binary nucleon-nucleon collisions using the nuclear modification factor

$$R_{AA}(p_T) = \frac{d^2N_{AA}/dydp_T}{N_{bin}d^2N_{pp}/dydp_T} \tag{5.1}$$

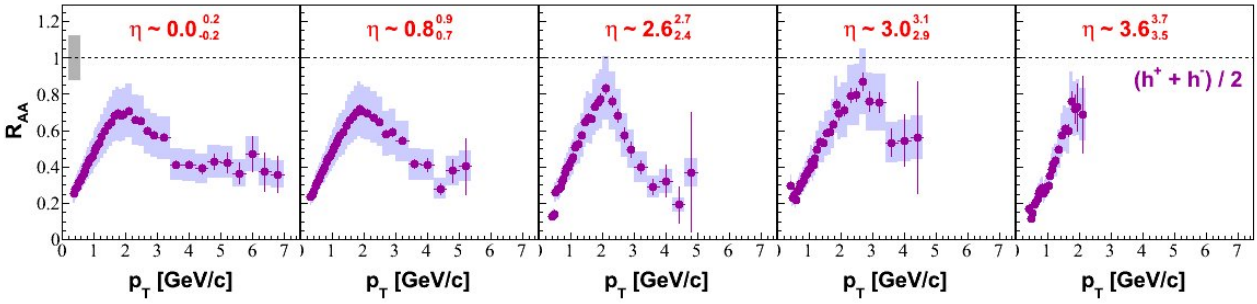

Figure 5.3: Nuclear modification factor R_{AA} at different η for the most central collisions (0-10% centrality). The error bars are statistical; the shaded bands are the systematic errors. The shaded band around unity show the systematic uncertainty in the number of binary collisions.

At low p_T ($p_T < 2$GeV/c), where soft production dominates the measured yields, R_{AA} is less than unity because soft production is expected to scale with the number of participants N_{part}. At high p_T and in the absence of nuclear medium effects, hard processes are expected to scale with the number of binary collisions, N_{bin}, and consequently, $R_{AA} = 1$. The effects of the strongly interacting medium in Au+Au collisions may be measured at high p_T by the deviation of $R_{AA}(p_T)$ from unity. The number of binary collisions, N_{bin} and the number of participants, N_{part} for different collision centralities used in this analysis are presented in the Table 4.1.

The nuclear modification factor R_{AA} as function of p_T for the most central Au+Au collisions at η =0, 0.8, 2.6, 3.0 and 3.6 is shown in Figure 5.3. Because there are no differences between R_{AA} for positive hadrons and for negative hadrons, we present the R_{AA} for $(h^+ + h^-)/2$. The shaded band around unity is the uncertainty on N_{bin}. Error bars are statistical.

The R_{AA} distributions rise from values of 0.2-0.3 at low p_T to a maximum of 0.6-0.8 at p_T=2 GeV/c. As p_T continues to increase above 2 GeV/c, the R_{AA} values decrease showing the suppression of the charged hadron yields relative to the p+p reference. At high p_T (p_T >4 GeV/c), the charged hadron yields are suppressed by a factor of ~ 3 as compared with binary scaled p+p yields.

For all the studied pseudorapidities, the R_{AA} distribution remains systematically lower than unity for central collisions. The R_{AA} shows a slight decrease of the high p_T suppression with respect to p+p collisions, going from midrapidity to forward rapidity.

The centrality dependence of the nuclear modification factors is presented in the Figure 5.4. For semi-peripheral collisions (40-60% centrality), $R_{AA}(p_T)$ saturates around unity at p_T >2 GeV/c for all the pseudorapidities, indicating approximate binary scaling. This could indicate that peripheral Au+Au collisions behave very much like a superposition of many p+p collisions, which implies the absence of any nuclear effects within errors. As one goes to more central collisions, the strong suppression of $R_{AA}(p_T)$ below unity, evidences strong nuclear effects.

To illustrate better the centrality dependence of the suppression we integrate both the Au+Au spectra and the reference p + p cross sections over $p_T > 4$ GeV/c and use these integrated quantities to determine an average suppression factor, R_{AA} for $p_T > 4$ GeV/c. Figure 5.5 shows the charged particle R_{AA} dependence on the number of participants, N_{part}, since the number of participant nucleons is a good indicator of the geometrical volume of the overlap. We see from the figure that the high p_T suppression evolves smoothly with N_{part}.

The R_{AA} values decrease with the number of participants, N_{part}, for all studied pseudorapidities. Charged hadrons show a much lower R_{AA} at high p_T in central than in semi-peripheral Au+Au collisions. In semi-peripheral collisions (40-60% centrality), R_{AA} approaches unity. Thus, the scaling with the number of binary collisions is only seen in peripheral events, while the particle production in central events is strongly suppressed, which points to strong medium effects. For pseudorapidity

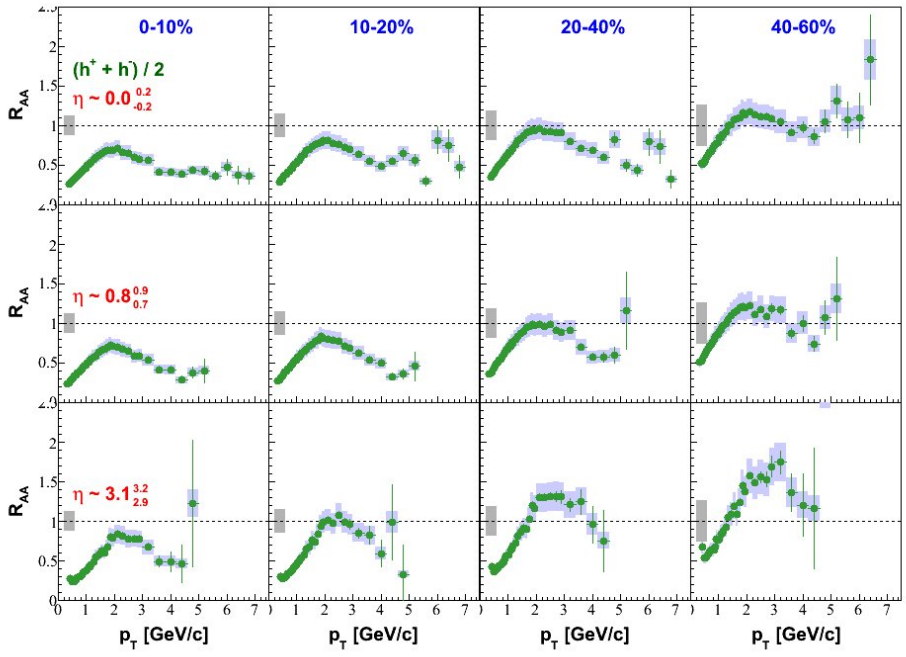

Figure 5.4: R_{AA} for charged hadrons $(h^+ + h^-)/2$ at $\eta = 0$ (top row), 0.8 (middle row) and 3.1 (bottom row) for the four centrality classes indicated. The magnitude of the uncertainty on N_{bin} is indicated with the shaded band around unity. The estimated systematic errors on the data points are indicated by the shaded boxes around the points.

η=3.1, the R_{AA} values are higher than the values at the other pseudorapidities for non-central Au+Au collisions at $\sqrt{s_{NN}}$=200 GeV.

The N_{part} dependence of the nuclear modification factor could be explained as a consequence of medium induced energy loss of partons traversing the hot, dense medium. For the smaller system sizes (peripheral Au+Au data), the path length traversed is smaller (on average) than for the larger system (central Au+Au).

In order to remove the systematic error introduced by the comparison from the measurements of nucleus-nucleus and p+p collisions, we construct the central-to-peripheral ratio R_{CP} defined as

$$R_{CP}(p_T) = \frac{N_{bin}^{peripheral}}{N_{bin}^{central}} \frac{d^2N_{central}/(dydp_T)}{d^2N_{peripheral}/(dydp_T)} \tag{5.2}$$

where $d^2N_{central(peripheral)}/dydp_T$ are the invariant yields in 0-10% (40-60%) Au+Au collisions, respectively. For N_{bin}^{0-10} and N_{bin}^{40-60} we use the values from the table 5.1. Nuclear medium effects are expected to be much stronger in central relative to peripheral collisions, which makes R_{CP} another measure of these effects.

Figure 5.6 shows the central-to-peripheral ratio, R_{CP} as a function of transverse momentum p_T for different pseudorapidities (0, 0.8, 2.6, 3.0, 3.6). The shaded band around unity is the uncertainty on N_{bin}. For p_T > 3 - 4 GeV/c, the R_{CP} values are between 0.3 and 0.4. Thus, in 0-10% most central Au+Au collisions, the charged hadron yields are strongly suppressed as compared to the semi-peripheral Au+Au collisions, when scaled with the number of binary collisions. The R_{CP} shows a roughly constant suppression with respect to semi-peripheral collisions, when goes from midrapidity to forward rapidity.

The pseudorapidity dependence of the high p_T suppression can also be investigate using the ratio $R_\eta = R_{CP}(\eta)/R_{CP}(\eta = 0)$. Most systematic errors arising from the determination of the N_{bin} values

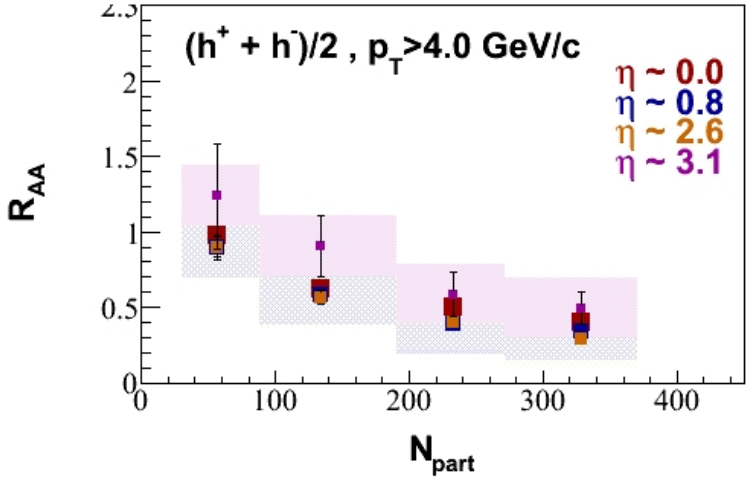

Figure 5.5: R_{AA} ($p_T > 4$ GeV/c) for charged hadrons produced in 200 GeV Au+Au collisions at different pseudorapidities $\eta = 0$, 0.8, 2.6, 3.1 as a function of the number of participants, N_{part}. The estimated systematic errors on the data points are indicated by the shaded boxes around the points.

corresponding to the centrality cuts cancel out in R_η. We observe from the Figure 5.7 that, within errors, R_η is almost constant at high p_T.

The results demonstrate that there is a strong and centrality dependent suppression of the production of high p_T charged hadrons relative to pQCD expectations. This suppression has been interpreted as due to the energy loss of the energetic partons traversing the produced hot and dense medium. The high p_T suppression observed in the most central Au+Au collisions at $\sqrt{s_{NN}}$=200 GeV persists over a wide range in pseudorapidity and it is almost constant for all the studied angles.

The p_T dependence of the R_{AA} is a result of the interplay between the Cronin effect, nuclear shadowing, jet quenching and the softening of the underlying p_T spectrum with increasing rapidity. Surprisingly, these effects build an approximately constant suppression pattern. It is tempting to describe the observed pseudorapidity independence of the R_{AA} and R_{CP} to the presence of a longitudinally extended hot and dense partonic medium; however, the rapidity dependence of the $\bar{p}/\pi^-$ obtained in 200 GeV Au+Au collisions, which will be presented in the next section does not sustain

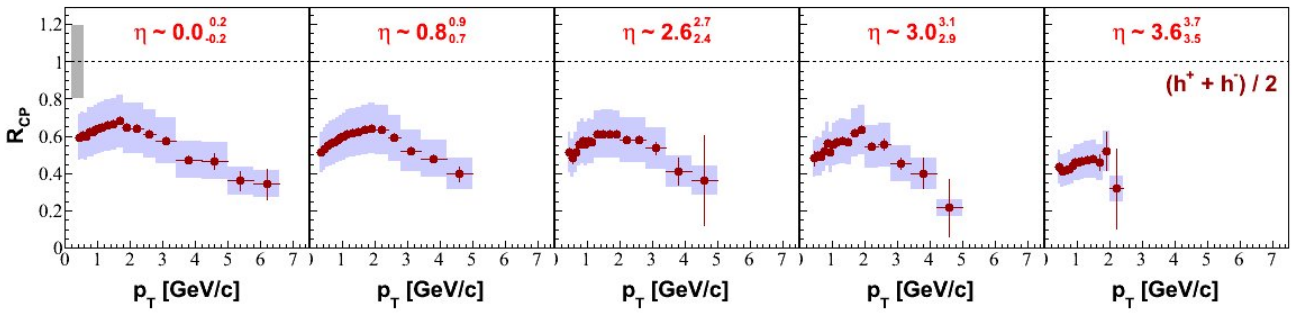

Figure 5.6: R_{CP} for charged hadrons $(h^+ + h^-)/2$ in Au+Au collisions at $\sqrt{s_{NN}}$=200GeV for pseudorapidities η= 0; 0.8; 2.6; 3.0; 3.6 as a function of transverse momentum p_T. The systematic uncertainties are shown as the shaded boxes around the data points. The shaded band around unity show the systematic uncertainty in the number of binary collisions.

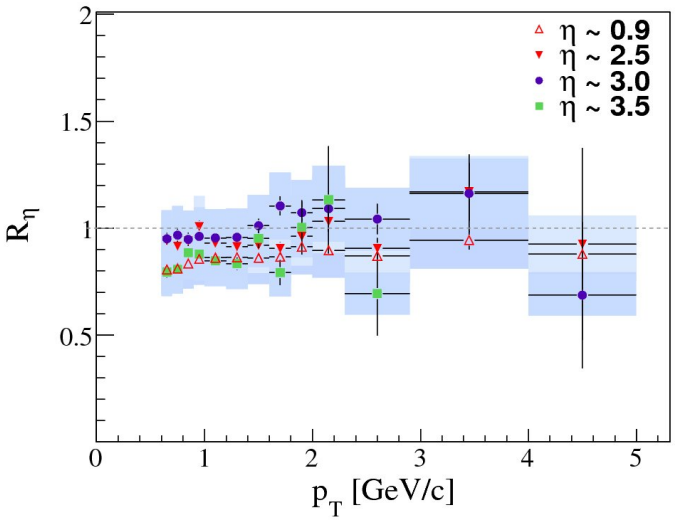

Figure 5.7: Ratio R_η of R_{CP} distributions at different η. Systematic errors are shown by the shaded boxes.

this hypothesis.

5.2 PID

Measurements of identified particle yields in heavy ion collisions at RHIC show distinct patterns of suppression for mesons and baryons at intermediate p_T (2-5 GeV/c). The high p_T suppression is particle type dependent. The intermediate p_T region is very interesting to study because it is known to have contributions from both soft and hard hadron production mechanisms, an interplay between hydrodynamic flow, quark recombination and jet fragmentation.

5.2.1 Identified particle spectra

For the most central Au+Au events at $\sqrt{s_{NN}}$=200 GeV, the invariant transverse momentum spectra of pions, kaons, and (anti)protons are presented next. At low p_T, the spectra are dominated by collision dynamics which include soft collective effects (radial flow) and resonances. High p_T component of the spectra is sensitive to the parton dynamics generated early in the collision (hard processes).

The (y, p_T) phase space coverage of the $\pi^{\pm}$, $K^{\pm}$, p and $\bar{p}$ data used in this analysis is shown in Figure 5.8.

Figure 5.9 shows the transverse momentum spectra of π^+, π^-, K^+, K^-, p and $\bar{p}$ produced in the 10% most central Au+Au (left) and p+p (right) collisions at $\sqrt{s_{NN}}$=200 GeV around five different rapidities y = 0, 0.8, 2.6, 3.1, 3.4.

The spectra are obtained from rapidity windows of width ±0.1 both in the MRS and FS. Narrow rapidity bins are required to reduce the effects of rapidly changing cross sections, in particular at higher p_T. The shape of p_T spectra is similar for particles and antiparticles. The error bars are statistical. For clarity, the particle spectra are scaled by the next factors: 1, 10^{-2}, 10^{-4}, 10^{-6}, 10^{-8}.

The data are corrected for the geometrical acceptance of the spectrometers, tracking efficiencies, PID efficiencies, multiple scattering, decays and absorption in the material along the path of the detected particles. The proton and antiproton spectra are not corrected for Λ and $\bar{\Lambda}$ decays.

The p+p spectra are corrected also for trigger inefficiency. It was estimated, based on events generated with PYTHIA and a GEANT simulation of the BRAHMS setup, that the minimum bias trigger covers 70±5 % of the total inelastic proton-proton cross section of 41 mb. Using the simulations it was estimated the bias introduced by the CC detectors in the spectrometer trigger. The deduced

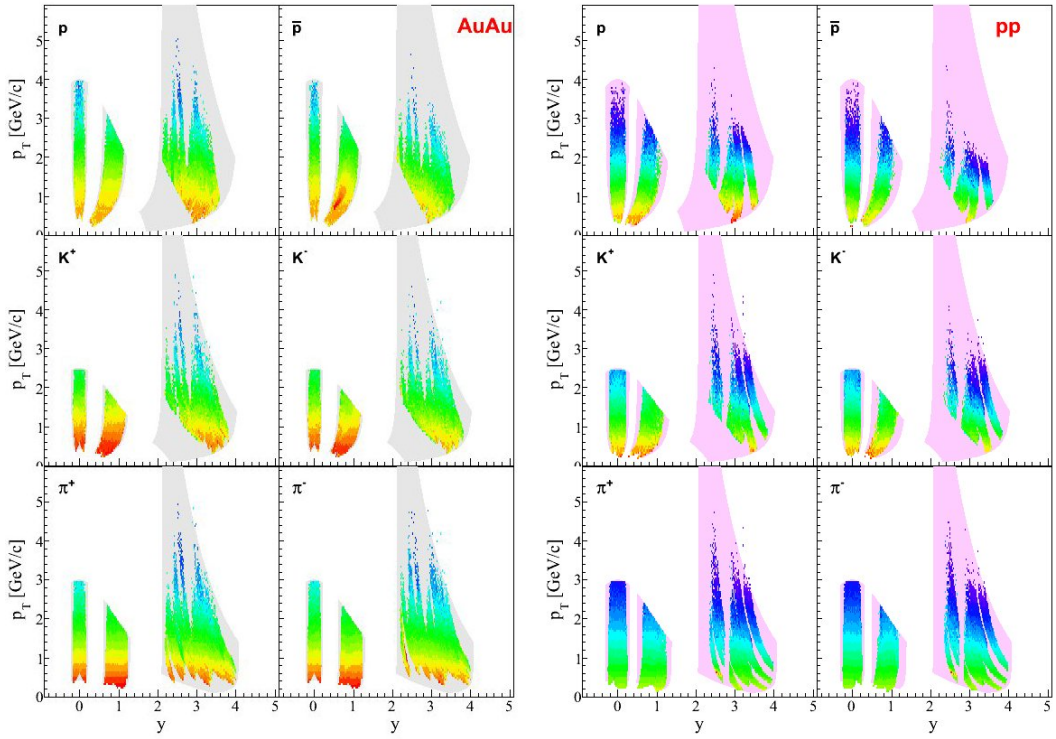

Figure 5.8: The BRAHMS pion, kaons, protons and antiprotons produced in Au+Au (left panels) and p+p collisions (right panels) at $\sqrt{s_{NN}}$=200GeV used in this analysis in the (y, p_T) phase-space. In the MRS the pions were identified with TOFW and TFW2 and in the FS with RICH.

correction is 13±7%, approximately independent of p_T and rapidity, and was applied to all p+p spectra.

The π^+ and π^- transverse momentum spectra shapes are similar for p+p and Au+Au. The K^+, K^-, p and $\bar{p}$ transverse momentum spectra spectra show a progressive flattening from p+p to central Au+Au events. At low p_T, the shape of the transverse momentum spectra is sensitive to the collective radial expansion. As central collisions produce more particles, collective effects are stronger and heavier particles should be boosted to higher transverse momenta. This cause the flattening of the spectra; this effect depends on the particle mass, is stronger when the mass is higher.

At higher p_T, beyond the soft sector, the p_T and centrality dependences of the produced particle spectra develop a systematic difference between mesons and baryons, distinct from the mass-dependence observed at lower p_T. This difference can be studied by the nuclear modification factor R_{AA} and binary-scaled central-to-peripheral ratio R_{CP} of identified particle yields.

5.2.2 Nuclear modification factors

Nuclear modification factors for π^+, π^-, p and $\bar{p}$ produced in Au+Au collisions at $\sqrt{s_{NN}}$=200 GeV for five rapidities y = 0.0, 0.8, 2.6, 3.1, 3.4 are presented in the Figure 5.10. Error bars represent statistical errors. The shaded band around unity indicates the systematic error associated with the uncertainty in the number of binary collisions.

Similar to the unidentified charged hadrons, the pion R_{AA} distributions rise from values of 0.1-0.2 at low p_T to a maximum of 0.4-0.5 at p_T=1.5-2 GeV/c. As p_T continues to increase above 2 GeV/c, the R_{AA} values decrease showing that charged pion yields are suppressed with respect to the expectation from the binary scaled p+p reference. At high p_T, the charged pion yields are suppressed by a factor of $\sim$ 5 as compared with binary scaled p+p pion yields. There are not differences between particles

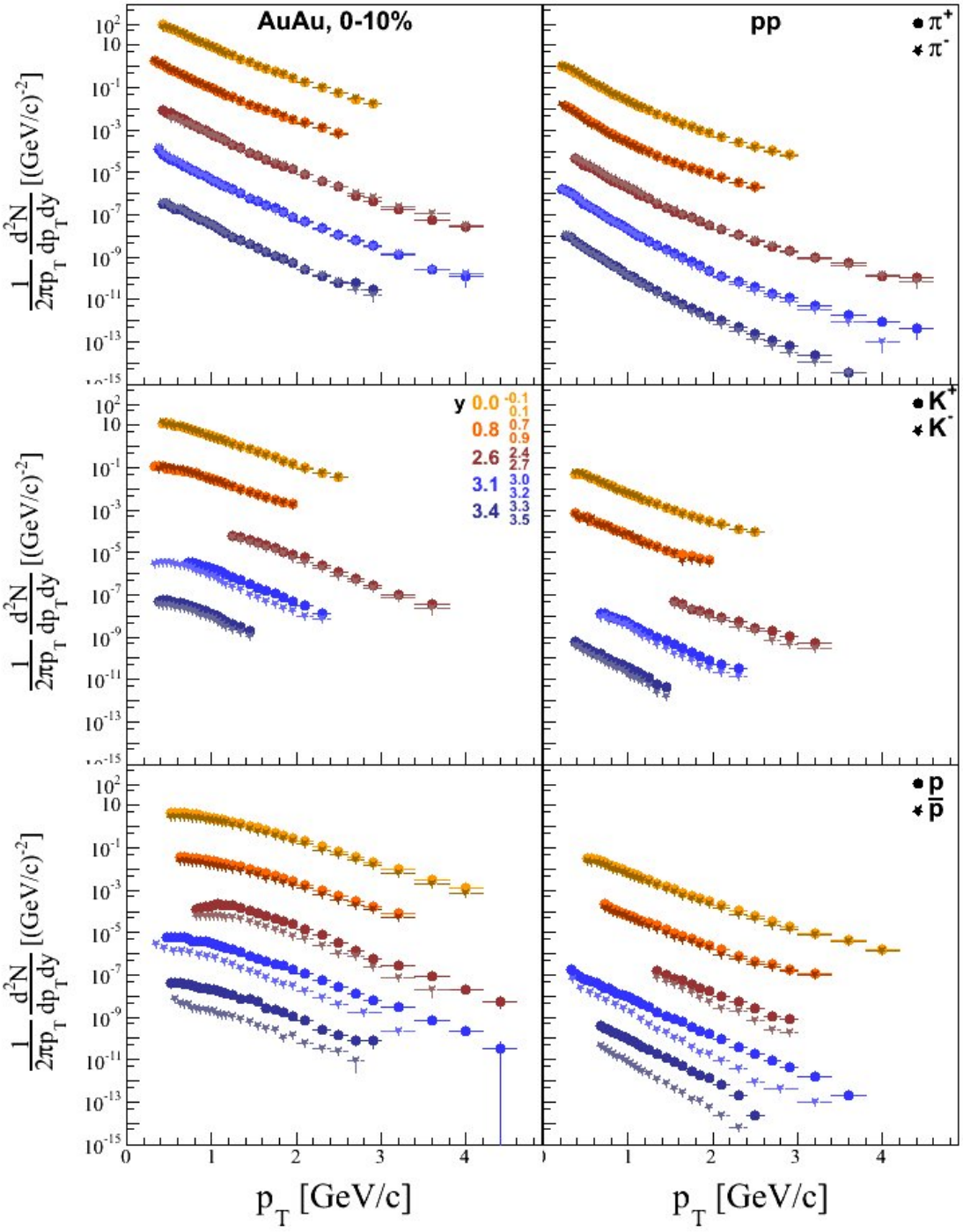

Figure 5.9: Invariant p_T spectra for charged pions (upper panel), charged kaons (middle panel), protons and antiprotons (bottom panel) produced in the 10% most central Au+Au collisions (left panels) and p+p collisions (right panels) at $\sqrt{s_{NN}}$ = 200 GeV for y = 0, 0.8, 2.6, 3.1 and 3.4. For clarity, the PID spectra have been scaled with the factors: 1, 10^{-2}, 10^{-4}, 10^{-6}, 10^{-8}. Circle points represent the particles and star points represent the antiparticles. Errors are statistical.

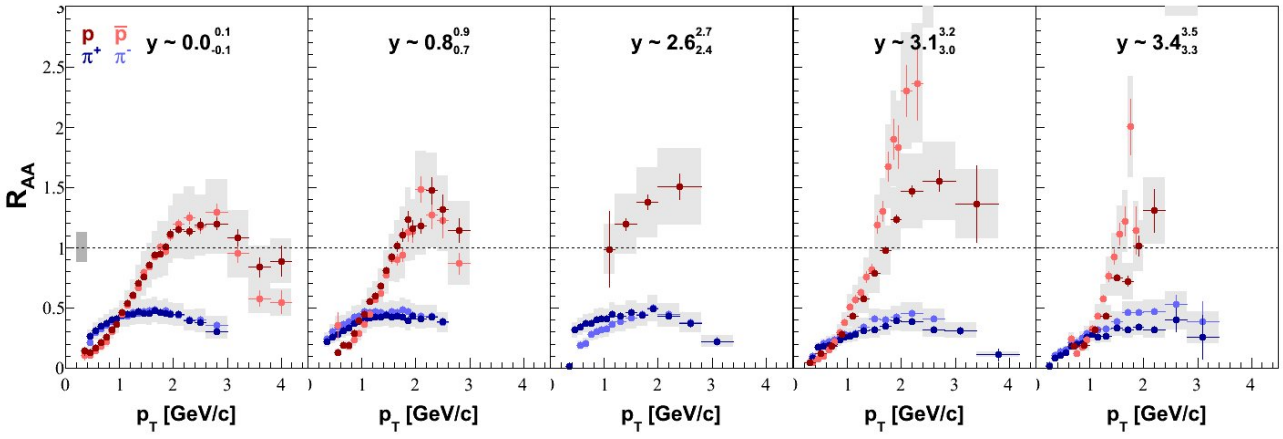

Figure 5.10: Nuclear modification factor R_{AA} for pions, protons and antiprotons at different y for the most central collisions (0-10% centrality). Error bars are statistical. Systematic errors are shown by the shaded boxes around points. The dotted lines indicate the expectation of binary scaling. The shaded band around unity indicates the systematic error associated with the uncertainty in the number of binary collisions.

and antiparticles. The suppression of pions at high p_T compared with p+p collisions indicates that the partons undergo a large energy loss due to a hot, dense medium created during the collisions.

For all the studied rapidities, the pion R_{AA} distribution remains systematically lower than unity for most central Au+Au collisions at $\sqrt{s_{NN}}$= 200 GeV. The R_{AA} shows a constant high p_T suppression with respect to p+p collisions, going from midrapidity to forward rapidity. This result could be an indication that other nuclear effects than parton energy loss might contribute to the rapidity constant suppression.

In contrast, the proton and antiproton yields do not show suppression with respect to binary scaling, in the intermediate p_T range for all the rapidities. Due to the poor statistics, for rapidity y=2.6±0.1 which correspond to the FS positioned at 8^0 relative to the beam line, we present only the R_{AA} for protons. The R_{AA} distributions for protons and antiprotons are, within errors, approximately independent on the rapidity.

The R_{AA} of protons and antiprotons rise faster than R_{AA} of charged pions to a maximum at $p_T \sim$ 2GeV/c. As p_T continues to increase above 2 GeV/c, the R_{AA} seems to saturate at values higher than those corresponding to binary scaling with the p+p data. The protons and antiprotons are enhanced relative to pions in the intermediate p_T region. At higher p_T ($p_T >$ 3GeV/c), the R_{AA} values start to decrease.

Coalescence or recombination of constituent quarks from a thermalized parton system (a quark gluon plasma) at hadronization temperature gives an attractive explanation for both results. It is more efficient to produce baryons than mesons at the same p_T: to produce a baryon, three quarks each at $p_T/3$ coalesce where they are much more abundant than at $p_T/2$ where two quarks coalesce into a meson.

If constituent quark coalescence is the production mechanism giving rise to the baryon-meson difference at intermediate p_T, when hadronization of the bulk medium does occur, then it's possible to conclude that a deconfined phase of quarks and gluons is created, prior to the hadronization.

In 0-12% central Au+Au collisions at $\sqrt{s_{NN}}$=200GeV, the STAR experiment has reported that at midrapidity and for $p_T >$ 5-6 GeV/c, the baryons are strongly suppressed and show a common degree of suppression as the mesons [172]. These results suggest that the influence of collective and recombination effects is reduced going to higher p_T and that above $p_T \sim$ 6 GeV/c fragmentation becomes the dominant production mechanism for all particle species. This could indicate that the

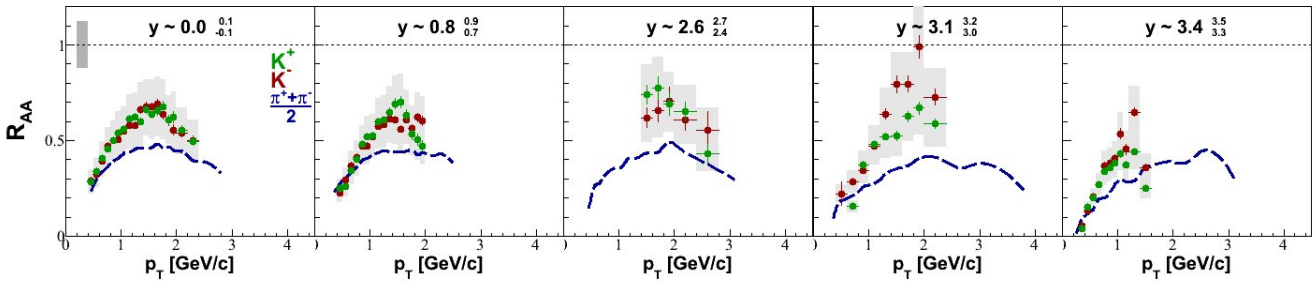

Figure 5.11: Nuclear modification factor R_{AA} for charged kaons at different y for the most central Au+Au collisions (0-10% centrality) at $\sqrt{s_{NN}}$=200 GeV. For comparison, with blue lines are shown also the R_{AA} distributions for charged pions. Error bars are statistical. Systematic errors are shown by the shaded boxes around points. The shaded band around unity indicates the systematic error associated with the uncertainty in the number of binary collisions.

partonic sources of charged pions, protons and antiprotons have similar energy loss when traversing the nuclear medium.

The R_{AA} distributions for charged kaons at different rapidities (0, 0.8, 2.6, 3.1, 3.4) are presented in the Figure 5.11. With blue lines are shown also the R_{AA} of charged pions for comparison. The charged kaon R_{AA} has the same p_T dependence as the R_{AA} for charged pions, but R_{AA} values for kaons are higher than for pions. For p_T >1.5 GeV/c, the charged kaon R_{AA} values decrease showing that also charged kaon yields are suppressed with respect to the expectation from the binary scaled p+p reference. The level of high p_T suppression seems to be smaller for positive and negative kaons than for pions.

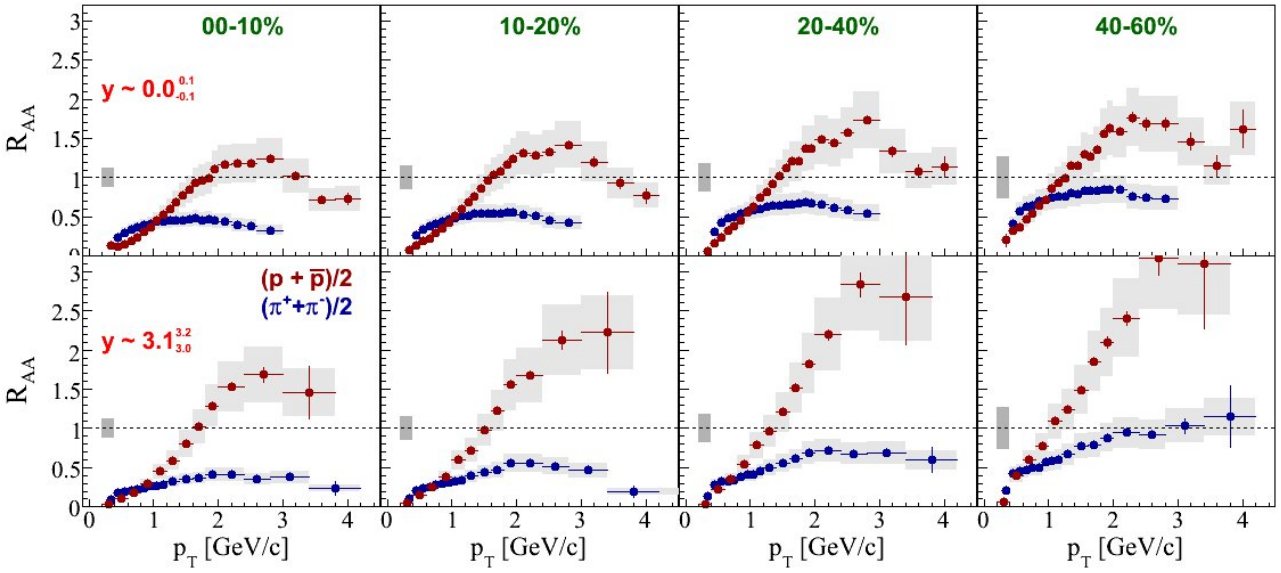

Figure 5.12: The centrality dependence of the nuclear modification factor R_{AA} for $(\pi^+ + \pi^-)/2$ (blue points) and $(p + \bar{p})/2$ (red points) at two rapidities, y=0 and y=3.1. Error bars are statistical. Systematic errors are shown by the shaded boxes around points. The dotted lines indicate the expectation of binary scaling. The shaded band around unity indicates the systematic error associated with the uncertainty in the number of binary collisions.

It would be interesting to see if theoretical models could explain the difference between K^+ and K^- seen at forward rapidity. However, the statistic for kaons is too poor at forward rapidity and

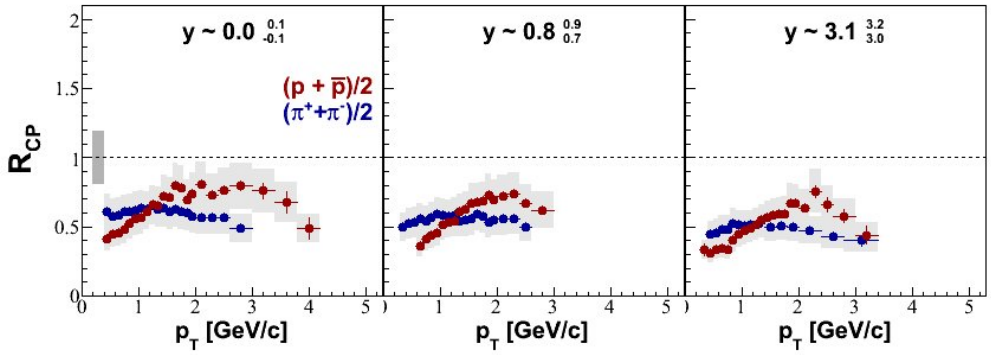

Figure 5.13: Central-to-peripheral factor R_{CP} for charged pions, protons and antiprotons at three different rapidities. Error bars are statistical. Systematic errors are shown by the shaded boxes around points. The shaded band around unity indicates the systematic error associated with the uncertainty in the number of binary collisions.

does not permit us to address physics issues about difference between the K^+ and K^-.

The centrality dependence of the nuclear modification factors for pions, $(\pi^+ + \pi^-)/2$, and for protons and antiprotons, $(p + \bar{p})/2$, is presented in the Figure 5.12 for two rapidities (0 and 3.1). R_{AA} for $(\pi^+ + \pi^-)/2$ evolves with centrality from a value of 0.3 around p_T ~3 GeV/c, showing the strong high p_T suppression seen in the most central 10% Au+Au collisions. In the last centrality window studied, in semi-peripheral collisions (40-60% centrality), R_{AA} for $(\pi^+ + \pi^-)/2$ reaches a value around unity, starting with p_T ~2 GeV/c, indicating approximate binary scaling. For the two rapidities, R_{AA} shows the same behavior from 0-10% to 40-60% centrality.

In the low p_T region (p_T <2GeV/c), the slope of the R_{AA} distributions for $(p + \bar{p})/2$ is the same for all the collision centralities at midrapidity and forward rapidity. For the R_{AA} of the $(\pi^+ + \pi^-)/2$ is a difference in slope for the low p_T part going from midrapidity to forward rapidity at all the centralities studied.

The p_T dependence of R_{CP} at three rapidities (0, 0.8, 3.1) for pions, $(\pi^+ + \pi^-)/2$, and for protons and antiprotons, $(p + \bar{p})/2$, is presented in the Figure 5.13. There is a distinct difference in the p_T dependence between the R_{CP} for $(\pi^+ + \pi^-)/2$ and the R_{CP} for $(p + \bar{p})/2$ at intermediate transverse momentum. From midrapidity to forward rapidity, R_{CP} for charged pions obtained in the most central 10% Au+Au collisions shows a suppression compared to that in semi-peripheral Au+Au (40-60% centrality), scaled with the number of binary collisions.

At intermediate p_T, the protons and antiprotons are less suppressed, than pions in the most central 10% Au+Au collisions with respect to semi-peripheral Au+Au (40-60%), at $\sqrt{s_{NN}}$=200GeV. This behavior is found to be independent on the rapidity.

Comparing the R_{CP} and R_{AA} for bayons, R_{CP} shows suppression whereas R_{AA} reveals an enhancement with the peak at $p_T \sim 2$ GeV/c. It is clear that for baryons the ratio to p+p is different from the ratio to peripheral Au+Au. Thus, semi-peripheral collisions (40-60% centrality) Au+Au collisions are not the same as p+p collisions.

The difference between elementary p+p collisions and peripheral Au+Au collisions could be that initial state effects should be present in Au+Au but not in p+p collisions. Assuming same initial state effects in peripheral and central collisions of Au+Au, R_{CP} contains information only about final state effects, whereas R_{AA} ratios, sample both initial and final states effects.

5.2.3 Particle ratios

The p_T dependence of $\bar{p}/\pi^-$ and p/π^+ ratios in both central Au+Au and in p+p collisions at $\sqrt{s_{NN}}$=200 GeV is presented in Figure 5.14 and confirm the reported high production of protons

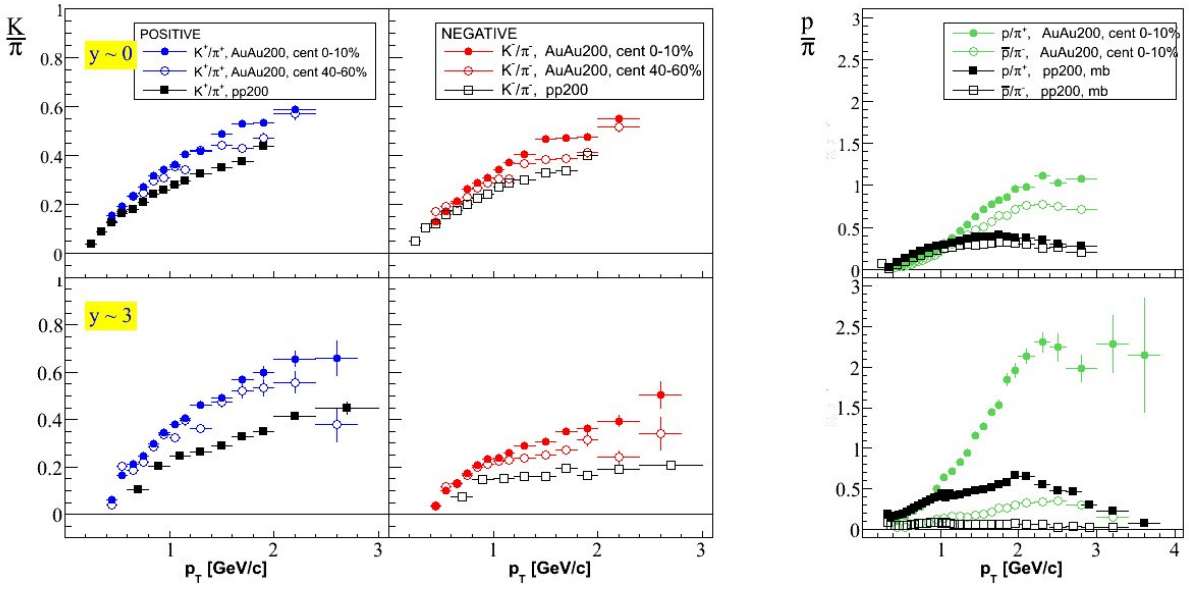

Figure 5.14: p/π^+, $\bar{p}/\pi^-$, K^+/π^+ and K^-/π^- ratios at midrapidity (upper panels) and forward rapidity at y=3 (bottom panels) in central (0-10%) Au+Au collisions and p+p at 200 GeV as function of p_T. Error bars are statistical.

and antiprotons (at midrapidity) in central Au+Au collisions in the intermediate transverse momentum range.

At midrapidity, as well as at forward rapidity, both $\bar{p}/\pi^-$ and p/π^+ ratios show smooth increase as a function of transverse momentum at low p_T, reaching the maximum around 2 GeV/c. At higher transverse momentum ($p_T > 2$ GeV/c), the $\bar{p}/\pi^-$ and p/π^+ ratios are independent of p_T. At intermediate p_T, there is an increase of the $\bar{p}/\pi^-$ and p/π^+ ratios obtained in the central Au+Au collisions as compared with the ratios from the p+p at the same energy. Clearly, the observed baryon enhancement is a property of the produced medium in central Au+Au collisions. This enhancement could be related with the existence of final state effects in Au+Au collisions and possibly some other hadronization mechanism than parton fragmentation, such as recombination.

At midrapidity, the $\bar{p}/\pi^-$ and p/π^+ ratios indicate that almost equal amounts of baryons and mesons are produced in central Au+Au collisions in the p_T range where recombination is expected to dominate ($2 < p_T < 5$ GeV/c). This is again in contradiction to the pQCD calculations, that give $p/\pi \sim 0.1$ - 0.2. Peripheral Au+Au data are found to have baryon to meson ratios similar to that in the elementary collision.

Another explanation for the approximate equal number of protons and the pions for $p_T > 2$ GeV/c at midrapidity is that the high p_T pions suffer from jet-quenching, which decreases the p_T of the measured pion spectrum, while the (anti)proton spectrum is influenced much stronger by the hydrodynamics boost that extends the p_T range of soft production for heavier particles due to the collective radial flow.

This hypothesis was tested by the PHENIX [157] and STAR [173]. They compare the ϕ meson behavior to that of protons, since they have similar masses. If mass is the mechanism that makes pions and protons different, then the ϕ and p should behave in the same way. But it was found that ϕ production is suppressed, unlike the production of protons and anti-protons. Thus, the difference between mesons and baryons is not very sensitive to the mass of the hadron, but rather depends on the number of valence quarks contained within it. These results suggest that the created matter is of partonic nature.

The difference between p/π^+ and $\bar{p}/\pi^-$ at forward rapidities is very interesting. The $\bar{p}/\pi^-$ ratio in Au+Au collisions shows a strong decrease when going from midrapidity to forward rapidity (y=3).

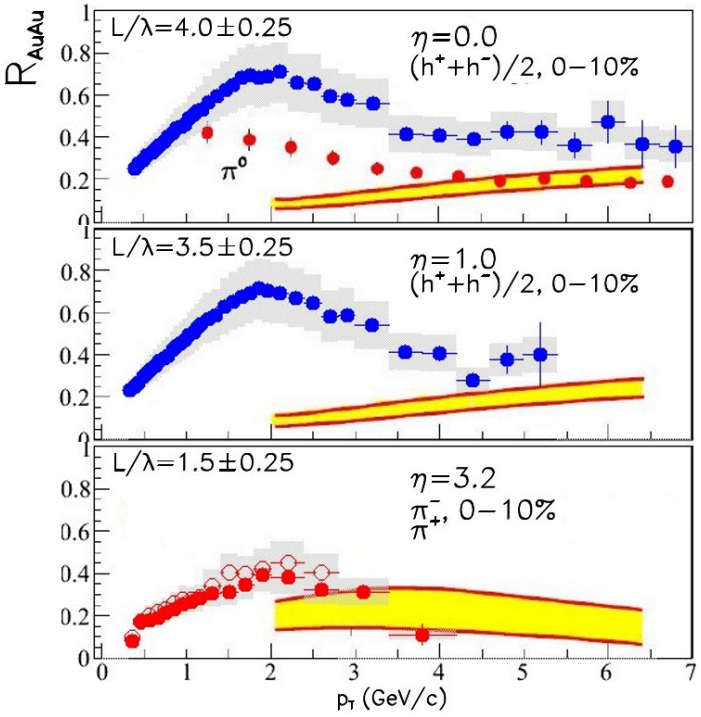

Figure 5.15: The pQCD results and the appropriate opacities, L/λ, at different rapidities for charged hadron and pion production in Au+Au collisions at $\sqrt{s_{NN}}$= 200 GeV, taken from [153]. Data are from this analysis. The π^0 mid-rapidity data are from PHENIX.

If recombination is the effect that drives the $\bar{p}/\pi^-$ ratio, the behavior of the $\bar{p}/\pi^-$ ratio seems to indicate that the partonic medium does not extend to high rapidity, or if it does, its effects on partons traversing it at high rapidity are not the same as at midrapidity. Therefore, for the almost constant suppression seen in the Au+Au at $\sqrt{s_{NN}}$=200 GeV there may be contributing other nuclear effects than parton energy loss in the produced medium.

The p/π^+ ratio is enhanced at forward rapidity compared to midrapidity, as shown in Figure 5.14. At forward rapidity, the p/π^+ ratio indicates approximately double amount of protons compared with pions in central Au+Au collisions in the intermediate p_T range ($2 < p_T < 5$ GeV/c). Such large yield may be related to the mechanism of baryon transport in the longitudinal direction in nucleus-nucleus collisions at RHIC.

In the Figure 5.14 are also shown the K^+/π^+ and K^-/π^- ratios at midrapidity and forward rapidity at y=3 in central (0-10%) Au+Au collisions and p+p at 200 GeV as function of p_T. At midrapidity, the negative and positive ratios behave similar. The K^-/π^- ratio in Au+Au collisions decreases by a factor of 2/3 when going from midrapidity to forward rapidity (y=3). However, the enhancement of K^-/π^- ratio in Au+Au over the same ratio in p+p increases. The K^+/π^+ ratio in Au+Au collisions at midrapidity is similar to that at forward rapidity (y=3). The enhancement of K^+/π^+ ratio in Au+Au over the same ratio in p+p increases.

5.2.4 Model comparison

The high p_T BRAHMS results obtained in the most central Au+Au collisions at $\sqrt{s_{NN}}$=200 GeV at different rapidities, from y = 0 at y = 3.4, were very challenging for theoretical models to interpret and to determine the energy loss and modified parton fragmentation in strongly interacting matter created in these collisions.

While a balance between a reduction in medium density and a possible change in path length might lead to a relatively constant R_{AA} value, the observed behavior is also consistent with jet

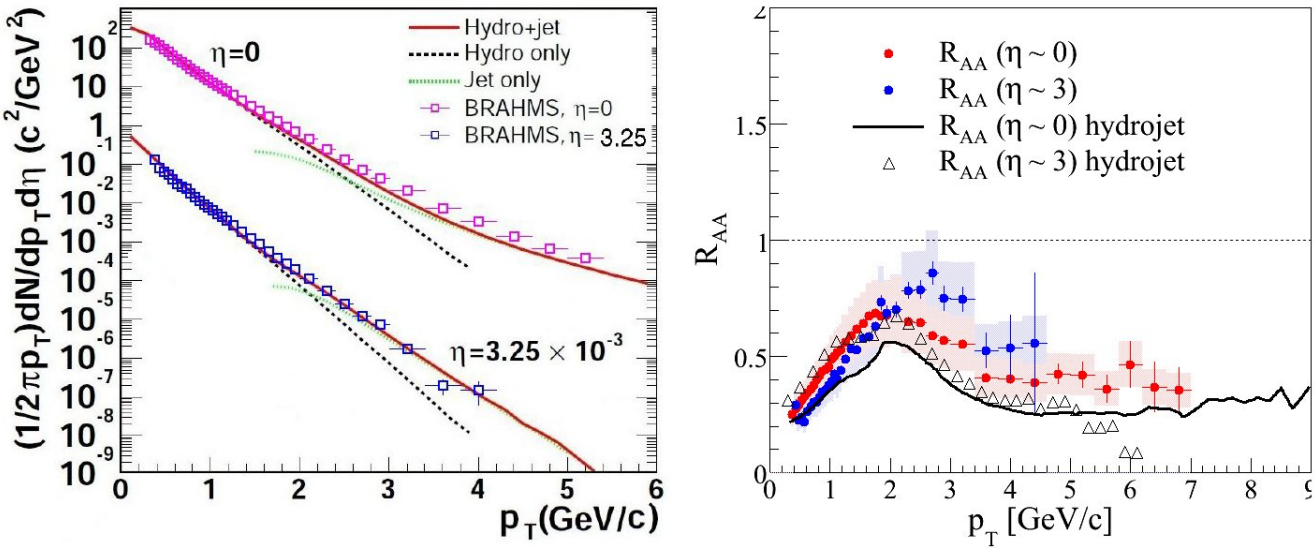

Figure 5.16: Left: Transverse momentum distributions of charged hadrons in Au+Au collisions at $\sqrt{s_{NN}}$ = 200 GeV obtained with the hydro+jet model of Hirano and Nara [152] are compared to data from this analysis at η=0 and 3.25. Solid lines represent the hydro+jet result averaged over $|\eta|$ <0.1 and 3.0< $|\eta|$ <3.5. The impact parameter for 0-10% centrality is taken to be b = 3.7 fm. Right: The nuclear modification factors calculated with the Hirano-Nara model compared to the BRAHMS data in Au+Au collisions at $\sqrt{s_{NN}}$ = 200 GeV. The black line is model calculation at midrapidity. The black triangles are the model calculation at forward rapidity, y=3.25. Data are from this analysis.

surface emission (see section 2.2.5), which assumes that only partons produced in the vicinity of the surface and propagating outward can escape from the medium with sufficiently high energy to fragment into high p_T hadrons, the others being absorbed. This implies that the sensitivity of the R_{AA} to the properties of the medium is rather limited.

In the Barnafoldi et al. model (see section 2.3.3), the authors consider that the combination of appropriate geometry of the hot and dense partonic region and the competing nuclear effects, namely shadowing, multiscattering, and induced energy loss could explain the constant high p_T suppression with rapidity. They extend the pQCD based calculation from midrapidity to forward rapidity and include these latter nuclear effects. Figure 5.15 shows the Barnafoldi et al. model calculation results in the pseudorapidity regions η = 0.0, 1.0 and 3.2 for central Au+Au collisions at $\sqrt{s_{NN}}$ = 200 GeV. Data are from this analysis; charged hadrons at η = 0.0, 1.0 and pions at η = 3.2. The π^0 mid-rapidity data are from PHENIX. The extended bands indicate the theoretical uncertainties on the induced energy loss denoted by the errors in the opacity values.

While for intermediate p_T values (2 < p_T < 5 GeV/c) the total charged particle production is suppressed less than pion production, the charged hadron and π^0 R_{AA} values become equal, within errors, at high p_T. This evolution in the charged particle suppression is related to contributions from the (anti)protons. The protons and antiprotons do not show suppression in the intermediate p_T range. At high p_T, the baryons are strongly suppressed and show a common degree of suppression as the mesons.

The opacity parameter[2], L/λ, is determined by finding the best fit for energy loss and comparing the theoretical results to the data points on the nuclear modification factor. The opacity parameter is decreasing with increasing rapidity from L/λ = 4.0 ± 0.25 at mid-rapidity to L/λ = 1.5 ± 0.25 at η = 3.2. One can see a factor of 3 difference when comparing the extracted opacity values in the mid-rapidity and in the most forward rapidity. According to the model assumption the produced hot dense deconfined matter is homogeneous, thus is characterized by a uniform λ value. The above

[2]L is the path length of the parton in the medium and λ is the mean free path.

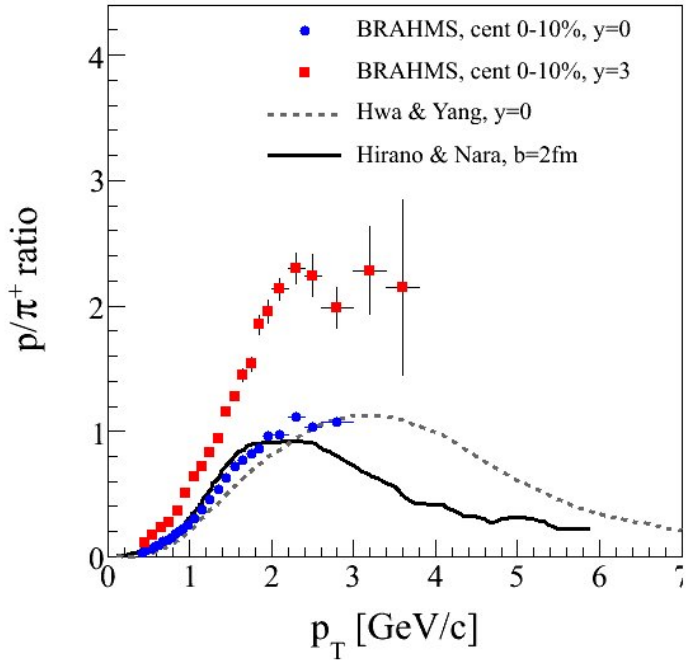

Figure 5.17: p/π^+ and p/π^- ratios at midrapidity and forward rapidity (y=3) in central (0-10%) Au+Au collisions at 200 GeV as function of p_T. Error bars are statistical. The dashed line is the Hwa and Yang recombination model prediction for midrapidity. The full line is the hydrojet model calculation of Hirano and Nara for midrapidity.

result indicates that longitudinally traveling partons see less colored matter than those traveling in the transverse direction. The authors consider that at large forward rapidities the interplay between a stronger shadowing and weaker quenching effects is able to maintain a rapidity independent nuclear modification factor.

The left panel of the Figure 5.16 shows the transverse momentum distributions of charged hadrons in Au + Au collisions at $\sqrt{s_{NN}}$ = 200 GeV obtained with the hydro+jet model of Hirano and Nara (see section 2.3.2) and comparison to data from this analysis for two pseudorapidities, η=0 and 3.25. The authors developed a two component dynamical model (hydro+jet model) with a fully three dimensional hydrodynamic model for the soft sector and pQCD jets for the hard sector which are computed via the PYTHIA code. Each spectrum is the sum of the soft component and the hard component, which are represented in the figure with dotted lines (black for soft, hydro part and green for hard, jet part). The slope from pQCD components in high p_T region becomes steeper as η increases.

At low transverse momentum region ($p_T < 2$ GeV/c), the charged hadron spectra shapes remain the same as hydro predictions as it can be seen in the Figure 5.16. The transverse momentum spectra for charged hadrons produced in 200 GeV Au+Au collisions are well described by the hydro+jet model calculation at η=3.25 in the full p_T range. At pseudorapidity η=0, the model calculation describes well the low p_T part of the spectrum and underestimates the high p_T part of the spectrum.

Hydro+jet model calculation (without CGC initial conditions) for the nuclear modification factors R_{AA} for charged hadrons at $\eta = 0$ and 3.25 in Au+Au collisions at RHIC are shown in right panel of Figure 5.16. The nuclear modification factor R_{AA} in low p_T region ($p_T \leq 2$ GeV/c), where the hydrodynamic component dominates, is different between $\eta = 0$ and 3.5. The authors explain that the result of model calculation for nuclear modification factor at η= 3.25 in the range $p_T < 5$ GeV/c is larger than at midrapidity, because of the 40% smaller thermalized parton density at $\eta = 3.25$. The

authors consider that the $R_{AA}(\eta = 3.25)$ becomes smaller than the one for η=0 in high p_T region (p_T >5 GeV/c) due to the much steeper slope at high p_T.

However, the experimental data from this analysis do not follow the theoretical hydro+jet calculation. At low p_T, the charged hadron R_{AA} values are larger at midrapidity than at forward pseudorapidity. In the p_T >3 GeV/c region, the R_{AA} values for η=0 are smaller than the values for η=3. Thus, the slope effect is compensated by other nuclear effects.

Figure 5.17 shows the p/π^+ ratio obtained in 200 GeV Au+Au collisions at midrapidity and at rapidity y=3 and two theoretical model predictions for midrapidity. The Hwa and Yang recombination model (see section 2.4) calculation is presented with dashed line.

The 3D hydrodynamic model calculation of Hirano and Nara is presented with full line in the Figure 5.17. The authors obtain a p/π^+ ratio close to unity due to the hadron species dependent p_{Tcross}. The crossing point of transverse momentum p_{Tcross} is the point at which the yield from the soft part is identical to that from the hard part. p_{Tcross} moves toward high momentum with mass of particles because of the effects of radial flow. The authors note that, if the baryon chemical potential is included in the hydrodynamic simulation, p/π ratio can slightly be changed in low p_T region. Baryon chemical potential pushes up proton yield from hydrodynamic component.

The data agree qualitatively with the models prediction at midrapidity (therefore, none of the models is ruled out). It would be interesting to test p/π^+ ratio with the models for the forward rapidity.

Chapter 6

Conclusions

In this work, we have presented the rapidity and centrality dependence of the transverse momentum spectra of charged hadrons, as well as identified pions, kaons, protons and their antiparticles produced in Au+Au and p+p collisions at $\sqrt{s_{NN}}$=200 GeV with the BRAHMS experiment at RHIC. The main focus of this work is the (pseudo)rapidity dependence of the high p_T suppression. Studying the rapidity dependence of various particle species in intermediate and higher p_T regions provides an experimental tool for investigating energy loss mechanisms in the medium, to understand hadron production mechanisms and also baryon transport in the longitudinal direction in nucleus-nucleus collisions at RHIC. The BRAHMS experiment has the unique capability to measure centrality dependent high p_T particle production, not only at midrapidity, but over a wide p_T and rapidity range ($0.3< p_T <$2.5-7 GeV/c, $0< y <4$).

The results demonstrate that there is a strong, centrality dependent and almost rapidity independent suppression of the production of high p_T charged hadrons relative to pQCD expectations. For the most central 10% Au+Au collisions, the R_{AA} for charged hadrons shows a slight decrease of the high p_T suppression with respect to binary scaled p+p collisions, when goes from η=0 to forward pseudorapidity, η=3.6. This suppression was observed to increase from peripheral to central collisions and is found to be N_{part} dependent. The N_{part} dependence of the nuclear modification factor could be explained as a consequence of medium induced energy loss of hard-scattered partons traversing the hot, dense medium created during the collisions. For the smaller system sizes (peripheral Au+Au data), the path length traversed is smaller (on average) than for the larger system (central Au+Au). The R_{CP} and R_η shows a roughly constant suppression at high p_T for all studied pseudorapidities.

The p_T dependence of the R_{AA} is a result of the interplay between initial effects (Cronin effect, nuclear shadowing), jet quenching and the softening of the underlying p_T spectrum with increasing rapidity. Surprisingly, these effects build an approximately constant suppression pattern with pseudorapidity.

The nuclear modification factors for identified particles show a distinct meson/baryon dependence. In most central Au+Au collisions at $\sqrt{s_{NN}}$=200 GeV, at high p_T the charged pion yields are suppressed by a factor of $\sim$ 5 as compared with binary scaled p+p pion yields. The high p_T suppression is stronger for pions than for the inclusive charged hadrons. The central-to-peripheral ratio R_{CP} of charged hadrons is 20% higher than that of pions. The R_{AA} shows a constant high p_T pion suppression with respect to p+p collisions, from midrapidity to forward rapidity. The charged kaon R_{AA} has the same p_T dependence as the R_{AA} for pions, however the level suppression is smaller than for pions.

We report enhanced baryon production in Au+Au collisions, when compared to the scaled p+p data from the same energy. The R_{AA} distributions for protons and antiprotons are, within errors, approximately independent on the rapidity. The R_{CP} shows suppression whereas R_{AA} reveals an enhancement with the peak at $p_T \sim 2$ GeV/c. Assuming same initial state effects in peripheral and central collisions of Au+Au, R_{CP} contains information only about final state effects, whereas R_{AA} ratios, sample both initial and final states effects.

The mechanism based on initial hard parton scattering and jet fragmentation is not sufficient to explain this particle type dependence in the intermediate p_T region. Hadronization processes through multi-parton dynamics such as recombination and coalescence models are likely to be important for explaining baryon enhancement relative to mesons in high-energy Au+Au collisions.

At midrapidity, the $\bar{p}/\pi^-$ and p/π^+ ratios indicate that almost equal amounts of baryons and mesons are produced in central Au+Au collisions in the p_T range where recombination is expected to dominate ($2 < p_T < 5$ GeV/c). The ratios of p/π^+ and $\bar{p}/\pi^-$ are a factor of 2-3 higher than those in p+p collisions at similar energies.

There is a strong dependence of the $\bar{p}/\pi^-$ and p/π^+ obtained in Au+Au collisions at $\sqrt{s_{NN}}$=200 GeV. The $\bar{p}/\pi^-$ ratio shows a strong decrease from midrapidity to forward rapidity (y=3) whereas p/π^+ ratio is enhanced at forward rapidity compared to midrapidity. Such large proton yield may be related to the mechanism of baryon transport in the longitudinal direction in nucleus-nucleus collisions at RHIC. If recombination is the mechanism of particle production, the behavior of the $\bar{p}/\pi^-$ ratio with rapidity seems to indicate that the partonic medium does not extend to high rapidity, or if it does, its effects on partons traversing it at high rapidity are not the same as at midrapidity. Therefore, for the almost constant suppression seen in the Au+Au at $\sqrt{s_{NN}}$=200 GeV may be contributing other nuclear effects than parton energy loss in the longitudinally extended hot and dense matter created in collisions.

The results are compared with the prediction of several theoretical models. The p/π^+ agree qualitatively with the Hwa and Yang recombination model prediction as well as with the hydro+jet model prediction at midrapidity. It would be interesting to test p/π^+ ratio with the models for the forward rapidity.

The transverse momentum spectra for charged hadrons produced in 200 GeV Au+Au collisions are well described by the hydro+jet model calculation at η=3.25 in the full p_T range. At pseudorapidity η=0, the model calculation describe well the low p_T part of the spectrum and underestimate the high p_T part of the spectrum. However, the charged hadron R_{AA} from this analysis does not follow the theoretical hydro+jet calculation. At low p_T, the charged hadron R_{AA} values are larger at midrapidity than at forward pseudorapidity and in the $p_T > 3$ GeV/c region, the R_{AA} values for η=0 are smaller than the values for η=3. Therefore must be other nuclear effects at forward rapidity to compensate the steeper slope of the spectrum.

In the Barnafoldi et al. model, it is considered that the combination of appropriate geometry of the partonic region and the competing nuclear effects, namely shadowing, multiscattering, and induced energy loss could explain the constant high p_T suppression with rapidity.

Throughout this thesis, we have presented large suppression factors of the high p_T particles, from midrapidity to forward rapidity. These evidences support the idea of a dense QGP formed at early times in the most central Au+Au collision. However, there is still debate over the subject of the high p_T suppression. Most probable, this type of measurements, together with other signals will eventually lead to some definitive conclusions.

Appendix A

The BRAHMS Collaboration

I. Arsene[10], I. G. Bearden[7], D. Beavis[1], C. Besliu[10], B. Budick[6], H. Bøggild[7], C. Chasman[1], C. H. Christensen[7], P. Christiansen[7], J. Cibor[3], R. Debbe[1], E. Enger[12], J. J. Gaardhøje[7], M. Germinario[7], K. Hagel[8], H. Ito[1], A. Jipa[10], F. Jundt[2], J. I. Jørdre[9], C. E. Jørgensen[7], R. Karabowicz[4], E. J. Kim[1,11], T. Kozik[4], T. M. Larsen[12], J. H. Lee[1], Y. K. Lee[5], S. Lindal[12], R. Lystad[9], G. Løvhøiden[12], Z. Majka[4], A. Makeev[8], M. Mikelsen[12], M. Murray[8,11], J. Natowitz[8], B. Neumann[11], B. S. Nielsen[7], D. Ouerdane[7], R. Płaneta[4], F. Rami[2], C. Ristea[7], O. Ristea[10], D. Röhrich[9], B. H. Samset[12], D. Sandberg[7], S. J. Sanders[11], R. A. Scheetz[1], P. Staszel[7], T. S. Tveter[12], F. Videbæk[1], R. Wada[8], Z. Yin[9], and I. S. Zgura[10]

[1] Brookhaven National Laboratory, Upton, New York 11973
[2] Institut de Recherches Subatomiques and Université Louis Pasteur, Strasbourg, France
[3] Institute of Nuclear Physics, Krakow, Poland
[4] Smoluchkowski Inst. of Physics, Jagiellonian University, Krakow, Poland
[5] Johns Hopkins University, Baltimore 21218
[6] New York University, New York 10003
[7] Niels Bohr Institute, Blegdamsvej 17, University of Copenhagen, Copenhagen 2100, Denmark
[8] Texas A&M University, College Station, Texas, 17843
[9] University of Bergen, Department of Physics, Bergen, Norway
[10] University of Bucharest, Romania
[11] University of Kansas, Lawerence, Kansas 66049
[12] University of Oslo, Department of Physics, Oslo, Norway

Appendix B

Kinematic Variables

The kinematic variables used in the thesis are introduced next. It is useful to describe them with Lorentz invariant variables or variables which have simple Lorentz transformation properties, because we deal with relativistic particles and system.

A particle produced from the collision is characterized by its mass m and three momentum components p_x, p_y and p_z. Of special interest is the transverse momentum, the projection of the particle's momentum perpendicular to the collision axis, z:

$$p_T = \sqrt{p_x^2 + p_y^2} = p \cdot \sin\theta \tag{B.1}$$

because it is invariant under the Lorentz transformations along the beam direction. θ is the polar angle (the angle between the particle momentum p and the beam axis z). A common variable derived from this is the transverse mass of a particle of mass m is

$$m_T = \sqrt{p_T^2 + m^2} \tag{B.2}$$

The variable rapidity y is defined as

$$y = \frac{1}{2}\ln\frac{E + p_z}{E - p_z} = \frac{1}{2}\ln\frac{1 + p_z/E}{1 - p_z/E} \tag{B.3}$$

where $E = \sqrt{p^2 + m^2}$ is the particle energy and $p_z = p \cdot \cos\theta$ is the longitudinal momentum (the particles momentum along the beam axis). Rapidity is additive under Lorentz transformations along the axis z. As $p = \gamma m v$, $E = \gamma m c^2$, then

$$\frac{p_z}{E} = \beta\cos\theta \tag{B.4}$$

and substituting into B.3

$$y = \frac{1}{2}\ln\frac{(1 + \beta cos\theta)}{(1 - \beta cos\theta)} \tag{B.5}$$

Using the equation B.3, we can write

$$e^y = \sqrt{\frac{E + p_z}{E - p_z}} \tag{B.6}$$

Therefore, the total energy and longitudinal momentum of a particle can be easily related to its transverse mass and rapidity as

$$E = m_T \cdot \cosh y, \qquad p_z = m_T \cdot \sinh y \tag{B.7}$$

In the experiments, the detected particles are often not identified, and we do not know their masses which are required to determine the rapidity. However, the particle momentum can be measured experimentally. In that case, it is used the pseudo-rapidity that defined as

$$\eta = -\ln[\tan(\theta/2)] \tag{B.8}$$

The pseudo-rapidity is only determined by the angle θ of the particle direction of motion with respect to the beam axis. For this reason it is usually easier to determine the pseudorapidity than the rapidity of a particle. The momentum and longitudinal momentum can be written as:

$$p = p_T \cdot \cosh\eta, \qquad p_z = p_T \cdot \sinh\eta \tag{B.9}$$

For a relativistic particle, m$\ll$p, so $\beta \to 1$,

$$y = \frac{1}{2}\ln\frac{E + p_z}{E - p_z} \approx \frac{1}{2}\ln\frac{|p| + p_z}{|p| - p_z} = \ln\sqrt{\frac{(1 + cos\theta)}{(1 - cos\theta)}} = -\ln[\tan(\theta/2)] \equiv \eta \tag{B.10}$$

Appendix C

DIS

The term Deep Inelastic Scattering (DIS) describes inelastic lepton-nucleon collisions in which the momentum transfer between the lepton and the nucleon is sufficient that, in accordance with the Heisenberg uncertainty relation, distances significantly smaller than the nucleon radius can be resolved. In an analogue to the Rutherford scattering experiments which first revealed atomic structure, the lepton in DIS acts as a probe which can reveal substructures within the nucleon.

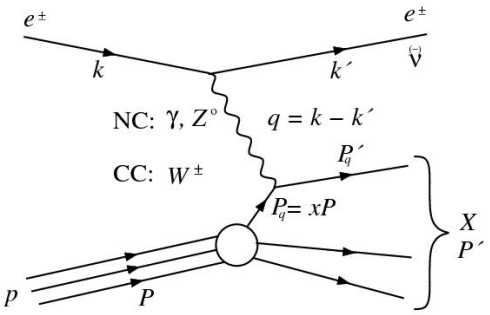

Figure C.1: Feyman diagram of the deep inelastic scattering.

The mediating boson in DIS can be a γ or Z^0 boson (neutral current) where the lepton retains its identity, or a $W^{\pm}$ boson (charged current), where the lepton identity changes. The proton ussually breaks up, forming a final state X of hadrons, which are often emitted in jets. A basic process of electron-proton interaction is shown schematically in the figure C.1.

Apart from the center of mass energy squared, $s = (k + P)^2$, which is fixed for any given experimental conditions by the four-momentum of the initial lepton, k, and that of the target nucleon, P, other Lorentz invariants define the kinematics, such as,

- $Q^2 = -q^2 = -(k - k')^2$, the virtuality of the virtual photon (the square of the four momentum transferred from the lepton to the target nucleon);
- $\nu = \frac{P \cdot q}{M}$, the virtual photon energy;
- $x = \frac{Q^2}{2P \cdot q}$, the Bjorken scaling variable (the fraction of nucleon momentum carried by parton);
- $y = \frac{P \cdot q}{P \cdot k}$, in the proton rest frame is the fraction of incoming electron energy carried by virtual photon.

where the mass M is conventionally taken to be that of the proton [101].

DIS cross section

The general form of the inclusive DIS cross section can be factorized into a leptonic tensor $L_{\mu\nu}$ and a hadronic tensor $W^{\mu\nu}$

$$d\sigma \sim L_{\mu\nu} W^{\mu\nu} \tag{C.1}$$

The leptonic tensor $L_{\mu\nu}$, which describes the interaction of the electron with the exchanged boson (defines the leptonic vertex $e^- \rightarrow \gamma^* + e^-$), is calculable from QED and has the form:

$$L_{\mu\nu} = 2[k'_\mu k_\nu + k'_\nu k_\mu + (q^2/2)g_{\mu\nu}] \tag{C.2}$$

where $g_{\mu\nu}$ is the metric tensor. The hadronic tensor $W_{\mu\nu}$ for an a priori unknown structure of proton is presented in terms of structure functions, the four-momenta at the the hadronic vertex $\gamma^* + p \rightarrow X$:

$$W_{\mu\nu} = W_1(-g_{\mu\nu} + \frac{q_\mu q_\nu}{q^2}) + \frac{W_2}{M^2}(p_\mu - \frac{p \cdot q}{q^2}q_\mu)(p_\nu - \frac{p \cdot q}{q^2}q_\nu) \tag{C.3}$$

where M is the proton mass and $W_{1,2}$ are more commonly defined in terms of the structure functions:

$$F_1(x, Q^2) = M \cdot W_1(x, Q^2), \qquad F_2(x, Q^2) = \frac{Q^2}{2Mx}W_2(x, Q^2) \tag{C.4}$$

These structure functions contain information about the inner structure of the target nucleon and thus, define the partonic content of the proton. The electron-proton cross section can be written as

$$\frac{d^2\sigma}{dQ^2dx} = \frac{4\pi\alpha^2}{xQ^4}[(1-y)F_2(Q^2, x) + y^2xF_1(Q^2, x)] \tag{C.5}$$

where α is the electromagnetic coupling constant. F_1 and F_2 can be expressed in terms of the distributions of quarks $f(x)$ and antiquarks $\bar{f}(x)$ in the proton

$$F_1(x, Q^2) = \frac{1}{2}\sum_i^{quarks} e_i^2[f_i(x, Q^2) + \bar{f}_i(x, Q^2)], \qquad F_2(x, Q^2) = \sum_i^{quarks} e_i^2 x[f_i(x, Q^2) + \bar{f}_i(x, Q^2)] \tag{C.6}$$

where the sum i is over the quark flavous, e_i is the charge of a quark of flavour i, the f_i is the parton distribution function (PDF) of quarks defined as the probability to find a quark carrying a fraction x of the proton momentum and the xf_i is the parton momentum distribution. The relation between structure functions F_1 and F_2 is called the Callan-Gross relation [101]

$$2xF_1(x, Q^2) = F_2(x, Q^2) \tag{C.7}$$

The structure functions F_1 and F_2 have been investigated in great detail over the last decaded using both electron and muon beams.

Bjorken had predicted that in the high energy limit $Q^2 \rightarrow \infty$ and $\nu = p \cdot q/p^2 \rightarrow \infty$, but Q^2/ν finite, the structure functions should scale, i.e. become independent on the Q^2. This is the Bjorken scaling hypothesis [101]. Scaling can be interpreted as a sign of the fact that the virtual photon is absorbed, inside the nucleon, by pointlike electrically charged objects, first named partons by Feynman and later identified with quarks. Since the quarks are assumed to be non-interacting static particles confined within the proton, the structure functions are expected to be a function of x, but not Q^2, because changes in Q^2 correspond to changes in the scale probed by the exchanged boson, which would be irrelevant for point-like constituents, i.e. $F_i(x, Q^2) = F_i(x)$.

Appendix D

Spectra

In this section we discuss about the differential cross sections and yields that are Lorentz invariant. The differential yields are corresponding to the number of particles emitted into a particular region in momentum space per interaction. The total yield of a particular particle is the total number of such particles emitted into any point in momentum space per interaction,

$$N = \int \frac{d^3N}{dp^3} d^3p \tag{D.1}$$

which must be Lorentz invariant. The momentum-space volume element, $d^3p = dp_x dp_y dp_z$, however, is not invariant since the differential momentum element along the direction of a boost between frames transforms as $dp^{'} = \gamma dp$.

In order to compare the results from different experiments, we have to find an expression for the differential yield which is manifestly invariant. In any event, the momentum-space volume element d^3p/E is Lorentz invariant. Therefore, the differential yield, Ed^3N/dp^3 and the total yield

$$N = \int E \frac{d^3N}{dp^3} \frac{d^3p}{E} \tag{D.2}$$

The momentum-space volume element can be write using instead of (p_x, p_y, pz) the (p_T, y, ϕ) variables

$$\frac{dp_x dp_y dp_z}{E} = p_T dp_T dy d\phi \tag{D.3}$$

Therefore, the total yield is

$$N = \int \frac{d^3N}{p_T dp_T dy d\phi} p_T dp_T dy d\phi \tag{D.4}$$

If we assume the azimuthal distribution to be isotropic, the integral in ϕ can be performed immediately. In order to use a form equivalent to Ed^3N/dp^3 for the presentation of different yields, we need to quote the average rather than the sum over ϕ. The expression for total yield becomes:

$$N = \int \frac{d^3N}{2\pi p_T dp_T dy} 2\pi p_T dp_T dy \tag{D.5}$$

and the differential yield is

$$\frac{1}{2\pi p_T} \frac{d^2N}{dp_T dy} \tag{D.6}$$

If we want to use the transverse mass, $m_T = \sqrt{p_T^2 + m^2}$:

$$\frac{dm_T}{dp_T} = \frac{p_T}{\sqrt{p_T^2 + m^2}} = \frac{p_T}{m_T} \tag{D.7}$$

and $p_T dp_T = m_T dm_T$. The equation D.6, with transverse mass m_T in place of transverse momentum p_T, is an equally valid form for the invariant yield.

The integrand of Equation D.5 is Lorentz invariant for boosts along the collision axis since N is dimensionless and p_T, dp_T, and dy are invariant for such boosts.

Bibliography

[1] M. Gell-Mann , Phys. Rev. Lett. **8**, 214 (1964).

[2] P. D. Group , J. Phys. G. **33** (2006).

[3] S. Bethke , `hep-ex/0211012`.

[4] A. Benvenutti *et al.* , Phys. Lett. **B223**, 490 (1989).

[5] D. Gross and F. Wilczek , Phys. Rev. Lett. **30**, 1343 (1973).

[6] J. Blaizot and E. Iancu , Phys.Rep. **A681**, 119 (2001).

[7] W. Bartel , Phys. Lett. **B28**, 148 (1968).

[8] H. Satz , J. Phys. **G32**, R25 (2006).

[9] H. Satz , Rept.Prog.Phys. **63**, 1511 (2000).

[10] F. Karsch, M. Mehr, and H. Satz , Z. Phys. **C37**, 617 (1988).

[11] H. Satz , Nucl. Phys. **A488**, 511c (1988).

[12] J. Collins and M. Perry , Phys. Rev. Lett. **34**, 1353 (1975).

[13] E. Shuryak , Phys. Lett. **A78**, 150 (1978).

[14] O. Kalashnikov and V. Klimov , Phys. Lett. **B88**, 328 (1979).

[15] J. Kapusta , Nucl. Phys. **B148**, 461 (1979).

[16] S. Weinberg , Primele trei minute ale Universului, Editura Tehnica (19xx).

[17] N. Glendenning and F. Weber , `astro-ph/0003426`.

[18] K. Rajagopal, M. Alford, and F. Wilczek , Phys. Lett. **B422**, 247 (1998).

[19] P. Braun-Munzinger , Nucl. Phys. **A681**, 119 (2001).

[20] S. Mrowczynski , Acta Phys.Polon. **B29**, 3711 (1998).

[21] www.bnl.gov/RHIC/.

[22] F. Karsch , Nucl. Phys. **A698**, 199 (2002).

[23] F. Karsch, E. Laermann, and A. Peikert , `hep-lat/0012023`.

[24] F. Karsch *et al.* , Nucl. Phys. **B605**, 579 (2001).

[25] F. Karsch *et al.* , Phys. Rev. **D74**, 054507 (2006).

[26] F. Karsch, E. Laermann, and A. Peikert , Phys. Lett. **B478**, 447 (2000).

[27] S. Gottlieb *et al.* , Phys. Rev. **D47**, 3619 (1993).

[28] H. Ito , Ph.D. Thesis, Kansas University (2002).

[29] X. Wang , Nucl. Phys. **A698**, 296 (2002).

[30] D. Kharzeev and M. Nardi , Phys. Lett. **B507**, 121 (2001).

[31] R. Glauber and J. Nathiane , Nucl. Phys. **B21**, 135 (1970).

[32] C. Wong and Z. Lu , Phys. Rev. **D39**, 2606 (1989).

[33] L. D. Landau , Izv. Akad. Nauk. Ser. Fiz. **17**, 51 (1953).

[34] J. D. Bjorken , Phys. Rev. **D27**, 140 (1983).

[35] P. Christiansen. PhD thesis, University of Copenhagen, 2003.

[36] BRAHMS Collaboration, I. G. Bearden *et al.* , Phys. Rev. Lett. **93**, 102301 (2004).

[37] BRAHMS Collaboration, I. Arsene *et al.* , Nucl. Phys. **A757**, 1 (2005).

[38] E802 Collaboration, L. Ahle *et al.* , Phys. Rev. **C60**, 064901 (1999).

[39] E877 Collaboration, J. Barette *et al.* , Phys. Rev. **C62**, 024901 (2000).

[40] NA49 Collaboration, H. Appelshauser *et al.* , Phys. Rev. Lett. **82**, 2471 (1999).

[41] L. McLerran **,** `hep-ph/0311018`.

[42] L. McLerran **,** `hep-ph/0402137`.

[43] L. McLerran , Pramana **60**, 575 (2003).

[44] L. Van Hove , Phys. Lett. **B118**, 138 (1982).

[45] J. Kapusta, S. Pratt, L. McLerran, and H. Gersdorff , Phys. Lett. **B163**, 253 (1985).

[46] H. Gersdorff , Nucl. Phys. **A461**, 251c (1987).

[47] S. Pratt , Phys. Rev. Lett. **53**, 1219 (1984).

[48] G. Bertsch , Nucl. Phys. **A498**, 173c (1989).

[49] P. Kolb and U. Heinz **,** `nucl-th/0305084`.

[50] STAR Collaboration, J. Adams *et al.* , Phys. Rev. **C72**, 014904 (2005).

[51] PHENIX Collaboration, A. Adare *et al.* **,** `nucl-exp/0608033`.

[52] U. Heinz **,** `nucl-th/0512051`.

[53] P. Kolb, J. Sollfrank, and U. Heinz , Phys. Rev. **C 62**, 054909 (2000).

[54] Z. Lin and C. Ko , Phys. Rev. Lett. **89**, 202302 (2002).

[55] D. Molnar and S. Voloshin , Phys. Rev. Lett. **91**, 092301 (2003).

[56] R. Fries , J. Phys. **G30**, S853 (2004).

[57] BRAHMS Collaboration, E. Johnson *et al.* , AIP Conf.Proc. **842**, 137 (2006).

[58] BRAHMS Collaboration, H. Ito *et al.* , Nucl. Phys. **A774**, 519 (2006).

[59] PHOBOS Collaboration, B. Back *et al.* , Phys. Rev. **C72**, 051901(R) (2005).

[60] PHOBOS Collaboration, B. Back *et al.* , Phys. Rev. Lett. **94**, 122303 (2005).

[61] M. Gyulassy and M. Plumer , Phys. Lett. **B243**, 432 (1990).

[62] X. Wang and M. Gyulassy , Phys. Rev. Lett. **68**, 1480 (1992).

[63] X. Wang, M. Gyulassy, and M. Plumer , Phys. Rev. **D51**, 3436 (1995).

[64] R. Baier *et al.* , Phys. Lett. **B345**, 277 (1995).

[65] R. Baier, D. Schiff, and B. Zakharov , Ann.Rev.Nucl.Part.Sci. **50**, 37 (2000).

[66] X. Wang , Phys. Rev. **C58**, 2321 (1998).

[67] PHENIX Collaboration, K. Adcox *et al.* , Phys. Rev. Lett. **88**, 022301 (2002).

[68] STAR Collaboration, C. Adler *et al.* , Phys. Rev. Lett. **89**, 202301 (2002).

[69] BRAHMS Collaboration, I. Arsene *et al.* , Phys. Rev. Lett. **91**, 072305 (2003).

[70] STAR Collaboration, J. Adams *et al.* , Phys. Rev. Lett. **91**, 172302 (2003).

[71] PHENIX Collaboration, S. S. Adler *et al.* , Phys. Rev. Lett. **91**, 072303 (2003).

[72] PHOBOS Collaboration, B. Back *et al.* , Phys. Rev. Lett. **91**, 072302 (2003).

[73] J. Rafelski , Phys. Rep. **88**, 331 (1982).

[74] J. Rafelski and B. Muller , Phys. Rev. Lett. **48**, 1066 (1982).

[75] P. Koch *et al.* , Phys. Rep. **142**, 169 (1986).

[76] E. Shuryak , Phys. Rev. Lett. **68**, 3270 (1992).

[77] WA97 Collaboration, E. Anderson *et al.* , Phys. Lett. **B449**, 401 (1999).

[78] NA57 Collaboration, F. Antinori *et al.* , J. Phys. **G32**, 427 (2006).

[79] STAR Collaboration, J. Adams *et al.* , Phys. Rev. Lett. **92**, 182301 (2004).

[80] J. Rafelski and J. Letessier , `hep-ph/0610106`.

[81] J. Harris and B. Muller , Ann.Rev.Nucl.Part.Sci. **46**, 71 (1996).

[82] K. K., J. Kapusta, L. McLerran, and A. Mekjian , Phys. Rev. **D34**, 2746 (1986).

[83] PHENIX Collaboration, S. Adler *et al.* , Phys. Rev. Lett., **94**, 232301 (2005).

[84] J. Kapusta *et al.* , Phys. Rev. **D44**, 2774 (1991).

[85] P. Siemens and S. Chin , Phys. Rev. Lett. **55**, 1266 (1985).

[86] CERES Collaboration, B. Lenkeit *et al.* , Nucl. Phys. **A661**, 23c (1999).

[87] R. Rapp , `nucl-th/0204003`.

[88] R. Rapp and J. Wambach , `hep-ph/9909229`.

[89] I. Ravinovich *et al.* , Nucl. Phys. **A774**, 903 (2006).

[90] J. Harris , Eur.Phys.J. **C43**, 445 (2005).

[91] J. Aubert *et al.* , Phys. Rev. Lett. **33**, 1404 (1974).

[92] J. Augustin *et al.* , Phys. Rev. Lett. **33**, 1406 (1974).

[93] M. Leitch , `nucl-exp/0610031`.

[94] T. Matsui and H. Satz , Phys. Lett. **B178**, 416 (1986).

[95] F. Karsch and H. Satz , Z. Phys. **C51**, 209 (1991).

[96] NA50 Collaboration, M. Abreu *et al.* , Phys. Lett. **B477**, 28 (2000).

[97] R. Thewes *et al.* , J. Phys. G: Nucl. Part. Phys. **27**, 715 (2001).

[98] F. Karsch, D. Kharzeev, and H. Satz , Phys. Lett. **B637**, 75 (2006).

[99] H. Specht `nucl-ex/0111011`.

[100] J. C. Collins, D. Soper, and G. Sterman , Nucl. Phys. **B261**, 104 (1985).

[101] A. Cooper-Sarkar, R. Devenish, and A. De Roeck `hep-ph/9712301`.

[102] S. Alekhin `hep-ph/0601012`.

[103] G. Altarelli and G. Parisi , Nucl. Phys. **B126**, 298 (1977).

[104] V. Gribov and L. Lipatov , Sov. Journ. Nucl. Phys. **15**, 438 (1972).

[105] Y. Dokshitzer , Sov. Phys. JETP **46**, 641 (1977).

[106] A. Martin *et al.* , Eur. Phys. Jour. **C23**, 73 (2003).

[107] CTEQ Collaboration, H. Lai *et al.* , Eur. Phys. J. **C12**, 375 (2000).

[108] M. Gluck, E. Reya, and A. Vogt , Z. Phys. **C67**, 433 (1995).

[109] M. Hirai, S. Kumano, T. Nagai, and K. Sudoh `hep-ph/0612009`.

[110] M. Arneodo , Phys. Rep. **240**, 301 (1994).

[111] C. Bilchak, D. Schildknecht, and J. Stroughair , Phys. Lett. **B233**, 461 (1989).

[112] G. Piller *et al.* , Phys. Rev. **C42**, R1834 (1990).

[113] N. Nikolaev and B. Zakharov , Z. Phys. **C49**, 607 (1991).

[114] K. Eskola, V. Kolhinen, and P. Ruuskanen , Nucl. Phys. **B535**, 351 (1998).

[115] M. Hirai, S. Kumano, and M. Miyama , Phys. Rev. **D64**, 034003 (2001).

[116] K. Eskola, H. Honkanen, V. Kolhinen, and C. Salgado `hep-ph/0201256`.

[117] L. Shi-Yuan and X.-N. Wang , Phys. Lett. **B527**, 85 (2002).

[118] C. C. N. Brown *et al.* , Phys. Rev. **C54**, 3195 (1996).

[119] D. D'Enterria , J. Phys. **G31**, S491 (2005).

[120] J. Cronin *et al.* , Phys. Rev. **D11**, 3105 (1975).

[121] WA98 Collaboration, M. Aggarwal *et al.* , Eur. Phys. J. **C23**, 225 (2002).

[122] E. Iancu `hep-ph/0608086`.

[123] F. Gelis `hep-ph/0701225`.

[124] H1 Collaboration, C. Adloff *et al.* , Acta Phys. Polon. **B33**, 2841 (2002).

[125] ZEUS Collaboration, M. Derrick *et al.* , Phys. Lett. **B345**, 576 (1995).

[126] BRAHMS Collaboration, I. Arsene *et al.* , Phys. Rev. Lett. **93**, 242303 (2004).

[127] D. Kharzeev, E. Levin, and M. Nardi , Nucl. Phys. **A747**, 609 (2005).

[128] N. Armesto, C. Salgado, and U. Wiedemann , Phys. Rev. Lett. **94**, 022002 (2005).

[129] T. Hirano and Y. Nara , Nucl. Phys. **A743**, 305 (2004).

[130] A. Accardi *et al.* `hep-ph/0310274`.

[131] M. Gyulassy and X. Wang , Nucl. Phys. **B420**, 583 (1994).

[132] R. Baier, Y. Dokshitzer, A. Mueller, S. Peigne, and D. Schiff , Nucl. Phys. **B483**, 291 (1997).

[133] M. Gyulassy, P. Levai, and I. Vitev , Nucl. Phys. **B594**, 371 (2001).

[134] M. Gyulassy, I. Vitev, X. Wang, and B. Zhang `nucl-th/0302077`.

[135] I. Vitev , Phys. Lett. **B639**, 38 (2006).

[136] I. Vitev `hep-ph/0511237`.

[137] I. Vitev and M. Gyulassy , Phys. Rev. **C65**, 041902 (2002).

[138] K. Eskola, H. Honkanen, C. Salgado, and U. Wiedemann , Nucl. Phys. **A747**, 511 (2005).

[139] C. Salgado and U. Wiedemann , Phys. Rev. **D68**, 014008 (2003).

[140] A. Dainese, C. Loizides, and G. Paic , Acta Physica Hungarica **A27**, x (2006).

[141] A. Dainese, C. Loizides, and G. Paic , Eur. Phys. J. **C38**, 461 (2005).

[142] A. Dainese, C. Loizides, and G. Paic `hep-ph/0608133`.

[143] P. Jacobs and X. Wang , Prog. Part. Nucl. Phys. **54**, 443 (2005).

[144] X. Wang and X. Guo , Nucl. Phys. **A696**, 788 (2001).

[145] X. Wang , Nucl. Phys. **A774**, 215 (2006).

[146] HERMES Collaboration, A. Airapetian *et al.* , Eur. Phys. J. **C20**, 479 (2001).

[147] H. Zhang, J. Owens, E. Wang, and X. Wang `nucl-th/0701045`.

[148] A. Polleri and F. Yuan `nucl-th/0108056`.

[149] B. Kniehl, G. Kramer, and B. Potter , Nucl. Phys. **B597**, 337 (2001).

[150] T. Hirano and Y. Nara , J. Phys. **G30**, S1139 (2004).

[151] T. T. Sjostrand, P. Eden, C. Friberg, L. Lonnblad, G. Miu, S. Mrenna, and E. Norrbin , Comput. Phys. Commun. **135**, 238 (2001).

[152] T. Hirano and Y. Nara , Phys. Rev. **C68**, 064902 (2003).

[153] G. Barnafoldi, L. Levai, G. Papp, and G. Fai `hep-ph/0609023`.

[154] G. Barnafoldi, L. Levai, G. Papp, and G. Fai , Nucl. Phys. **A774**, 801 (2006).

[155] X.-N. Wang and M. Gyulassy , Phys. Rev. **D44**, 3501 (1991).

[156] STAR Collaboration, B. Abelev *et al.* `nucl-ex/0609021`.

[157] PHENIX Collaboration, K. Adcox *et al.* , Nucl. Phys. **A757**, 184 (2005).

[158] STAR Collaboration, J. Adams *et al.* , Nucl. Phys. **A757**, 102 (2005).

[159] R. Hwa and C. Yang , Phys. Rev. **C70**, 024905 (2004).

[160] R. Hwa and C. Yang , Phys. Rev. **C71**, 024902 (2005).

[161] R. Hwa and C. Yang , Phys. Rev. **C70**, 024904 (2004).

[162] R. Hwa and C. Yang `nucl-th/0605037`.

[163] BRAHMS Collaboration, I. Arsene *et al.* , Submitted to Phys. Lett. B (2006) `nucl-ex/0602018`.

[164] H. Hahn *et al.* , Nucl. Instrum. Meth. **A499**, 245 (2003).

[165] BRAHMS Collaboration, M. Adamczyk *et al.* , Nucl. Instrum. Meth. **A499**, 437–468 (2003).

[166] H. Ito. PhD thesis, Kansas University, 2002.

[167] Y. Blyakhman. PhD thesis, University of New York, 2001.

[168] R. Debbe, C. Jorgensen, J. Olness, and Z. Yin , Nucl. Instrum. Meth. **A570**, 216 (2007).

[169] T. Larsen Master's thesis, University of Oslo, 2003.

[170] P. Staszel, 'Brahms analysis notes 34, 38.'

[171] C. Jorgensen , Ph.D. Thesis, Copenhagen University (2004).

[172] STAR Collaboration, B. Abelev *et al.* , Phys. Rev. Lett. **97**, 152301 (2006).

[173] STAR Collaboration, B. Abelev *et al.* `nucl-ex/0703033`.